

STUDY OF CRYSTAL STRUCTURES AND PHASE TRANSITIONS OF
SOLID DEUTERIUM IODIDE

A thesis submitted for the degree of Doctor of Philosophy
of London University

by

John Hartley Clarke

Department of Physics
Queen Mary College
Mile End Road
LONDON E14 4NS

April 1975

STUDY OF CRYSTAL STRUCTURES AND PHASE TRANSITIONS OF
SOLID DEUTERIUM IODIDE

Abstract

The crystal structure of solid deuterium iodide was studied by thermal neutron and X-ray diffraction at three temperatures. At 4.2K the low phase structure is ordered, monoclinic space group $C2/c$, with 16 molecules in the unit cell. At 84K a two-fold disordered orthorhombic structure, space group $Bbcm$, is proposed with four molecules in the unit cell, each deuterium atom oscillating between two equivalent positions 180° apart. This middle phase is isomorphous with deuterium bromide.

At 137K a twelve-fold disordered cubic structure is proposed, space group $Fm\bar{3}m$, with four molecules in the face-centred unit cell. The deuterium atom occupies in turn twelve statistically equivalent positions. This structure is isomorphous with the high phases of deuterium chloride and bromide.

Phase transitions between the monoclinic and orthorhombic phases at 77K and the orthorhombic and cubic phases at 127K were studied by neutron diffraction in the temperature intervals 45-80K and 110-130K. Order parameters for these transitions have been calculated from the neutron diffraction data and agreement obtained with those calculated from calorimetric data for the lower transition.

ACKNOWLEDGEMENTS

It is a pleasure to thank Dr E Sándor, my supervisor, for his guidance and encouragement during the course of this work.

I would also like to thank: C Hotston, P Cruze and R Putney of Queen Mary College for technical assistance, Professor G O Jones, Professor A Ashmore and Professor D H Martin for the research facilities at Queen Mary College and Mr D H C Harris and his staff for assistance with the neutron diffraction experiments at A.E.R.E., Harwell.

Finally I thank the Science Research Council for a research studentship and the Neutron Beam Research Committee for providing neutron facilities.

TABLE OF CONTENTS

	<u>Page</u>
Abstract	2
Acknowledgements	3
Table of contents	4
List of figures	7
List of tables	15
 <u>CHAPTER ONE - Review of previous work on HI and DI</u>	 18
1.1 Introduction	18
1.2 Calorimetric experiments	19
1.3 X-ray experiments	21
1.4 Optical experiments	23
1.5 Dielectric experiments	24
(a) Static dielectric constant measurements	24
(b) Complex dielectric constant measurements	27
1.6 Nuclear magnetic resonance experiments (NMR)	35
1.7 Infra-red spectroscopy	45
1.8 Theories of phase transitions in molecular crystals	49
 <u>CHAPTER TWO - Experimental work</u>	 52
2.1 Chemical preparations	52
(a) Indirect preparation of HI/DI	53
(b) Direct preparation of DI	55
2.2 X-ray diffraction study of DI	57
2.3 Neutron diffraction study of DI	65
(a) Dido 'Curran' powder diffractometer	66
(b) Dido 'Badger' powder diffractometer	69
(c) Pluto 'Panda' powder diffractometer	69
2.4 Cryostats used in neutron diffraction experiments	74
(a) T.B.T. cryostat	74
(b) B.O.C. cryostat	74

	<u>Page</u>
<u>CHAPTER THREE - X-ray powder diffraction study of the iodine</u>	79
<u>sublattice in the three solid phases of DI</u>	
3.1 Introductory theory of diffraction	79
3.2 X-ray diffraction experiments	83
(a) The low phase of DI	83
(b) The middle and high phases of DI	87
<u>CHAPTER FOUR - Neutron powder diffraction study of the crystal</u>	92
<u>structure of the low phase of DI at 4.2K</u>	
4.1 Summary of the neutron diffraction experiments	92
4.2 The unit cell of the low phase	94
4.3 Models based on orthorhombic space groups	99
4.4 Models based on monoclinic space groups	102
4.5 Refinement of the model based on space group C2/c (No.15)	119
4.6 Analysis of the intensity transform of the neutron powder pattern of the low phase	134
4.7 Conclusion	143
<u>CHAPTER FIVE - Neutron powder diffraction study of the crystal</u>	147
<u>structure of the middle phase of DI</u>	
<u>CHAPTER SIX - Neutron powder diffraction study of the crystal</u>	155
<u>structure of the high phase of DI</u>	
6.1 Zinc-sulphide-type model space group Fm3m (No.225)	157
6.2 Sodium-chloride-type model space group Fm3m (No.225)	157
6.3 Four-fold disordered model space group $F\bar{4}3m$ (No.216)	158
6.4 Six-fold disordered model space group Fm3m (No.225)	158
6.5 Eight-fold disordered model space group Fm3 (No.202)	158
6.6 Twelve-fold disordered model space group Fm3m (No.225)	158
6.7 Freely-rotating or randomly disordered model	159
6.8 Comparison of observed structure factors with structure factors calculated from disordered models	160

	<u>Page</u>
<u>CHAPTER SEVEN - Neutron powder diffraction study of the two</u>	170
<u>phase transitions in solid DI</u>	
7.1 The lower phase transition	170
7.2 The upper phase transition	180
7.3 Conclusion	192
 <u>CHAPTER EIGHT - Summary</u>	 194
8.1 Conclusions of the earlier experimental studies concerning the crystal structure of DI	194
8.2 The crystal structure of DI as determined by X-ray and neutron diffraction	196
8.3 The nature of the two phase transitions in solid DI	197
8.4 Suggested further experiments on HI/DI	199
(a) Neutron powder diffraction	199
(b) Neutron single-crystal diffraction	200
(c) Inelastic neutron scattering	200
 <u>APPENDIX ONE - Computer programs</u>	 202
A1.1 Least-squares refinement of crystal structures	202
A1.2 Least-squares refinement of cell dimensions	203
A1.3 Calculation of powder peak positions	204
A1.4 Calculation of random-orientation structure factors	204
A1.5 LPSG, Low phase symmetry generator	204
A1.6 The Rietveld program	205
 <u>APPENDIX TWO - Temperature measurement and control circuit</u>	 207
<u>of the variable temperature cryostat</u>	
 <u>List of References</u>	 212

List of figures

Chapter one

- 1.1 Specific heats of HI/DI at constant pressure as a function of temperature, Clusius and Wolf (1947).
- 1.2 Static dielectric constants of HCl, HBr/DBr and HI/DI as a function of temperature, Cole and Havriliak (1957), Brown and Cole (1953) and Swenson and Cole (1954).
- 1.3 Imaginary versus real dielectric constant of HI/DI below the lower phase transition point, Cole and Havriliak (1957).
- 1.4 Imaginary versus real dielectric constant of HI/DI above the lower phase transition point, Cole and Havriliak (1957).
- 1.5 Absorption conductance of DI and DBr as a function of frequency, Cole and Havriliak (1957).
- 1.6 Relaxation times for hydrogen halides as a function of temperature determined by dielectric absorption methods, Cole and Havriliak (1957).
- 1.7 Imaginary versus real dielectric constant of HI as a function of temperature, Groenewegen and Cole (1966).
- 1.8 Reduced locus of the imaginary dielectric constant versus the real part, Groenewegen and Cole (1966).
- 1.9 Relaxation frequency as a function of temperature for HBr and HI, Groenewegen and Cole (1966).
- 1.10 NMR line width versus temperature for HI, Alpert (1949).
- 1.11 Spin-lattice relaxation times versus temperature for DCl, DBr and DI, Genin et al (1968).

- 1.12 Spin-lattice, rotating frame and spin-spin relaxation times, and second moment data for HCl, HBr and HI as a function of temperature, Genin et al (1968).
- 1.13 Relaxation times as a function of temperature derived from NMR and dielectric loss measurements on HI, Genin et al (1968) and Groenewegen and Cole (1966).
- 1.14 NMR dispersion signal in polycrystalline DI at 96K and 7 MHz, Genin et al (1968).
- 1.15 NQR coupling constants of polycrystalline DCl, DBr and DI, as a function of temperature, Genin et al (1968).
- 1.16 Infra-red transmission spectra of HI as a function of temperature on cooling through the lower phase transition at 70K, Hornig and Osberg (1955).
- 1.17 Infra-red transmission spectra of HI as a function of temperature, Hiebert and Hornig (1957).

Chapter two

- 2.1 HI and DI sample preparation system used for the indirect method §2.1a.
- 2.2 DI sample preparation system used for the direct method §2.1b.
- 2.3 DI sample purification system used for the direct method §2.1b.
- 2.4 Low temperature X-ray goniometer used at Queen Mary College.
- 2.5 Liquid helium cryostat used on the Queen Mary College X-ray powder diffractometer.
- 2.6 The configuration of the Dido 'Curran' neutron powder diffractometer.
- 2.7 Photograph of the Dido 'Curran' neutron powder diffractometer.

- 2.8 The configuration of the Pluto 'Panda' neutron powder diffractometer.
- 2.9 Photograph of the Pluto 'Panda' neutron powder diffractometer.
- 2.10 The variable temperature cryostat used for studying the lower phase transition of DI by neutron diffraction.

Chapter three

- 3.1 Low-angle X-ray powder photograph of DI at 84K and 50K.
- 3.2 X-ray powder pattern of DI at 4.2K (low phase) chart recorder output.
- 3.3 X-ray powder photograph of DI at 117K (middle phase).
- 3.4 X-ray powder photograph of DI at 130K (high phase).
- 3.5 Lattice parameters of HI and DI as a function of temperature.

Chapter four

- 4.1 Neutron powder diffraction pattern of DI at 4.2K (low phase) recorded with Dido 'Curran'.
- 4.2 Neutron powder diffraction pattern of DI at 4.2K (low phase) recorded with Pluto 'Panda'.
- 4.3 Proposed structure for DI low phase space-group Fdd2 (No.43), model No.1.
- 4.4 Proposed structure for DI low phase space-group Fdd2 (No.43), model No.2.
- 4.5 Proposed structure for DI low phase space-group Fdd2 (No.43), model No.3.
- 4.6 The six methods of transforming the large orthorhombic unit cell to the smaller monoclinic unit cell.
- 4.7 Middle phase structure of DI drawn in a monoclinic unit cell, type No.1.

- 4.8 Middle phase structure of DI drawn in a monoclinic unit cell, type No.2
- 4.9 Middle phase structure of DI drawn in a monoclinic unit cell, type No.3.
- 4.10 Middle phase structure of DI drawn in a monoclinic unit cell, type No.4.
- 4.11 Middle phase structure of DI drawn in a monoclinic unit cell, type No.5.
- 4.12 Middle phase structure of DI drawn in a monoclinic unit cell, type No.6.
- 4.13 Middle phase structure of DI drawn in a monoclinic unit cell, type No.3
projected onto the (001) monoclinic plane.
- 4.14 Middle phase structure of DI drawn in a monoclinic unit cell, type No.4
projected onto the (001) monoclinic plane.
- 4.15 Proposed structure for DI low phase space group Cc (No.9) model No.1.
- 4.16 Proposed structure for DI low phase space group Cc (No.9) model No.2.
- 4.17 Proposed structure for DI low phase space group Cc (No.9) model No.3.
- 4.18 Proposed structure for DI low phase space group Cc (No.9) model No.4.
- 4.19 Proposed structure for DI low phase space group Cc (No.9) model No.5.
- 4.20 Proposed structure for DI low phase space group Cc (No.9) model No.6.
- 4.21 Calculated (continuous line) and observed (crosses) intensities for DI
low phase, 'Curran' 4.2K model No.3.
- 4.22 Calculated (continuous line) and observed (crosses) intensities for DI
low phase, 'Curran' 4.2K model No.4.
- 4.23 Calculated (continuous line) and observed (crosses) intensities for DI
low phase, 'Curran' 4.2K model No.5.
- 4.24 Calculated (continuous line) and observed (crosses) intensities for DI
low phase, 'Curran' 4.2K model No.6.

- 4.25 Middle phase structure of DI drawn in an orthorhombic unit cell showing the 8 molecules of the basis chosen to produce 128 models.
- 4.26 Middle phase structure of DI drawn in a monoclinic unit cell type No.6 showing the 6 molecules of the basis chosen to produce 32 models with space group Cm (No.8).
- 4.27 Proposed structure for DI low phase space group C2/c, model No.5 in unit cell No.4.
- 4.28 (a)(b) Observed (crosses) and calculated (solid line) intensities based on model No.5 for DI with Dido 'Curran' at 4.2K.
- 4.29 (a)(b) Observed (crosses) and calculated (solid line) intensities based on model No.5 for DI with Pluto 'Panda' at 4.2K.
- 4.30 Observed (crosses) and calculated (solid line) intensities based on model No.5 for DI with Pluto 'Panda' at 4.2K with the molecule tilted at 5° to the $(001)_m$ plane.
- 4.31 Resolution function of the intensity transform (using a 'window' function) of the neutron powder diffraction pattern of DI recorded on the 'Panda' at 4.2K.
- 4.32 Resolution function of the intensity transform (using no 'window' function) of the neutron powder diffraction pattern of DI recorded on the 'Panda' at 4.2K.
- 4.33 Intensity transform of the neutron powder diffraction pattern of DI recorded on the 'Panda' at 4.2K.
- 4.34 Intensity transform of a neutron powder diffraction pattern of DI calculated on the basis of the model shown in figure 4.19.
- 4.35 Calculated neutron powder diffraction pattern of the iodine sublattice.

- 4.36 Intensity transform of the calculated neutron powder diffraction pattern of the iodine sublattice showing the first six iodine atom nearest neighbour distances calculated from the lattice parameters of table 4.2.
- 4.37 Neutron powder diffraction pattern of DI recorded on 'Panda' at 4.2K minus the calculated neutron powder diffraction pattern of the iodine sublattice.
- 4.38 Intensity transform of the neutron powder diffraction pattern of DI recorded on 'Panda' at 4.2K minus the calculated neutron powder diffraction pattern of the iodine sublattice.
- 4.39 Neutron powder diffraction pattern of DI calculated on the basis of the model shown in figure 4.19 minus the calculated neutron powder diffraction pattern of the iodine sublattice.
- 4.40 Intensity transform of the neutron powder diffraction pattern of DI calculated on the basis of the model shown in figure 4.19 minus the calculated neutron powder diffraction pattern of the iodine sublattice.

Chapter five

- 5.1 Neutron powder diffraction pattern of DI at 84K (middle phase) recorded with the Dido 'Curran' diffractometer.
- 5.2 Two-fold disordered model for DI middle phase, space group Bba2 (No.41).
- 5.3 Four-fold disordered model for DI middle phase, space group Bbcm (No.64).
- 5.4 Proposed two-fold disordered model for DI middle phase, space group Bbcm (No.64).
- 5.5 Observed intensities of neutron powder peaks for DI middle phase recorded at 84K with Dido 'Curran'.
- 5.6 Calculated intensities of neutron powder peaks for two-fold disordered model of DI middle phase space group Bbcm (No.64).

Chapter six

- 6.1 Neutron powder diffraction pattern of DI at 137K (high phase) recorded with the Dido 'Curran' diffractometer.
- 6.2 Zinc-sulphide model for DI high phase, space group $Fm\bar{3}m$ (No.225).
- 6.3 Sodium-chloride model for DI high phase, space group $Fm\bar{3}m$ (No.225).
- 6.4 Four-fold disordered model for DI high phase, space group $F\bar{4}3m$ (No.216).
- 6.5 Six-fold disordered model for DI high phase, space group $Fm\bar{3}m$ (No.225).
- 6.6 Eight-fold disordered model for DI high phase, space group $Fm\bar{3}$ (No.202).
- 6.7 Twelve-fold disordered model for DI high phase, space group $Fm\bar{3}m$ (No.225).
- 6.8 Freely rotating model for DI high phase.
- 6.9 Calculated structure factors for four-fold disordered model of DI high phase, space group $F\bar{4}3m$ (No.216).
- 6.10 Calculated structure factors for six-fold disordered model of DI high phase, space group $Fm\bar{3}m$ (No.225).
- 6.11 Calculated structure factors for eight-fold disordered model of DI high phase, space group, $Fm\bar{3}$ (No.202).
- 6.12 Calculated structure factors for freely-rotating model of DI high phase.
- 6.13 Calculated structure factors for twelve-fold disordered model of DI high phase, space group $Fm\bar{3}m$ (No.225).
- 6.14 Observed and normalized structure factors for DI high phase recorded on Dido 'Curran' at 137K.

Chapter seven

- 7.1 Temperature dependence of the intensity ratio $R(T) = \frac{\sqrt{I(110)+I(11\bar{1})}}{I(220)+I(22\bar{2})}$ measured over the lower phase transition of DI with increasing (X) and decreasing (O) temperatures.
- 7.2 Order parameter $q(T)$ derived from neutron diffraction experiments (+) and specific heat measurements (solid line) over the lower phase transition region of DI.
- 7.3 Temperature dependence of the intensity ratio $I(002)/I(111)$ measured over the upper phase transition of DI with increasing (X) and decreasing (O) temperatures.
- 7.4 Order parameters $q'(T)$ derived from neutron diffraction experiments (+) and specific heat measurements (solid and dotted lines) over the upper phase transition of DI.

Appendix two

- A2.1 Temperature measurement and control circuit for the variable temperature cryostat used in neutron diffraction experiments.
- A2.2 Temperature gradient across sample, as a function of temperature, for the sample tube used for the lower phase transition neutron diffraction experiment on DI.

List of tablesChapter one

- 1.1 Melting, boiling and phase transition temperatures for HI/DI.
- 1.2 The lattice parameters of HI measured by X-ray diffraction.
- 1.3 Activation energies for molecular re-orientation determined from dielectric constant measurements.
- 1.4 Static dielectric constant and maximum absorption frequency vs temperature for HI.
- 1.5 Rotational correlation times and activation energies for DCl, DBr and DI as determined by NMR experiments.
- 1.6 Correlation times for translational diffusion in HCl, HBr and HI calculated by random-walk theory.
- 1.7 Observed and calculated second moments of NMR line shape for HCl, HBr and HI.
- 1.8 Quadrupolar coupling constants measured by NQR experiments for DCl, DBr and DI.
- 1.9 Frequencies of infra-red absorption lines for HI (middle phase).

Chapter three

- 3.1 Lattice parameters of HI and DI measured by neutron and X-ray powder diffraction.

Chapter four

- 4.1 Results of the lattice parameter refinement obtained with the program PARAM for the low phase of DI at 4.2K. The refinement is based upon the powder diffraction pattern recorded with the 'Panda' with a neutron wavelength of $\lambda = 1.886\text{\AA}$.
- 4.2 Miller indices of Bragg peaks observed in the neutron powder diffraction pattern of DI in the orthorhombic and the six monoclinic unit cells.
- 4.3 Summary of the unit cells and space groups considered for the structure of the low phase of DI.

Chapter five

- 5.1 Structural parameters of DI at 84K (middle phase).

Chapter six

- 6.1 R-factors obtained in the least-squares refinement of four disordered models proposed for the high phase of DI.
- 6.2 Structural parameters of DI at 137K (high phase).

Chapter seven

- 7.1 Intensities of neutron powder peaks measured over the lower phase transition of DI with increasing and decreasing temperature and the $R(T)$ and $q(T)$ values derived from these measurements.
- 7.2 Temperature dependence of the anomalous specific heat over the lower transition of DI. The values listed were calculated from the data of Clusius and Wolf (1947).

- 7.3 Intensities of neutron powder peaks measured over the upper phase transition of DI with increasing and decreasing temperature and the ratio and $q'(T)$ values derived from them.
- 7.4 Temperature dependence of the anomalous specific heat over the upper phase transition of DI. The values in this table were calculated from the data of Clusius and Wolf (1947).

CHAPTER ONE

Review of previous work on HI and DI

1.1 Introduction

This study of the crystal structures and phase transitions of the hydrogen and deuterium iodides was undertaken as the last of a series of experiments on the hydrogen and deuterium halides at Queen Mary College.

Due to similarities in the calorimetric and dielectric properties of deuterium bromide and deuterium iodide, it was expected to find that the two compounds had similar structures. It was therefore interesting that, although the middle and high phases of deuterium iodide and deuterium bromide were isomorphous, their low phases had quite different symmetries. The low phase of deuterium iodide was in fact monoclinic as opposed to the orthorhombic low phase of deuterium bromide.

The hydrogen and deuterium iodides, hereafter referred to as HI and DI, have similar physical properties which are summarized below in table 1.1. Three of the hydrogen halides, HCl, HBr and HI, possess more than one solid phase which are stable within well-defined temperature ranges. This thesis describes the determination of the crystal structures of the three solid phases of DI and the mechanisms of the two phase transitions between them.

The experimental work performed on HI/DI prior to this thesis will now be described in detail.

Compound	Melting Point	Boiling Point	T_C^* (lower)	T_C^* (upper)
HI	223.2K	237.6K	70.1K	125.7K
DI	221.2K	237.25K	77.3K	128.3K

Table 1.1 Melting, boiling and phase transition temperatures for HI and DI

T_C^* is the temperature where the phase transition is complete, when observed with increasing temperature.

1.2 Calorimetric experiments

The specific heat of HI at constant pressure C_p was first measured by Eucken and Karwat (1924) over the temperature range of 58 to 237K. Subsequently as part of a series of very accurate experiments designed to test the validity of the third law of thermodynamics, the specific heats of the hydrogen and deuterium iodides were remeasured first by Giauque and Wiebe (1929) (HI only) and then by Clusius and Wolf (1947) (both HI and DI). The results of Clusius and Wolf are shown in figure 1.1. The earlier results obtained by Eucken and Karwat were similar only the statistical scatter was greater.

Both the C_p versus T graphs in figure 1.1 show two anomalies which are attributed to second-order phase transitions. A first-order phase transition is defined as a discontinuous change in a thermodynamic variable (such as C_p) and is usually associated with a change of structural symmetry. A second-order phase transition is associated with a change in a first-derivative of a thermodynamic variable. The two transitions in figure 1.1 are of this type and are also referred to as lambda transitions due to the characteristic shape of the C_p versus T graph in the transition region.

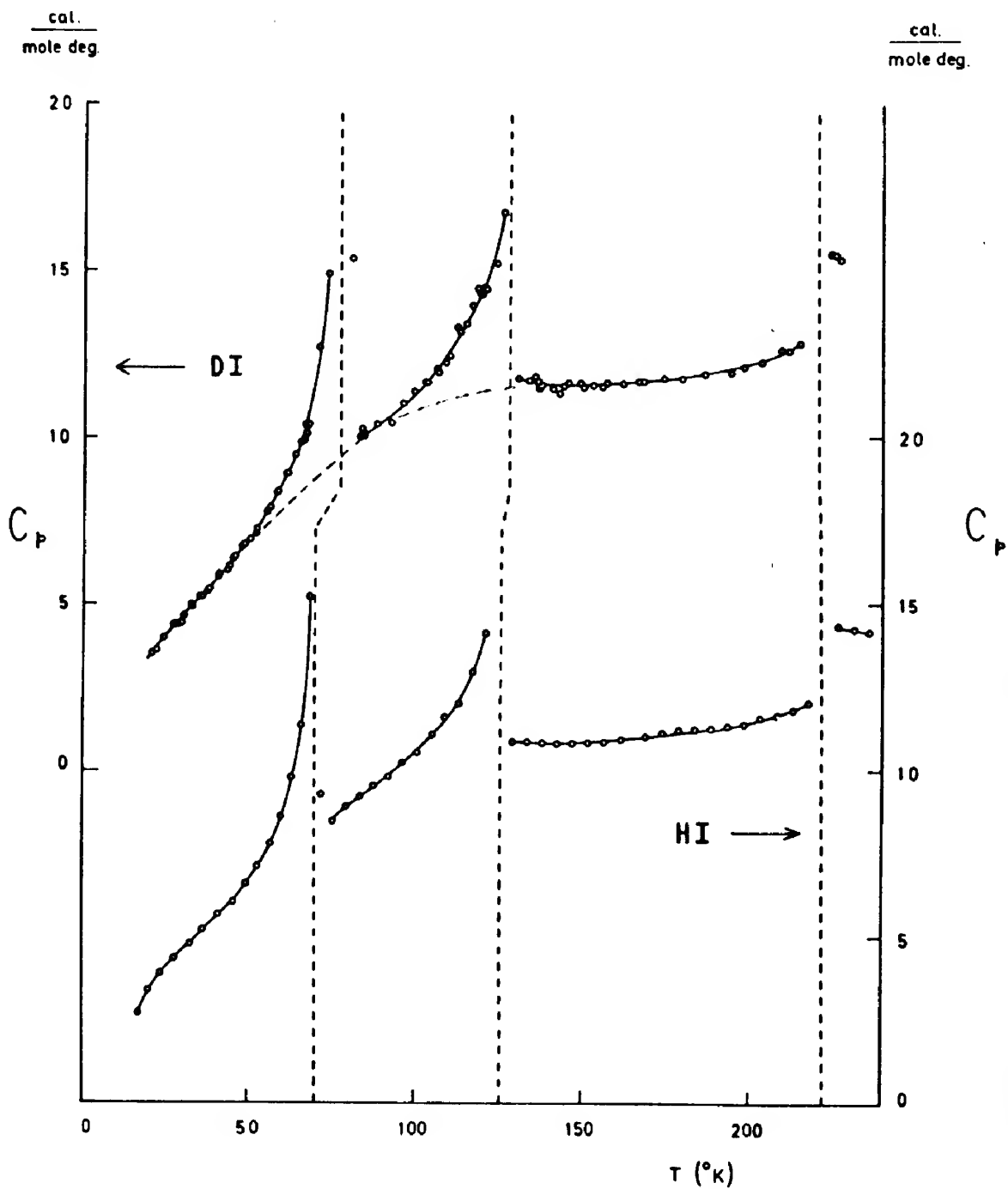


Figure 1.1 Specific heats of HI and DI at constant pressure as a function of temperature, Clusius and Wolf (1947).

The two λ -transitions in HI and DI are associated with the reorientation of the molecules in the crystal. By considering the changes in the molecular configuration when undergoing a transition between two solid phases, it is possible to calculate the anomalous entropy associated with the two second-order phase transitions. This will be discussed in a later chapter.

The C_p versus T graphs of HI and DI are similar to that of DBr but are unlike those of HF/DF, HCl/DCI and HBr. The different behaviour of HBr and DBr is an unusual isotope effect which was studied by Johnson (1970). The HCl/DCI transition is of the first order and was shown to be due to a change from an ordered orthorhombic structure to a disordered cubic phase by Farrow (1969), and Sándor and Farrow (1969). HF/DF has no solid-solid phase transitions and its structure has been determined, Johnson and Sándor (1975).

1.3 X-ray experiments

The X-ray powder diffraction pattern of solid HI was studied by Natta (1930 and 1931), by Ruhemann and Simon (1931) using photographic techniques and later by Mauer and Keffer using counter methods (1964). The experiments gave information only about the positions of the iodine atoms.

- (a) Natta in his first paper (1930) reported that HI was cubic at 103K (middle phase). For his second paper (1931) he obtained better quality photographs and was able to assign Miller indices to powder lines which he had previously considered as being due to possible impurities such as ice or iodine (caused by dissociation of the HI samples during irradiation by X-rays).

He reported the lattice parameters of a tetragonal face-centred lattice at 100K and also described photographs taken at 188K, 112K, 90K and 77K. These showed tetragonal symmetry but the lattice parameters were not reported. He did not appear to have observed the cubic phase above 125K, nor the orthorhombic nature of the middle phase, as was found in our experiments. Discrimination between the tetragonal and orthorhombic symmetry may have been beyond the resolution of the X-ray photographs, which is not surprising as the orthorhombic lattice parameters differ by only 1%. The absence of the cubic phase can only be implied from his report as lattice parameters are only quoted for a temperature of 100K.

- (b) Ruhemann and Simon (1931) recorded the X-ray powder diffraction pattern of solid HI with a 48mm diameter camera using $\text{CuK}\alpha$ radiation. Photographs were taken of the three solid phases at the following temperatures: 21K (low), 82K (middle) and 125K (high phase). All the powder patterns were indexed on the basis of a face-centred tetragonal structure. The non-observation of the cubic high phase could probably be explained by a systematic error in the temperature measurement.
- (c) Mauer and Keffer (1964) studied X-ray diffraction patterns from a flat plate of HI powder by a counter diffractometer at six temperatures. They found that the structure of HI was face-centred tetragonal in the low and middle phases, and face-centred cubic in the high phase above 125K.

A summary of the published X-ray work on HI is given in Table 1.2. Some recent X-ray experiments on the middle and high phases of HI are described in chapter three (Simon 1970).

Temperature	$a \text{ \AA}$	c/a	Phase	Author
103K	6.18	1.0	fcc	Natta (1930)
77K	-	-))
90K	-	-))
112K	-	-)) Natta (1931)
188K	-	-))
100K	6.10	1.08))
21K	5.94 ± 0.01	1.08) fct) Ruhemann and
82K	6.03 ± 0.01	1.08)) Simon (1931)
125K	6.19 ± 0.01	1.08))
4.2K	5.987	1.082)) Mauer and
39K	6.000	1.082)) Keffer (1964)
77K	6.042	1.080))
120K	6.106	1.072))
130K	6.246	1.0))
180K	6.295	1.0) fcc)

Table 1.2 The lattice parameters of HI measured by X-ray diffraction

1.4 Optical experiments

The optical isotropy of the hydrogen halides was studied in 1938 by Kruis and Kaischew. They investigated the rotation of the plane of polarization of a beam of polarized light incident on a 1mm thick sample of the crystalline hydrogen halide. The temperature of the sample was varied from 40K to 220K and the polarization of the transmitted beam observed.

Their results indicated that HCl, HBr and HI were optically isotropic

in the high phase and anisotropic in the lower phases. The phase transition from the anisotropic lower phases to the isotropic high phase could be observed in each compound but transitions between the anisotropic lower phases of HBr and HI could not. These results are consistent with the high phase of each compound possessing cubic symmetry and the other phases lower symmetries.

1.5 Dielectric experiments

(a) Static dielectric constant measurements

The static dielectric constant of an isotropic medium ϵ is defined by the equation:

$$\epsilon = \frac{D}{E} = \frac{E + 4\pi P}{E} \quad (1)$$

where \underline{E} is the applied electric field, \underline{D} the displacement field and \underline{P} is the polarization induced inside the material by the applied field. \underline{P} is equal to the dipole moment per unit volume, the dipole moment of a sample of N atoms being defined as:

$$\underline{P} = \sum_{n=1}^N \underline{r}_n q_n \quad (2)$$

where \underline{r}_n is the position vector of the n th atom with charge q_n . The dipole moment is measured in Debye units (10^{-18} e.s.u.). This is approximately the charge of one electron multiplied by one Ångström. In S.I. units:

$$1D = 3.336 \times 10^{-30} \text{ Cm}$$

The dielectric constant is a dimensionless number. The dipole moments of the hydrogen halide molecules are:

$$\mu(\text{HF}) = 1.91 \text{ D}$$

$$\mu(\text{HCl}) = 1.12 \text{ D}$$

$$\mu(\text{HBr}) = 0.85 \text{ D}$$

$$\mu(\text{HI}) = 0.40 \text{ D}$$

These values were obtained from the temperature dependence of the static dielectric constant. The technique, using the Clausius-Mossotti and the Languin-Debye equations, is described by Kittel (1967a).

The static dielectric constant of solid HI was first studied by Smyth and Hitchcock in 1933. A later series of experiments performed by Cole and Havriliak in 1957 covered a wider temperature range and their results are reproduced in figure 1.2. The low phase section of figure 1.2 for HI/DI shows a low value for the dielectric constant indicating that the structure is ordered. As the temperature rises, an increase in the dielectric constant is observed and can be attributed to the greater orientational freedom of the molecules. The temperature range over which the transition occurs is approximately 20°K wide suggesting that the onset of molecular re-orientation is gradual.

The subsequent decrease of the dielectric constant with increasing temperature suggests a disordered structure in the middle phase. The behaviour of the dielectric constants of HBr and DBr is very similar to HI/DI. HBr has an additional solid phase, mentioned in section 1.2, which is stable just below the upper phase transition point. The static dielectric constant of HBr at 118K can be seen to differ from DBr and have an additional minimum value in figure 1.2. In HCl the single phase transition is very sharp, and is accentuated by a discontinuous rise in the static dielectric constant (see figure 1.2).

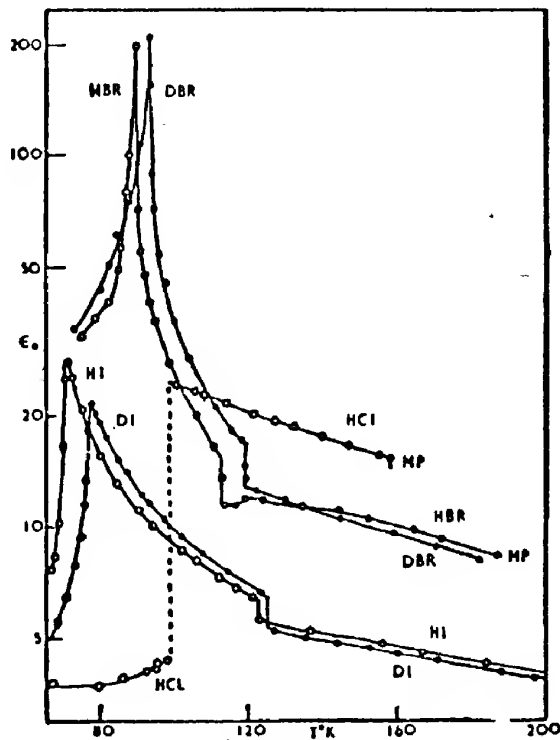


Figure 1.2 Static dielectric constants of HCl, HBr, DBr, HI and DI as a function of temperature, Cole and Havriliak (1957), Brown and Cole (1953) and Swenson and Cole (1954).

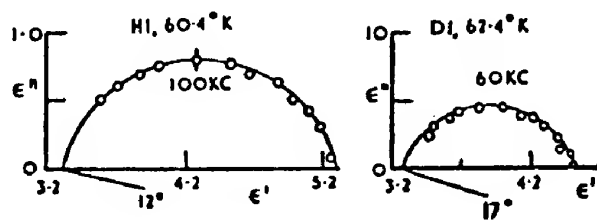


Figure 1.3 Imaginary versus real dielectric constant of HI and DI below the lower phase transition point, Cole and Havriliak (1957).

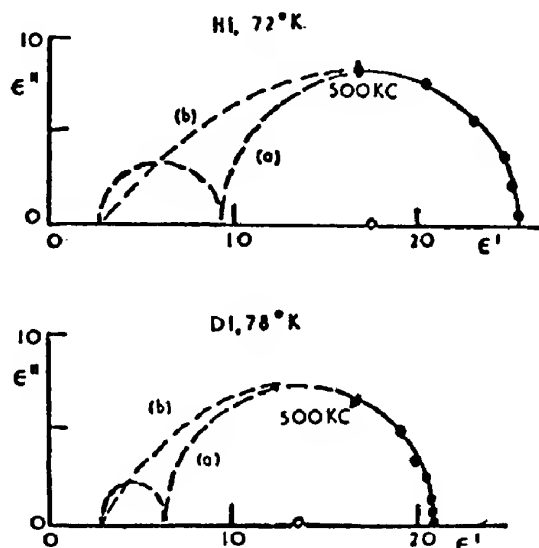


Figure 1.4 Imaginary versus real dielectric constant of HI and DI above the lower phase transition point, Cole and Havriliak (1957).

The decrease of the static dielectric constant with temperature is similar to that of a disordered structure. The resultant dipole moment is reduced by the greater thermal motion of the molecules. This Debye-behaviour is described in liquids by the Langevin function as discussed by Kittel (1967b).

$$L(x) = \coth(x) - 1/x \quad (3)$$

$x = \frac{pE}{kT}$, p is the dipole moment, E the electric field, k the Boltzmann constant and T the absolute temperature.

Above the upper phase transition point, a sharp decrease in the static dielectric constant occurs which can be attributed to a decrease in density and/or an increase in orientational disorder, possibly from two to three dimensions. This is followed by a further continuous decrease due to the larger thermal motion as the sample approaches its melting point.

(b) Complex dielectric constant measurements

An oscillating external electric field may be applied to the material being studied and the molecular dipoles will attempt to re-orient in phase with this field. However, the intermolecular forces, thermal motion and the inertia of the molecules retard this re-orientation process.

The average time taken for a molecule to return to equilibrium from a polarized state via a re-orientation process is defined as the relaxation time. To describe this behaviour mathematically the dielectric constant is treated as a complex quantity, ϵ^* . This complex dielectric constant has been measured in HI and DI by Cole and co-workers.

The frequency-dependent behaviour of the dielectric constant is best represented by the empirical formula of Cole and Cole (1941):

$$\epsilon^* = \epsilon' - i\epsilon'' = (\epsilon_0 - \epsilon_\infty) / [1 + (i\omega\tau_0)^{1-\alpha}] \quad (4)$$

This is a modification of the theoretical formula for polar liquids derived by Debye (1929).

$$\epsilon^* - \epsilon_\infty = (\epsilon_0 - \epsilon_\infty) / (1 + i\omega\tau_0) \quad (5)$$

where ϵ_0 is the static dielectric constant. ϵ_∞ is referred to as the infinite-frequency value and represents the electronic polarizability since at high frequencies the ionic and orientational polarizabilities are small due to the inertia of the molecules. τ_0 is a generalized relaxation time, α is an empirical constant varying between 0 and 1 and ω is the frequency.

The complex dielectric constant appears as the arc of a circle with its centre on or below the real x-axis when drawn in the complex plane of an Argand diagram. This empirical formula of Cole and Cole, eqn. (4), has been found to describe adequately the behaviour of the complex dielectric constant of a number of substances. Such diagrams are referred to in the literature as 'Cole-Cole' plots after the original paper of Cole and Cole (1941). Each point on the arc represents a different frequency and the absorption maximum is at the point of maximum ϵ'' .

Figures 1.3 and 1.4 show the complex dielectric constant of HI/DI at temperatures below and above the lower phase transition point, Cole and Havriliak (1957). The arcs drawn by Cole for figure 1.4 were stated to be exactly semi-circular although only frequencies up to 500 Hz had been recorded. The subsidiary arcs were suggested by Cole as continuations to higher frequencies. Above the lower phase transition point the centre of the arc lies on the ϵ' -axis, while below the transition point the centre of the arc lies below the ϵ' -axis. To verify the semi-circular shape of the arcs in figure 1.4, Cole plotted logarithms of the frequency against a

function called the absorption conductance which is proportional to $\omega\epsilon''$ and is measured in siemens or reciprocal ohms and obtained the lines of figure 1.5. When $\omega\tau_0 \ll 1$ only low frequencies are considered and Debye's equation can be approximated to give:

$$\omega\epsilon'' \approx (\epsilon_0 - \epsilon_\infty) \tau_0 \omega^2 \quad (6)$$

Cole plotted $\log_{10}(\omega\epsilon'')$ versus $\log_{10}(\frac{\omega}{2\pi})$ and obtained a straight line of slope 2. This confirmed that α , the empirical constant of Cole and Cole (1941), was zero and that the frequency dependence of ϵ^* , the complex dielectric constant had a Debye form of relaxation. When performing these experiments in 1957 Cole and Havriliak were unable to extend the frequency range of their measurements beyond 1 MHz and were therefore unable to observe any dispersion in the high phases of H1 and D1.

Since the maximum absorption occurs at the resonance frequency, the relaxation time τ_0 which is characteristic of this absorption is the reciprocal of the frequency. Cole plotted the logarithm of this relaxation time versus the reciprocal of the temperature and obtained the curves of figure 1.6. A frequency term A related to the probability of the dipole undergoing a relaxation process was defined by the expression:

$$A = \frac{1}{\tau_0} \exp(E_a/2.3RT) \quad (7)$$

where E_a is an activation energy and R is proportional to the Boltzmann constant. Cole applied the relation:

$$\log_{10} \tau_0 = -\log_{10} A + E_a/2.3RT \quad (8)$$

to these data and obtained a series of activation energies tabulated in table 1.3.

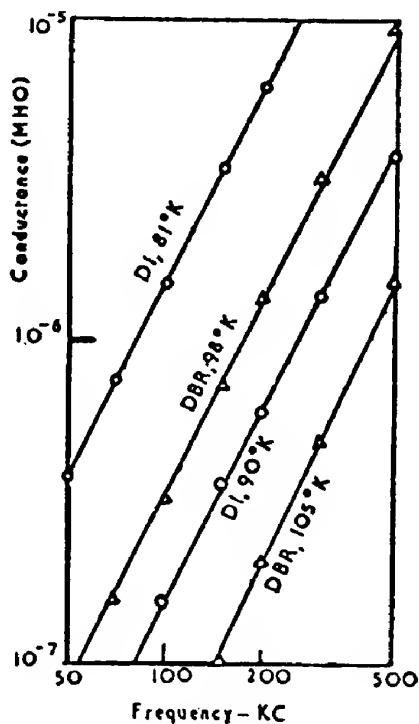


Figure 1.5 Absorption conductance of DI and DBr as a function of frequency, Cole and Havriliak (1957).

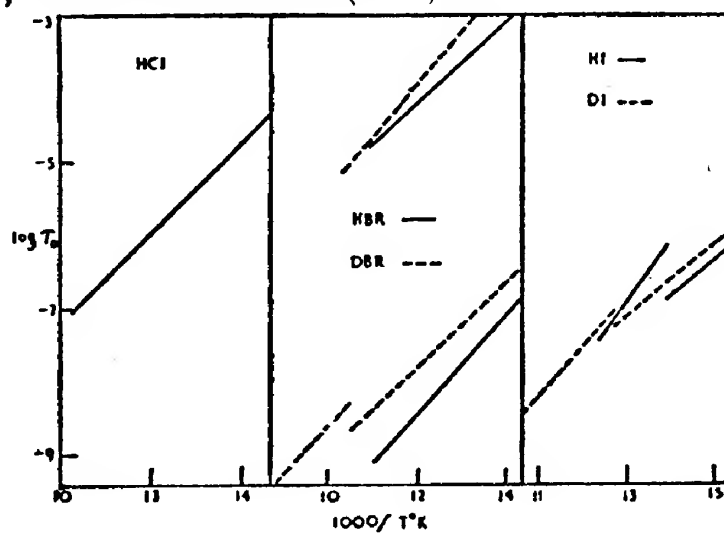


Figure 1.6 Relaxation times for hydrogen halides as a function of temperature determined by dielectric absorption methods, Cole and Havriliak (1957).

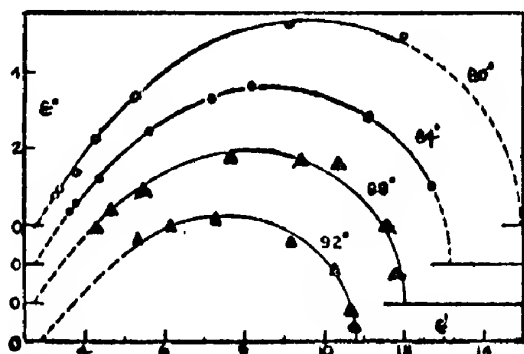


Figure 1.7 Imaginary versus real dielectric constant of HI as a function of temperature, Groenewegen and Cole (1966).

Compound	Temperature K	$\log_{10} A$	$E_a \text{ J mol}^{-1}$
HI	68-62	-13.6	9,200
	80-70	-17.2	15,000
DI	75-63	-13.3	9,200
	100-78	-15.6	13,000

Table 1.3 Activation energies for molecular re-orientation determined from dielectric constant measurements.

The high frequency dielectric dispersion of HI was measured by Groenewegen and Cole in 1966. The results were represented by an empirical expression similar to (4) referred to as a skewed-arc function which is shown for their data in figure 1.7.

$$\epsilon^* - \epsilon_\infty = (\epsilon_0 - \epsilon_\infty) / (1 + i\omega\tau_0)^\beta \quad 0 < \beta < 1 \quad (9)$$

Table 1.4 summarizes the values of the static dielectric constants ϵ_0 and the frequency of maximum absorption loss ω_m for HI.

Temperature K	ϵ_0 D	ω_m MHz
78	17.4	4.6
80	15.9	8.4
84	13.4	21.5
88	11.8	44
92	10.6	86

Table 1.4 Static dielectric constant and maximum absorption frequency versus temperature for HI

A value for ϵ_∞ was obtained by extrapolating the low temperature data to high frequencies giving $\epsilon_\infty = 2.90$. Using this value a normalized function $\left(\frac{\epsilon^* - \epsilon_\infty}{\epsilon_0 - \epsilon_\infty}\right)$ was plotted and is shown in figure 1.8. The value of the empirical constant β , eqn.(9), defined by Groenewegen and Cole (1966) was 0.67.

In the discussion of their results, Groenewegen and Cole compare the behaviour of ϵ^* for HI with that of simple polar liquids such as liquid glycols studied by Davidson and Cole (1951, 1960 and 1961). They remark upon the similarity between the two results and that such behaviour has not been observed in any other solid. At low frequencies the dielectric constant obeys the simple Debye type of relaxation. However, the width of the absorption maximum is broader than that predicted by a single relaxation time. This difference in width persisted in all their experiments at high frequencies.

The differences between the loci of ϵ^* above and below the lower phase transition point are more noticeable at lower frequencies and are attributed to a persistence of dipole correlations over a longer time, i.e.

$$\phi(t) \propto \left(\frac{t}{\tau_0}\right)^{-(1-\alpha)} \quad \text{below the transition point} \quad (10)$$

$$\phi(t) \propto \exp\left(\frac{-t}{\tau_0}\right) \quad \text{above the transition point} \quad (11)$$

$\phi(t)$ is the dipole correlation function representing the ratio of the dipole moment at a time t to the dipole moment at a time zero. An average is taken over the whole sample for the case of no applied electric field. $\phi(t)$ is discussed by Kubo (1957), Glarum (1960) and Cole (1965).

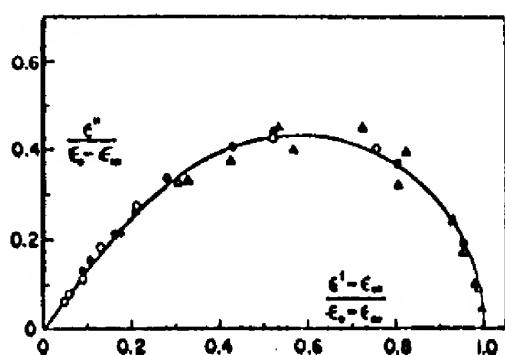


Figure 1.8 Reduced locus of the imaginary dielectric constant versus the real part, Groenewegen and Cole (1966).

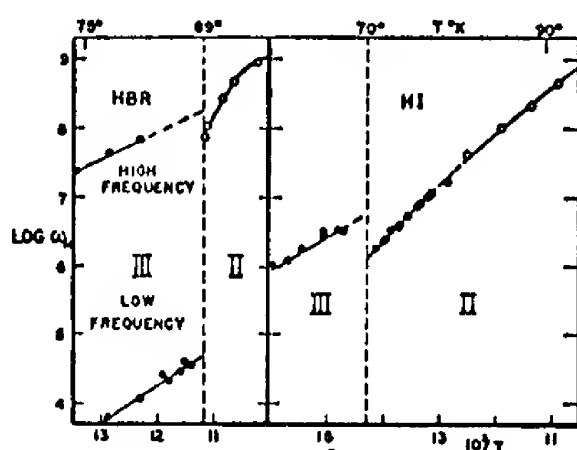


Figure 1.9 Relaxation frequency as a function of temperature for HBr and HI, Groenewegen and Cole (1966).

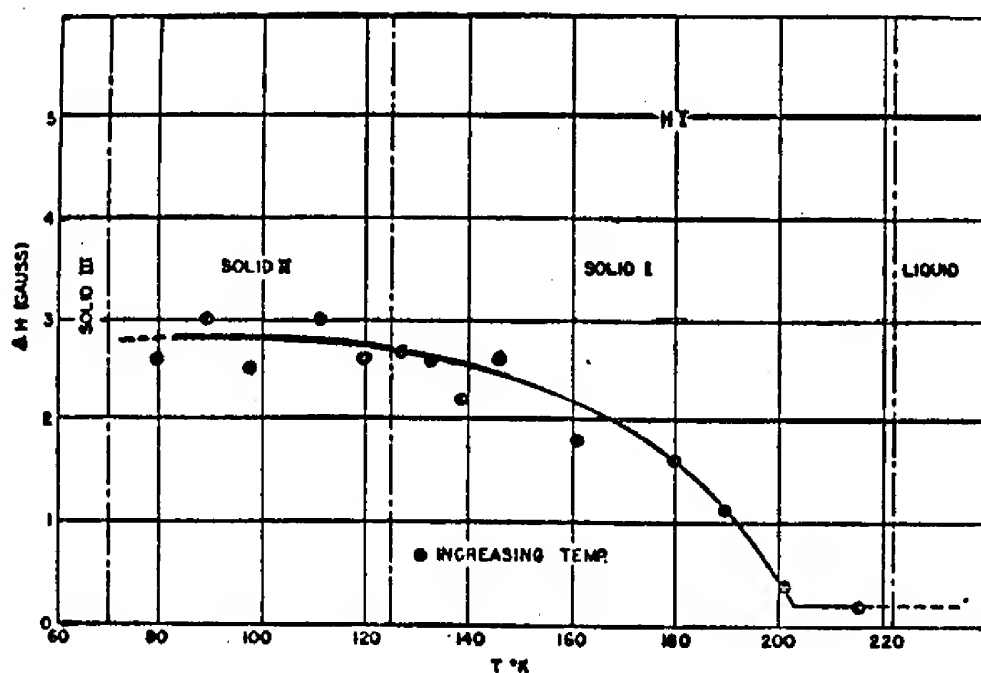


Figure 1.10 NMR line width versus temperature for HI, Alpert (1949).

Glarum and Cole discuss the possibility of describing the relaxation time as a distribution of relaxation times. This is qualitatively similar to a diffusion process. Two theories which describe the behaviour of the dipole correlation function by the use of sums of exponential decay functions are discussed. Zwanzig (1963) analyses the dipole-dipole coupling by a series expansion in terms of $(1/kT)$ where k and T are the Boltzmann constant and absolute temperature. Though their results are in qualitative agreement with the experimental data their dipole correlation functions, eqn.(10), decay too quickly to describe the observed relaxation times. This discrepancy is thought to arise because the energies of the dipole-dipole interactions in HI are larger than kT . This means that Zwanzig's series expansion is of doubtful validity.

A second theory due to Adam (1965) attributes the reduction in the relaxation time to the presence of defects in the solid. This theory also agrees qualitatively with the experimental data but requires an excessively high concentration of defects for quantitative agreement. In addition the theory has difficulty in explaining the behaviour of the relaxation constant at the phase transition.

In figure 1.9 the relaxation frequencies are plotted as a function of temperature. Their behaviour is considered to provide evidence for a co-operative effect at the phase transition. The frequencies are fitted by Groenewegen and Cole to an Arrhenius rate law of the form:

$$\omega_m = A \exp(-\Delta H^*/RT) \quad (12)$$

ΔH^* is the enthalpy of the barrier to free rotation and A is the frequency at which the dipole crosses the barrier.

For HI in the middle phase:

$$A = 1.3 \times 10^{15} \text{ Hz} \quad \text{and} \quad H = 12,600 \text{ J.}$$

This is considered a high value for A, as 'stiff' molecular vibration frequencies are of the order of 10^{14} Hz. Groenewegen and Cole conclude that the correct interpretation of the data requires more sophisticated theories and better understanding of the crystal structures of the various solid phases.

1.6 Nuclear magnetic resonance experiments (NMR)

NMR experiments with solid HI were first performed by Alpert (1949). The first NMR work had been reported by Purcell, Torrey and Pound and by Bloch, Hansen and Packard (1946). The theory of NMR has been covered extensively by Abragam (1961) and a short introduction only will be given here.

The nuclei of all atoms acquire an induced magnetic moment when placed in an external magnetic field. If a radio-frequency magnetic field is introduced in a plane perpendicular to the applied steady magnetic field, the magnetic moment of the nucleus will precess about the axis of the uniform field. If this radio-frequency field has the correct frequency, a resonance will occur at a critical Larmor frequency ν_0 , where:

$$\nu_0 = \frac{\mu_0 H_0}{I\hbar} \quad (13)$$

H_0 is the static magnetic field, μ_0 is the nuclear magnetic moment, I the nuclear angular momentum quantum number and \hbar the Planck constant divided by 2π .

For diamagnetic materials, i.e. those with no intrinsic nuclear magnetic moment, the ratio of ν_0 to H_0 is independent of the nature of the material containing the nucleus which is however coupled to the material and

can lose energy to it. There are two main methods of energy transfer in the sample causing a line-width in the resonance absorption curve.

- a) Spin-lattice coupling or relaxation is the exchange of energy between the nuclear magnetic moment and the thermal motion of the lattice.
- b) Spin-spin relaxation is the exchange of energy between different nuclei by means of their magnetic moments.

These relaxations are described by characteristic times; T_1 the spin-lattice relaxation time and T_2 the spin-spin relaxation time. In general one may say that T_2 depends upon the local magnetic field at the nucleus. It is therefore strongly dependent upon inhomogeneities in the applied field H_0 . These act as a limit to the accuracy of line-width measurements in cases where large magnetic pole faces and field strengths are used. NMR is a useful technique for studying second-order phase transitions such as those observed in the hydrogen and deuterium halides.

At the time of Alpert's work there were two theories of the phase transitions which will be briefly discussed here.

- a) Pauling (1930) and Fowler (1935 and 1936) advanced the theory that below the transition point the molecules were librating while above the transition point they rotated freely. The molecular rotation was assumed to be a co-operative phenomenon and a lambda-point transition was deduced from a statistical analysis.
- b) Frenkel (1946) and Landau (1937) proposed an order-disorder transition mechanism similar to that observed in alloys. According to this view, below the lower phase transition point the molecules have fixed orientations (are ordered) while above the transition point they librate between equilibrium orientations (are disordered).

Alpert analysed re-orientation effects in liquid normal-propanol and in solid ice-I and obtained order-of-magnitude values for the characteristic correlation or 'flipping' time τ_0 . These are 1.8×10^{-7} s for ice and 10^{-10} s for propanol. These two times characterize re-orientation between equilibrium positions and free rotation respectively.

For an (a)-type phase transition mechanism, the width of the resonance line is expected to decrease rapidly on entering the higher phase due to the large change in correlation time. The lower limit of the line-width would be determined by the inhomogeneity of the magnetic field. For a (b)-type transition a slight discontinuity is expected at the phase transition point due to a change in crystal symmetry or density. This would be followed by a decrease in line-width due to a gradual increase in the frequency of oscillation as the temperature increased. Again a lower limit would exist due to the field inhomogeneity. The curve shown in figure 1.10 shows strong evidence for a (b)-type transition mechanism until the field inhomogeneity limit is reached at 200K. These data suggest that the correlation times for the molecular re-orientation are of the order of 5×10^{-6} s falling to 5×10^{-7} s at the higher temperatures. Alpert observed (a)-type transitions in CH_4 and CH_3D at their upper phase transitions, indicating free-rotation.

No further NMR experiments were performed on HI until 1968 when Genin and co-workers studied HI/DI over a temperature range of 50-200K and obtained values for the four parameters:

T_1 the spin-lattice relaxation time,

T_2 the spin-spin relaxation time,

$T_{1\rho}$ the rotating frame relaxation time,

and M_2 the second-moment of the polycrystalline NMR curve profile.

Two new parameters are introduced here; $T_{1\rho}$, the rotating-frame relaxation time, is a useful experimental quantity measured by an interesting technique.

In the compound under study a pulsed magnetization is produced at 90° to the static magnetic field H_0 of eqn.(13) and is maintained by a similar transverse magnetic field which is rotated at the Larmor frequency. The spin-spin coupling is nullified by rotating all the nuclear magnetic moments in phase. However, the energies involved are much lower than for T_1 , or spin-lattice, type relaxation processes and thus the frequency range of re-orientations observed is in the KHz range instead of MHz. Essentially, as the name implies, the spin-lattice decay time T_1 is measured in a new frame of reference which is rotating at the Larmor frequency. M_2 is the second moment of the resonance curve profile $f(\omega)$ measured in a polycrystalline sample. In general the moments are defined as:

$$M_n = \int (\omega - \omega_0)^n f(\omega) d\omega \quad \text{Abragam (1961)} \quad (14)$$

It is a useful function indicating the width of the resonance curve which can also be calculated from the Hamiltonian of a simple spin system.

Figure 1.11 shows the temperature dependence of T_1 in the high phases of DI, DBr and DCl. Table 1.5 lists the rotational correlation times τ_c and the activation energies ΔE in the high phase. The tabulated values were derived from the results plotted in figure 1.11 using the formulae:

$$\tau_c = \frac{2}{3\pi^2} \left\{ \frac{H}{eqQ} \right\}^2 \frac{1}{T_1} \quad (15)$$

and

$$\tau_c = \tau_c^\infty \exp \left(\frac{\Delta E}{KT} \right) \quad (16)$$

Q is the quadrupole moment and the other parameters and constants have their usual meanings.

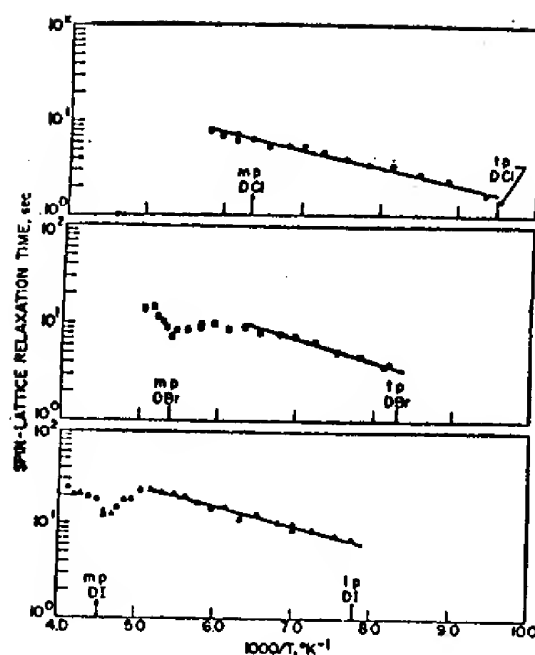


Figure 1.11 Spin-lattice relaxation times versus temperature for DCl, DBr and DI, Genin et al. (1968).

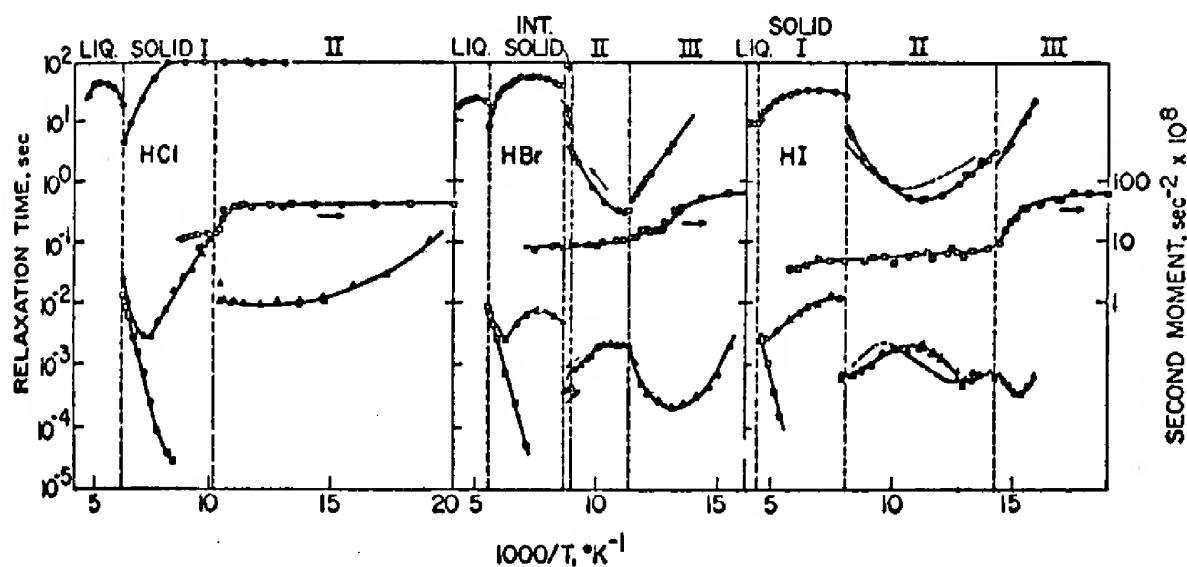


Figure 1.12 Spin-lattice \odot , rotating-frame \triangle and spin-spin \square relaxation times and second moment data \square for HCl, HBr and HI as a function of temperature, Genin et al. (1968).

Compound	τ_c at upper transition	ΔE	τ_c^∞
DCI	$2 \times 10^{-13} \text{ s}$	3560 J	$3 \times 10^{-15} \text{ s}$
DBr	$1.5 \times 10^{-12} \text{ s}$	4560 J	$2 \times 10^{-14} \text{ s}$
DI	$1.4 \times 10^{-12} \text{ s}$	4060 J	$3 \times 10^{-14} \text{ s}$

Table 1.5 Rotational correlation times and activation energies for DCI, DBr and DI as determined by NMR experiments.

Genin attributes this rapid rate of re-orientation, which is nearly 10^8 MHz, to the 'twelve-fold disordered' structure of the high phase proposed by Sándor and Farrow (1967 and 1969). This is statistically a face-centred cubic structure in which the DI molecule points randomly towards each of its twelve nearest-neighbours. The orientation of the molecule changes by the deuterium atom moving to different equilibrium positions. The iodine atoms remain fixed in their face-centred positions. The model will be discussed in a later chapter.

The decrease in T_1 with increase in temperature, which occurs in the high phase of DI and DBr near the melting point, was attributed by Genin to translational diffusion of the molecules. An explanation of the interpretation of resonance line narrowing in terms of diffusion is given by Kittel (1967c). Evidence of diffusion was also provided by the minima shown in $T_{1\rho}$ in figure 1.12. Using the random-walk theory of diffusion and the method of Torrey (1953) and Resing and Torrey (1963), Genin was able to calculate correlation times for translational diffusion which are listed in table 1.6. As can be seen, the correlation times for translational diffusion are of the same order of magnitude as for rotational re-orientation. However the calculated activation energies are larger as would be expected in a crystal lattice.

Compound	Energy	τ_c^∞
HCl	16300 J	$6 \times 10^{-13} \text{ s}$
HBr	25900 J	$1 \times 10^{-14} \text{ s}$
HI	25500 J	$8 \times 10^{-13} \text{ s}$

Table 1.6. Correlation times for translational diffusion in HCl, HBr and HI calculated by random-walk theory.

Genin also observed an anomalous curvature of the $T_{1\rho}$ versus temperature graph in figure 1.12. He attributed this curvature to quadrupolar interaction between the iodine nuclei. A minimum value of $T_{1\rho}$ due to this interaction was calculated assuming that slow translational diffusion was at a minimum. A value of $1.9 \times 10^{-3} \text{ s}$ was obtained for $T_{1\rho}$ which is in agreement with the data of figure 1.12. The anomalous curvature was not observed in HCl because the quadrupole moment was much smaller.

Values of M_2 , the second moment, are listed in table 1.7. These were calculated by considering the hydrogen atom to be at the iodine site, i.e. at the time average of the twelve disordered positions.

Compound	M_2 obs.	M_2 calc.
HCl	$11 \times 10^{-8} \text{ s}^{-2}$	$9.2 \times 10^{-8} \text{ s}^{-2}$
HBr	$8 \times 10^{-8} \text{ s}^{-2}$	$7.6 \times 10^{-8} \text{ s}^{-2}$
HI	$4 \times 10^{-8} \text{ s}^{-2}$	$5.3 \times 10^{-8} \text{ s}^{-2}$

Table 1.7. Observed and calculated second moments of NMR line shape for HCl, HBr and HI.

Another minimum occurs in $T_{1\rho}$ in the upper region of the middle phase (see figure 1.12), Genin attributes this minimum to a 'three-plane' re-orientation process. He assumes a slow re-orientation between adjacent sites in the x-y plane, with fast re-orientations between sites in the x-z and the y-z plane. By 'fast' are meant re-orientation processes occurring at frequencies greater than ω_1 , the re-orientation frequency in the rotating frame system. The sites referred to are in the planes (101), ($\bar{1}01$), (10 $\bar{1}$), ($\bar{1}0\bar{1}$), etc.

In the lower region of the middle phase of HI, a minimum is observed in T_1 near the phase transition point (see figure 1.12). Genin attributes this to a 'two-plane' re-orientation process in the x-z and y-z planes. In a 180° re-orientation the intramolecular dipole interaction is unchanged unlike the intermolecular interaction which is different. Thus in DI the relaxation times for a 180° re-orientation would be different from those in HI. Expressions for the change in relaxation time have been derived by O'Reilly and Tsang (1967). For a 2:1 mixture of DI:HI, the values of T_1 and $T_{1\rho}$ were only slightly shifted and it was concluded that 90° re-orientations alone are important. Genin calculated a value for T_1 for this process and claimed good agreement with his observed data.

In the low phase of HI a single-plane re-orientation was proposed between the (110) and (1 $\bar{1}$ 0) planes. $T_{1\rho}$ was calculated for this process and agreement claimed with the observed data. The correlation times calculated from these data are shown in figure 1.13 together with the correlation times obtained from dielectric constant measurements by Cole and Havriliak (1957) and Groenewegen and Cole (1966). As mentioned earlier, the low frequency effects are determined from the $T_{1\rho}$ measurements and the high frequency effects from the T_1 and dielectric constant measurements.

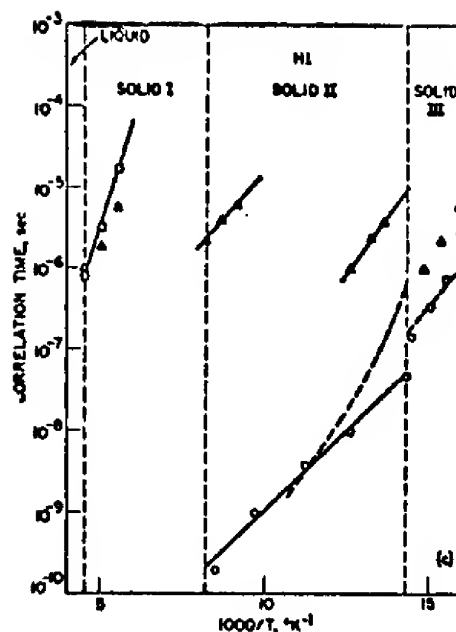


Figure 1.13 Relaxation times as a function of temperature derived from NMR and dielectric loss measurements on HI, Genin et al. (1968) and Groenewegen and Cole (1966).

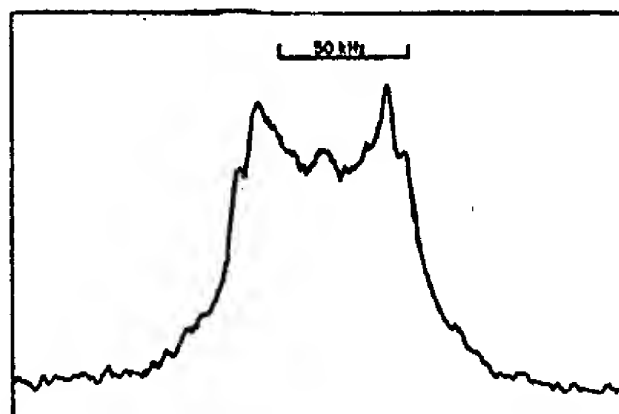


Figure 1.14 NMR dispersion signal in polycrystalline DI at 96K and 7MHz, Genin et al. (1968).

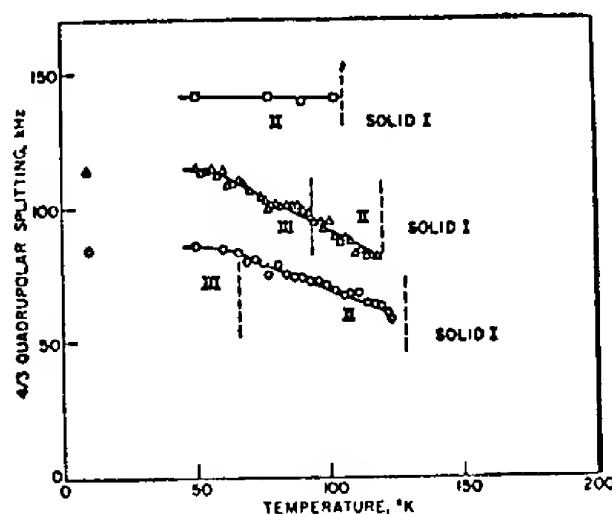


Figure 1.15 NQR coupling constants of polycrystalline DCl, DBr and DI as a function of temperature, Genin et al. (1968).

Genin also studied polycrystalline DI by a technique known as continuous-wave dispersion which has been described by O'Reilly (1958). A polycrystalline sample is placed in a constant magnetic field which is modulated by an audio-frequency magnetic field. Nuclei which possess a nuclear quadrupole moment, where the magnetic quantum number is $\geq \frac{1}{2}$, exhibit peaks in the modulated signal. These peaks result from the different energy levels available to the nucleus in the local field and are an average over all orientations of the powder sample.

DI was studied in the low and middle phases at 7 MHz. Figure 1.14 shows an observed dispersion signal for DI at 96K. The quadrupolar splitting Δ and the coupling constant C are connected by the equation:

$$C = \frac{4}{3} \Delta = \frac{e^2 q Q}{h} \quad (17)$$

where e is the electronic charge, q is the field gradient tensor and Q is the nuclear quadrupole moment.

Table 1.8 lists the quadrupolar coupling constants C derived from the powder NQR spectra of Genin at 50K. Figure 1.15 shows the variation of C with temperature. By using his one- and two-plane re-orientation processes, Genin predicted minima in the value of C at the same temperatures as the minima in T_1 in figure 1.12. These minima are not seen in figure 1.15 and their absence is explained by Genin on the grounds that the 90° re-orientation sites do not possess equal occupational probabilities.

Genin concludes by stating that the relaxation times derived from magnetic resonance experiments and dielectric-loss measurements agree to an order of magnitude. For free rotation they would be expected to differ by a factor of three. The results of the NMR measurements show clearly that

the onset of the re-orientation processes coincides with the phase transitions.

Compound	$\frac{e^2 q Q}{h}$
DCI	190 KHz
DBr	153 KHz
DI	113 KHz

Table 1.8. Quadrupolar coupling constants measured by NQR experiments for DCI, DBr and DI.

1.7 Infra-red spectroscopy

Infra-red spectroscopy is an experimental technique which determines either: the complex dielectric constant ϵ^* by reflecting infra-red radiation from a crystal or the absorption coefficient which is measured as a function of frequency by transmission through a thin film or plate.

The vibrational motion of a molecule in a crystal may be described by a system of normal modes. The frequencies and intensities of the absorption lines are characteristic of these modes. By the use of group theory on the frequencies of the lines the data can be interpreted to provide a possible site or point group symmetry for the crystal. Review papers on this technique have been written by Bhagavantam and Venkataryuda (1939), Halford (1946) and Winston and Halford (1949).

The infra-red spectrum of solid HI was first studied by Zunino (1936) and later by Hornig and Osberg (1955). The infra-red reflectivity for molecular crystals such as the hydrogen halides is generally weak so that the absorption coefficient is usually measured.

Hornig and Osberg recorded the infra-red spectrum of HI at 83K and then continued to cool their sample by evaporating liquid nitrogen at a reduced pressure. Figure 1.16 shows the transmission spectra after 30 minutes and 1 hour, the final spectrum being recorded at 66K. The type of spectrum change observed by Hornig and Osberg depended on the thickness of the film. No change was observed in the infra-red spectrum of the thickest films due probably to incomplete transition. Although the frequency of the main absorption line in HI was temperature independent, additional smaller sharp peaks appeared in the spectrum below the lower phase transition point (see figure 1.16). Table 1.9 summarizes Hornig's results.

Frequency cm^{-1}	THz	Comments
2120	63.5	Main absorption line
2130	63.8) Subsidiaries present in) the low phase
2110	63.2	
2075	62.2	Weak band
2180	65.3	Very weak, observed only in thick film band

Table 1.9. Frequencies of infra-red absorption lines for HI (middle phase)

The last two bands are probably sum and difference bands of a 50 cm^{-1} lattice vibration frequency, coupled with the main absorption line.

Hornig discusses HI very briefly. He appears to have misinterpreted the data of Kruis and Kaischew (1938) as to the optical isotropy of HI. Apart from this he suggests two possible structures for the low phase.

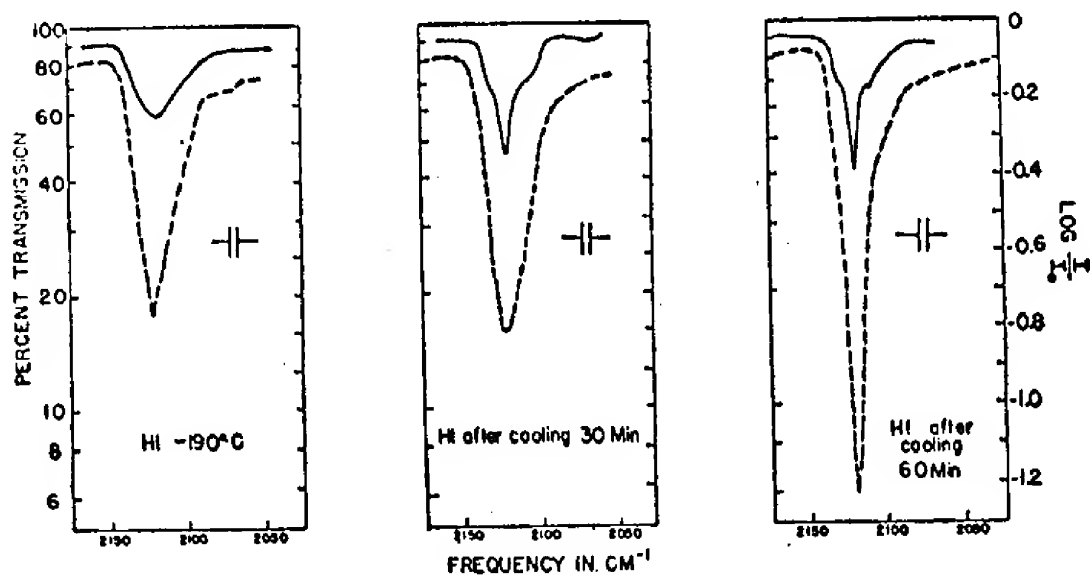


Figure 1.16 Infra-red transmission spectra of HI as a function of temperature on cooling through the lower phase transition at 70K, Hornig and Osberg (1955).

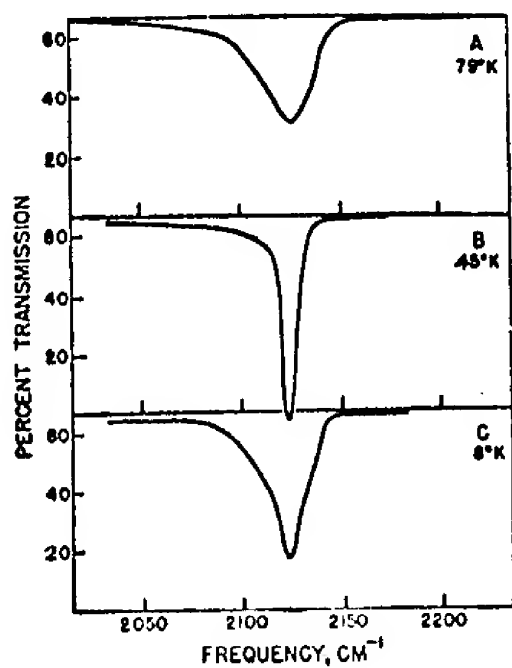


Figure 1.17 Infra-red transmission spectra of HI as a function of temperature, Hiebert and Hornig (1957).

- (a) Parallel or anti-parallel chains along the tetragonal axis.
- (b) Sets of four molecules arranged perpendicular to the tetragonal axis. (It is not made clear in what arrangement).

The main component of the infra-red absorption spectrum is associated with the frequency of the intramolecular stretching vibration. As part of a set of calculations of force constants for HCl and HBr, Hornig touches briefly upon HI.

$$2V = \sum_i \sum_j \sum_k \sum_l f_{ij}^{kl} r_i^k r_j^l \quad (18)$$

is the potential energy change when the crystal is distorted by the i th and j th co-ordinates r_i^k and r_j^l in the k th and l th unit cells, then for solid HI;

$$f_{11} = 266 \text{ Nm}^{-1}$$

for HI as a gas;

$$f_{11} = 295 \text{ Nm}^{-1}$$

where f_{11} is the diagonal element of the force-constant matrix. The difference between the gas and solid phase values of f_{11} is taken by Hornig as an indication of considerable molecular interaction in solid HI.

Hiebert and Hornig in 1957 recorded the infra-red absorption spectra of HI using a liquid helium cooled infra-red spectrometer. The infra-red spectra are shown in figure 1.17. The following conclusions were drawn:

- (a) Between 25K and 70K, HI crystallizes in an ordered structure different from that of HCl and HBr.
- (b) Below 25K, HI undergoes a transition to a phase of lower symmetry with possibly more molecules in the unit cell.

- (c) This lowest phase transition is reversible, shows no hysteresis and has a negligible heat of transition.

In 1964 Reeves, Robinson and Taimsalu published a conference abstract on the vibrational spectra of five phases of solid HI. The lowest phase was reported to have a vibrational pattern similar to HCl and HBr suggesting isomorphous structures.

In a thesis abstract in 1964, Reeves reported that HI has a helical hydrogen-bonded structure with chains randomly directed parallel or antiparallel to the tetragonal axis of the crystal. This phase was stable below 10K.

Savoie and Anderson (1966) attempted to clarify the position in a footnote to their paper on HCl/DCI and HBr/DBr. In a reference to Reeves et al they point out that the early experiments, described in sections 1.2 to 1.6 of this chapter, and some unpublished Raman spectroscopy experiments on HI disagree with Reeves' results. Reeves' results are attributed to a metastable phase such as have been observed in solid argon and ammonia. The method of depositing thin films from the vapour phase onto a cold substrate was considered to favour the occurrence of such metastable phases. The three solid phases of DI observed in the present neutron diffraction studies are in agreement with the results of Giauque, Cole, Alpert, Genin etc. who all studied bulk samples and observed three solid phases.

1.8 Theories of phase transitions in molecular crystals

A detailed review of the different theories of phase transitions in molecular crystals has been given by Johnson (1970). The work of the following authors has been reviewed; Pauling (1930), Chang (1937), Kirkwood (1940), Tisza (1947), Bragg and Williams (1934), Powles (1952) and

Krieger and James (1954). Further relevant papers have been published since this review; Hanamura (1970), Kobayashi et al. (1969) and Hanamura (1970).

Kobayashi et al propose a two-dimensional mathematical model of a hydrogen halide using two sub-lattices which are the low phase structures of DCl and DBr proposed by Sándor and Farrow (1967) and Sándor and Johnson (1968). Order parameters are derived in terms of the dipole moments of the sub-lattices using the consistency relations and internal field approximation of Krieger and James (1954). These equations are solved by an expansion method enabling the internal energy to be calculated as a function of temperature. The force constant used in the mathematical model is allowed to have three different ranges of value. The calculated internal energy predicts the orders of the lower phase transitions of each compound. HCl lies in one range giving a first-order transition and HBr/HI in another giving a second-order transition. (HI was assumed to be isomorphous with HBr in the low phase). No numerical values of transition temperatures were computed.

Hanamura summarizes the published structural data on the hydrogen halides and concludes that 90° zig-zag bonding is most likely. Dipolar and quadrupolar bonding energies are tabulated for each hydrogen halide. The upper phase transition in HBr and HI is said to be due to ordering of chains of molecules by quadrupolar interactions, the lower is due to dipolar interactions.

The internal field approximation is used to calculate potentials between the chains. Three zig-zag models are considered and their dipolar energies calculated. For the low phase, the model corresponding to the proposed structure of Sándor and Johnson (1968) has the lowest energy. If only

quadrupolar coupling is retained, the middle phase of HBr is generated as a random mixture of two of the three structural models considered by Hanamura.

CHAPTER TWO

Experimental work

The experimental work is divided into three sections; the preparation of samples of HI and DI of high chemical and isotopic purity, the X-ray powder diffraction study of HI/DI and the neutron powder diffraction study of DI. The neutron diffraction work was carried out at the Atomic Energy Research Establishment, Harwell, using powder diffractometers attached to the research reactors "Dido" and "Pluto".

2.1 Chemical preparations

In both preparations Pyrex glass systems were used with ground-glass vacuum joints, hydrogen-free PTFE vacuum grease and greaseless valves made by Springams Ltd. The glassware was carefully cleaned with detergents, chromic acid and distilled water in turn. The dry components were then assembled, evacuated and maintained at a pressure of approximately 10^{-6} mm of Mercury for several days. During this period the glassware was heated by a hot-air blower to remove any residual internal film of water vapour. In all cases where chemicals were weighed, measured or placed into flasks, the operations were carried out in a glove-box filled with dry nitrogen.

The reagents were purchased from the Koch Light Chemical Company with the following stated purities.

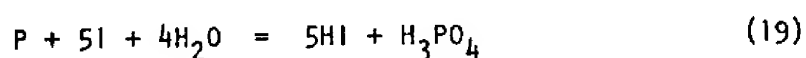
Iodine	99.998%
Heavy Water	99.7%
Red phosphorus	99.999%

where ordinary water was used it was first doubly distilled in a conventional Liebig system.

In the preparation of DI it was essential to keep the amount of HI impurity to a minimum as the incoherent neutron scattering cross-section of hydrogen is much larger than those of deuterium or iodine. For this reason DI was at no time allowed to come into contact with any hydrogenous material with which isotopic exchange reactions could occur.

(a) Indirect preparation of HI/DI

This method used the reaction of red phosphorus and water on iodine;



The iodine and red phosphorus were weighed, then ground together with a pestle and mortar in a glove box and the mixture was poured into flask A (figure 2.1). The preparation system shown in figure 2.1 was evacuated and sealed at V. Water or heavy water was allowed to run into flask A through a dropping funnel B.

The HI/DI evolving in flask A was then passed through cold traps at C (cooled to -70°C with a mixture of solid carbon dioxide and methanol) to remove any traces of iodine, water, phosphine (PH_3) or phosphonium iodide (PH_4I). The formation of the last two compounds was kept to a minimum by ensuring an excess of iodine in the initial reaction. The HI/DI was condensed in flask D which was cooled with liquid nitrogen. The reaction, which proceeded steadily at room temperature, produced approximately 20ml of solid HI/DI in 12 hours. The amount of water or heavy water running into flask A from the funnel B was regulated in such a way that the pressure of the evolving gas was kept below 300mm of mercury, as recorded by the small aneroid vacuum gauge G. The rate of reaction could be slowed down by cooling flask A with liquid nitrogen.

After 12 hours the flask D was sealed off and flask A replaced by an

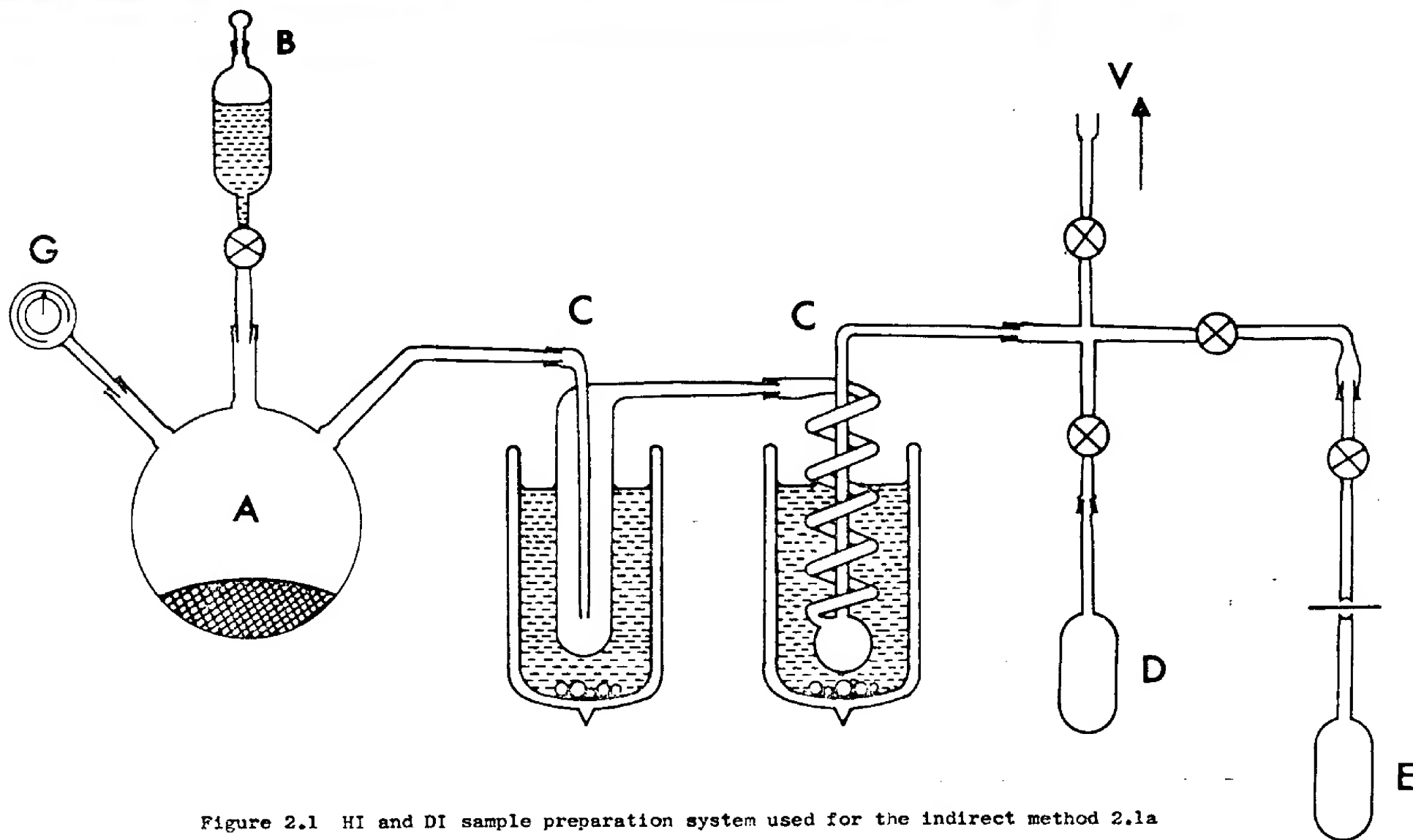
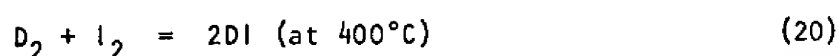


Figure 2.1 HI and DI sample preparation system used for the indirect method 2.1a

empty flask. The system was re-evacuated and the HI/DI transferred from D to A through the cold traps several times and finally condensed in the 1-metre storage tube E, which was subsequently stored in a 25-litre aluminium liquid-nitrogen dewar made by Spembley Ltd. The whole preparation was carried out in a photographic dark room with a weak "safe-light" because of the light sensitivity of HI/DI. The sample produced was a pure white, polycrystalline solid.

(b) Direct preparation of DI

To test whether the method of sample preparation had any influence on the neutron powder diffraction pattern, a sample of DI was prepared by a direct method of catalytic combination. Iodine and gaseous deuterium were combined (at 400°C) in the presence of platinized asbestos as a catalyst in the apparatus shown in figure 2.2. This direct method used the reaction;



The rate of this reaction is very slow, less than 2ml of solid DI being produced per day. However the sample was expected to be of higher purity than the one prepared by the previous method due to the absence of any phosphorus compounds. The neutron diffraction patterns recorded for the two samples of DI prepared by methods (a) and (b) were identical within statistical error.

The electrolysis plant D of figure 2.2 was filled with heavy water and D_2SO_4 in a dry glove-box. The 5-litre flask A and the catalyst were heated for a day at 400°C to remove any grease or contamination. The iodine was introduced into flask A in a dry glove-box. The system was evacuated and the 1-litre flask P was filled to a pressure of 1 atmosphere of deuterium at room temperature as recorded on the pressure gauge G. The deuterium was produced by electrolysis of the mixture of heavy water and D_2SO_4 using a

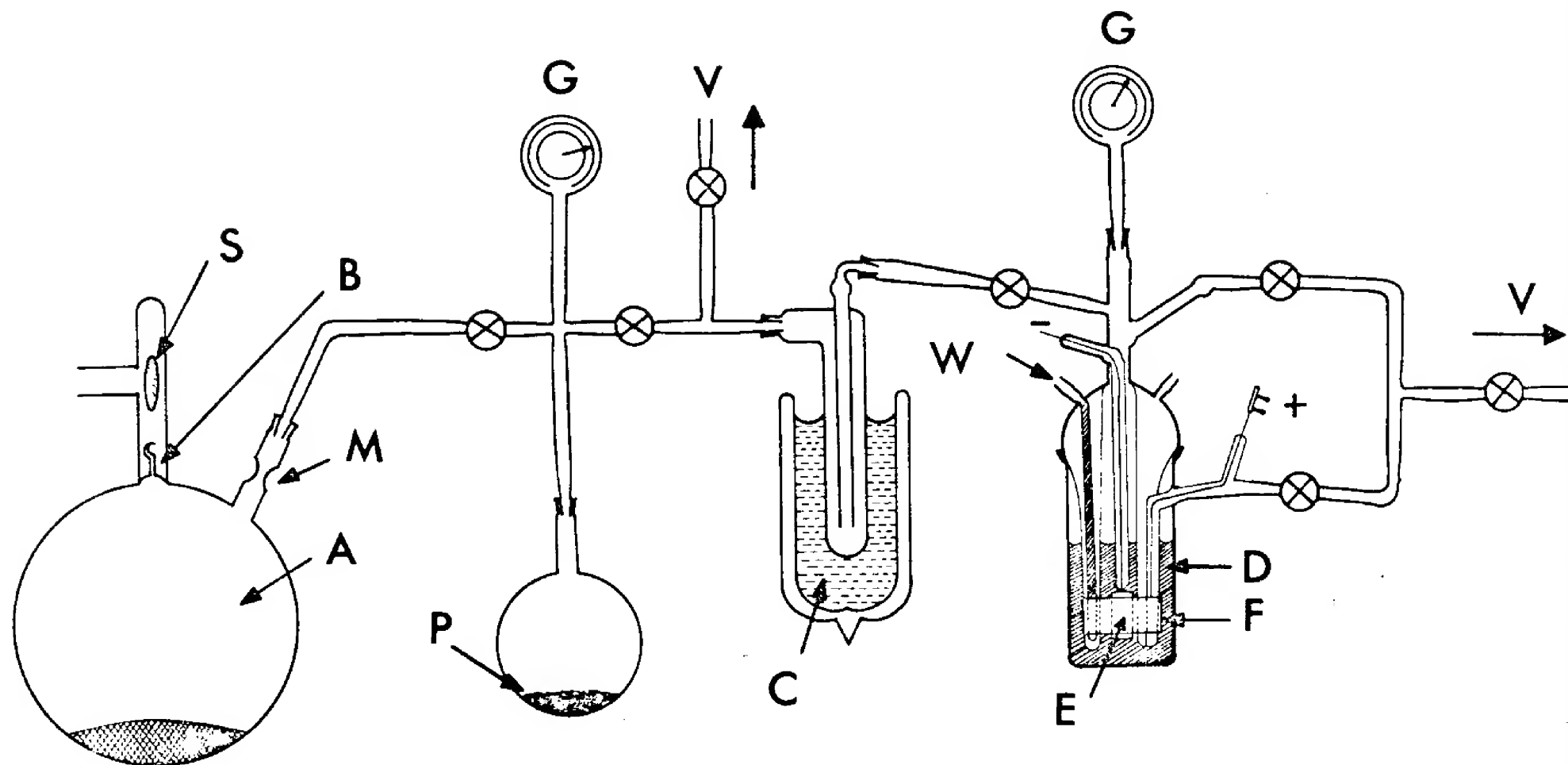


Figure 2.2. DI sample preparation system used for the direct method 2.1b.

current of 5A, the electrodes E and F being cooled by an external water supply W. The oxygen produced was removed by a rotary pump via a needle valve at V.

The deuterium was dried by letting it pass through a condenser C at liquid nitrogen temperature. Any oxygen present was either condensed or converted to D_2O by heating with a hot air blower over some platinum catalyst in P. The 5-litre flask A, which was initially evacuated and sealed off by a valve, was opened to the remainder of the system so that the 1-atmosphere of deuterium in the 1-litre flask P now filled a volume of 6 litres. The 5-litre flask containing iodine and deuterium at the resultant pressure of 1/6th of an atmosphere was resealed by the valve and wrapped in an asbestos blanket and sealed completely by melting the glass at M. This was somewhat hazardous due to the risk of an explosion being caused by the glass-blowing torch.

Flask A containing iodine and deuterium was heated for 12 hours at $400^\circ C$ in an oven and after cooling was connected to the system shown in figure 2.3. The seal at B was broken by lifting the steel bar S with a magnet. The DI produced in the flask was condensed in the evacuated system at D and purified in the same manner as described in section (a) above by cold traps at C. This latter operation was again performed in darkness. Both of these preparations are also described in less detail by Brauer (1963).

2.2 X-ray diffraction study of DI

(a) X-ray diffraction photographs were taken of DI at Queen Mary College with a Nonius and a Unicam Weissenberg goniometer using them as low-temperature powder cameras.

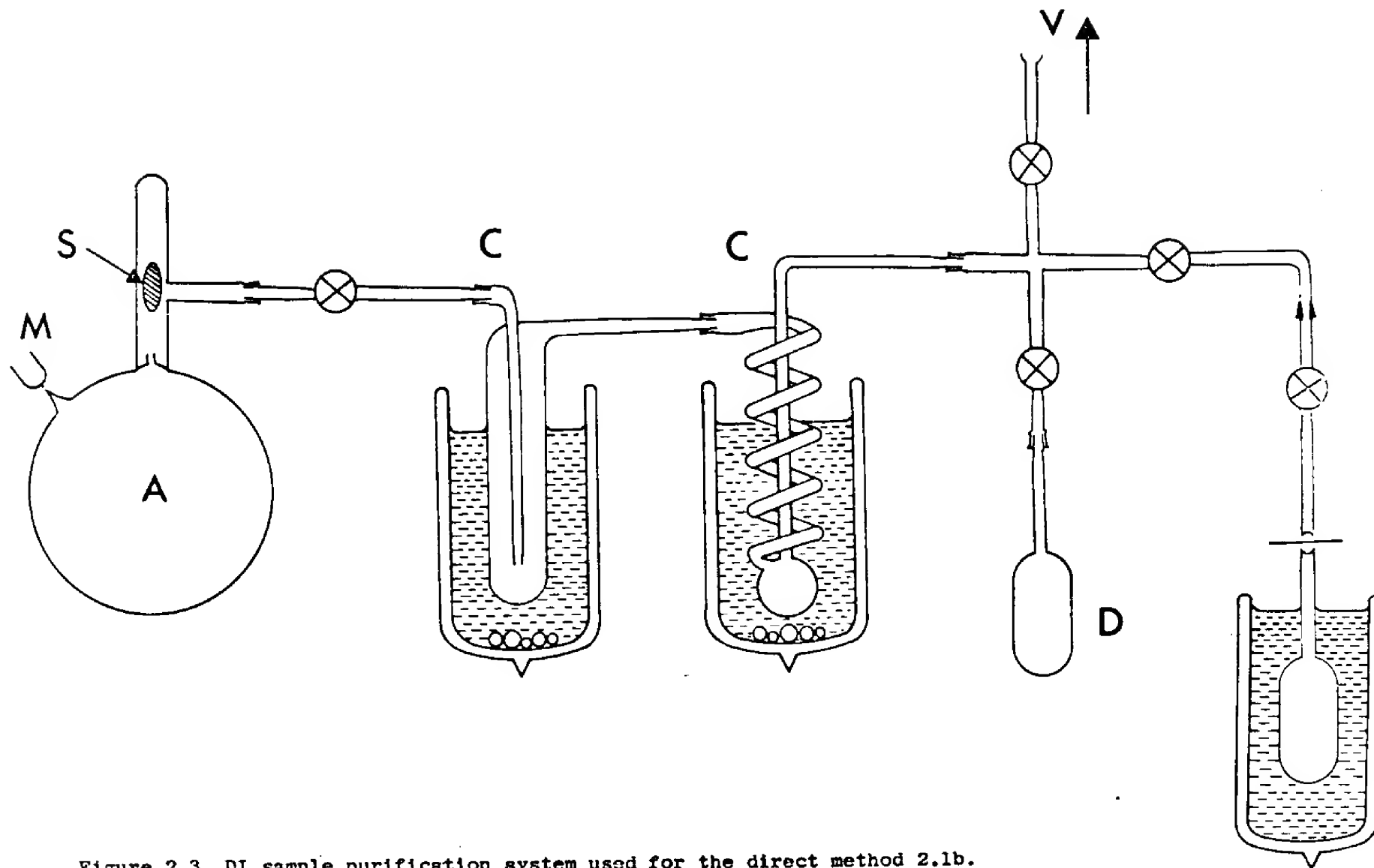


Figure 2.3 DI sample purification system used for the direct method 2.1b.

Samples of DI were sealed into Lindemann glass capillaries of wall thickness .01mm and diameter .1mm. The sealed capillaries were cooled by a continuous flow of cold nitrogen gas produced by boiling liquid nitrogen in a pressurized glass dewar with an electrical heater. The temperature of the sample was recorded by a copper-constantan thermocouple attached to the capillary and the thermoelectric emf was fed back to control a heater in the dewar arm as shown in figure 2.4. The temperature control system used in this experiment is described in detail by Farrow (1969) and Johnson (1970). The lowest temperature attainable with this equipment was approximately 83K. This limited the use of the cameras to the study of the middle and high phases of HI and DI.

The X-ray beam was monochromated by a point-focusing monochromator using a doubly-curved lithium fluoride single crystal plate, cleaved along the (001) planes.

(b) X-ray powder diffraction patterns were recorded at 4.2K at Imperial College, London using a Siemens powder diffractometer with a small liquid helium cryostat which retained liquid helium for two to three hours. The diffractometer and cryostat has been described by King (1967). A flat-plate reflection geometry was used which had two distinct disadvantages;

- (i) The flat DI powder sample had to be supported by a transparent film mounted in front of it. A "Melinex" film of thickness 0.001 in. was used for this purpose which gave a very intense, broad diffraction peak which made it very difficult to observe the first dozen peaks in DI.
- (ii) More important was the uncertainty of whether the sample was or was not poly-crystalline. Since the powder was condensed

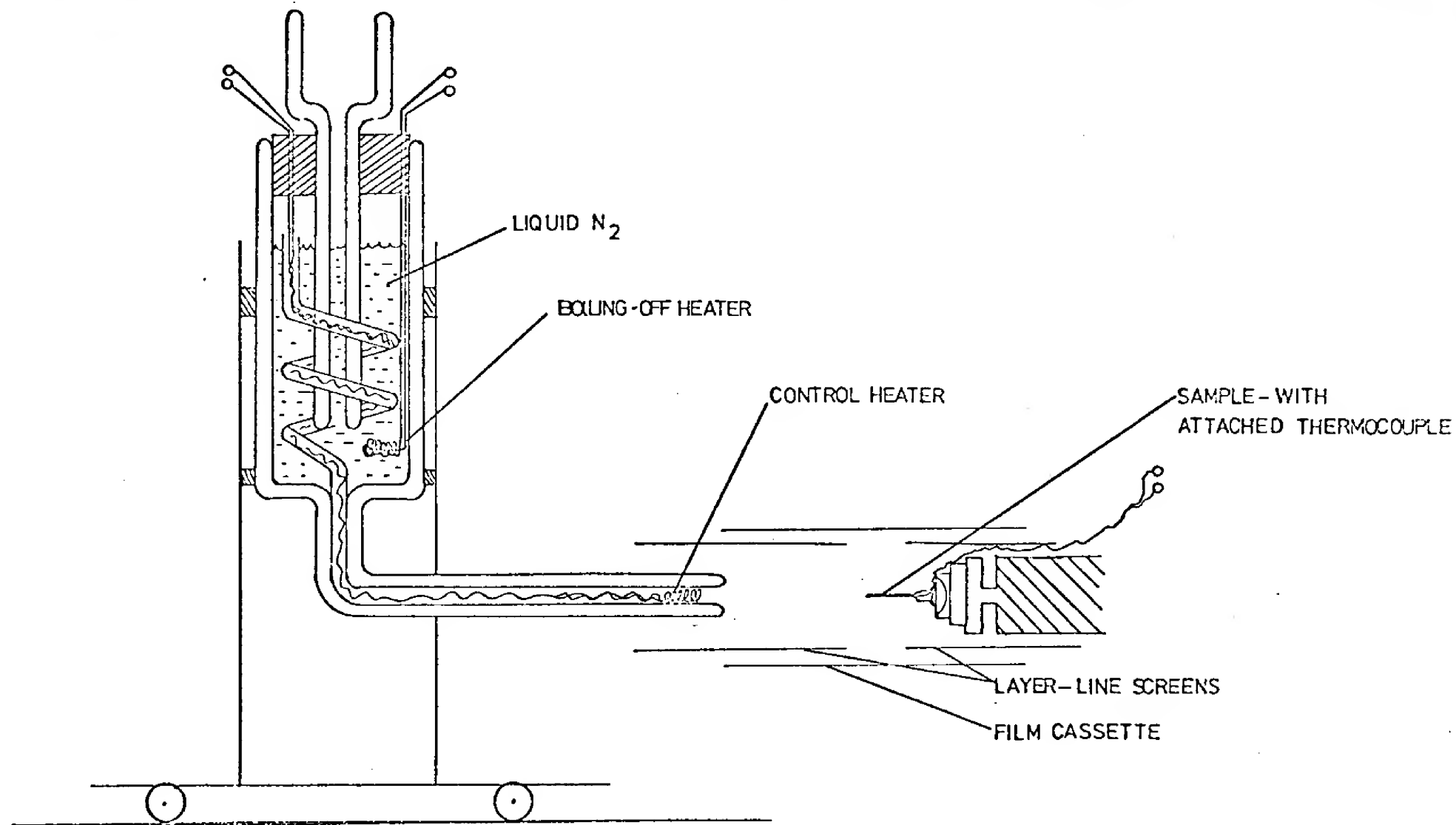


Figure 2.4 Low temperature x-ray goniometer used at Queen Mary College.

directly from the vapour phase, the size and orientation of the crystallites could not be altered. Previous experiments, using the Nonius camera as described above, had shown that on average only 10% of the samples condensed were completely polycrystalline. The diffraction photographs contained powder lines with higher intensity spots due to larger crystallites within the sample. Because the Siemens diffractometer recorded an integrated intensity from the whole surface of the sample plate it was important to know if the sample were completely polycrystalline. A reflection photograph was unsatisfactory due to focussing problems and a transmission photograph was not possible as the sample and container were 5mm thick.

(c) To overcome these difficulties a low-temperature X-ray powder diffractometer was assembled at Queen Mary College incorporating the following features.

- (i) A large, well-tested cryostat capable of retaining liquid helium for 50 hours.
- (ii) Cylindrical sample geometry, using thin-walled Lindemann glass capillaries.
- (iii) An X-ray proportional detector either scanning continuously with a chart-recorder output or counting at fixed angular intervals and printing the recorded intensities on a teleprinter enabling weak peaks to be observed.

(d) These three features will be described in more detail below.

(i) The cryostat

A British Oxygen Company modular research cryostat was used to keep

the sample at 4.2K. The liquid helium capacity was 3 litres and it retained liquid helium for approximately 50 hours. The cryostat is shown in figure 2.5. The incident X-ray beam is shown at B passing through three cylinders surrounding the sample S (known as 'tails'). The tails were made of solid beryllium ingots machined into tubes with a window thickness of 0.005 in. The three tails serve as:

- (a) an outer vacuum jacket,
- (b) a radiation shield maintained at the temperature of liquid nitrogen,
- (c) a radiation and vacuum shield at liquid helium temperature.

These components were made at A.E.R.E., Harwell and A.W.R.E., Aldermaston.

Due to the thinness of the tails the cryostat was supported in an aluminium alloy stand with a large section machined away leaving a minimum amount of material in the area of the diffracted beam. Aluminium was used to avoid X-ray fluorescence caused by the copper radiation. The sample space was thermally insulated from the liquid helium container LH by an evacuated exchange space ES. The sample of DI was condensed as a solid into a Lindemann capillary tube using liquid nitrogen and an ancillary glass apparatus (Johnson 1970). The capillary was sealed by melting at each end and was then mounted on the tip of a long thin stainless steel tube of low thermal conductivity. Thermocouples were attached to the capillary with varnish and a low power heater (10mW) of fine gauge wire was wound onto the capillary above the sample region. The capillary was dipped quickly into liquid nitrogen outside the cryostat to form a polycrystalline sample of solid DI. The long tube and sample were next transferred to the exchange space ES while liquid nitrogen was poured slowly over the capillary to prevent the sample melting and annealing into a powder with preferred orientation.

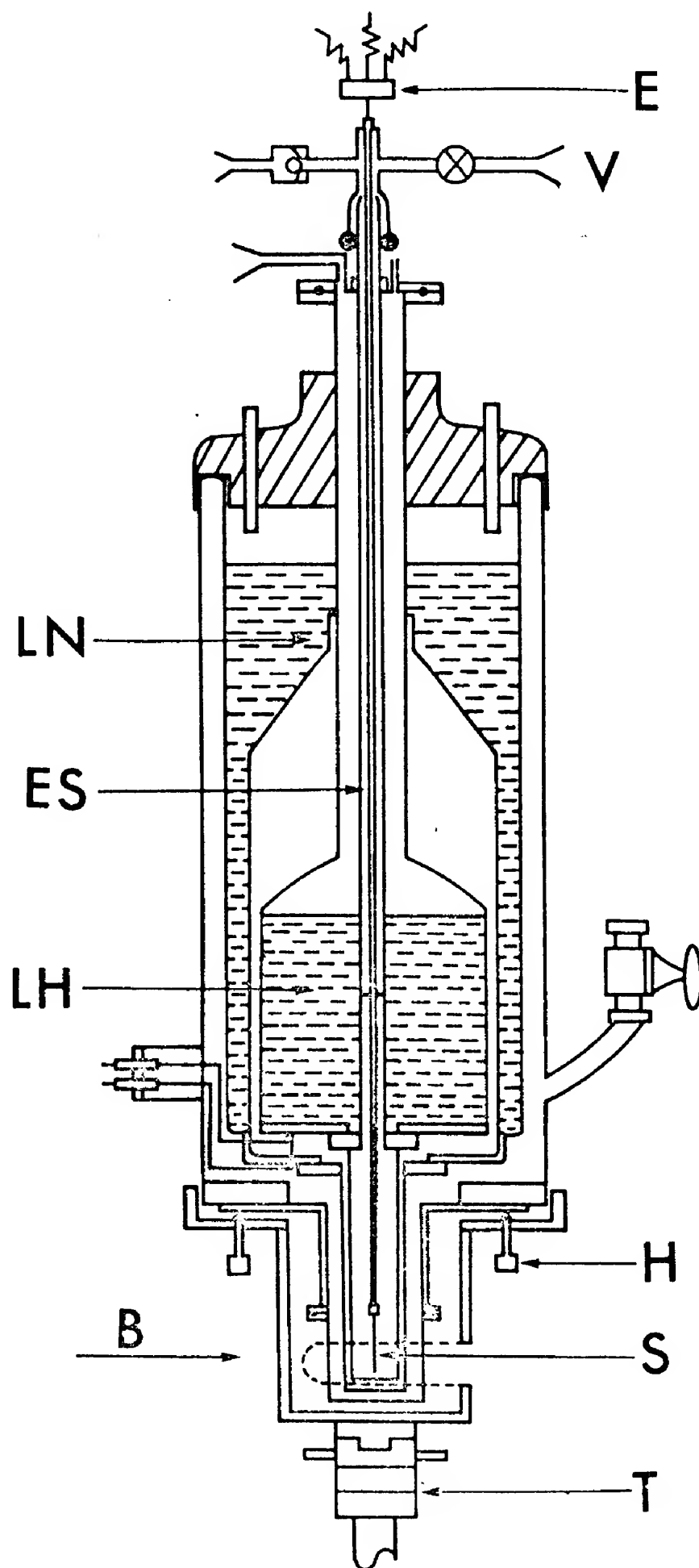


Figure 2.5 Liquid helium cryostat used on the Queen Mary College x-ray powder diffractometer.

The exchange space ES was then evacuated at V. The sample was aligned in the beam by means of two transverse slides T and three vertical tilting bolts H. The sample was first aligned in the X-ray beam optically using a fluorescent zinc sulphide screen. Final alignment was completed using short exposure X-ray transmission photographs. The position of the capillary could easily be detected due to absorption in the thermocouple leads and sample. Electrical leads to the sample passed through a neoprene vacuum seal at E (Batchelder and Sidey 1969).

(ii) To test the nature of the sample a short exposure X-ray diffraction photograph was taken at low angles to study the (111) and (002) powder peaks. After several attempts it was usually possible to form a good powder sample with continuous powder lines. The sample temperature was monitored by means of a gold-iron versus chromel thermocouple attached to the capillary with an ice reference junction in a glass dewar. The temperature was controlled by means of an Oxford Instruments 'Harwell' temperature controller with the low power 10mW heater (described previously) attached to the capillary.

(iii) The electronic control system of the diffractometer was constructed of 'Harwell 2000 series' electronics. The X-rays were detected by a proportional counter filled with xenon. The amount of 'white' radiation recorded by the counting system was reduced by the use of an amplifier and a pulse-height analyser on the signal from the proportional counter.

The instrument could either be used as a continuously scanning counter with a rate-meter and chart recorder output, or with a preset step length and count time in which case the output was printed on an ASR33 teleprinter and also punched on a paper tape. The scattered intensities were then drawn on a computer-controlled graph plotter.

The X-ray powder diffractometer was made by Maclean Engineering Ltd., and was a less sophisticated version of the Harwell 'Apex' goniometer (Baker et al. 1966).

2.3 Neutron diffraction study of D1

The neutron diffraction experiments were carried out with three different powder diffractometers (Dido 'Curran', Dido 'Badger II' and Pluto 'Panda') at the 25 MW thermal reactors Dido and Pluto (SRC, 1973). The three diffractometers have the following features in common.

- (i) The use of boron trifluoride proportional detectors. The boron is enriched in the isotope B^{10} which has a high neutron absorption cross-section and undergoes a nuclear capture reaction yielding a pulse-producing alpha particle according to the expression,



- (ii) The counting time is controlled by a monitor counter. Counting for fixed times at small angular increments is unreliable due to fluctuations in reactor power, particularly in the last week of a four week reactor cycle when spent fuel elements are removed so changing the neutron flux at certain beam holes. To overcome this difficulty a small fission detector is placed in the incident monochromatic beam in front of the sample and acts as a monitor while removing less than 1% of the incident beam.
- (iii) Automatic data printing. The use of this technique is necessary because the counting rate is so low that the recording of a powder pattern can take several days. The reactor operates for 24 days before refuelling.

- (iv) The use of 'Boral' (boron carbide compressed between aluminium sheets) shielding. Boral is used to define the incoming monochromatic neutron beam and the collimator is adjusted by taking neutron radiographs of the sample with a polaroid camera fitted with a lithium-loaded zinc sulphide scintillator. Small, highly absorbing cadmium strips are fixed to the top and bottom of the sample container to define the sample position in the radiograph.

The next section will describe each diffractometer in more detail.

(a) Dido 'Curran' powder diffractometer

The bulk of the neutron diffraction work was performed using this instrument of which the experimental layout is shown in figures 2.6 and 2.7. There are five counters C1 to C5 fixed at 10° intervals relative to each other in a shielding block SH. The block can move on a track T and is supported on a cushion of compressed air, the total angular range covered by the first counter (C1) being from -25° to 35° in 2θ . The sample was at S and could be rotated at half the angular velocity of the counter block.

Monochromatic neutrons of wavelength 1.06\AA were provided by a lead monochromator crystal M which reflected neutrons at an angle of 22° from the (111) lattice planes. By rotating the sample at half the angular velocity of the counter bank and using the full angular range available it was possible to record the diffraction pattern from $\theta = 7.5^\circ$ to 17.5° with five counters from five sets of crystallites. Other regions were covered with fewer counters, the whole procedure providing a useful check on preferred orientation in the powder sample and (after correction for detector efficiencies) a composite set of data from five counters. This will be shown in section 4.5.

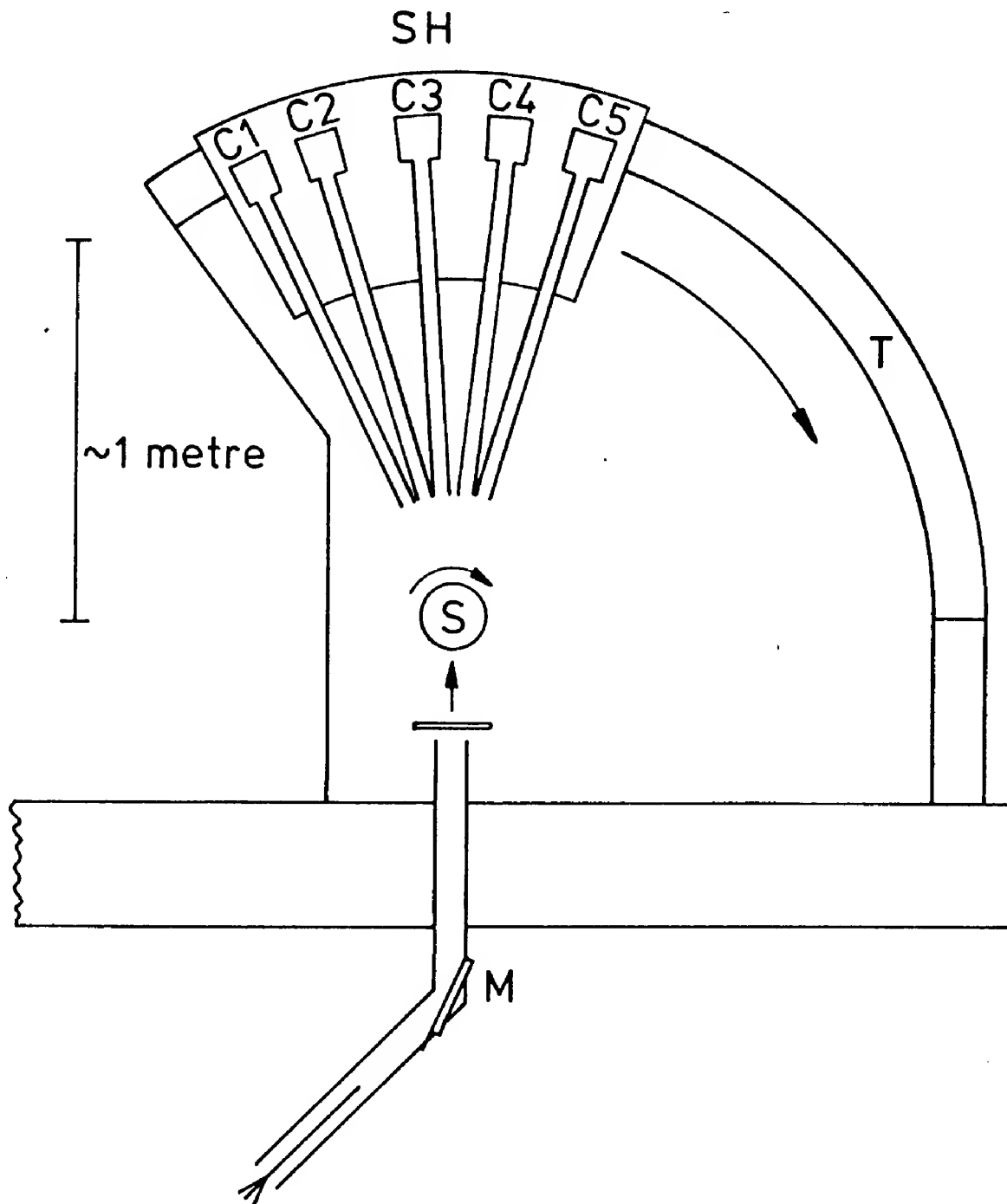
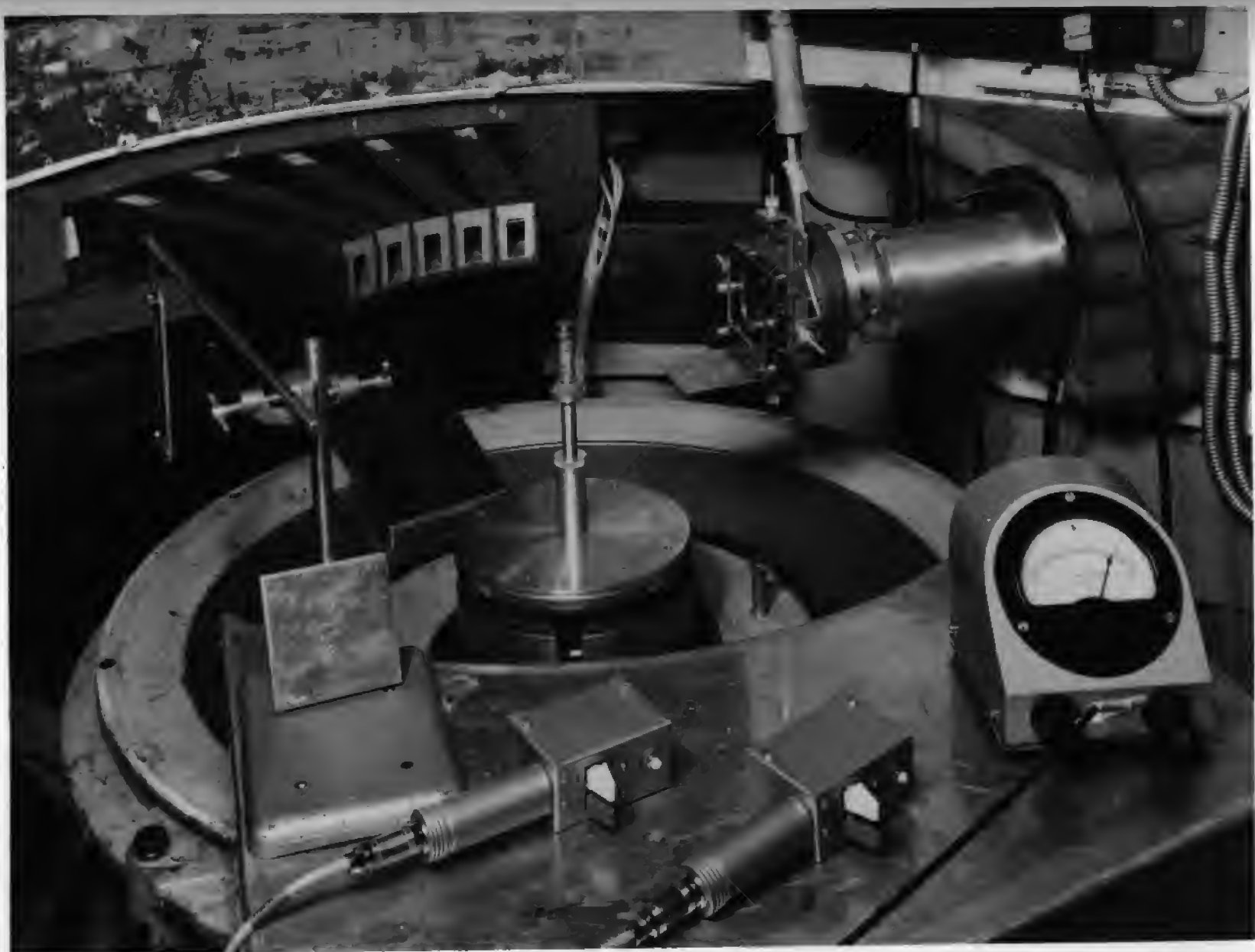


Figure 2.6 The configuration of the Dido Curran neutron powder diffractometer.

Figure 2.7 Photograph of the Dido Curran neutron powder diffractometer.



(b) Dido 'Badger' powder diffractometer

This machine was a simpler version of the 'Curran' with a single detector and a monochromatic incident wavelength of 1.113\AA reflected from the (111) lattice planes of a lead monochromator. The neutron flux was less than half that of the 'Curran' and in the angular range of $\theta = 5^\circ$ to 15° the angular resolution was comparable. This machine was used for studying the upper phase transition in DI which involved scanning three powder peaks at different temperatures. For this purpose the machine was quite adequate.

(c) Pluto 'Panda' powder diffractometer

In this machine the monochromator housing could be rotated and hence the wavelength and take-off angle could be varied. A 'squashed' germanium monochromator crystal was used in transmission at wavelengths of 1.89\AA and 2.4\AA . The 'squashing' increased the mosaic spread of the crystal and hence the reflected intensity (Bacon 1955a).

The energy distribution of the neutron beam emerging from the moderator in the reactor is approximately Maxwellian with a characteristic temperature of 60°C and a peak intensity at a wavelength of approximately 1.4\AA . In contrast to the energy spectrum of an X-ray tube with its sharp characteristic peaks superimposed on a continuous background, the neutron spectrum has no characteristic wavelength. Moreover at neutron wavelengths greater than 1.1\AA a monochromatic beam may become contaminated by shorter wavelengths. These are caused by second- and third-order Bragg reflections from the monochromator and occur at one half and one third of the fundamental or intended wavelength.

The configuration of the 'Panda' neutron powder diffractometer is shown in figures 2.8 and 2.9. The main beam from the core of the reactor

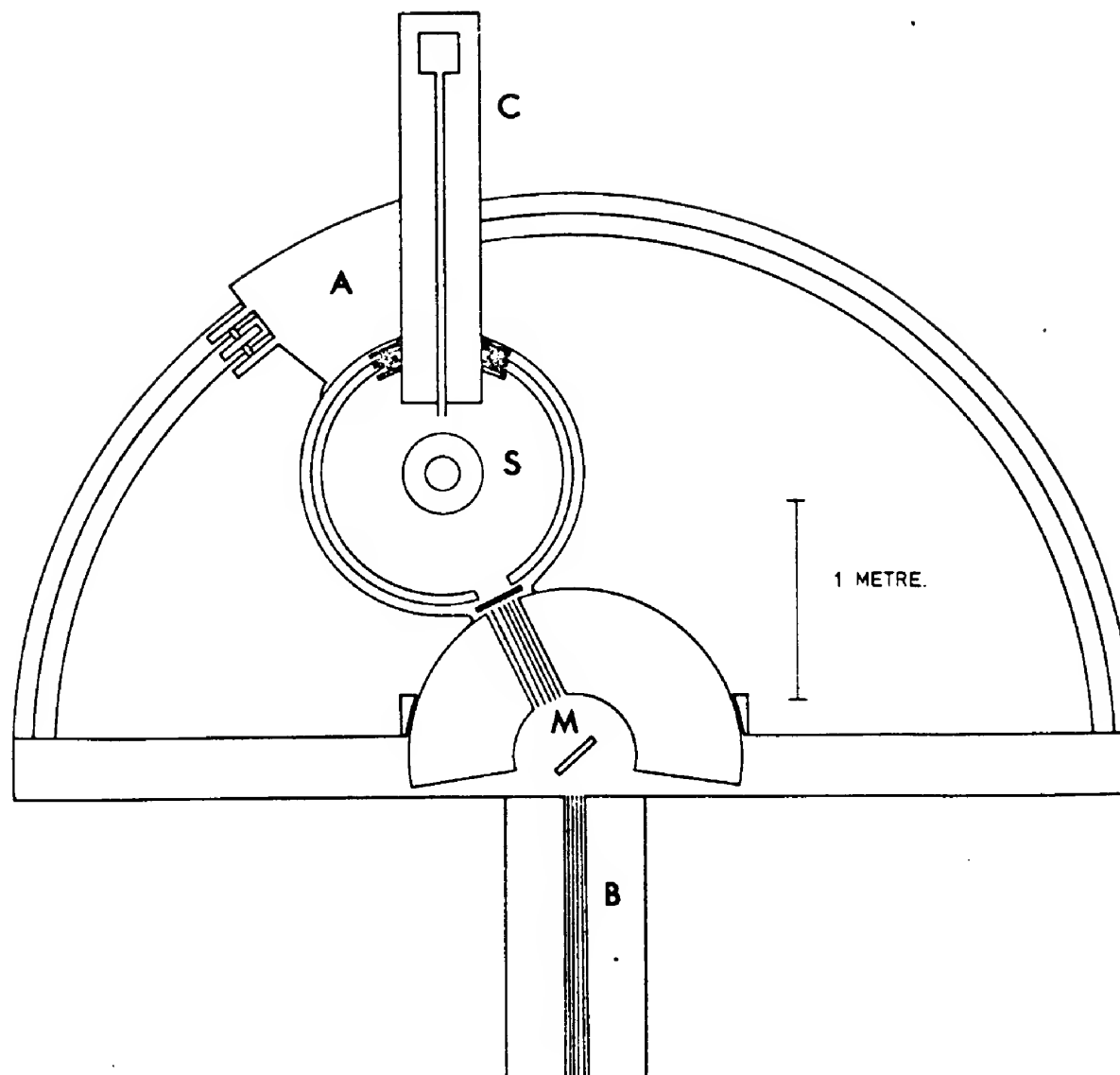


Figure 2.8 The configuration of the Pluto Panda neutron powder diffractometer.

2.8 Photograph of the Pluto Panda neutron powder diffractometer.



enters through a collimator at B and falls on the monochromator at M. The monochromatic neutron beam is then incident on the sample at S. A detector C moves on a circular track with its centre at S. The carriage A moves on another circular track centred at M enabling the take-off angle of the monochromator and the wavelength to be varied. The wavelength can be determined from the diffraction pattern of a cylinder of nickel powder, for which the lattice parameters are well known. The diffraction pattern of the nickel standard also reveals the presence of any short wavelength (higher order) contamination.

To study diffraction patterns at long wavelengths it is necessary to use the reflections from the (111) and (113) lattice planes of the germanium monochromator. Since germanium has the space group $Fd\bar{3}m$ (no.227), the reflections (222) and (226) are absent preventing the occurrence of second-order contamination in the monochromatic incident beam. Using the germanium (113) reflection and a wavelength of 1.89\AA the only contamination came from the third harmonic of the incident radiation, i.e. the (339) germanium reflection for which $\lambda = 0.63\text{\AA}$. This was negligible for three reasons:

- (i) The contribution of the wavelength 0.63\AA to the energy spectrum is small.
- (ii) The geometrical structure factor for the (339) germanium reflection is small.
- (iii) The reflectivity of the sample increases with wavelength according to the formula.

$$R \propto \lambda^3 \quad (22)$$

Thus the reflectivity for $\lambda = 0.63\text{\AA}$ is 27 times smaller than that of the fundamental wavelength.

With a wavelength of 2.4\AA the third order contamination from the 0.8\AA wavelength was more serious due to its greater contribution to the energy spectrum. This was eliminated by the use of a pyrolytic graphite filter in which the hexagonal c-axis of the crystallites is oriented along the direction of the incident beam. The other crystal axes are oriented randomly in the (001) plane for each crystallite. Only neutrons with wavelengths which satisfy the Bragg equation for graphite are diffracted away from the direction of the incident beam into Debye-Scherrer cones formed by the diffraction from crystallites having their a-axes randomly oriented. These graphite powder diffraction neutron peaks are absorbed in the cadmium shielding surrounding the filter.

The neutron diffraction in the filter reduces the intensity of the transmitted neutron beam at certain characteristic wavelengths. For pyrolytic graphite aligned with its c-axis along the incident monochromatic beam a low transmission occurs at 0.8\AA . The widths of the transmission minima caused by diffraction in the filter vary from one filter to the next according to the variation in the angular distribution of the direction of the c-axis in the filter. Accounts of these filters are given by Loopstra (1966) and Shirane and Minkiewicz (1970).

The advantages of the variable monochromator take-off angle were;

- (i) By choosing suitably long wavelengths overlapping powder peaks could be partially or wholly resolved.
- (ii) When the diffracted beam is parallel to the polychromatic primary neutron beam from the reactor, the diffractometer is in a parallel focusing geometry (Bacon 1955b). In this arrangement the angular resolution of the diffractometer is highest when the Bragg angle of diffraction from the sample is equal to the

lasted at least ten days. As thermal hysteresis effects were expected to be present during the phase transition it was important to keep the liquid helium bin full and the sample at a constant temperature.

The sample tube used in this experiment was of a more complex design consisting of a narrow thin-walled vitreous silica tube approximately 10mm in diameter mounted co-axially inside a similar outer tube of nearly twice the diameter. The B.O.C. cryostat and the double-walled tube are shown in figure 2.10. The solid DI sample S was in the inner tube. The annular exchange space between the tubes ES was kept at a pressure of less than 10^{-6} mm of mercury by a vacuum pump at V. The whole assembly was immersed in the liquid helium bin LH surrounded by a radiation shield cooled by liquid nitrogen LN.

The outer vacuum tail of the B.O.C. cryostat was made of aluminium with a thin window for the neutron beam B to pass through. Apart from a small PTFE spacing disc T of low thermal conductivity the sample in the inner tube was thermally isolated from its surroundings and so, in time it would have slowly cooled down to 4.2K by radiation to the liquid helium LH. By having two small heaters fitted above and below the sample S it was possible to vary its temperature above 4.2K. The minimum temperature attainable with this arrangement was limited (i) by the conduction of heat down the walls of the inner tube as well as along the heater and thermocouple leads H and TC and (ii) by thermal radiation from the top of the sample tube (which was at room temperature). These effects were minimized by the use of very fine wires and by platinum foil P in the sample tube to act as a radiation shield. A compromise had to be made however between the fineness of the electrical leads (to reduce thermal conduction) and the resultant increase of electrical resistance in the control circuits. The temperature measurement, thermocouple calibration and circuits used in temperature control will be described in appendix two.

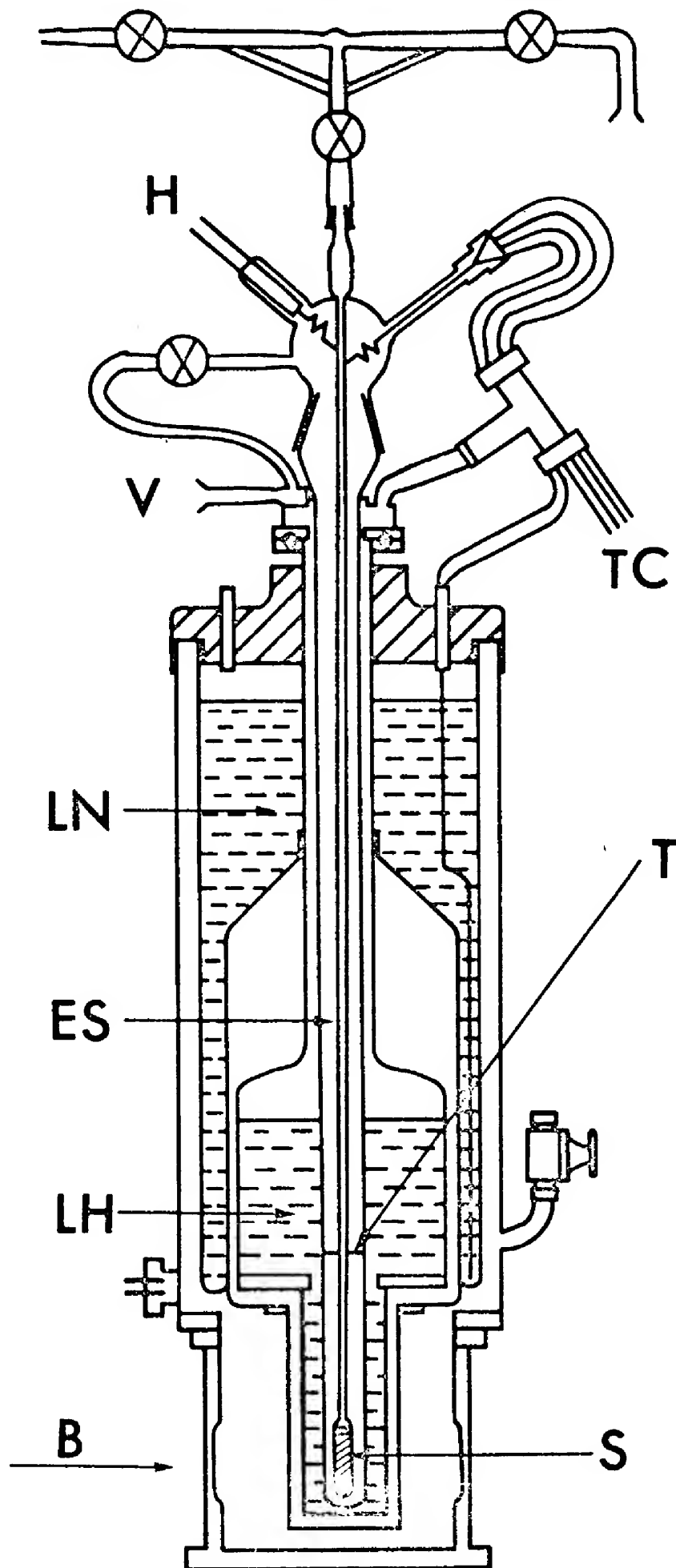


Figure 2.10 The variable temperature cryostat used for studying the lower phase transition of DI by neutron diffraction.

The sample was transferred from the storage tube to the specimen tube by vacuum sublimation. The specimen tube was cooled by liquid nitrogen in a small dewar to condense the DI vapour coming from the storage tube which was kept at a slightly higher temperature. During the sample transfer the annular exchange space ES surrounding the sample S was filled with helium gas at one atmosphere pressure. Convection of the helium gas in the exchange space enabled the latent heat of sublimation to be extracted from the DI sample reasonably quickly and then transmitted to the liquid nitrogen. A sample transfer was completed in approximately 4 hours.

After the sample had been transferred to the double-walled specimen tube, the exchange space ES was evacuated and the specimen tube transferred to a helium cryostat. The sample then cooled down to 40K by radiation to the liquid helium over a period of some hours. Continuous evacuation of the exchange space was necessary (i) to prevent condensation of oxygen or nitrogen impurities in the helium gas on the surface of the exchange space and (ii) to prevent the condensation of solid nitrogen from the atmosphere through the neoprene electrical seals onto the surface of the exchange space. Nitrogen has a high coherent neutron scattering cross-section and even small quantities can seriously change a powder diffraction pattern particularly at low θ -angles.

The cryostat was refilled with liquid helium every 12 hours. The liquid helium transfer lines were precooled with liquid helium and the cryostat filled in approximately 5 minutes. The temperature of the outer vitreous silica tube and the sample varied negligibly during the transfer due to the insulation of the evacuated exchange space.

The back-transfer of the sample was a reversal of the transfer with the added problem of blockages in the narrow specimen tube. These were

always quickly cured by means of a hot-air blower and liquid nitrogen at suitable points.

CHAPTER THREE

X-ray powder diffraction study of the iodine sublattice in the three solid phases of DI

3.1 Introductory theory of diffraction

Thermal neutrons and X-rays when scattered by crystals give diffraction peaks (Bragg reflections) at angles which satisfy the Bragg equation:

$$n\lambda = 2d\sin\theta \quad (23)$$

where n is a positive integer, λ is the wavelength of the incident radiation, d is the interplanar spacing and θ is the diffraction angle (Bragg angle). The integrated intensity of a Bragg peak produced by a powder sample is (Bacon 1955d):

$$I_{\text{obs}}(hkl) = \frac{C |F^2(hkl)| A(\theta) j e^{-2W}}{\sin\theta \sin 2\theta} \quad (24)$$

where h , k and l are the Miller indices of the reflecting planes. C is a scale factor dependent on the flux of the incident radiation and the volume of the sample. $F(hkl)$ is the structure factor and j is the multiplicity factor for the Bragg reflection. $A(\theta)$ is the absorption correction for a randomly polarized X-ray or neutron beam and e^{-2W} is the temperature correction factor.

In equation (24) the crystal structure is described by the structure factor $F(hkl)$ which is defined by the expression:

$$F(hkl) = \sum_{n=1}^{Na} f_n(\theta) \exp [2\pi i (hx_n + ky_n + lz_n)] \quad (25)$$

where x_n , y_n and z_n are the fractional atomic co-ordinates of the n^{th} atom in the unit cell. These are related to the absolute atomic co-ordinates x' , y' and z' by the expression:

$$x = \frac{x'}{a}, \quad y = \frac{y'}{b} \quad \text{and} \quad z = \frac{z'}{c} \quad (26)$$

where a , b and c are the dimensions of the unit cell. $f_n(\theta)$ is the atomic scattering factor which will be discussed later.

The temperature factor (Debye-Waller factor) W in equation (24) describes the effects of thermal motion and can be represented in three forms:

(a) An overall temperature factor B as in equation 24:

$$e^{-2W} = \exp\left[-\frac{2B\sin^2\theta}{\lambda^2}\right] \quad (27)$$

where θ and λ are the diffraction angle and wavelength defined in equation (23).

(b) Each atom in the unit cell is assigned an isotropic vibration amplitude u which is related to the atomic temperature factor B_n by the expression:

$$\langle u^2 \rangle = \frac{B_n}{16\pi^2} \quad (28)$$

The effect of the thermal motion of each atom on the observed intensity $I(hkl)$ is now included in the expression for the structure factor given in equation (25) so that the observed intensity previously described by equation (24) is given by:

$$I_{\text{obs}}(hkl) = \frac{CA(\theta)}{\sin\theta\sin2\theta} |F'(hkl)|^2 \quad (29)$$

$$\text{and} \quad F'(hkl) = \sum_{n=1}^{Na} f_n(\theta) \exp[2\pi i(hx_n + ky_n + lz_n)] \exp\left[-\frac{B_n \sin^2\theta}{\lambda^2}\right] \quad (30)$$

where the parameters are defined in equation (25).

(c) In the general case a symmetric tensor of nine components $\{b_{ij}^n\}$ is used to describe the thermal motion of each atom. The mean square amplitude of vibration of the n^{th} atom in the unit cell in the direction of the unit vector $\underline{q} = (q_1, q_2, q_3)$ is given by:

$$u_n^2(\underline{q}) = \sum_{i=1}^3 \sum_{j=1}^3 \frac{b_{ij}^n q_i q_j}{2\pi^2 |\underline{a}_i^*| \cdot |\underline{a}_j^*|} \quad (31)$$

where $\underline{a}^* = \frac{\underline{b} \times \underline{c}}{\underline{a} \cdot \underline{b} \times \underline{c}}$ etc. are the reciprocal lattice vectors.

A tensor of thermal motion $\{U_{ij}^n\}$ can be defined as:

$$\{U_{ij}^n\} = \frac{\{b_{ij}^n\}}{2\pi^2 |\underline{a}_i^*| \cdot |\underline{a}_j^*|} \quad (32)$$

and

$$u_n^2(\underline{q}) = \sum_{i=1}^3 \sum_{j=1}^3 U_{ij}^n q_i q_j \quad (33)$$

Since the tensor $\{b_{ij}^n\}$ is symmetric, it has six independent terms. The number of independent terms may be further reduced by symmetry if the atoms occupy special positions in the unit cell, see Levy (1956).

Using this general expression for the thermal vibration tensor the structure factor can be written as:

$$F^i(hkl) = \sum_{n=1}^{Na} f_n(\theta) \exp[2\pi i(hx_n + ky_n + lz_n)] \times \\ \exp[-(b_{11}^n h^2 + b_{22}^n k^2 + b_{33}^n l^2 + 2b_{12}^n hk + 2b_{23}^n kl + 2b_{13}^n hl)] \quad (34)$$

The preceding discussion has been pertinent to both X-ray and neutron

scattering. There are however two points of difference.

(a) The atomic scattering factor $f_n(\theta)$. Since the nucleus is effectively a point source the angular distribution of the scattered neutrons is isotropic and the scattering factor $f_n(\theta)$ is a constant, b_n . This is called the coherent scattering length and is a fundamental constant for each isotope of a particular element. X-rays are scattered by the electron core of an atom whose diameter is comparable to the wavelength of an X-ray. This X-ray scattering is described by an atomic scattering factor $f_n(\theta)$ which is proportional to the atomic number of the element and which decreases continuously with increasing scattering angle.

(b) When X-rays are monochromatized by a crystal monochromator the observed intensity in equation (24) is modified by a term p which corrects for polarization, Azaroff (1955).

$$I(hkl) = \frac{C |F^2(hkl)| A(\theta) j e^{-2W} p}{\sin\theta \sin 2\theta} \quad (35)$$

$$\text{where } p = \frac{[(\cos^2 2\theta_M \cos^2 \rho + \sin^2 \rho) \cos^2 2\theta + \cos^2 2\theta_M \sin^2 \rho + \cos^2 \rho]}{(1 + \cos^2 2\theta_M)} \quad (36)$$

θ_M is the Bragg angle of the monochromator and ρ is the angle between the normal to the plane of reflection of the monochromator and the normal to the plane of reflection of the sample.

The following chapters will describe the determination of the crystal structure of the three solid phases of DI from the observed neutron and X-ray powder diffraction patterns. Standard algorithms have been derived and are widely used for refinement of crystal structures and lattice parameters by iterative least-squares techniques.

The quality of the agreement between the intensities calculated for the proposed model and the observed intensities is assessed by a so-called R-factor which for the computer program used in this thesis (MPORFLS described in appendix one) is defined as:

$$R = \sqrt{\frac{\sum_{n=1}^{N_{\text{obs}}} W_n (I_{\text{obs}}^n - s I_{\text{calc}}^n)^2}{\sum_{n=1}^{N_{\text{obs}}} W_n I_{\text{obs}}^n}} \quad (37)$$

where N_{obs} is the number of observations and I_{obs} and I_{calc} are the observed and calculated intensities respectively. s is the scale factor and the weight assigned to the n^{th} observation is W_n .

3.2 X-ray diffraction experiments

X-ray powder diffraction patterns were recorded in all three solid phases of DI. These served several purposes; to verify the purity of the samples in the initial period of the work, to measure the lattice parameters and to provide values for the thermal parameters of the iodine atoms.

(a) The low phase of DI

An X-ray powder diffraction pattern of the low phase of DI was recorded at 4.2K at Queen Mary College using the powder diffractometer and cryostat described in chapter two. It was very difficult to form good quality powder samples in the Lindemann glass capillaries used. Iodine has a high X-ray absorption coefficient and for a cylindrical sample the "optimum" thickness producing maximum diffracted intensity is given by the expression: (International Tables for Crystallography 1959)

$$\mu R = 1.5 \quad (38)$$

where R is the radius of the sample and μ is the linear absorption coefficient defined by:

$$I = I_0 \exp[-\mu t] \quad (39)$$

where I is the transmitted intensity, I_0 the incident intensity and t the thickness of the sample. For DI and CuK_α X-rays of wavelength 1.54178\AA μ is 1015 cm^{-1} and R (optimum) is 0.015 mm . The narrowest available Lindemann glass capillary had a radius of 0.05 mm , however capillaries of this size were always liable to become blocked while condensing the DI gas into the sample space. To overcome this problem a 0.1 mm radius capillary was used. The X-ray powder patterns obtained were of low intensity due to the absorption by the six layers of beryllium in the cryostat plus the fine detector collimation necessary to eliminate the beryllium diffraction patterns.

A suitable powder sample was grown and examined initially by Debye-Scherrer photographs at 84 K and 50 K shown in figure 3.1. (The first powder peak of beryllium occurs at a relatively large angle of 22° in θ). The first X-ray powder line recorded on the film occurred at about $\theta = 10^\circ$ for all of the samples investigated.

An X-ray powder diffraction pattern of the low phase of DI was recorded at 4.2 K with relatively poor statistics using a count-rate meter and chart recorder. The chart recorder output is shown in figure 3.2. Because of the very low scattering power of X-rays for deuterium, the diffraction pattern obtained represents X-ray scattering from the iodine atoms only.

All the observed powder lines could be indexed on the basis of a face-centred orthorhombic lattice where the approximate lattice parameters were derived by using the program PARAM described in appendix one. The following values were obtained:

$$\begin{aligned} a &= 5.94 \pm .02 \text{ \AA} \\ b &= 5.95 \pm .02 \text{ \AA} \\ c &= 6.22 \pm .02 \text{ \AA} \\ \alpha &= \beta = \gamma = 90^\circ \end{aligned}$$

Figure 3.1 Low-angle X-ray powder photograph of
DI at 84K and 50K. —————→



(111)

(111)

(111)



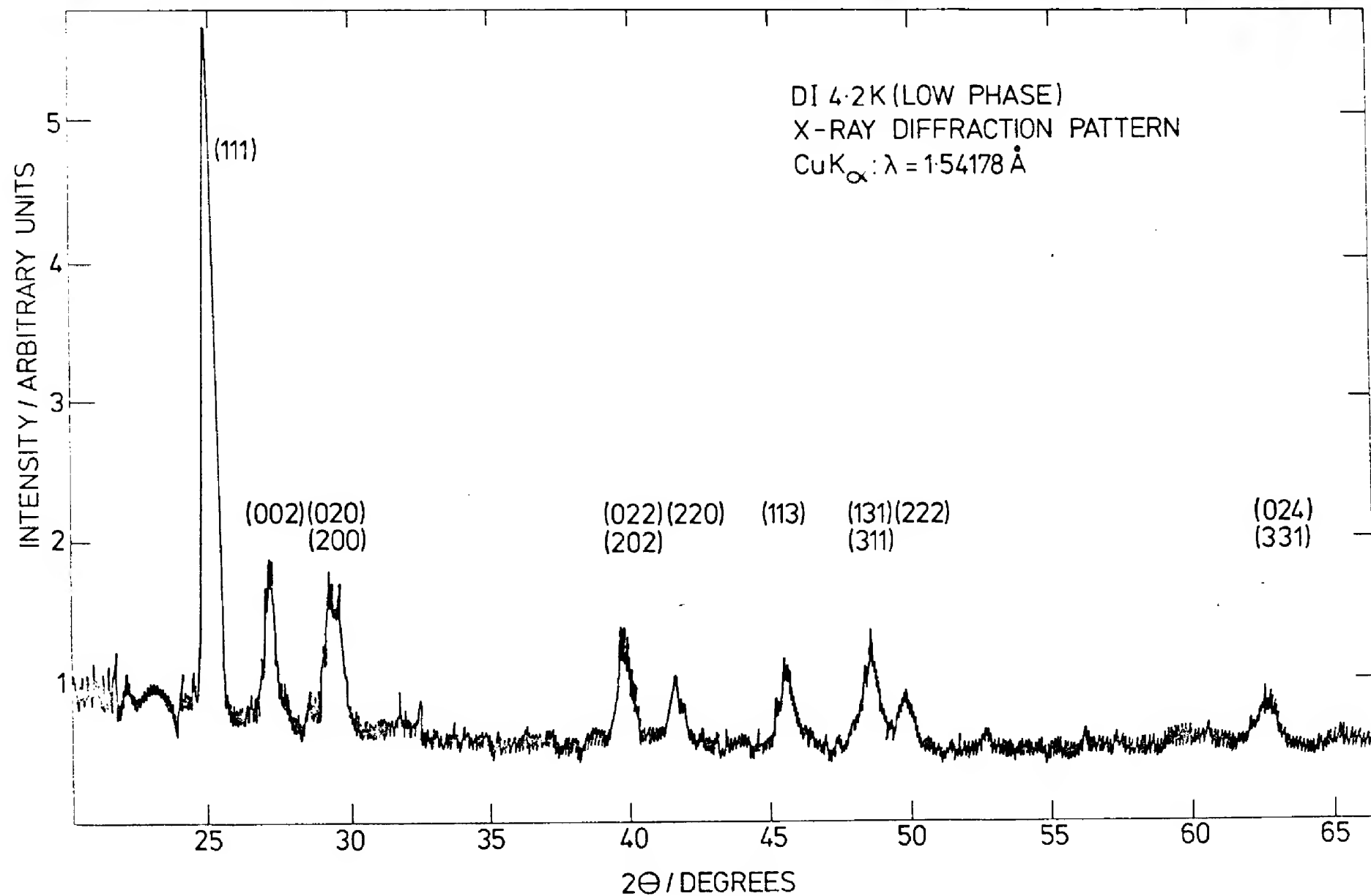


Figure 3.2 X-ray powder pattern of DI at 4.2K (low phase)
chart recorder output.

(b) The middle and high phases of DI

X-ray powder diffraction patterns were recorded at temperatures of 84K, 93K, 103K, 117K, 128K, 129K, 130K and 133K in the middle and high phases using the Nonius goniometer described in chapter two. The patterns recorded indicated a face-centred orthorhombic unit cell for the iodine sublattice in the middle phase. The separation of the (020), (200) doublet was only observed in a very few films, one of these is shown in figure 3.3. The iodine lattice in the high phase was found to be face-centred cubic. An X-ray photograph of the high phase of DI taken at 130K is shown in figure 3.4.

Good quality powder samples for the Nonius goniometer were not difficult to prepare, approximately one in ten powder samples was satisfactory for diffraction studies. After some hours of X-ray exposure the sample decomposed giving rise to a series of low-angle diffraction spots due to free iodine. Ice crystals formed on the outside of the Lindemann glass capillary after approximately twelve hours. In one experiment a series of X-ray photographs were recorded on one film using a very narrow layer-line shield space. This technique is limited by the uniformity of the cassette circumference away from the central zone where the film is held in place by spring clips.

The density profiles of the X-ray powder lines were recorded from these films using a Joyce-Loebl micro-densitometer. The values of the temperature factor derived from different films varied considerably. This was probably due to the high correlation between the absorption correction and the temperature factor. An additional source of error was the uncertainty in the volume of the powder sample. Most samples were not solid cylinders but hollow cylinders of varying thickness lining the inside wall of the capillary.

Figure 3.4 X-ray powder photograph of DI at 130K (high phase).

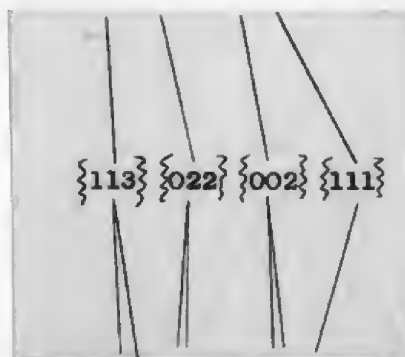


Figure 3.3 X-ray powder photograph of DI at 117K (middle phase).



Lattice parameter refinements were carried out on all recorded data and the results are shown in Table 3.1 and figure 3.5. The lattice parameters of HI recorded by Mauer and Keffer (1964) are shown in figure 3.5 as crosses in comparison with the lattice parameters of DI (shown as dots) obtained by X-ray and neutron diffraction experiments.

Some X-ray measurements on the middle and high phases of HI have been reported since the work of this thesis was carried out. Simon in 1970 has measured the lattice parameters of HI at 100K, 130K and 210K using a photographic powder technique and has also found that the middle phase of HI is orthorhombic. The complete results are given in table 3.1.

T°K.	a Å	b Å	c Å	Volume Å ³	Technique	Sample/phase
4.2	5.94 ± .02	5.95 ± .02	6.22 ± .02	220 ± 2	X-ray (diffractometer) Neutron (Panda) Neutron (Curran)	DI low phase
4.2	5.90 ± .004	5.94 ± .004	6.43 ± .003	225 ± .5		
45	5.89 ± .02	5.91 ± .02	6.43 ± .04	224 ± 3		
76	6.00 ± .04	6.00 ± .04	6.49 ± .08	234 ± 6		
84	5.979 ± .007	6.024 ± .007	6.517 ± .009	235	X-ray	DI middle phase
93	6.010 ± .006	6.065 ± .006	6.549 ± .007	239		
103	6.032 ± .012	6.098 ± .015	6.542 ± .016	241		
117	6.061 ± .006	6.146 ± .006	6.508 ± .011	242		
128	6.271 ± .003	-	-	247	(Nonius camera)	DI high phase
129	6.276 ± .003	-	-	247		
130	6.293 ± .006	-	-	249		
133	6.289 ± .018	-	-	249		
42	5.987	5.987	6.48	232	X-ray (Flat plate diffractometer) Mauer and Keffer (1964)	HI low phase
39	6.0	6.0	6.5	234		HI middle phase
77	6.042	6.042	6.52	238		HI high phase
120	6.106	6.106	6.56	245		
130	6.246	-	-	248		
180	6.295	-	-	249		
100	6.049 ± .003	6.127 ± .003	6.566 ± .003	243 ± .4	X-ray (powder camera) Simon (1970)	HI middle phase
130	6.290 ± .003	-	-	249 ± .4		HI high phase
210	6.403 ± .003	-	-	262.5 ± .4		

TABLE 3.1. Lattice parameters of HI and DI measured by
X-ray and neutron powder diffraction.

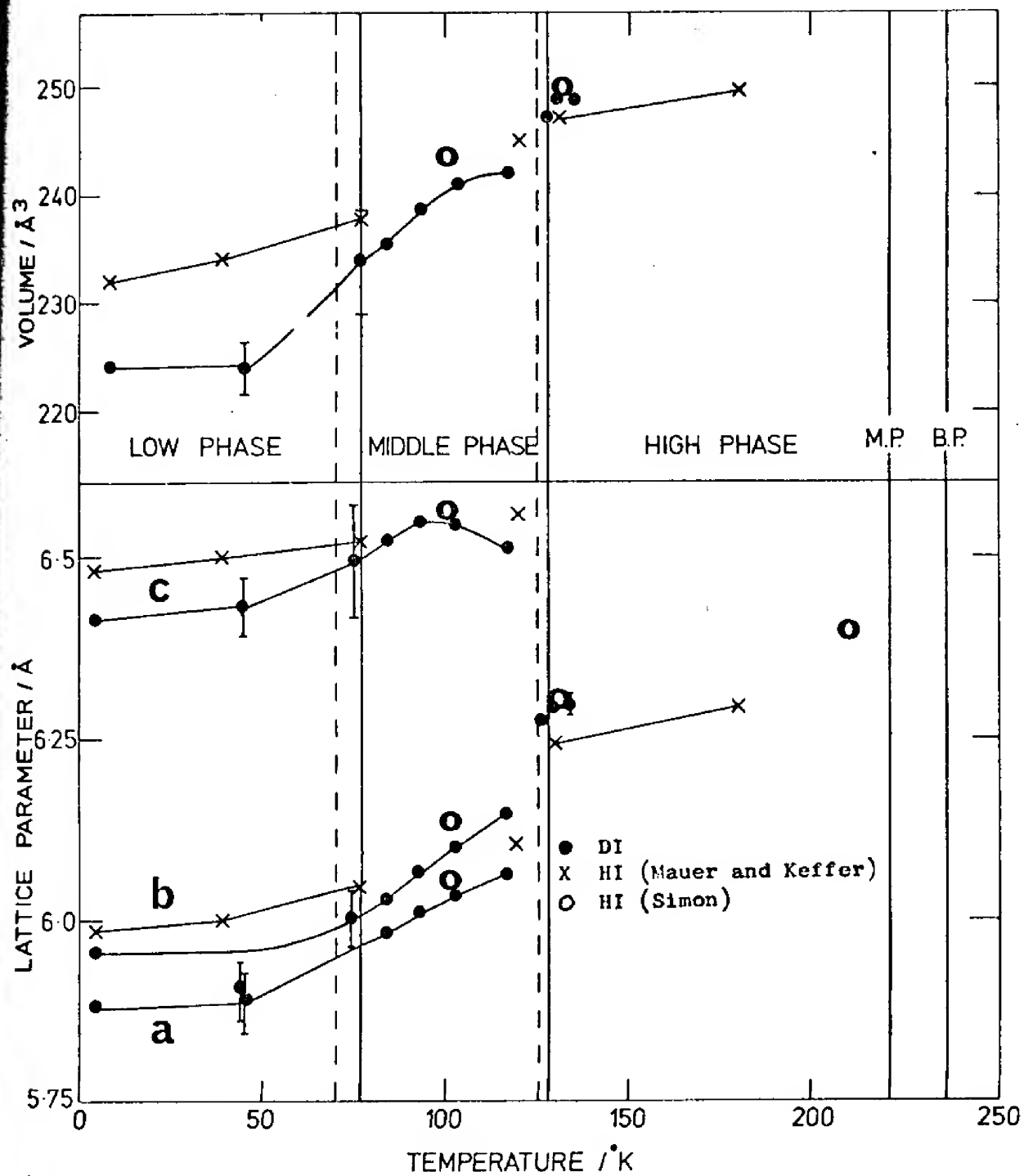


Figure 3.5 Lattice parameters of HI and DI as function of temperature.

CHAPTER FOUR

Neutron powder diffraction study of the low phase of

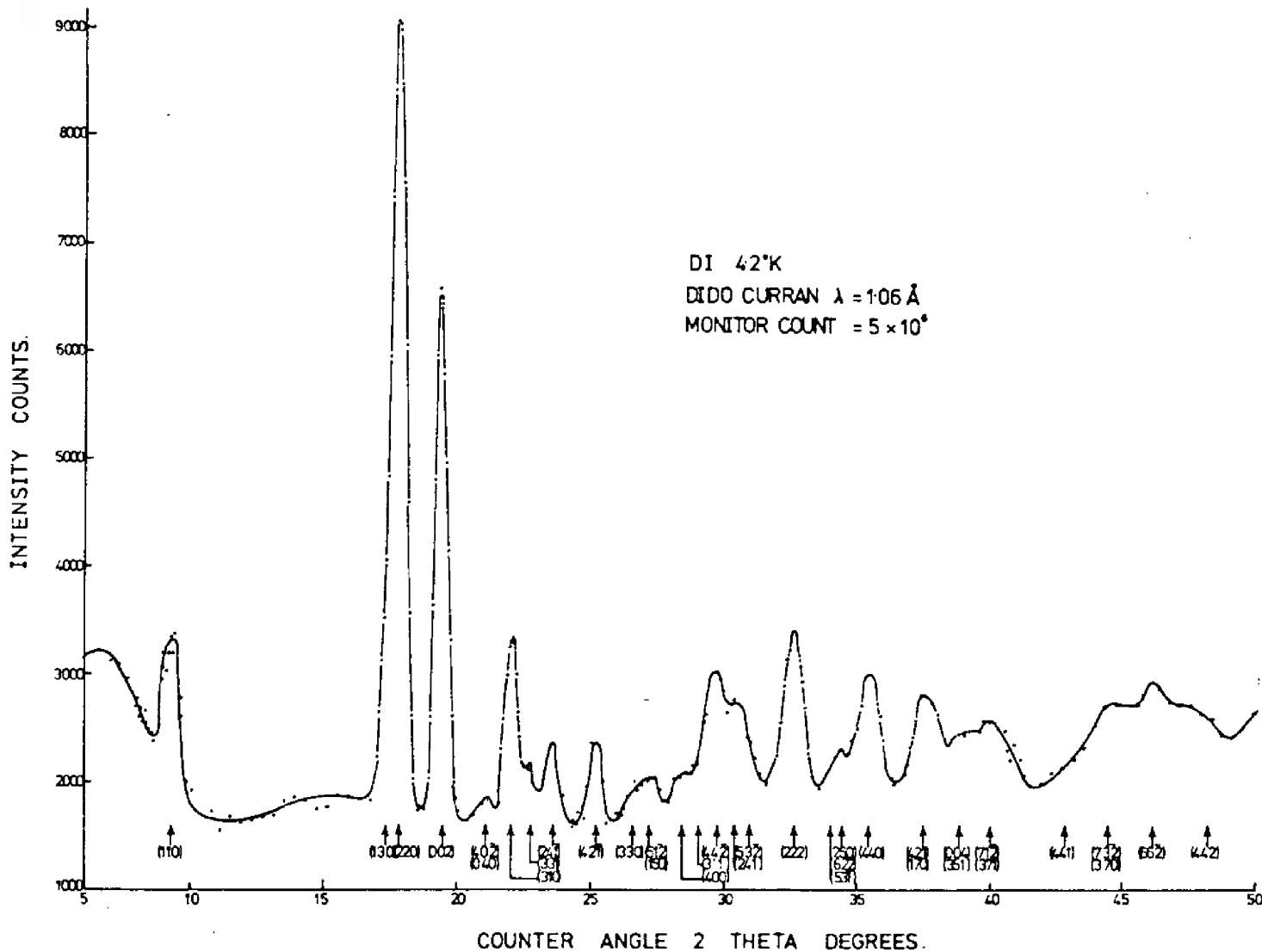
DI at 4.2K

4.1 Summary of the neutron diffraction experiments

The crystal structure of the low phase of DI at 4.2K was first studied by neutron powder diffraction techniques using the Dido 'Curran' diffractometer (see §2.3a) and a neutron wavelength of 1.06\AA . The sample was contained in a vitreous silica tube immersed in liquid helium inside a vanadium-tail cryostat (see §2.4). The neutron powder diffraction pattern recorded in this experiment is shown in figure 4.1; the broad low hump in the background at low 2θ -angles is due to neutrons scattered from the liquid helium and the walls of the vitreous silica sample container. As mentioned earlier in §2.4, the neutron scattering of vanadium is almost totally incoherent and isotropic. This experiment was subsequently repeated with the same diffractometer and the same neutron wavelength but using a DI sample prepared by a different method (see §§2.1a, b). The neutron powder pattern recorded in this experiment was similar to the one shown.

Neutron powder diffraction patterns of the low phase of DI were also recorded with wavelengths of 2.66\AA and 1.886\AA using the Pluto 'Panda' diffractometer under similar experimental conditions as described above. The former of these ($\lambda = 2.66\text{\AA}$) was a trial experiment and its results were not used in the final analysis due to the suspected presence of $\lambda/3$ contamination in the monochromatic neutron beam. Nevertheless, the improved angular resolution of the diffraction pattern recorded with $\lambda = 2.66\text{\AA}$ showed that many of the powder peaks, which appeared to be single in the diffraction pattern recorded with a wavelength of 1.06\AA using the 'Curran' diffractometer, were in fact multiple peaks containing several components.

(low phase) recorded with Dido Curran.



Finally, the neutron powder diffraction pattern of the low phase of DI was recorded with the 'Panda' diffractometer using a wavelength of 1.886\AA . This diffraction pattern had good angular resolution over a wide angular range and also good statistical accuracy; it is shown in figure 4.2.

4.2 The unit cell of the low phase

The most interesting feature of the neutron powder diffraction of the low phase of DI was the presence of a distinct peak at low angles not seen in the X-ray powder pattern (see the peak (110) in figure 4.1). Using approximate lattice parameters derived from the X-ray powder diffraction patterns of the low and middle phases of HI and DI (see §3.2) all neutron powder peaks observed in the low phase of DI could be assigned Miller Indices. A large orthorhombic unit cell was assumed with all three edges twice as large as the edges of the orthorhombic unit cell derived from the X-ray powder diffraction patterns of the low phase. This large orthorhombic unit cell contained 32 DI molecules.

Since it was known from X-ray powder diffraction studies that the iodine atoms formed a face-centred orthorhombic lattice with four iodine atoms in the unit cell, the much larger unit cell revealed by the neutron powder diffraction had to be attributed to a more complex arrangement of the deuterium atoms. This could not be detected by X-ray diffraction techniques because the X-ray scattering of the deuterium atoms is negligible compared with the X-ray scattering of the iodine atoms. Thus, X-ray diffraction of DI reveals only the position of the iodine atoms. In contrast, the neutron scattering cross-sections of deuterium and iodine are approximately equal, hence the neutron diffraction pattern reveals the location of the deuterium atoms as well.

A least-squares refinement of the lattice parameters was carried out

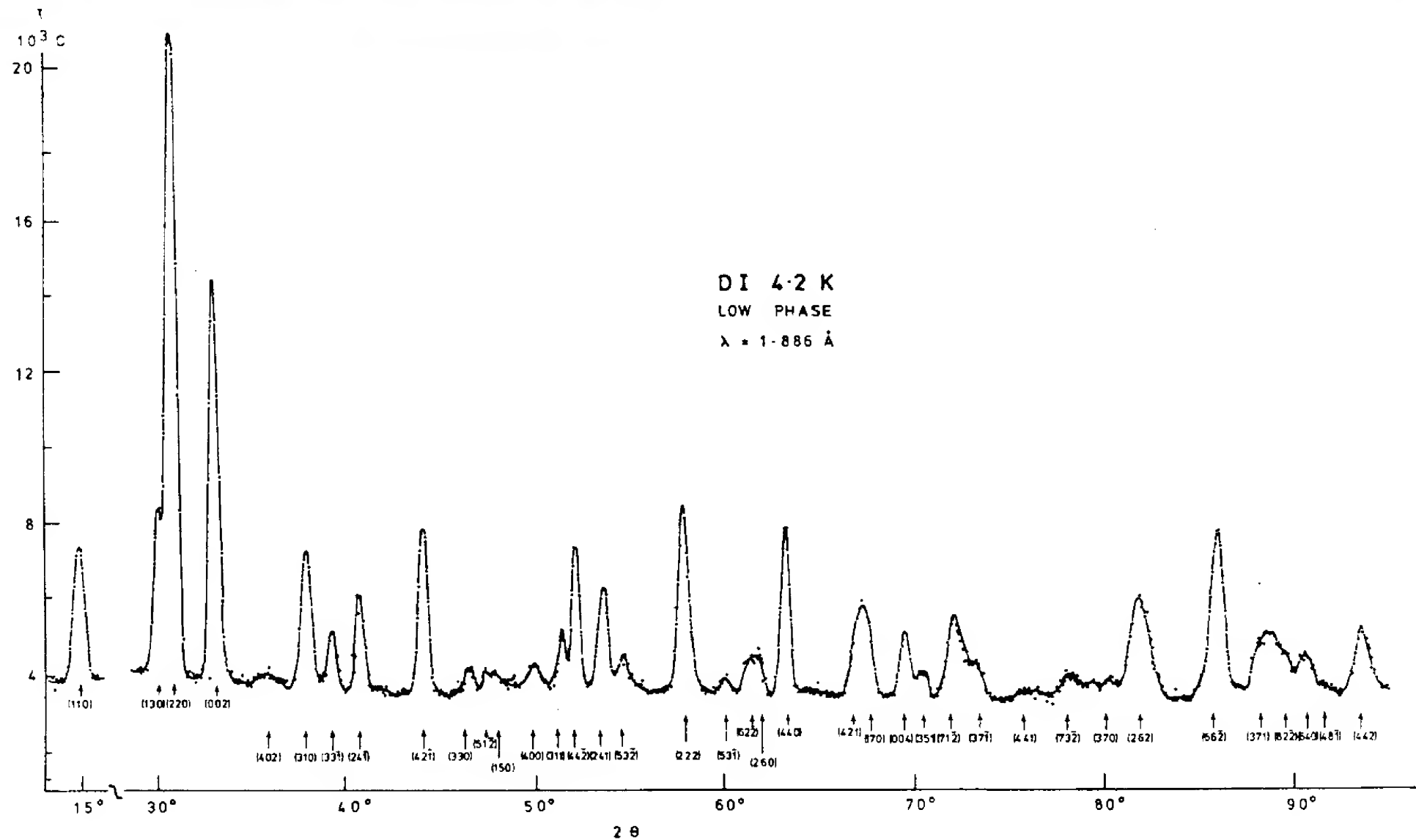


Figure 4.2 Neutron powder diffraction pattern of DI at 4.2K (low phase) recorded with Pluto Panda.

using the computer program PARAM (Appendix one). Since crystal-monochromated neutron beams give sharp peaks only in the so-called 'parallel-focusing' geometry (see Bacon 1955b), the neutron powder diffraction pattern was recorded only on one side of the incident beam. As a result the direction (zero-angle) of the incident beam had to be determined by calculation. It was varied via the computer program PARAM used to refine the lattice parameters. Table 4.1 lists the results of the lattice parameter refinement obtained with the program PARAM for the low phase of DI at 4.2K. The refinement is based on the powder diffraction pattern recorded with the 'Panda' diffractometer using a neutron wavelength of $\lambda = 1.886\text{\AA}$.

At this stage it will be useful to summarize briefly the structure of the middle phase of DI which will be described in greater detail in Chapter five. The crystal structure of the middle phase has a face-centred orthorhombic unit cell containing four molecules. The iodine atoms occupy face-centred positions and each deuterium atom has two equilibrium positions symmetrical about the iodine atoms. The two equilibrium positions are in the (001) plane 180° apart and the deuterium atoms 'flip' between them at random (two-fold disorder). The space group is Bbcm (no.64) and a projection of the time-average of the structure onto the (001) plane is shown in figure 5.4.

The calorimetric data described in §1.2 show a λ -anomaly in the specific heat of DI in the lower phase transition region associated with an anomalous increase in entropy. This 'excess' entropy can be interpreted as a change in the configurational entropy of the solid due to an increase in disorder on transition and will be discussed in detail in chapter seven. Here it is sufficient to state that the observed anomalous entropy change between the low and middle phases of DI is;

$$1.101 \text{ J mole}^{-1}$$

h	k	l	Observed 2 θ	Calculated 2 θ	$\frac{2\theta_{obs} - 2\theta_{calc}}{2\theta_{calc}}$
1	1	1	15.60	15.45188	0.14812
1	3	1	30.50	30.35504	0.14496
3	1	1	30.60	30.49224	0.10776
2	2	2	31.18	31.19404	-0.01404
0	0	4	34.12	34.11903	0.00097
0	4	0	36.88	37.04981	-0.16981
4	0	0	37.40	37.27984	0.12016
1	3	3	39.04	39.02716	0.01284
3	3	1	40.40	40.46930	-0.06930
4	2	0	41.80	41.82246	-0.02246
2	4	2	45.15	45.25101	-0.10101
3	3	3	47.55	47.56985	-0.01985
1	5	1	48.52	48.62210	-0.10210
5	1	1	49.01	48.89929	0.11071
0	4	4	51.30	51.24540	0.05460
1	3	5	52.80	52.79119	0.00881
4	4	0	53.56	53.57296	-0.01296
4	2	4	55.00	55.03411	-0.03411
3	5	1	56.00	56.02260	-0.02260
2	2	6	59.23	59.25846	-0.02846
3	5	3	61.80	61.78361	0.01639
2	6	2	63.01	63.15091	-0.14091
6	2	2	63.58	63.46199	0.11801
4	4	4	65.04	65.05976	-0.01976
2	4	6	68.90	68.91514	-0.01514
7	1	1	69.58	69.45674	0.12326
0	0	8	71.78	71.85058	-0.07058
5	3	5	72.68	72.64738	0.03262
1	7	3	74.40	74.20910	0.19090
7	3	1	75.48	75.52423	-0.04423
4	4	6	78.00	78.08179	-0.08179
3	7	3	80.10	80.21388	-0.11388
6	2	6	84.20	84.11457	0.08543
6	6	2	87.60	87.53464	0.06536
4	4	8	95.44	95.43435	0.00565

	<u>Old</u>	<u>New</u>	<u>Delta</u>	<u>Estimated</u> <u>Std. Dev.</u>
a	11.801530	11.801530	0.00	0.007836
b	11.872205	11.872205	-0.00	0.007409
c	12.857706	12.857706	0.00	0.004890
α	90.00	90.00	0.00	0.00
β	90.00	90.00	0.00	0.00
γ	90.00	90.00	0.00	0.00

The error of fit is 2.015030819

Correlation Coefficients

	<u>b</u>	<u>c</u>	<u>α</u>	<u>β</u>	<u>γ</u>
a	-0.69644	-0.10287	0.	0.	0.
b		-0.27791	0.	0.	0.
c			0.	0.	0.
α				0.	0.
β					0.
γ					

TABLE 4.1. Results of the lattice parameter refinement obtained with the program PARAM for the low phase of DI at 4.2K. The refinement is based upon the powder diffraction pattern recorded with the 'Panda' with a neutron wavelength of $\lambda = 1.866\text{\AA}$.

If this change is due to an increase in configurational entropy it should be equal to:

$$\Delta S_{1-2} = 1.101 = k \ln \frac{n_1}{n_2} \quad (40)$$

where k is the Boltzmann constant and $n_1 n_2$ are the number of equilibrium positions in the low and middle phases respectively. For the lower phase transition in DI;

$$\frac{n_{\text{middle}}}{n_{\text{low}}} = 1.74 \quad (41)$$

This value supports the assumption that the low phase is ordered and the middle phase is two-fold disordered. The heavy iodine atoms are expected to occupy essentially the same ordered positions in both the low and middle phases, while the deuterium atoms are expected to occupy positions which are likely to coincide with one of their equilibrium positions in the middle phase.

On passing through the lower phase transition point the two-fold disordered positions of the middle phase are expected to be achieved by re-orientation of the DI molecules through 180° . Though re-orientations through 90° seem to be less probable, they cannot be excluded at present from consideration.

Having found the true unit cell of the low phase the next step was to determine the space group from the systematic absences in the observed powder pattern and then propose suitable models for the structure of the low phase.

4.3 Models based on orthorhombic space groups

The neutron powder diffraction pattern of the low phase was initially assigned Miller indices on the basis of a large orthorhombic unit cell containing 32 DI molecules. The observed peaks obeyed the selection rules for a face-centred lattice;

$$h + k, k + l, (h + l) = 2n \quad (42)$$

There are five face-centred orthorhombic space groups; F222 (No.22), Fmm2 (No.42), Fdd2 (No.43), Fmmm (No.69) and Fddd (No.70).

Of these the space group Fddd can be excluded because it also requires that in

$$hk0; \quad h + k = 4n \quad (h, k = 2n) \quad (43)$$

hence it would not allow the observed (420) powder peak. Furthermore, the face-centred orthorhombic unit cell containing 32 DI molecules should be compatible with the iodine sublattice derived from the X-ray powder pattern of the low phase. This requires that the large orthorhombic unit cell should accommodate eight small face-centred orthorhombic unit cells containing four iodine atoms each, forming a 'super-face-centred' iodine sublattice. In addition, the symmetry operations of the face-centred orthorhombic space group (when applied to the deuterium atoms) should provide an ordered subgroup of the two-fold disordered DI middle phase described in the previous section.

It was found that, out of the four remaining orthorhombic space groups, F222 (No.22) and Fdd2 (No.43) could produce the 'super-face-centred' iodine sublattice. The 32 iodine positions in space group F222 (No.22) can occupy four 8-fold special positions, described in Wyckoff notation, as;

$$8e \quad (x, 0, 0), (\bar{x}, 0, 0) \quad (44)$$

$$8f (0,y,0), (0,\bar{y},0) \quad (45)$$

$$8g (0,0,z), (0,0,\bar{z}) \quad (46)$$

$$8i (\frac{1}{4},y,\frac{1}{4}), (\frac{1}{4},\frac{1}{2}-y,\frac{1}{4}) \quad (47)$$

Choosing x , y and z separately as $\frac{1}{4}$ leads to an iodine sublattice of the required type. However, it is not possible to choose co-ordinates for the deuterium atoms which provide an ordered subgroup of the middle phase.

In space group $Fdd2$ (No.43) the 32 iodine atoms can occupy two 16-fold special positions, described in Wyckoff notation as;

$$16b (x,y,z), (\bar{x},\bar{y},z), (\frac{1}{4}-x, \frac{1}{4}+y, \frac{1}{4}+z), (\frac{1}{4}+x, \frac{1}{4}-y, \frac{1}{4}+z) \\ (0,0,0; 0,\frac{1}{2},\frac{1}{2}; \frac{1}{2},0,\frac{1}{2}; \frac{1}{2},\frac{1}{2},0) + \quad (48)$$

Choosing (x,y,z) as $(\frac{1}{4},\frac{1}{4},0)$ and $(\frac{1}{4},\frac{1}{4},0)$ respectively leads to an iodine sublattice of the required kind and a deuterium lattice which is a subgroup of the middle phase.

Structure models of the low phase based on the orthorhombic space group $Fdd2$ (No.43) were generated in the following way. The deuterium atoms were constrained to remain in the (001) plane and occupy one of four positions. Two of these coincided with positions they occupy in the middle phase and the others were derived from these by a 90° rotation of the molecule about the orthorhombic c -axis passing through the iodine atom. Since there were two molecules in the asymmetric unit of this structure there were $2^4 = 16$ possible models (of which many were equivalent). There were only three different models among the sixteen possible and these are shown in figures 4.3 to 4.5.

The first model could be easily discarded since it could be described by a small unit cell containing four molecules. The second model was

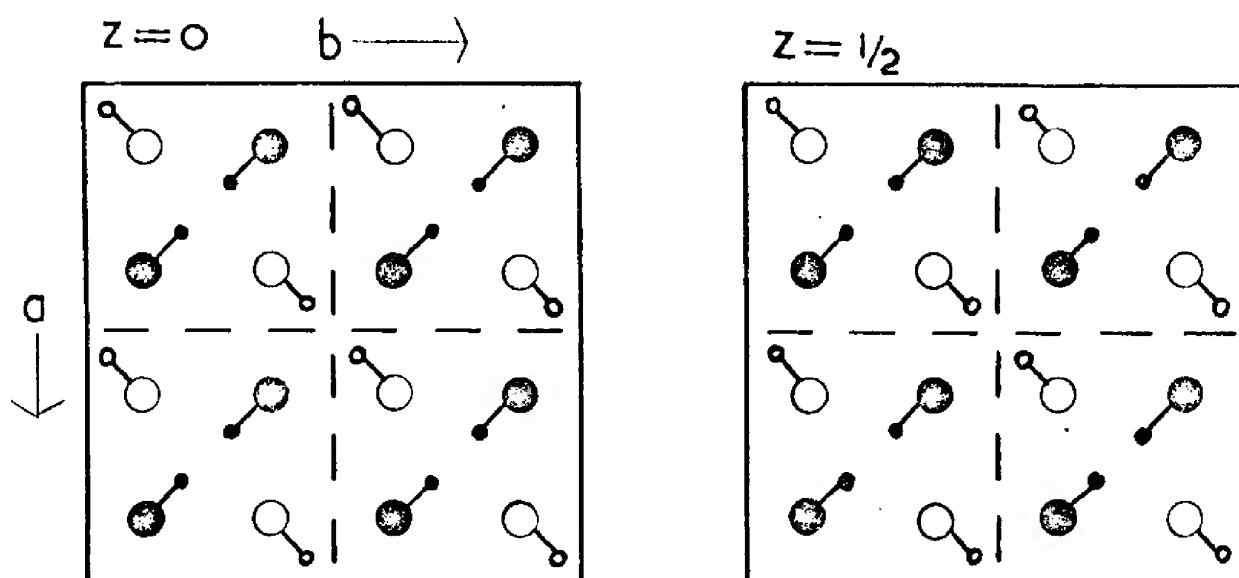


Figure 4.3 Proposed structure for DI low phase space-group Fdd2 (No.43), model No. 1.

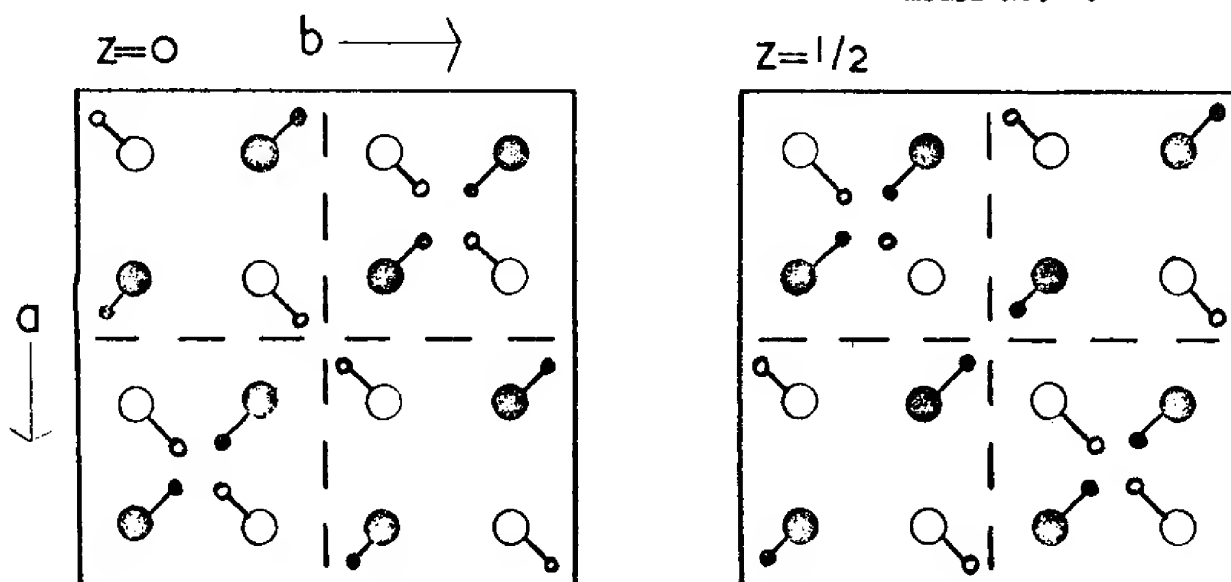


Figure 4.4 Proposed structure for DI low phase space-group Fdd2 (No.43), model No. 2.

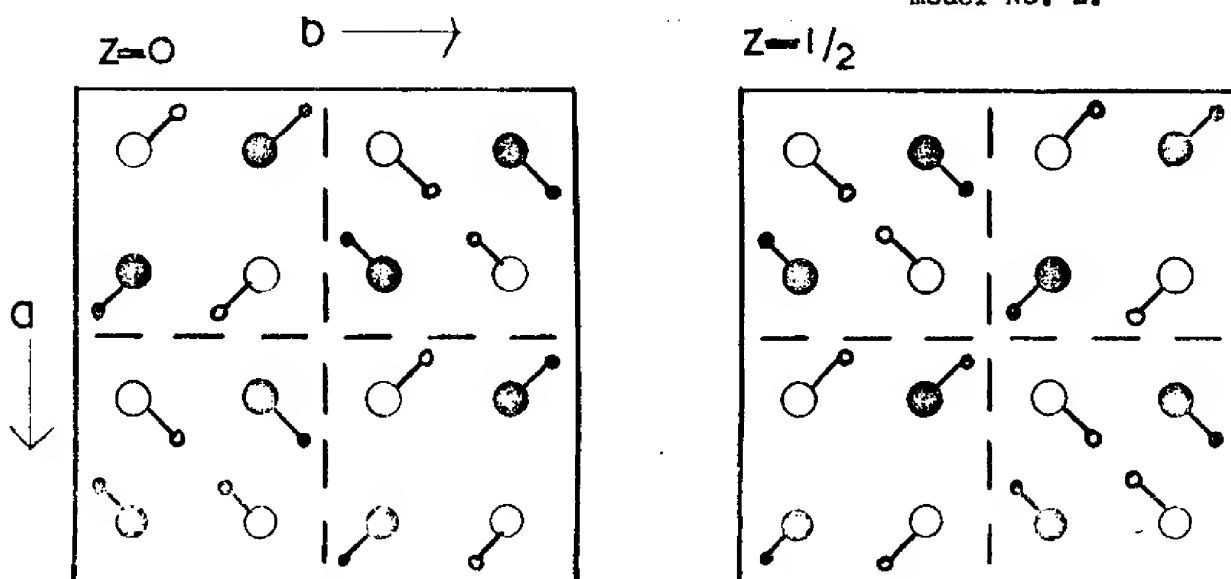


Figure 4.5 Proposed structure for DI low phase space-group Fdd2 (No.43), model No. 3.

theoretically possible but physically unlikely because the electrostatic repulsion is expected to prevent the deuterium atoms of neighbouring molecules facing one another. The third model was slightly more realistic since it contained ten adjacent deuterium atoms. Eventually all three models had to be discarded because the diffraction patterns calculated for them were quite unlike the observed pattern.

4.4 Models based on monoclinic space groups

As an alternative to the large face-centred orthorhombic unit cell containing 32 DI molecules the observed neutron powder peaks of the low phase could also be indexed on the basis of a C-centred monoclinic cell containing 16 molecules. The edges of the face-centred large orthorhombic unit cell can be transformed to the edges of the smaller monoclinic cell in six different ways. These transformations are described by the following matrices and are illustrated in figure 4.6.

No. 1

$$\begin{bmatrix} \underline{a'} \\ \underline{b'} \\ \underline{c'} \end{bmatrix}_{\text{monoclinic}} = \begin{bmatrix} 1 & 0 & 0 \\ 0 & 1 & 0 \\ -\frac{1}{2} & 0 & \frac{1}{2} \end{bmatrix} \begin{bmatrix} \underline{a} \\ \underline{b} \\ \underline{c} \end{bmatrix}_{\text{orthorhombic}}$$

$$\begin{aligned} a_1 &= a &= 11.802\text{\AA} \\ b_1 &= b &= 11.872\text{\AA} \\ c_1 &= \frac{\sqrt{a^2 + c^2}}{2} &= 8.727\text{\AA} \end{aligned} \quad (49)$$

No. 2

$$\begin{bmatrix} \underline{a'} \\ \underline{b'} \\ \underline{c'} \end{bmatrix}_{\text{monoclinic}} = \begin{bmatrix} 0 & 0 & 1 \\ 0 & 1 & 0 \\ -\frac{1}{2} & 0 & -\frac{1}{2} \end{bmatrix} \begin{bmatrix} \underline{a} \\ \underline{b} \\ \underline{c} \end{bmatrix}_{\text{orthorhombic}}$$

$$\begin{aligned} a_2 &= c &= 12.858\text{\AA} \\ b_2 &= b &= 11.872\text{\AA} \\ c_2 &= \frac{\sqrt{a^2 + c^2}}{2} &= 8.727\text{\AA} \end{aligned} \quad (50)$$

No. 3

$$\begin{bmatrix} \underline{a'} \\ \underline{b'} \\ \underline{c'} \end{bmatrix}_{\text{monoclinic}} = \begin{bmatrix} 0 & 0 & 1 \\ 1 & 0 & 0 \\ 0 & \frac{1}{2} & -\frac{1}{2} \end{bmatrix} \begin{bmatrix} \underline{a} \\ \underline{b} \\ \underline{c} \end{bmatrix}_{\text{orthorhombic}}$$

$$\begin{aligned} a_3 &= c &= 12.858\text{\AA} \\ b_3 &= a &= 11.802\text{\AA} \\ c_3 &= \frac{\sqrt{b^2 + c^2}}{2} &= 8.750\text{\AA} \end{aligned} \quad (51)$$

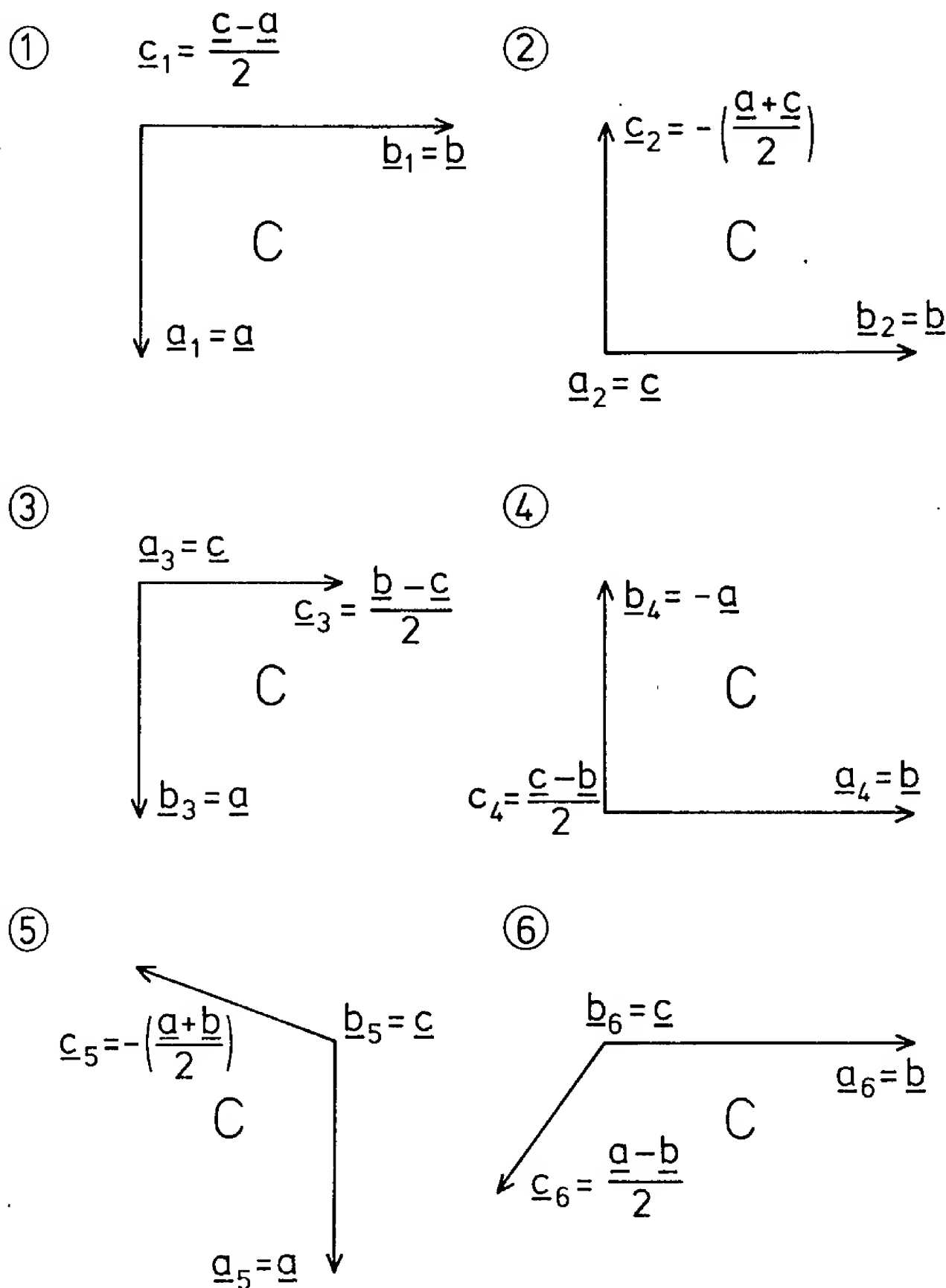


Figure 4.6 The six methods of transforming the large orthorhombic unit cell to the smaller monoclinic unit cell.

No. 4

$$\begin{bmatrix} \underline{a'} \\ \underline{b'} \\ \underline{c'} \end{bmatrix}_{\text{monoclinic}} = \begin{bmatrix} 0 & 1 & 0 \\ 1 & 0 & 0 \\ 0 & -\frac{1}{2} & \frac{1}{2} \end{bmatrix} \begin{bmatrix} \underline{a} \\ \underline{b} \\ \underline{c} \end{bmatrix}_{\text{orthorhombic}}$$

$$\begin{aligned} a_4 &= b = 11.872\text{\AA} \\ b_4 &= a = 11.802\text{\AA} \\ c_4 &= \frac{\sqrt{b^2 + c^2}}{2} = 8.750\text{\AA} \end{aligned} \quad (52)$$

No. 5

$$\begin{bmatrix} \underline{a'} \\ \underline{b'} \\ \underline{c'} \end{bmatrix}_{\text{monoclinic}} = \begin{bmatrix} 1 & 0 & 0 \\ 0 & 0 & 1 \\ -\frac{1}{2} & -\frac{1}{2} & 0 \end{bmatrix} \begin{bmatrix} \underline{a} \\ \underline{b} \\ \underline{c} \end{bmatrix}_{\text{orthorhombic}}$$

$$\begin{aligned} a_5 &= a = 11.802\text{\AA} \\ b_5 &= c = 12.858\text{\AA} \\ c_5 &= \frac{\sqrt{a^2 + b^2}}{2} = 8.370\text{\AA} \end{aligned} \quad (53)$$

No. 6

$$\begin{bmatrix} \underline{a'} \\ \underline{b'} \\ \underline{c'} \end{bmatrix}_{\text{monoclinic}} = \begin{bmatrix} 0 & 1 & 0 \\ 0 & 0 & 1 \\ \frac{1}{2} & -\frac{1}{2} & 0 \end{bmatrix} \begin{bmatrix} \underline{a} \\ \underline{b} \\ \underline{c} \end{bmatrix}_{\text{orthorhombic}}$$

$$\begin{aligned} a_6 &= b = 11.872\text{\AA} \\ b_6 &= c = 12.858\text{\AA} \\ c_6 &= \frac{\sqrt{a^2 + b^2}}{2} = 8.370\text{\AA} \end{aligned} \quad (54)$$

These matrices transform both the unit cell edges and the Miller indices of lattice planes. Table 4.2 lists the Miller indices of the Bragg peaks observed in the neutron powder diffraction pattern of the low phase of DI in the orthorhombic and six monoclinic unit cells. Since the lattice parameters of all these monoclinic unit cells are simply related to those of the large orthorhombic cell, it was unnecessary to carry out least squares refinement of the lattice parameters in the monoclinic system.

After the orthorhombic Miller indices had been transformed into the six corresponding sets of monoclinic indices by means of the matrices (49) to (54) they were examined for systematic absences. There are five C-centred monoclinic space groups;

C2 (No.5), Cm (No.8), Cc (No.9), C2/m (No.12) and C2/c (No.15).

Of these C2, Cm and C2/m have no selection rules other than those characterizing a C-centred lattice, i.e.

$$\text{in } hkl; \quad h+k = 2n, \quad h0l; \quad (h=2n), \quad 0k0; \quad (k=2n) \quad (55)$$

Face-centred orthorhombic unit cell	C-centred monoclinic unit cells					
	1	2	3	4	5	6
111 ($\frac{110}{11\bar{1}}$	$\frac{11\bar{1}}{\bar{1}10}$	$\frac{110}{\bar{1}11}$	$\frac{1\bar{1}0}{1\bar{1}\bar{1}}$	$\frac{11\bar{1}}{1\bar{1}\bar{1}}$	$\frac{110}{1\bar{1}0}$
113 ($\frac{111}{11\bar{2}}$	$\frac{31\bar{2}}{311}$	$\frac{31\bar{1}}{312}$	$\frac{1\bar{1}1}{1\bar{1}\bar{2}}$	$\frac{13\bar{1}}{13\bar{1}}$	$\frac{130}{130}$
131 ($\frac{130}{13\bar{1}}$	$\frac{13\bar{1}}{\bar{1}30}$	$\frac{111}{\bar{1}12}$	$\frac{31\bar{1}}{31\bar{2}}$	$\frac{11\bar{2}}{1\bar{1}\bar{2}}$	$\frac{31\bar{1}}{31\bar{1}}$
311 ($\frac{31\bar{1}}{31\bar{2}}$	$\frac{11\bar{2}}{\bar{1}1\bar{1}}$	$\frac{130}{\bar{1}31}$	$\frac{1\bar{3}0}{13\bar{1}}$	$\frac{31\bar{2}}{31\bar{2}}$	$\frac{111}{1\bar{1}1}$
222 ($\frac{220}{22\bar{2}}$	$\frac{22\bar{2}}{220}$	$\frac{220}{22\bar{2}}$	$\frac{2\bar{2}0}{22\bar{2}}$	$\frac{22\bar{2}}{22\bar{2}}$	$\frac{220}{220}$
004 ($\frac{002}{00\bar{2}}$	$\frac{40\bar{2}}{402}$	$\frac{40\bar{2}}{402}$	$\frac{002}{00\bar{2}}$	$\frac{040}{040}$	$\frac{040}{040}$
040	040	040	002	$40\bar{2}$	$00\bar{2}$	$40\bar{2}$
400	$40\bar{2}$	$00\bar{2}$	040	040	$40\bar{2}$	002
133 ($\frac{131}{13\bar{2}}$	$\frac{33\bar{2}}{331}$	$\frac{310}{313}$	$\frac{310}{31\bar{3}}$	$\frac{13\bar{2}}{13\bar{2}}$	$\frac{33\bar{1}}{33\bar{1}}$
331 ($\frac{33\bar{1}}{33\bar{2}}$	$\frac{13\bar{2}}{\bar{1}3\bar{1}}$	$\frac{131}{\bar{1}32}$	$\frac{33\bar{1}}{33\bar{2}}$	$\frac{31\bar{3}}{31\bar{3}}$	$\frac{310}{310}$
420	$42\bar{2}$	$02\bar{2}$	041	$24\bar{1}$	$40\bar{3}$	201
242 ($\frac{240}{24\bar{2}}$	$\frac{24\bar{2}}{240}$	$\frac{221}{223}$	$\frac{42\bar{1}}{423}$	$\frac{22\bar{3}}{223}$	$\frac{42\bar{1}}{42\bar{1}}$
333 ($\frac{330}{33\bar{3}}$	$\frac{33\bar{3}}{330}$	$\frac{330}{333}$	$\frac{330}{33\bar{3}}$	$\frac{33\bar{3}}{333}$	$\frac{330}{330}$
151 ($\frac{150}{15\bar{1}}$	$\frac{15\bar{1}}{\bar{1}50}$	$\frac{112}{\bar{1}13}$	$\frac{51\bar{2}}{513}$	$\frac{11\bar{3}}{113}$	$\frac{51\bar{2}}{51\bar{2}}$
511 ($\frac{51\bar{2}}{513}$	$\frac{11\bar{3}}{\bar{1}1\bar{2}}$	$\frac{150}{\bar{1}51}$	$\frac{1\bar{5}0}{15\bar{1}}$	$\frac{51\bar{3}}{513}$	$\frac{112}{11\bar{2}}$
044 ($\frac{042}{04\bar{2}}$	$\frac{44\bar{2}}{442}$	$\frac{400}{404}$	$\frac{400}{404}$	$\frac{04\bar{2}}{04\bar{2}}$	$\frac{44\bar{2}}{44\bar{2}}$
135 ($\frac{132}{13\bar{3}}$	$\frac{53\bar{3}}{532}$	$\frac{51\bar{1}}{514}$	$\frac{31\bar{1}}{314}$	$\frac{15\bar{2}}{15\bar{2}}$	$\frac{35\bar{1}}{35\bar{1}}$
440	$44\bar{2}$	$04\bar{2}$	042	$44\bar{2}$	404	400
424 ($\frac{420}{42\bar{4}}$	$\frac{42\bar{4}}{420}$	$\frac{44\bar{1}}{443}$	$\frac{24\bar{1}}{243}$	$\frac{44\bar{3}}{443}$	$\frac{241}{241}$
351 ($\frac{351}{35\bar{2}}$	$\frac{15\bar{2}}{\bar{1}5\bar{1}}$	$\frac{132}{\bar{1}33}$	$\frac{53\bar{2}}{533}$	$\frac{31\bar{4}}{314}$	$\frac{51\bar{1}}{51\bar{1}}$
226 ($\frac{222}{22\bar{4}}$	$\frac{62\bar{4}}{622}$	$\frac{62\bar{2}}{624}$	$\frac{22\bar{2}}{224}$	$\frac{26\bar{2}}{26\bar{2}}$	$\frac{260}{260}$

/continued

		1	2	3	4	5	6
353	(($\frac{350}{353}$	$\frac{35\bar{3}}{350}$	$\frac{331}{334}$	$\frac{53\bar{1}}{534}$	$\frac{33\bar{4}}{334}$	$\frac{53\bar{1}}{531}$
262	(($\frac{260}{262}$	$\frac{26\bar{2}}{260}$	$\frac{222}{224}$	$\frac{62\bar{2}}{624}$	$\frac{22\bar{4}}{224}$	$\frac{62\bar{2}}{622}$
622	(($\frac{62\bar{2}}{624}$	$\frac{22\bar{4}}{222}$	$\frac{260}{262}$	$\frac{2\bar{6}0}{262}$	$\frac{62\bar{4}}{624}$	$\frac{222}{222}$
444	(($\frac{440}{444}$	$\frac{44\bar{4}}{440}$	$\frac{440}{444}$	$\frac{4\bar{4}0}{444}$	$\frac{44\bar{4}}{444}$	$\frac{440}{440}$
246	(($\frac{242}{244}$	$\frac{64\bar{4}}{642}$	$\frac{62\bar{1}}{625}$	$\frac{4\bar{2}1}{425}$	$\frac{26\bar{3}}{263}$	$\frac{46\bar{1}}{461}$
711	(($\frac{71\bar{3}}{714}$	$\frac{11\bar{4}}{113}$	$\frac{170}{171}$	$\frac{1\bar{7}0}{171}$	$\frac{71\bar{4}}{714}$	$\frac{113}{113}$
008	(($\frac{004}{004}$	$\frac{80\bar{4}}{804}$	$\frac{80\bar{4}}{804}$	$\frac{004}{004}$	$\frac{080}{080}$	$\frac{080}{080}$
535	(($\frac{530}{535}$	$\frac{53\bar{5}}{530}$	$\frac{55\bar{1}}{554}$	$\frac{35\bar{1}}{354}$	$\frac{55\bar{4}}{554}$	$\frac{351}{351}$
173	(($\frac{171}{172}$	$\frac{37\bar{2}}{371}$	$\frac{312}{315}$	$\frac{71\bar{2}}{715}$	$\frac{13\bar{4}}{134}$	$\frac{73\bar{3}}{733}$
731	(($\frac{73\bar{3}}{734}$	$\frac{13\bar{4}}{133}$	$\frac{171}{172}$	$\frac{37\bar{1}}{372}$	$\frac{71\bar{5}}{715}$	$\frac{312}{312}$
446	(($\frac{441}{445}$	$\frac{64\bar{5}}{641}$	$\frac{64\bar{1}}{645}$	$\frac{4\bar{4}1}{445}$	$\frac{46\bar{4}}{464}$	$\frac{460}{460}$
373	(($\frac{370}{373}$	$\frac{37\bar{3}}{370}$	$\frac{332}{335}$	$\frac{73\bar{2}}{735}$	$\frac{33\bar{5}}{335}$	$\frac{73\bar{2}}{732}$
626	(($\frac{620}{626}$	$\frac{62\bar{6}}{620}$	$\frac{66\bar{2}}{664}$	$\frac{2\bar{6}2}{264}$	$\frac{66\bar{4}}{664}$	$\frac{262}{262}$
662	(($\frac{66\bar{2}}{664}$	$\frac{26\bar{4}}{262}$	$\frac{262}{264}$	$\frac{6\bar{6}2}{664}$	$\frac{62\bar{6}}{626}$	$\frac{620}{620}$
448	(($\frac{442}{446}$	$\frac{84\bar{6}}{842}$	$\frac{84\bar{2}}{846}$	$\frac{4\bar{4}2}{446}$	$\frac{48\bar{4}}{484}$	$\frac{480}{480}$

TABLE 4.2. Miller indices of Bragg peaks observed in the neutron powder diffraction pattern of DI in the orthorhombic and the six monoclinic unit cells.

On the other hand, the space groups Cc and C2/c have the additional requirements that;

$$\text{in } h0l; \quad l = 2n, \quad (h=2n) \quad (56)$$

The types of orthorhombic Miller indices necessary to give a monoclinic Bragg peak of type $(h0l)_m$, where $l = 2n+1$, are;

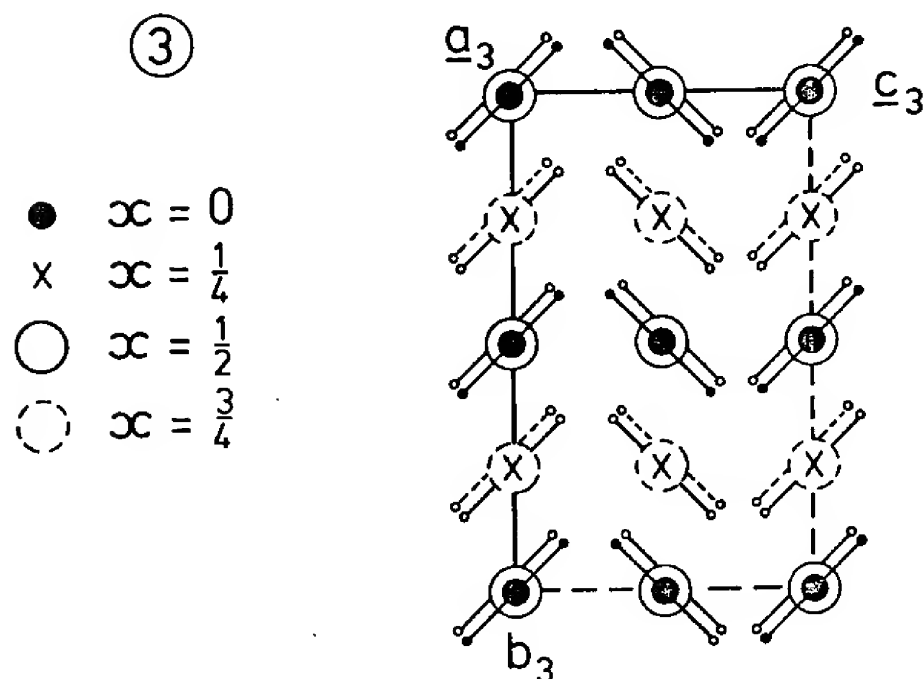
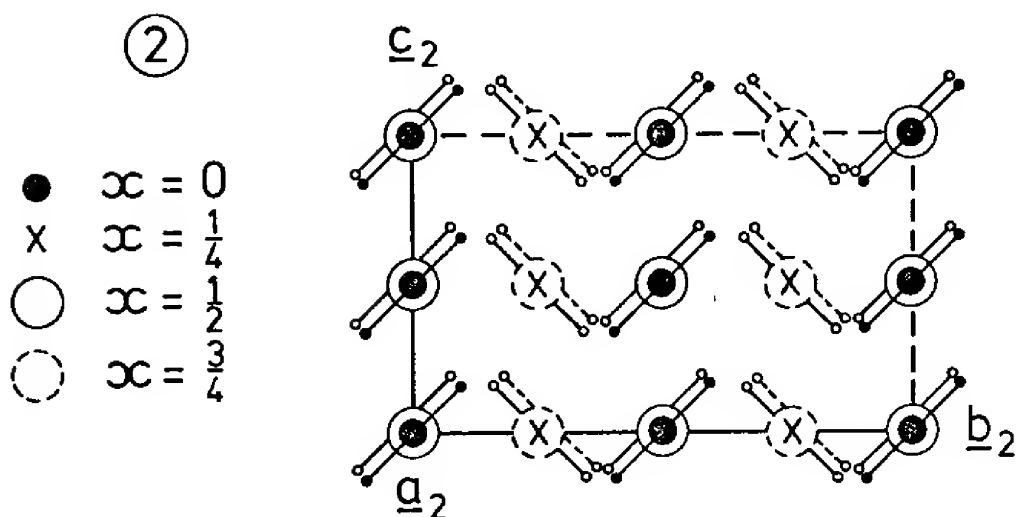
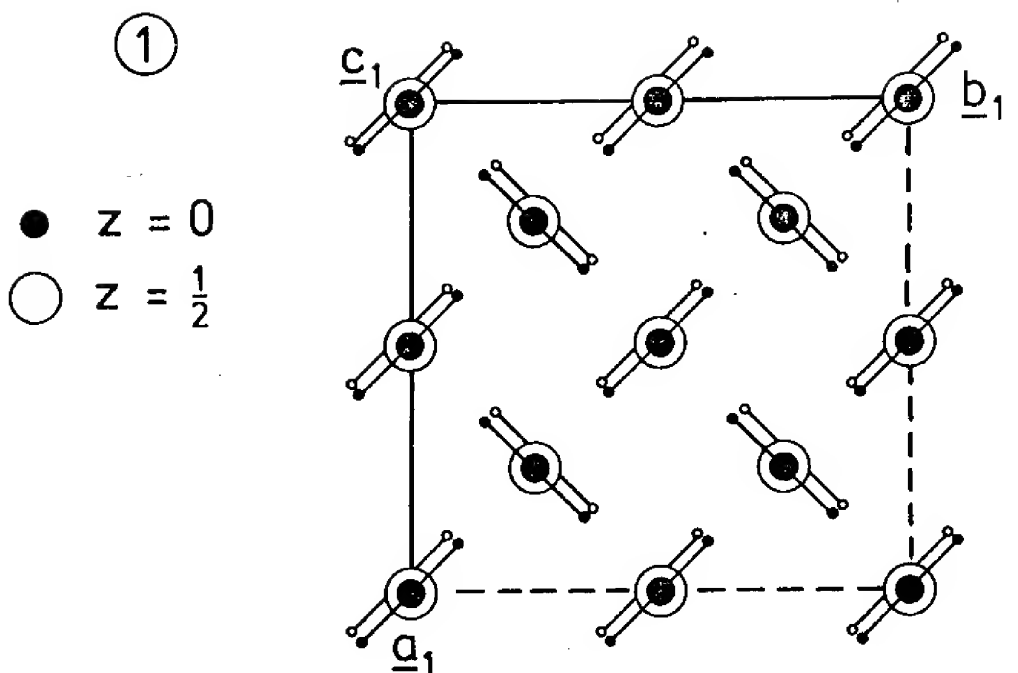
$$\begin{aligned} \text{Unit cells Nos. 1 and 2; } (h0l)_0; \quad l_o - h_o = 4n-2 \\ \text{e.g. } (002)_0, (204)_0 \dots \end{aligned} \quad (57)$$

$$\begin{aligned} \text{Unit cells Nos. 3 and 4; } (0kl)_0; \quad l_o - k_o = 4n-2 \\ \text{e.g. } (002)_0, (204)_0 \dots \end{aligned} \quad (58)$$

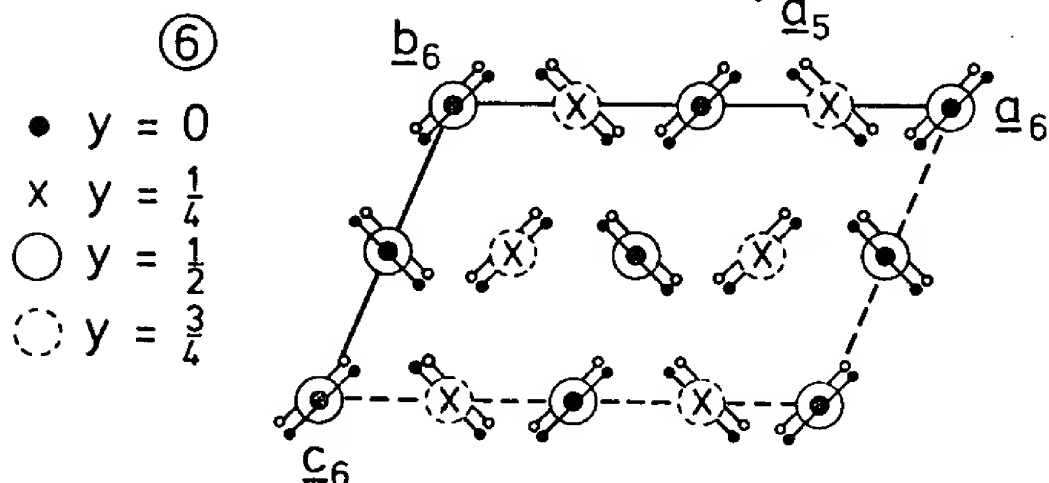
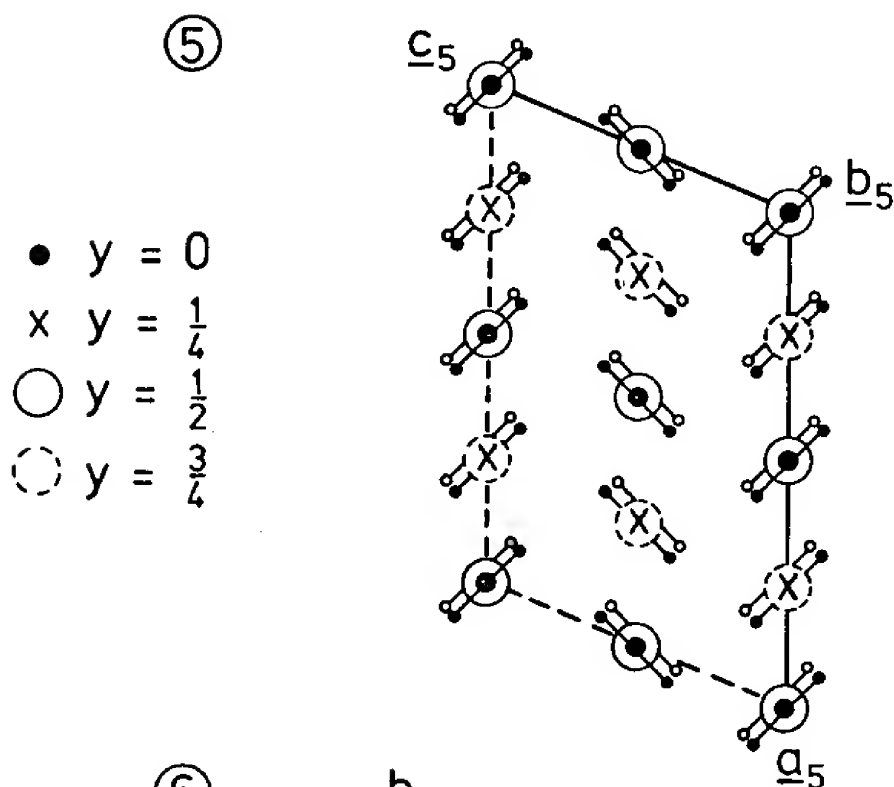
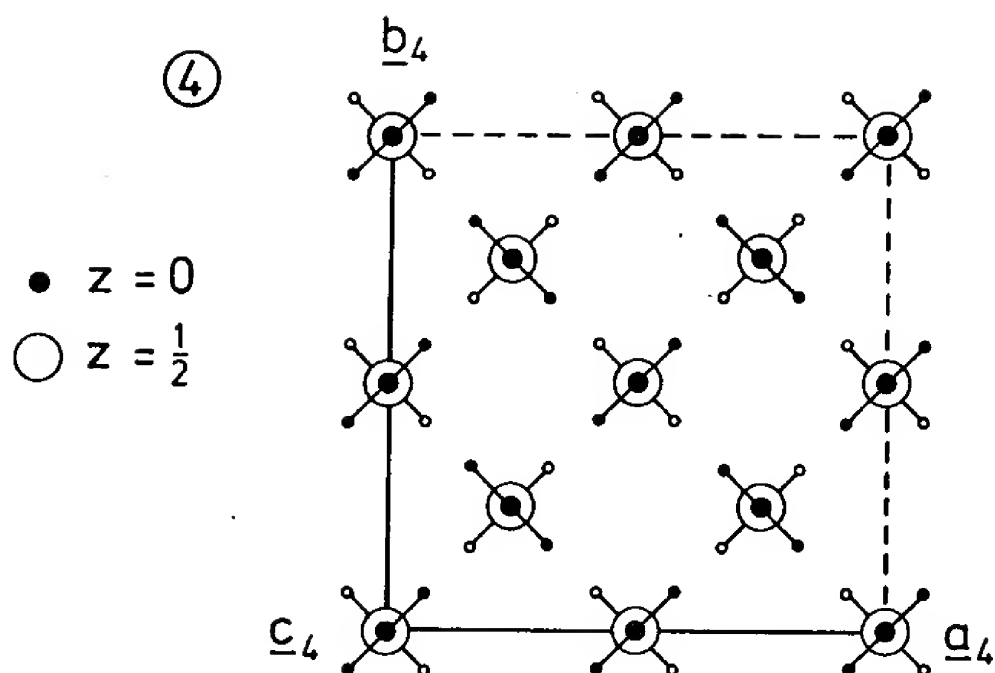
$$\begin{aligned} \text{Unit cells Nos. 5 and 6; } (hk0)_0; \quad h_o - k_o = 4n-2 \\ \text{e.g. } (420)_0 \text{ which was observed.} \end{aligned} \quad (59)$$

Of the orthorhombic peaks listed in table 4.1 only the $(420)_0$ peak was observed in the low phase of DI, which excluded space groups Cc and C2/c for the monoclinic unit cells nos. 5 and 6.

As discussed in §4.2 the middle phase of DI was expected to be related to the low phase by a 180° rotation of the DI molecules in the (001) plane about an axis passing through the iodine atom. In addition the monoclinic space group had to accommodate the face-centred iodine sub-lattice with four atoms in the unit cell. In the space groups mentioned above the only symmetry operations besides the C-centring are \underline{c} -glides, mirror planes and two-fold diad rotations about the \underline{b} -axis. Figures 4.7 to 4.12 show the middle phase of DI referred to the six C-centred monoclinic unit cells to see whether these arrangements can be described by the above-mentioned symmetry operations.



Figures 4.7 - 4.9 Middle phase structure of DI drawn in a monoclinic unit cell type No.s 1 - 3.



Figures 4.10 - 4.12 Middle phase structure of DI drawn in a monoclinic unit cell type No.s 4 - 6.

Figures 4.7 to 4.12 show clinographic projections of the middle phase arrangement onto the orthorhombic (001) plane. In cells No.1 and 2 no subgroups of the atomic arrangement can have a \underline{c} -glide or a mirror plane perpendicular to the \underline{b} -axis or a two-fold diad rotation parallel to the \underline{b} -axis. The arrangements are pseudo-monoclinic and should be described by primitive triclinic cells consisting of eight molecules each. In cells No.3 and No.4 subgroups can have \underline{c} - and n -glides perpendicular to, and 2 and 2₁ rotations parallel to the \underline{b} -axis. Figures 4.13 and 4.14 show clinographic projections of cells No.3 and No.4 drawn onto the (001) monoclinic plane to show the action of the monoclinic symmetry operations of space group Cc. It can be seen that in cells No.5 and No.6 \underline{c} -glides and diad rotations are excluded. However, mirror planes perpendicular to the \underline{b} -axis are allowed, thus these unit cells can accommodate atomic arrangements which are subgroups of the middle phase and have monoclinic space group symmetry Cm.

Thus the following monoclinic space groups are compatible with the six possible unit cells;

Cells No.1 and No.2; None

Cells No.3 and No.4; Cc and C2/c

Cells No.5 and No.6; Cm

If in the monoclinic unit cells No.3 and No.4 each deuterium atom is allowed to occupy one of the two disordered positions, it is possible to obtain eight different atomic arrangements for each unit cell, a total of sixteen. There is a basis of two molecules in space group C2/c and four molecules (labelled 1 to 4 in figures 4.13 and 4.14) in the lower symmetry space group Cc, so allowing 2^4 (16) arrangements per cell. This is reduced to eight per cell as the choice of the original direction is arbitrary.

Figure 4.13

Figure 4.14

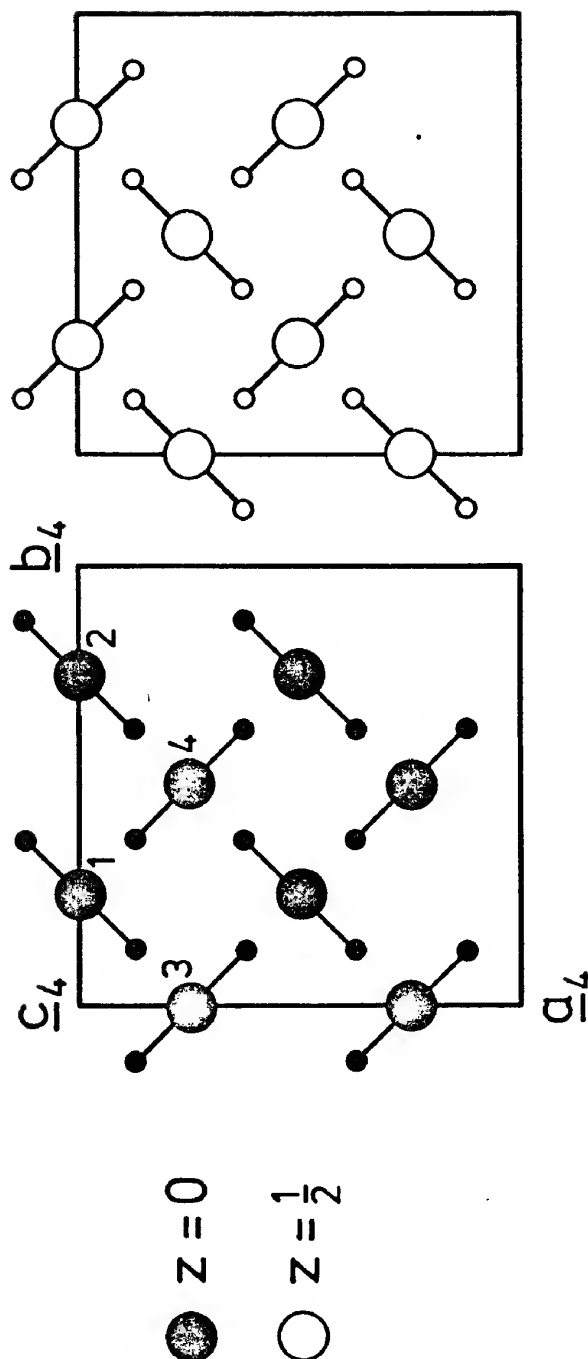
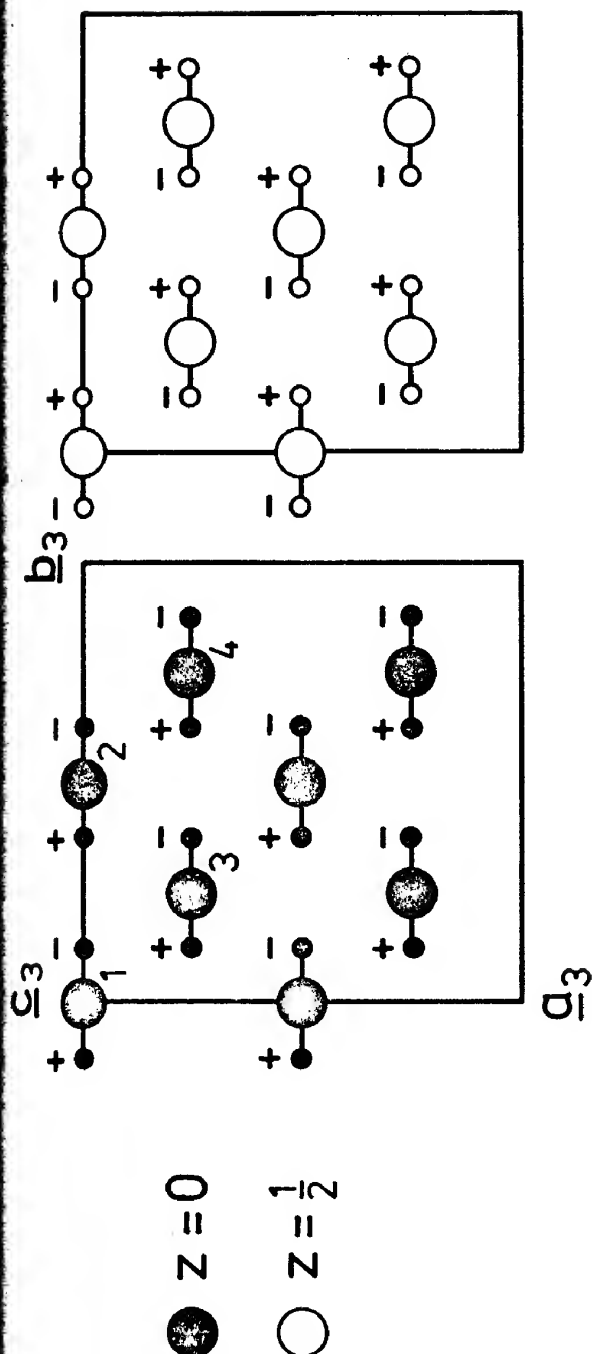


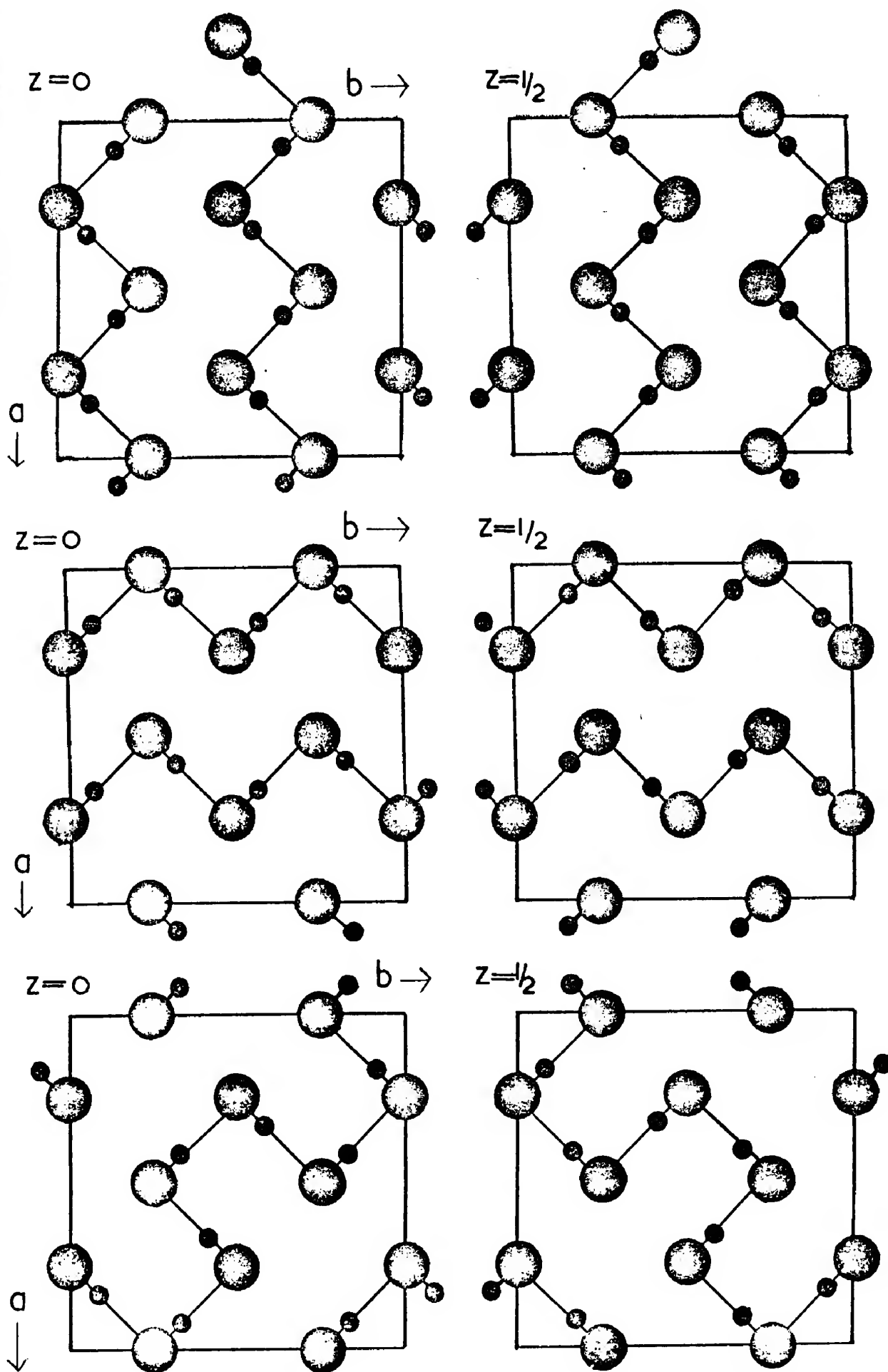
Figure 4.13 Middle phase structure of DI drawn in a monoclinic unit cell, type No.3, projected onto the (001) monoclinic plane.

Figure 4.14 Middle phase structure of DI drawn in a monoclinic unit cell, type No.4, projected onto the (001) monoclinic plane.

The eight models generated with cell No.3 are identical to the eight models of cell No.4. Of these eight models three pairs are equivalent to each other so that there are five essentially different models which are shown in cell No.4 in figures 4.15 to 4.19. Model No.1 corresponds to the ordered low phase structures of DCI, DBr and DF. The first two compounds are described by space group $Bb2_1m$ (No.36) and the last by $Bm2_1b$ (No.36) due to a change in the orientation of the major axis. Model No.2 is very similar to model No.1 except that in model No.2 the zig-zag chains are anti-parallel while in model No.1 they are parallel. However, both models No.1 and No.2 can be referred to a small orthorhombic unit cell containing four molecules.

If each molecule in the low phase is allowed to re-orientate through 90° as compared with its position in the two-fold disordered middle phase, then this would lead to 128 further models (many of which would be equivalent to each other). Moreover several of these models are expected to be non-physical (as in the orthorhombic $Fdd2$ models) because of unlikely configurations of adjacent dipoles. A computer program LPSG (Low Phase Symmetry Generator) described in Appendix one, was written to calculate the intensities of the first thirteen powder diffraction peaks for each of these 128 models. The 128 sets of calculated intensities were compared with the observed intensity pattern of the low phase of DI, particularly in the region between the first low phase peak (110) and the subsequent intense multiple peak (130-220) which remains practically unchanged in the middle phase diffraction pattern (figures 4.2 and 5.1). In this region there are no observed peaks although they are not excluded by any space group symmetry.

Eight of these models were found to give rise to calculated intensity distributions similar to the observed powder pattern. These were two sets of four equivalent structures of which one was model No.5 (figure 4.19) and



Figures 4.15 - 4.17 Proposed structure for DI low phase space-group Cc (No.9) models No. 1-3.

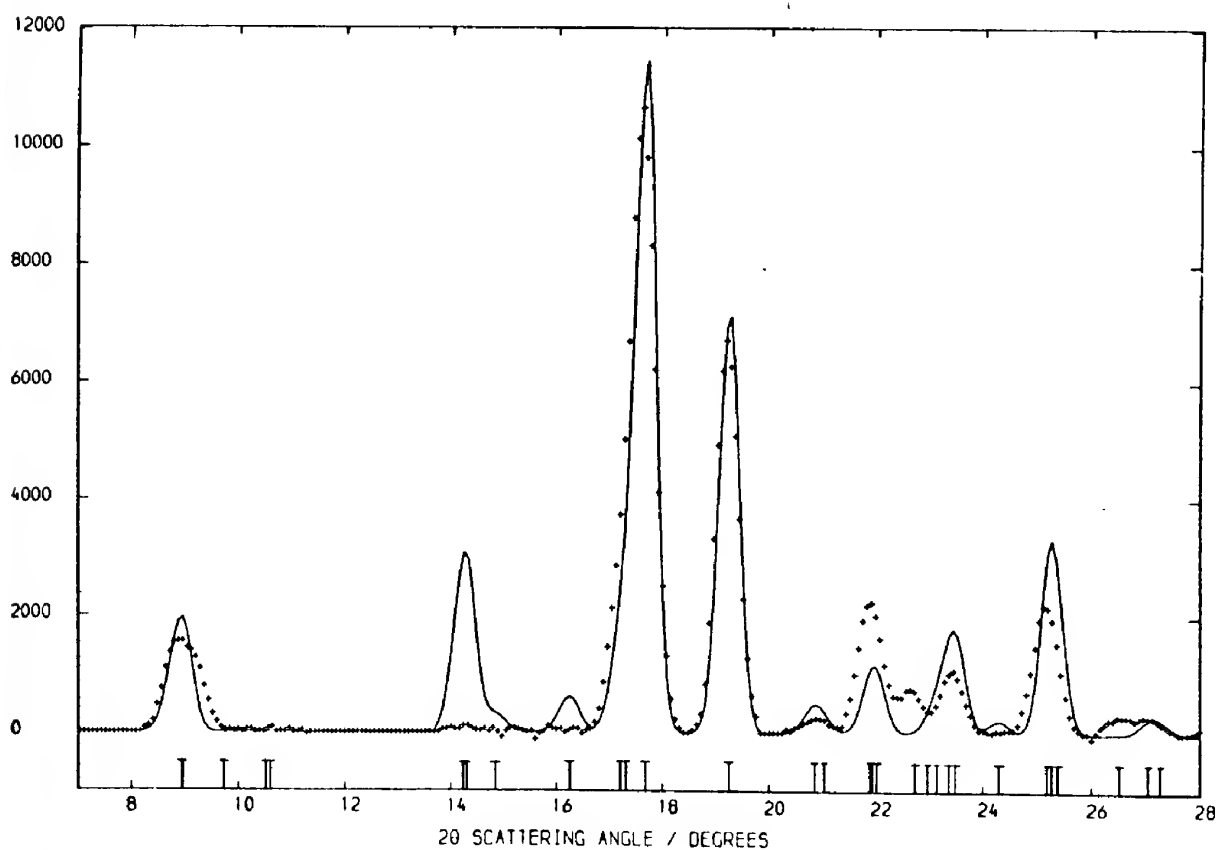
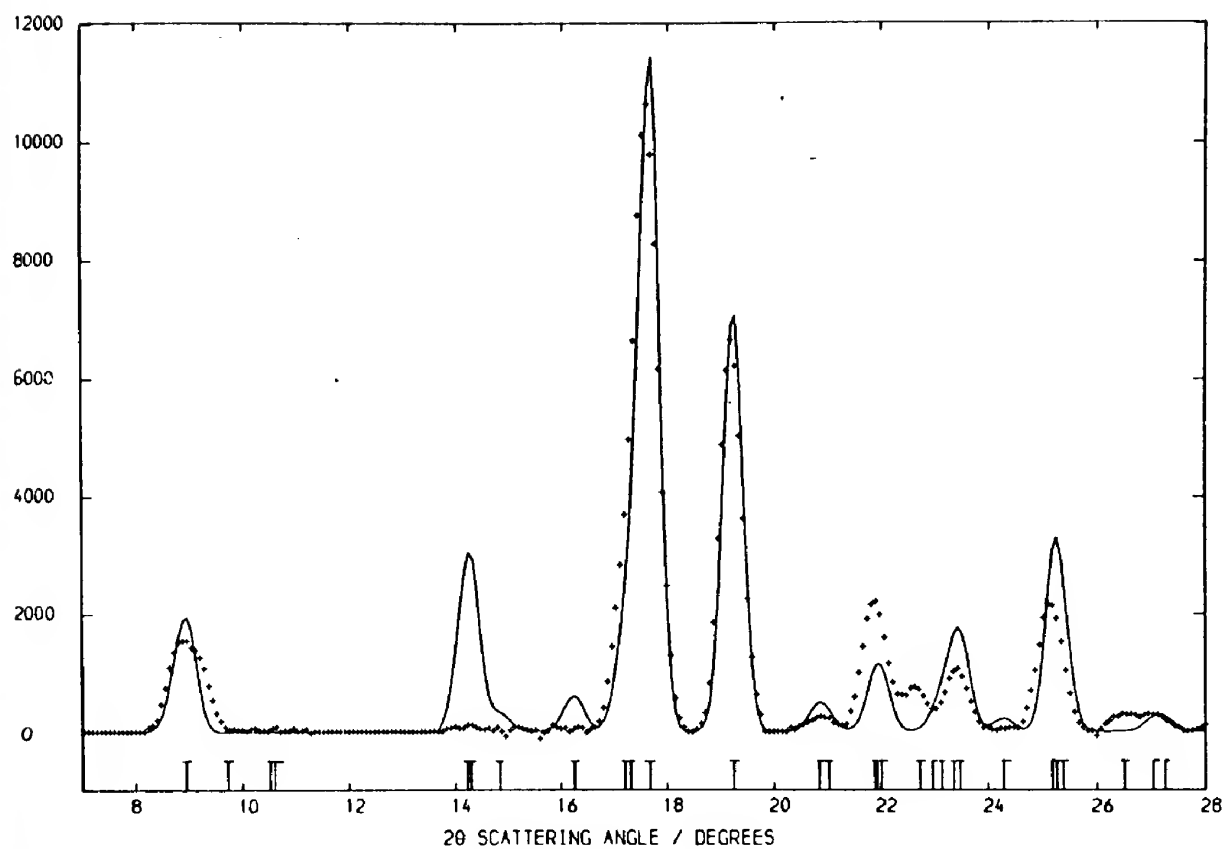
the other which is of a lower symmetry is shown in figure 4.20 as model No.6.

The diffraction patterns calculated for the four models with large unit cells, i.e. Nos. 3, 4, 5 and 6 shown in figures 4.17 to 4.20, are shown in figures 4.21 to 4.24 as continuous lines. The crosses represent the powder diffraction pattern of DI at 4.2K recorded by the 'Curran' diffractometer using a wavelength of $\lambda = 1.06\text{\AA}$. Models No.3 and No.4 were very similar to each other (see figures 4.17 and 4.18) and the calculated diffraction pattern based upon model No.5 was found to give the most reasonable fit, particularly at low angles (see figure 4.23). Models No.3, 4 and 6 could be described by space group Cc, while model No.5 had an additional centre of symmetry characteristic of space group C2/c.

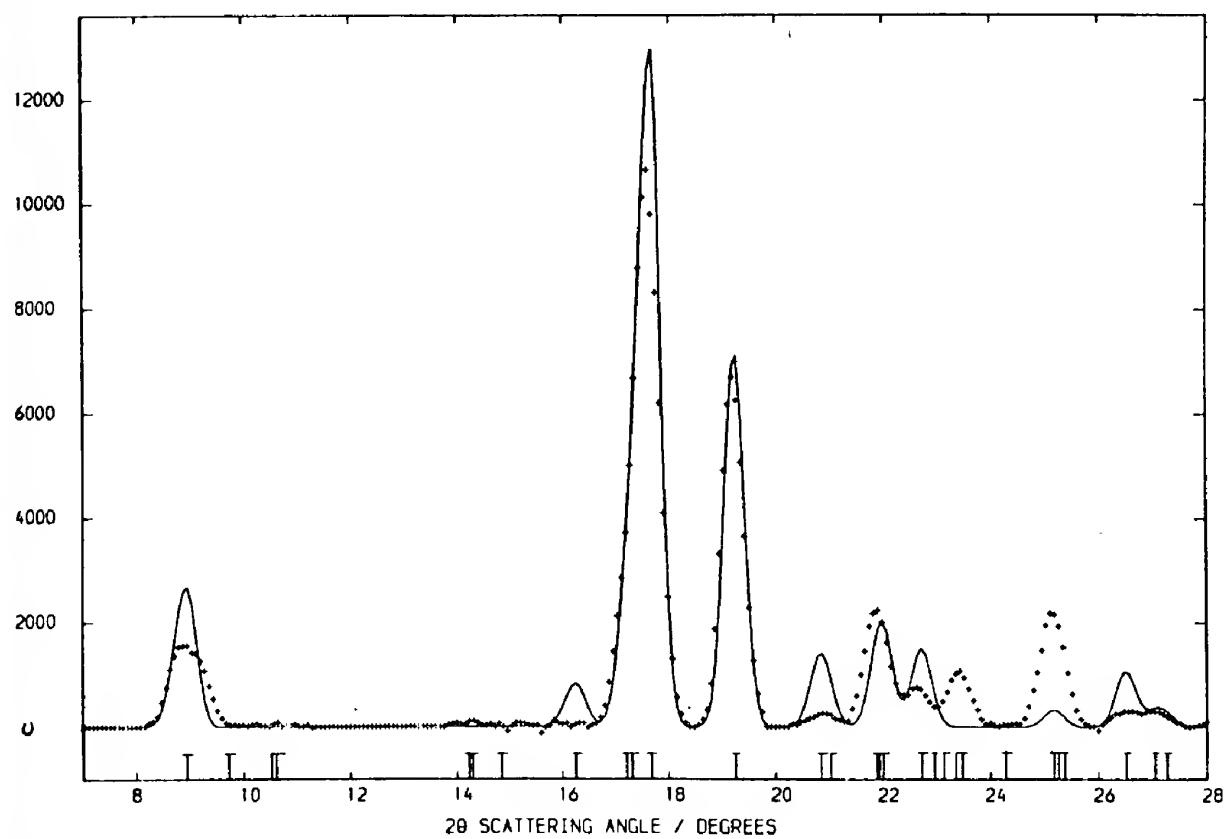
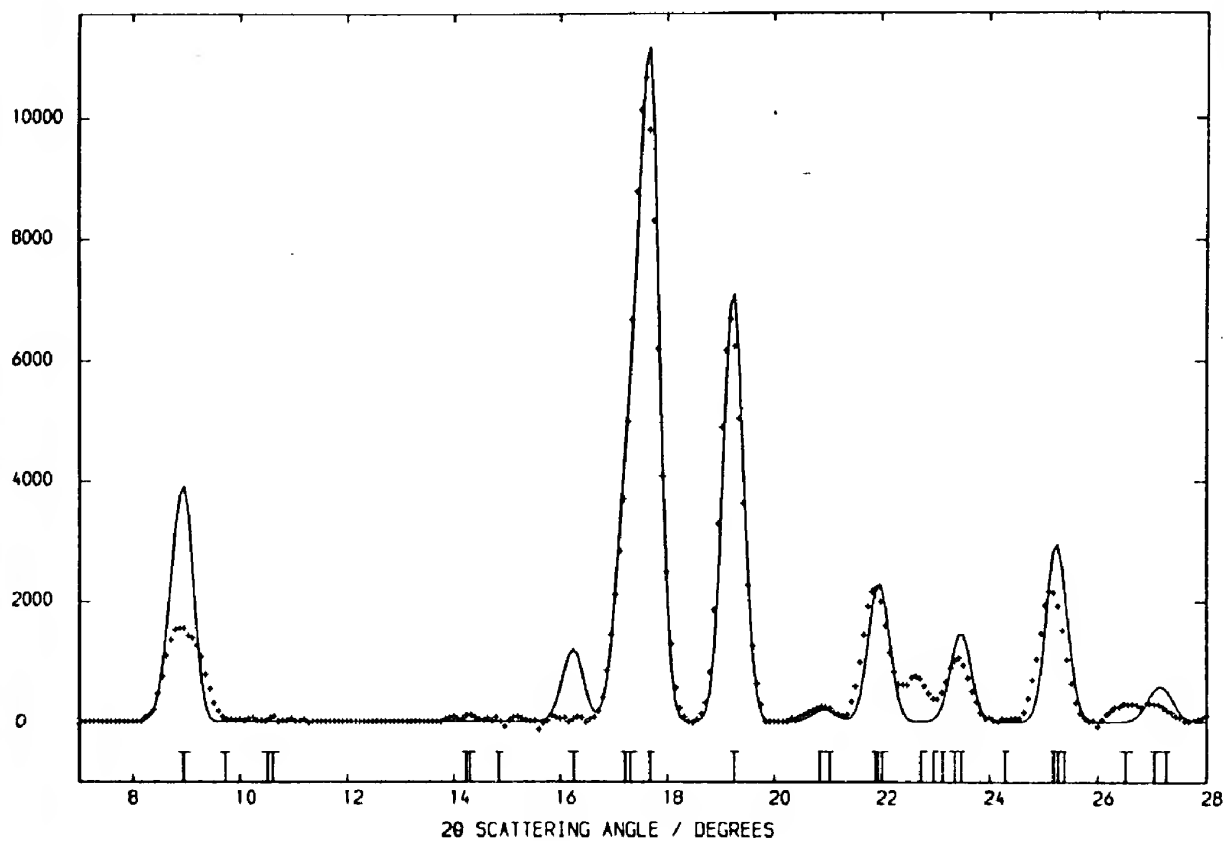
Although model No.5 based on space group C2/c gave the best agreement with the observed data, other possible monoclinic space groups were also investigated for completeness. In order to examine all of these possible models the large face-centred orthorhombic unit cell was again considered.

A basis of eight molecules was chosen (shown as 1-8 in figure 4.25) and the deuterium atoms were allowed to occupy one of the two disordered positions of the middle phase. The only permitted symmetry operation was that of face-centring so that the total number of models generated was $2^7(128)$. Of these 128 many were equivalent to one another so that there were 17 different structures. 5 of these had small unit cells and of the remaining 12, 3 had been previously considered in the cells Nos.3 and 4 and are shown in figures 4.17 to 4.19.

Diffraction patterns were calculated for the remaining 9 structure but they were all found to disagree with the observed neutron powder diffraction



Figures 4.21 and 4.22 Calculated (continuous line) and observed (crosses)
intensities for DI low phase, Curran 4.2K,
models No. 3 and 4.



Figures 4.23 and 4.24 Calculated (continuous line) and observed (crosses)
intensities for DI low phase, Curran 4.2K,
models No. 5 and 6.

Figure 4.25

- $z = 0$
 ○ $z = \frac{1}{4}$
 ⊗ $z = \frac{1}{2}$
 ⊖ $z = \frac{3}{4}$

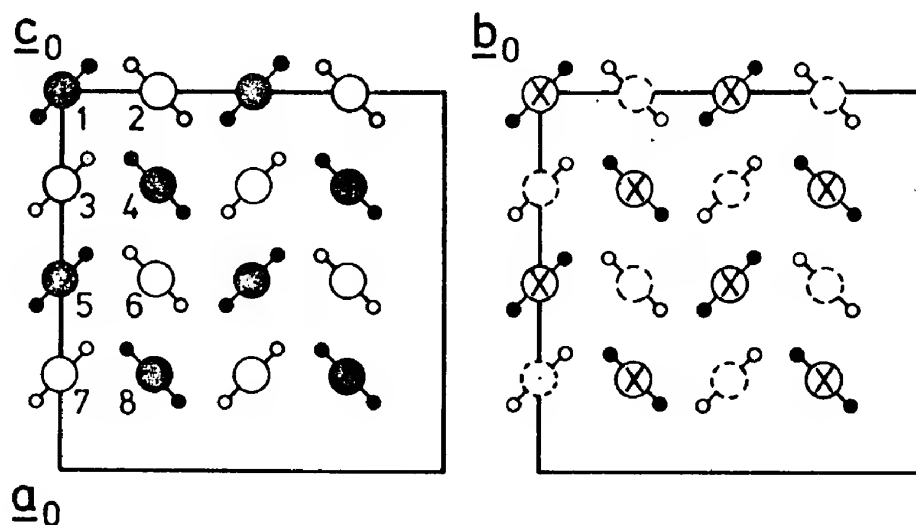


Figure 4.26

- $y = 0$
 ○ $y = \frac{1}{2}$

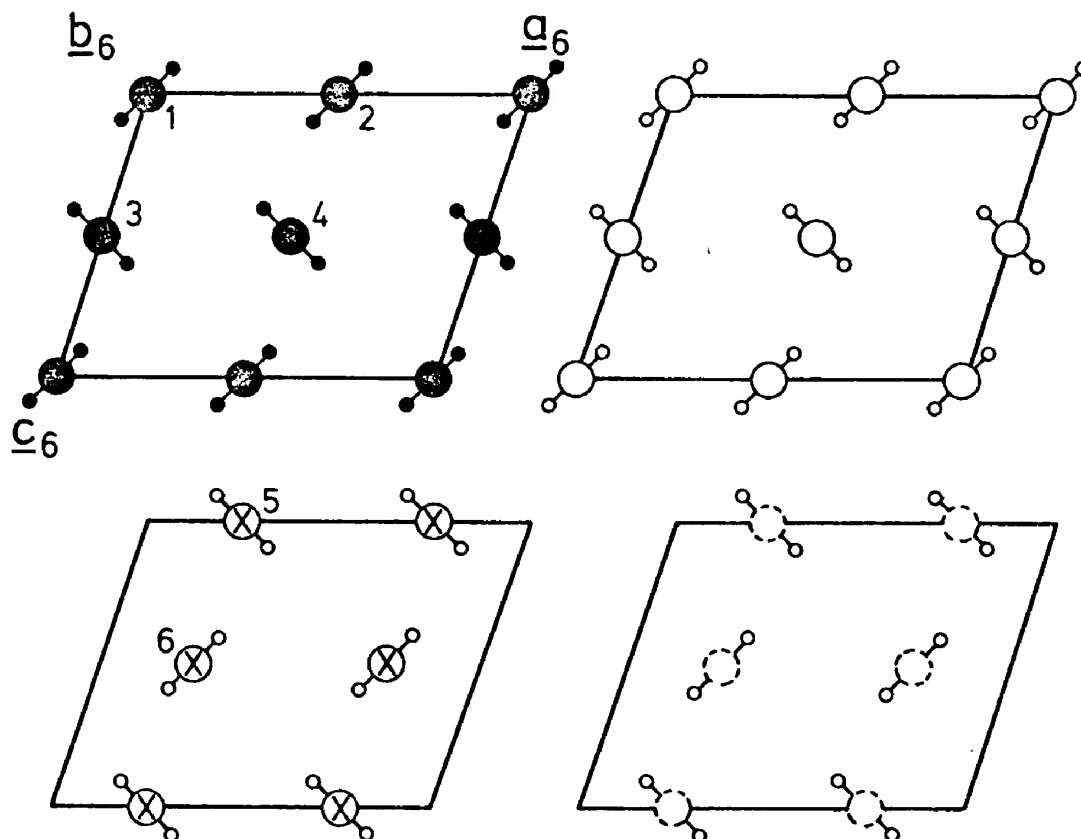


Figure 4.25 Middle phase structure of DI drawn in an orthorhombic unit cell showing the 8 molecules of the basis chosen to produce 128 models.

Figure 4.26 Middle phase structure of DI drawn in a monoclinic unit cell type No.6 showing the 6 molecules of the basis chosen to produce 32 models with space-group Cm (No.8).

pattern of the low phase of D1, particularly at low angles.

As discussed earlier cells No.5 and No.6 could contain structures with space group symmetry Cm. If the structure is assumed to form a subgroup of the middle phase (as shown in figures 4.11 and 4.12) it is necessary to consider 6 iodine atoms in cell No.6. Of these atoms, 4 are in the two-fold Wyckoff special position '2a' and 2 are in the general position '4b', i.e.

$$2a \quad (x, 0, z) \quad (60)$$

$$4b \quad (x, y, z), (x, \bar{y}, z) \quad (61)$$

$$(0, 0, 0; \frac{1}{2}, \frac{1}{2}, 0) +$$

Choosing (x, y, z) as $(0, 0, 0)$, $(0, 0, \frac{1}{2})$, $(\frac{1}{2}, 0, 0)$, $(\frac{1}{2}, 0, \frac{1}{2})$ and as $(\frac{1}{4}, \frac{1}{4}, 0)$, $(\frac{1}{4}, \frac{1}{4}, \frac{1}{2})$ respectively leads to a structure which is a subgroup of the middle phase. The unit cell No.6 is shown in figure 4.26 with the six atoms labelled as 1-6. Allowing the deuterium atoms to occupy one of the two equilibrium positions of the middle phase leads to $2^5(32)$ models for both cells No.5 and No.6. Examination of these models shows that they are all included in the 17 different structures generated within the large face-centred orthorhombic unit cell. Only the most general case remains of 8 molecules in the orthorhombic unit cell with 90° re-orientation. This leads to $2 \times 4^7(32768)$ models, an excessively large number to examine. Table 4.3 summarizes the unit cells and space groups considered.

4.5 Refinement of the models based on space group C2/c (No.15)

Two sets of data were used in the refinement; a set of data recorded with $\lambda = 1.886\text{\AA}$ using the 'Panda' diffractometer and a combined set of data derived from the ten powder patterns recorded with the five counters of the 'Curran' diffractometer using $\lambda = 1.06\text{\AA}$. The ten 'Curran' diffraction patterns were corrected separately for background and detector efficiency

before combining them into a single composite data set. The ten corrected diffraction patterns showed only statistical variation between each other indicating a lack of preferred orientation.

The Rietveld program described in Appendix one was used in an attempt to refine the model No.5 shown in figures 4.19 and 4.27. It was necessary to use this program for two reasons.

a) The superposition of monoclinic powder peaks

Because the lattice of the low phase is pseudo-orthorhombic, the orthorhombic powder peak $(h_o k_o l_o)$ which has a multiplicity of eight, becomes two superimposed monoclinic peaks,

$$\text{Cell No.3} \quad [l_o, k_o, (\frac{k_o - l_o}{2})] \quad \text{and} \quad [\bar{l}_o, k_o, (\frac{k_o + l_o}{2})] \quad (62)$$

$$\text{and Cell No.4} \quad [k_o, \bar{h}_o, -(\frac{k_o + l_o}{2})] \quad \text{and} \quad [k_o, \bar{h}_o, -(\frac{k_o - l_o}{2})] \quad (63)$$

each with a multiplicity of four.

On the other hand in the monoclinic space group C2/c, the geometrical structure factors obey the following identities;

$$F(hkl)_m = F(h\bar{k}l)_m \quad (64)$$

$$F(hkl)_m = F(h\bar{k}l)_m \neq F(\bar{h}kl)_m = F(hk\bar{l})_m \quad (h_m + k_m = 2n, l_m = 2n) \quad (65)$$

$$F(hkl)_m = -F(h\bar{k}l)_m \neq F(\bar{h}kl)_m = -F(hk\bar{l})_m \quad (h_m + k_m = 2n, l_m = 2n+1) \quad (66)$$

Thus for the two unit cells,

$$\text{Cell No.3} \quad I[l_o, k_o, (\frac{k_o - l_o}{2})] \neq I[\bar{l}_o, k_o, -(\frac{k_o - l_o}{2})] \quad (67)$$

$$\text{and Cell No.4} \quad I[k_o, h_o, -(\frac{k_o + l_o}{2})] \neq I[k_o, h_o, -(\frac{k_o - l_o}{2})] \quad (68)$$

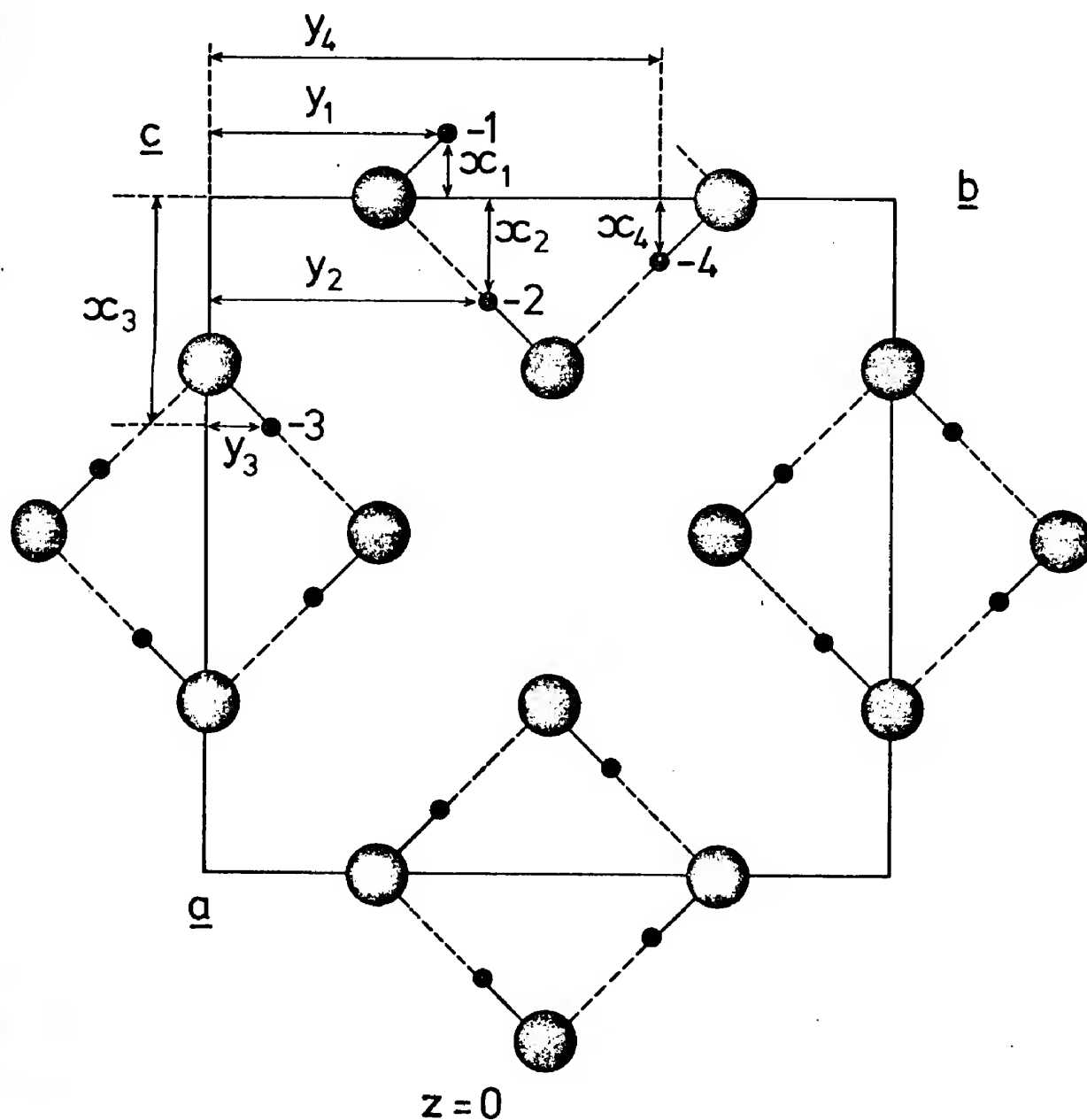


Figure 4.27 Proposed structure for DI low phase space group $C2/c$,
model No.5 in unit cell No.4.

although for

$$\text{Cell No.3} \quad \theta[l_o k_o, (\frac{k_o-1}{2}o)] = \theta[\bar{l}_o k_o, -(\frac{k_o-1}{2}o)] \quad (69)$$

and

$$\text{Cell No.4} \quad \theta[k_o, h_o, -(\frac{k_o+1}{2}o)] = \theta[k_o, h_o, -(\frac{k_o-1}{2}o)] \quad (70)$$

Thus in the powder diffraction pattern of the low phase, each peak is the superposition of two whose intensities are generally different. A similar situation occurs in a cubic powder pattern where the peaks (115), (333) and (006), (224) always overlap.

b) The large number of unresolved peaks

The powder intensity distributions of the low phase of DI recorded by the 'Curran' and 'Panda' diffractometers at 4.2K, after correction for background are shown in figures 4.28 and 4.29 (a,b) by crosses; the smooth line is the intensity distribution calculated for the proposed model No.5 and the vertical lines represent the angular positions of the powder peaks compatible with the space group. No powder data were recorded in the angular range of 17-28° with the 'Panda' diffractometer (see figure 4.29a). The total number of powder peaks allowed in the angular range covered by the 'Panda' experiment is 250 (effectively 125 considering the effect of superposition). Very few of these were recorded as 'single' peaks despite the relatively good angular resolution of the instrument. In addition the high angle peaks of the 'Curran' diffraction pattern (see figure 4.28b) are broad. The version of the Rietveld program used for this work (Hewat 1971) was unable to cope with such broad peaks.

The intensity distributions shown in figures 4.28 and 4.29 are calculated for model No.5 shown in figures 4.19 and 4.27. The intramolecular bond length chosen initially for the model was that of the middle phase and the molecules were constrained to point towards nearest neighbour Iodine

Figure 4.28a Observed (crosses) and calculated (solid line) intensities based on model No.5 for DI with Dido Curran at 4.2K.

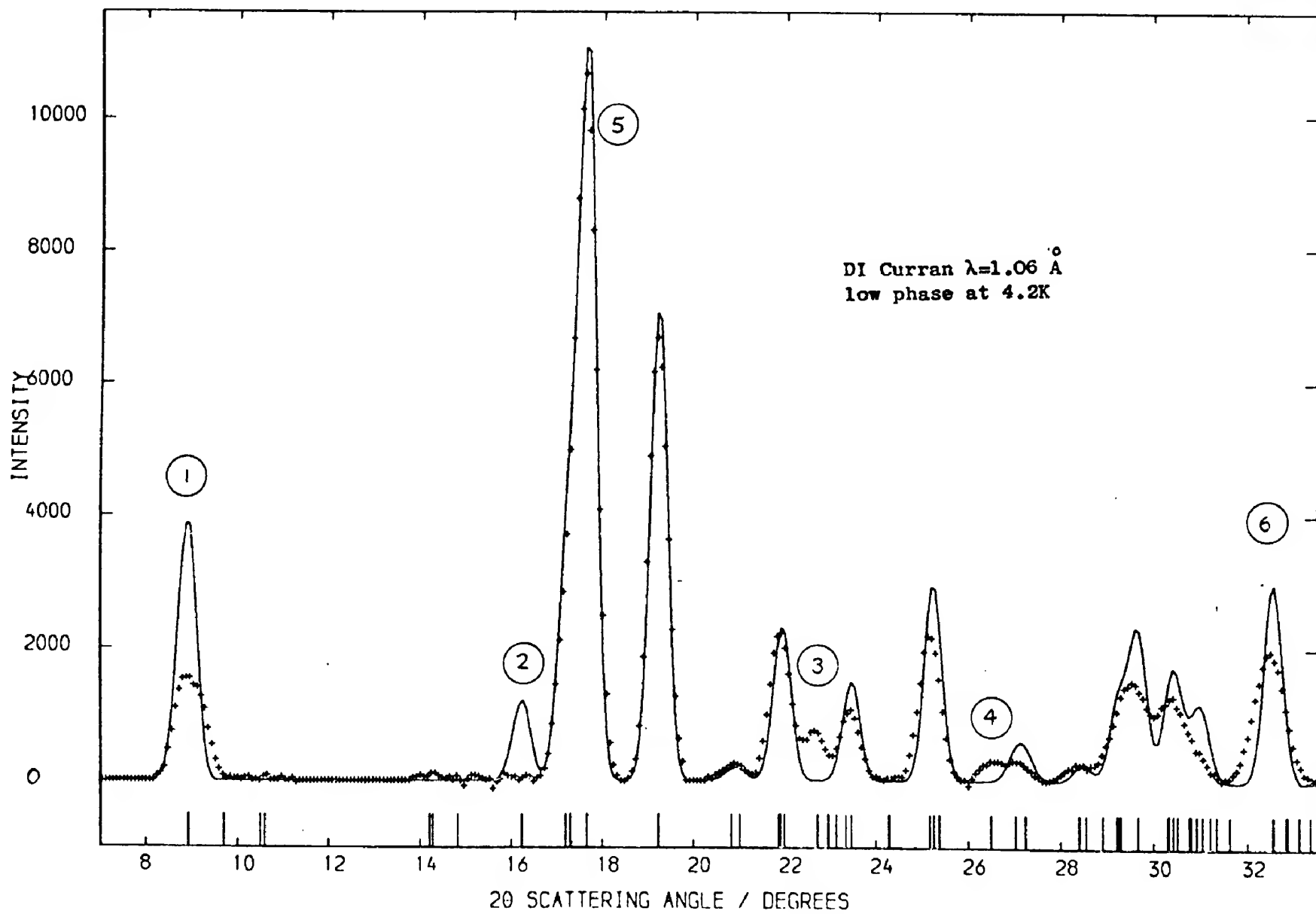


Figure 4.28b Observed (crosses) and calculated (solid line) intensities
based on model No.5 for DI with Dido Curran at 4.2K.

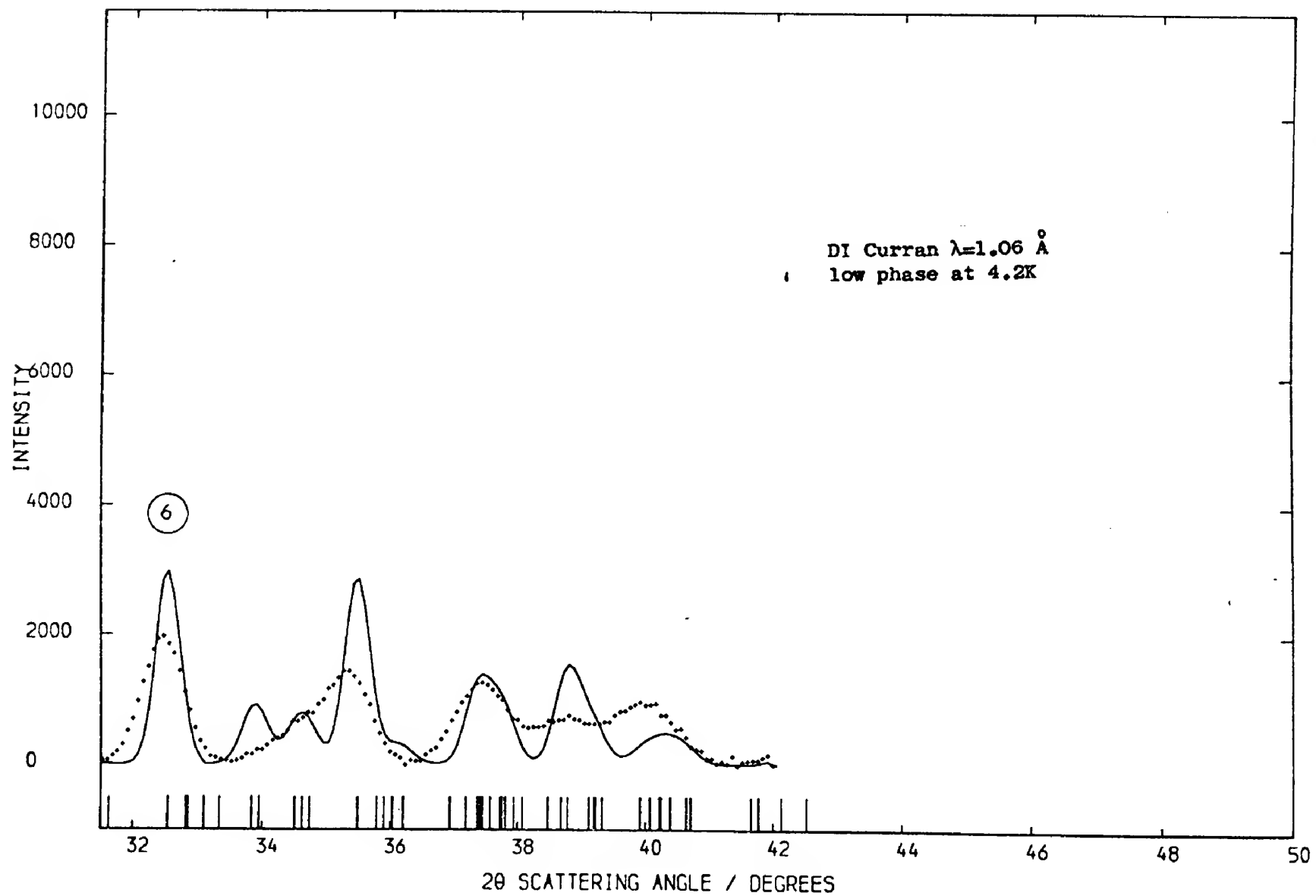


Figure 4.29a Observed (crosses) and calculated (solid line) intensities
based on model No.5 for DI with Pluto Panda at 4.2K.

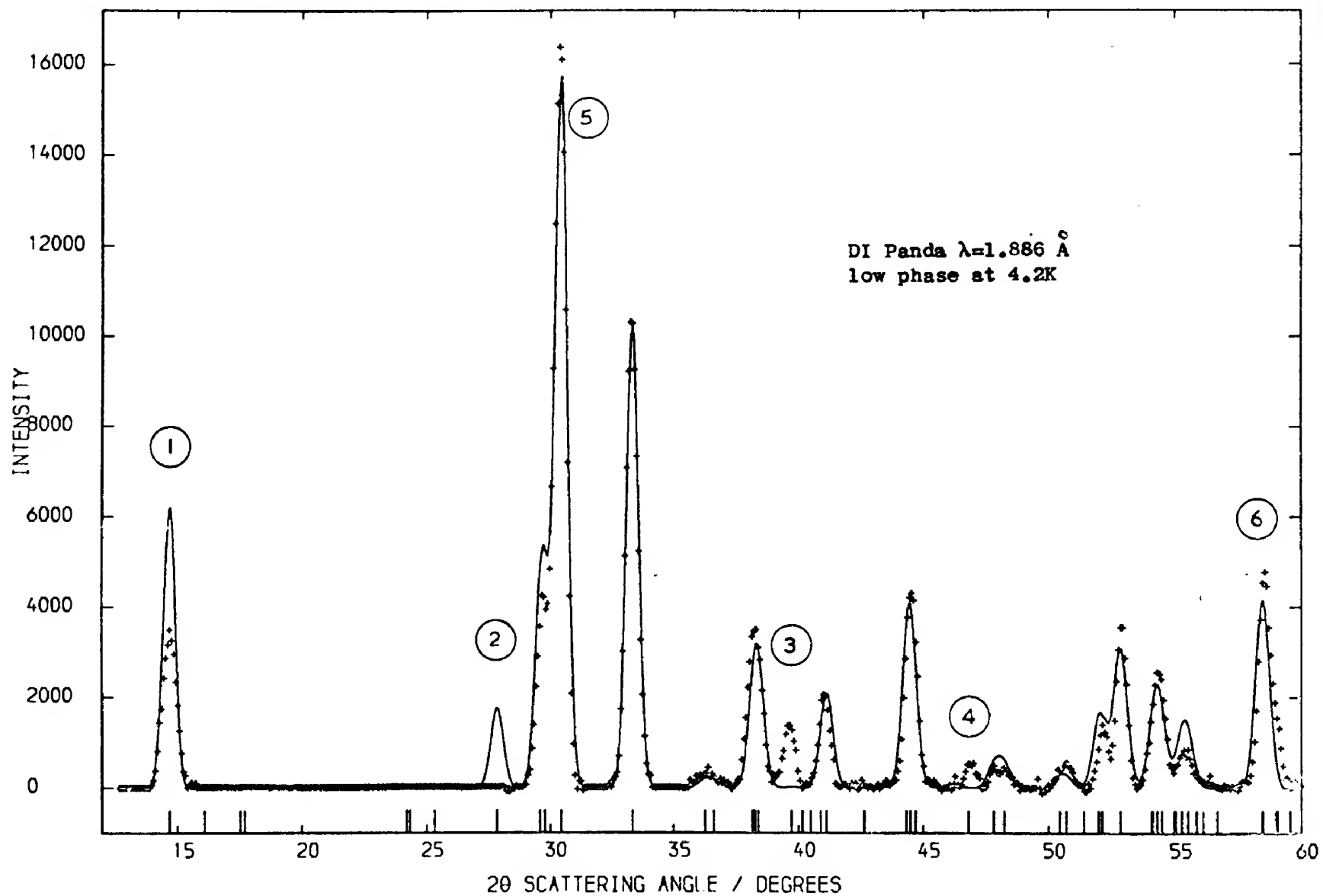
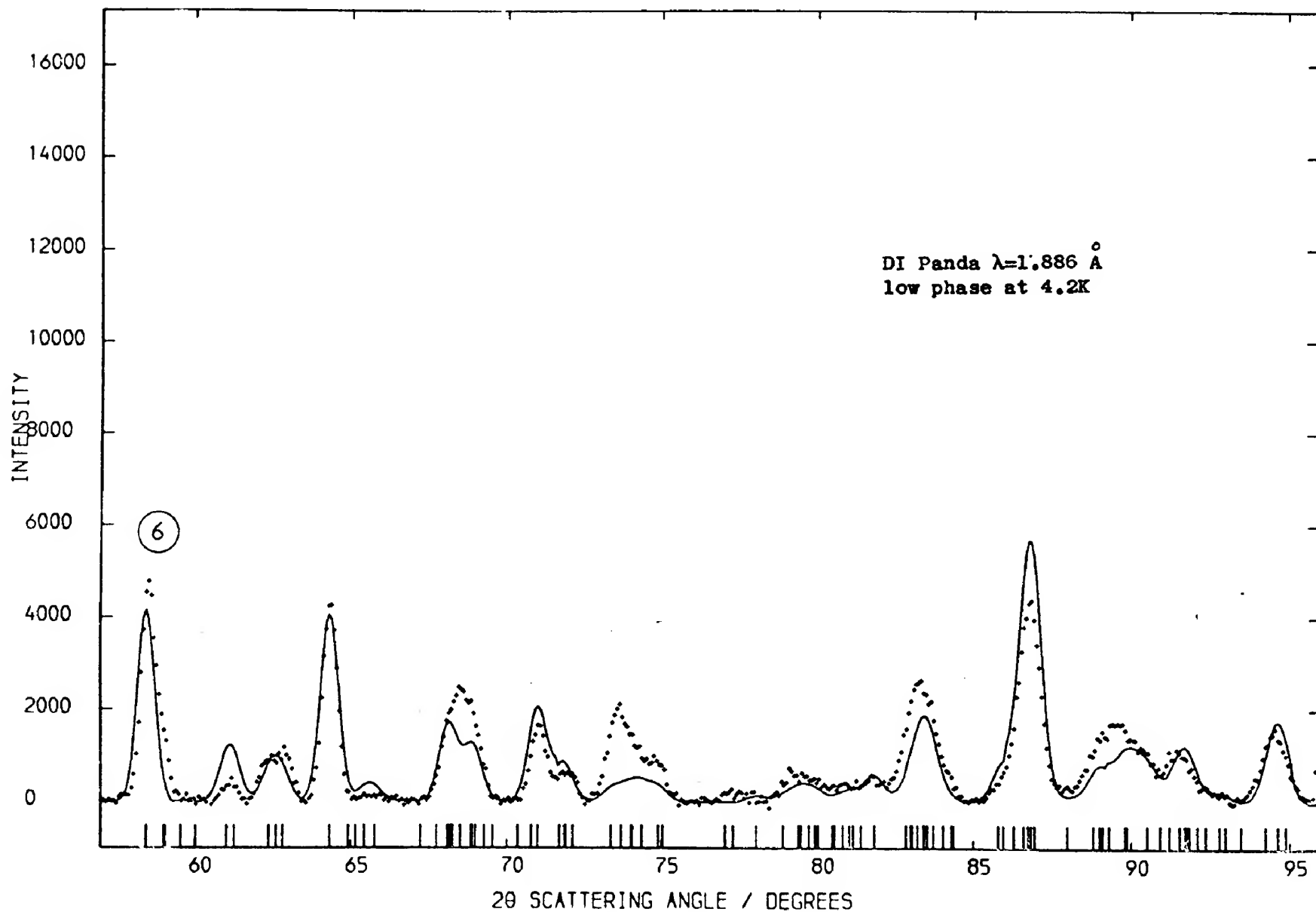


Figure 4.23b Observed (crosses) and calculated (solid line) intensities based on model No.5 for DI with Pluto Panda at 4.2K.



bonds. Apart from disagreements at higher angles, where the poorly defined background was expected to cause difficulties, the main differences between the observed and calculated diffraction patterns shown in figures 4.28a and 4.29a are in the peaks labelled 1 to 4. These peaks have the following Miller indices;

<u>Peak No.</u>	<u>Cell No.3</u>	<u>Cell No.4</u>
(1)	$(110) + (\bar{1}11)$	$(1\bar{1}0) + (1\bar{1}1)$
(2)	$(31\bar{1}) + (\bar{3}12)$	$(1\bar{1}1) + (1\bar{1}2)$
(3)	$(131) + (\bar{1}32)$	$(33\bar{1}) + (3\bar{3}2)$
(4)	$(330) + (\bar{3}33)$	$(3\bar{3}0) + (3\bar{3}3)$

For peaks (1) and (2) the calculated intensity is greater than the observed one and for peaks (3) and (4) the situation is reversed; in unit cell No.3 two peaks are of type (hhl) while in unit cell No.4 all four peaks are of type (hhl). The peaks (5) and (6) in figures 4.28 and 4.29 are the second orders of peaks (1) and (2). The good agreement between the observed and calculated values of peaks (5) and (6) as well as the close similarity of the ten 'Curran' diffraction patterns, practically excluded preferred orientation effects as a possible cause for the discrepancies in peaks (1) to (4).

To account for the observed discrepancies the deuterium atoms were allowed to rotate about the iodine atoms in the orthorhombic (001) plane. Appropriate pseudo-symmetry operations were used to connect the two molecules of the asymmetric unit (see molecules (1) and (2) in figure 4.27). The angular rotation covered a range of 0.5° to 7.5° in both directions and the intramolecular bond length was also allowed to vary separately from 1.2\AA to 1.6\AA . These distortions of the model produced either only slight improvements or, in some cases, gross disagreement between the observed and calculated diffraction patterns.

An examination of the geometrical structure for these peaks was more informative. The geometrical structure factors for the space group C2/c are

$$A = 8\cos 2\pi(hx+lz)\cos 2\pi ky \quad h+k=2n, \quad l=2m \quad (71)$$

$$B = 0$$

$$A = -8\sin 2\pi(hx+lz)\sin 2\pi ky \quad h+k=2n, \quad l=2m+1 \quad (72)$$

$$B = 0$$

$$\text{and } A = B = 0 \quad h+k=2n+1 \quad (73)$$

For the peaks labelled (1) and (2) in figures 4.28 and 4.29 based on model No.5 (see figure 4.27) the geometrical structure factors are:

Cell No.3

$$F^2(1\bar{1}0) + F^2(\bar{1}11) = F^2(1) = 64 \{ [\cos 2\pi x_{31} \cos 2\pi y_{31} + \cos 2\pi x_{32} \cos 2\pi y_{32}]^2 + [\sin 2\pi(z_{31} - x_{31}) \sin 2\pi y_{31} + \sin 2\pi(z_{32} - x_{32}) \sin 2\pi y_{32}]^2 \} \quad (74)$$

$$F^2(31\bar{1}) + F^2(\bar{3}12) = F^2(2) = 64 \{ [\cos 2\pi(2z_{31} - 3x_{31}) \cos 2\pi y_{31} + \cos 2\pi(2z_{32} - 3x_{32}) \cos 2\pi y_{32}]^2 + [\sin 2\pi(3x_{31} - z_{31}) \sin 2\pi y_{31} + \sin 2\pi(3x_{32} - z_{32}) \sin 2\pi y_{32}]^2 \} \quad (75)$$

Cell No.4

$$F^2(1\bar{1}0) + F^2(1\bar{1}\bar{1}) = F^2(1) = 64 \{ [\cos 2\pi x_{41} \cos 2\pi y_{41} + \cos 2\pi x_{42} \cos 2\pi y_{42}]^2 + [\sin 2\pi(x_{41} - z_{41}) \sin 2\pi y_{41} + \sin 2\pi(x_{42} - z_{42}) \sin 2\pi y_{42}]^2 \} \quad (76)$$

$$F^2(1\bar{1}1) + F^2(1\bar{1}2) = F^2(2) = 64 \{ [\cos 2\pi(x_{41} - 2z_{41}) \cos 2\pi y_{41} + \cos 2\pi(x_{42} - 2z_{42}) \cos 2\pi y_{42}]^2 + [\sin 2\pi(x_{41} + z_{41}) \sin 2\pi y_{41} + \sin 2\pi(x_{42} + z_{42}) \sin 2\pi y_{42}]^2 \} \quad (77)$$

where the co-ordinates x_{ij} etc. describe the j^{th} atom of the asymmetric unit ($j=1,2$) and i is the unit cell chosen ($i=3,4$).

The unit cell edge-vectors ($\underline{a}_0, \underline{b}_0, \underline{c}_0$) and the Miller indices ($h_0 k_0 l_0$) of the large orthorhombic unit cell can be transformed to those of the monoclinic cells No.3 and No.4 by the matrices (51) and (52). The fractional atomic co-ordinates (x_0, y_0, z_0) are transformed by a different matrix (the transpose of the inverse unit-cell transformation matrix). If

$\underline{A} = \{A_{ij}\}$ is the unit cell matrix and $\underline{R} = \{R_{kl}\}$ is the fractional co-ordinate matrix then $R_{kl} = (A^{-1})_{ji}$.

Cell No.3

$$\begin{bmatrix} \underline{a}_3 \\ \underline{b}_3 \\ \underline{c}_3 \end{bmatrix} = \begin{bmatrix} 0 & 0 & 1 \\ 1 & 0 & 0 \\ 0 & \frac{1}{2} & -\frac{1}{2} \end{bmatrix} \begin{bmatrix} \underline{a}_0 \\ \underline{b}_0 \\ \underline{c}_0 \end{bmatrix} \quad \& \quad \begin{bmatrix} \underline{a}_0 \\ \underline{b}_0 \\ \underline{c}_0 \end{bmatrix} = \begin{bmatrix} 0 & 1 & 0 \\ 1 & 0 & 2 \\ 1 & 0 & 0 \end{bmatrix} \begin{bmatrix} \underline{a}_3 \\ \underline{b}_3 \\ \underline{c}_3 \end{bmatrix} \quad (51)$$

$$\begin{bmatrix} x_3 \\ y_3 \\ z_3 \end{bmatrix} = \begin{bmatrix} 0 & 1 & 1 \\ 1 & 0 & 0 \\ 0 & 2 & 0 \end{bmatrix} \begin{bmatrix} x_0 \\ y_0 \\ z_0 \end{bmatrix} \quad \& \quad \begin{bmatrix} x_0 \\ y_0 \\ z_0 \end{bmatrix} = \begin{bmatrix} 0 & 1 & 0 \\ 0 & 0 & \frac{1}{2} \\ 1 & 0 & -\frac{1}{2} \end{bmatrix} \begin{bmatrix} x_3 \\ y_3 \\ z_3 \end{bmatrix} \quad (79)$$

$$(80)$$

Cell No.4

$$\begin{bmatrix} \underline{a}_4 \\ \underline{b}_4 \\ \underline{c}_4 \end{bmatrix} = \begin{bmatrix} 0 & 1 & 0 \\ \overline{1} & 0 & 0 \\ 0 & -\frac{1}{2} & \frac{1}{2} \end{bmatrix} \begin{bmatrix} \underline{a}_0 \\ \underline{b}_0 \\ \underline{c}_0 \end{bmatrix} \quad \& \quad \begin{bmatrix} \underline{a}_0 \\ \underline{b}_0 \\ \underline{c}_0 \end{bmatrix} = \begin{bmatrix} 0 & \overline{1} & 0 \\ 1 & 0 & 0 \\ 1 & 0 & 2 \end{bmatrix} \begin{bmatrix} \underline{a}_4 \\ \underline{b}_4 \\ \underline{c}_4 \end{bmatrix} \quad (52)$$

$$(81)$$

$$\begin{bmatrix} x_4 \\ y_4 \\ z_4 \end{bmatrix} = \begin{bmatrix} 0 & 1 & 1 \\ \overline{1} & 0 & 0 \\ 0 & 0 & 2 \end{bmatrix} \begin{bmatrix} x_0 \\ y_0 \\ z_0 \end{bmatrix} \quad \& \quad \begin{bmatrix} x_0 \\ y_0 \\ z_0 \end{bmatrix} = \begin{bmatrix} 0 & \overline{1} & 0 \\ 1 & 0 & -\frac{1}{2} \\ 0 & 0 & \frac{1}{2} \end{bmatrix} \begin{bmatrix} x_4 \\ y_4 \\ z_4 \end{bmatrix} \quad (82)$$

$$(83)$$

If the expressions for the geometrical structure factors of the peaks (1) and (2) given by equations (74) - (77) are transformed by the matrices (79) - (83) into the orthorhombic unit cell it is seen that the geometrical structure factors of these peaks are the same in both cells No.3 and No.4 and are given by:

$$F^2(1) = 64 \{ [\cos 2\pi(y_{01} + z_{01}) \cos 2\pi x_{01} + \cos 2\pi(y_{02} + z_{02}) \cos 2\pi x_{02}]^2 + [\sin 2\pi(y_{01} - z_{01}) \sin 2\pi x_{01} + \sin 2\pi(y_{02} - z_{02}) \sin 2\pi x_{02}]^2 \} \quad (84)$$

$$F^2(2) = 64 \{ [\cos 2\pi(y_{01} - 3z_{01}) \cos 2\pi x_{01} + \cos 2\pi(y_{02} - 3z_{02}) \cos 2\pi x_{02}]^2 + \quad (85)$$

$$[\sin 2\pi(y_{01} + 3z_{01}) \sin 2\pi x_{01} + \sin 2\pi(y_{02} + 3z_{02}) \sin 2\pi x_{02}]^2 \}$$

Hence if the DI molecules lie in the $(001)_0$ plane it is found that for

$$\text{Cell No. 3 } x_{31} = \frac{z_{31}}{2} \quad \text{and} \quad \text{Cell No. 4 } z_{41} = 0$$

and for the orthorhombic cell, $z_{01} = 0$.

Having shown that the geometrical structure factors are the same irrespective of whether calculated in cell No. 3 or No. 4, the remaining discussion will refer to cell No. 4. Substituting $z_{41} = z_{42} = 0$ in eqns (76) and (77) shows that for a planar structure the geometrical structure factors of peaks (1) and (2) are equal.

Cell No. 4

$$F_{\text{calc}}^2(1) = F_{\text{calc}}^2(2) = 64 \{ [\cos 2\pi x_{41} \cos 2\pi y_{41} + \cos 2\pi x_{42} \cos 2\pi y_{42}]^2 + \quad (86)$$

$$[\sin 2\pi x_{41} \sin 2\pi y_{41} + \sin 2\pi x_{42} \sin 2\pi y_{42}]^2 \}$$

The intensities of the observed powder diffraction peaks (1) and (2) can be seen in figure 4.28. It can be seen that the intensity of peak (2) is practically zero so that the observed powder diffraction peak intensities are described by the inequality:

$$\text{Cell No. 4} \quad I_{\text{obs}}(1\bar{1}0 + 1\bar{1}\bar{1}) \gg I_{\text{obs}}(1\bar{1}1 + 1\bar{1}\bar{2}) \quad (87)$$

$$\text{or} \quad \frac{j F_{\text{obs}}^2(1\bar{1}0 + 1\bar{1}\bar{1}) e^{-\frac{B \sin^2 \theta_1}{\lambda^2}}}{\sin \theta_1 \sin 2\theta_1} \gg \frac{j F_{\text{obs}}^2(1\bar{1}1 + 1\bar{1}\bar{2}) e^{-\frac{B \sin^2 \theta_2}{\lambda^2}}}{\sin \theta_2 \sin 2\theta_2} \quad (88)$$

where θ_1 and θ_2 are the angular positions of peaks (1) and (2), B is the temperature factor, λ the wavelength and j the multiplicity.

The multiplicity j is 4 for all of these peaks while on increasing the value of θ from peak (1) to peak (2) the temperature factor term $[\exp(-\frac{B \sin^2 \theta}{\lambda^2})]$

decreases by 4% and the Lorentz term ($\sin\theta\sin2\theta$) increases by a factor of 4.

Thus the observed structure factors obey the relation:

$$F_{\text{obs}}^2(1) \gg F_{\text{obs}}^2(2) \quad (89)$$

$$\text{while from (86)} \quad F_{\text{calc}}^2(1) = F_{\text{calc}}^2(2) \quad (86)$$

These conclusions are the same for both cells No.3 and No.4. The only way of altering equation (86) is to allow non-zero values for z_{41} and z_{42} in equations (76) and (77) thereby allowing the DI molecule to tilt out of the (001) plane in cell No.4. This is unlikely because in the middle phase the planar arrangement of the DI molecules is well established.

Nevertheless calculations of the expected diffraction pattern were also carried out on the assumption that the arrangement of the DI molecules in the low phase is not planar. The distortion of a planar arrangement can be carried out in the following way. If the space group is C2/c there are two molecules in the asymmetric unit (see (1) and (2) in figure 4.27). Assuming that the two molecules do not lie in the (001) plane, their co-ordinates are related by the equations:

Cell No.4

$$x_2 = \frac{1}{2} + x_1, \quad y_2 = \frac{1}{2} - y_1, \quad z_2 = \pm z_1 \quad (90)$$

These relationships give four methods of distortion as follows

$$(x_1, y_1, z_1), (x_2, y_2, z_2) \quad (91)$$

$$(x_1, y_1, z_1), (x_2, y_2, -z_2) \quad (92)$$

$$(x_1, y_1, -z_1), (x_2, y_2, z_2) \quad (93)$$

$$(x_1, y_1, -z_1), (x_2, y_2, -z_2) \quad (94)$$

If the space group is Cc there are four molecules in the asymmetric unit and these are related by the following additional equations:

$$x_3 = \frac{1}{4} - x_1, \quad y_3 = y_1 - \frac{1}{4}, \quad z_3 = \pm z_1 \quad (95)$$

$$x_4 = -x_1, \quad y_4 = -y_1, \quad z_4 = \pm z_1 \quad (96)$$

These three expressions (90), (95) and (96) give a total of sixteen methods of distortion as follows:

$$(x_1, y_1, z_1), (x_2, y_2, z_2), (x_3, y_3, z_3), (x_4, y_4, z_4) \quad (97)$$

$$(x_1, y_1, z_1), (x_2, y_2, z_2), (x_3, y_3, z_3), (x_4, y_4, -z_4) \quad (98)$$

$$\dots \vdots$$

$$(x_1, y_1, -z_1), (x_2, y_2, -z_2), (x_3, y_3, -z_3), (x_4, y_4, -z_4) \quad (99)$$

Of these sixteen the number of non-equivalent methods of distortion was found to be ten. These ten modes were investigated for out-of-plane angles (θ) of 2.5° and 5° . Only one mode of distortion showed any significant improvement namely,

$$x_2 = \frac{1}{4} + x_1, \quad y_2 = \frac{3}{4} - y_1, \quad z_2 = -z_1 \quad (100)$$

in the space group $C2/c$. This model was investigated for θ -values in the range 0° to 15° ; the best agreement, although only slightly better than the $\theta = 0^\circ$ case, was observed for $\theta = 7.5^\circ$ and the powder pattern calculated for this case is shown in figure 4.30.

The results of this distortion on the calculated intensities of the powder peaks of model No.5 in unit cell No.4 may be summarized as follows:

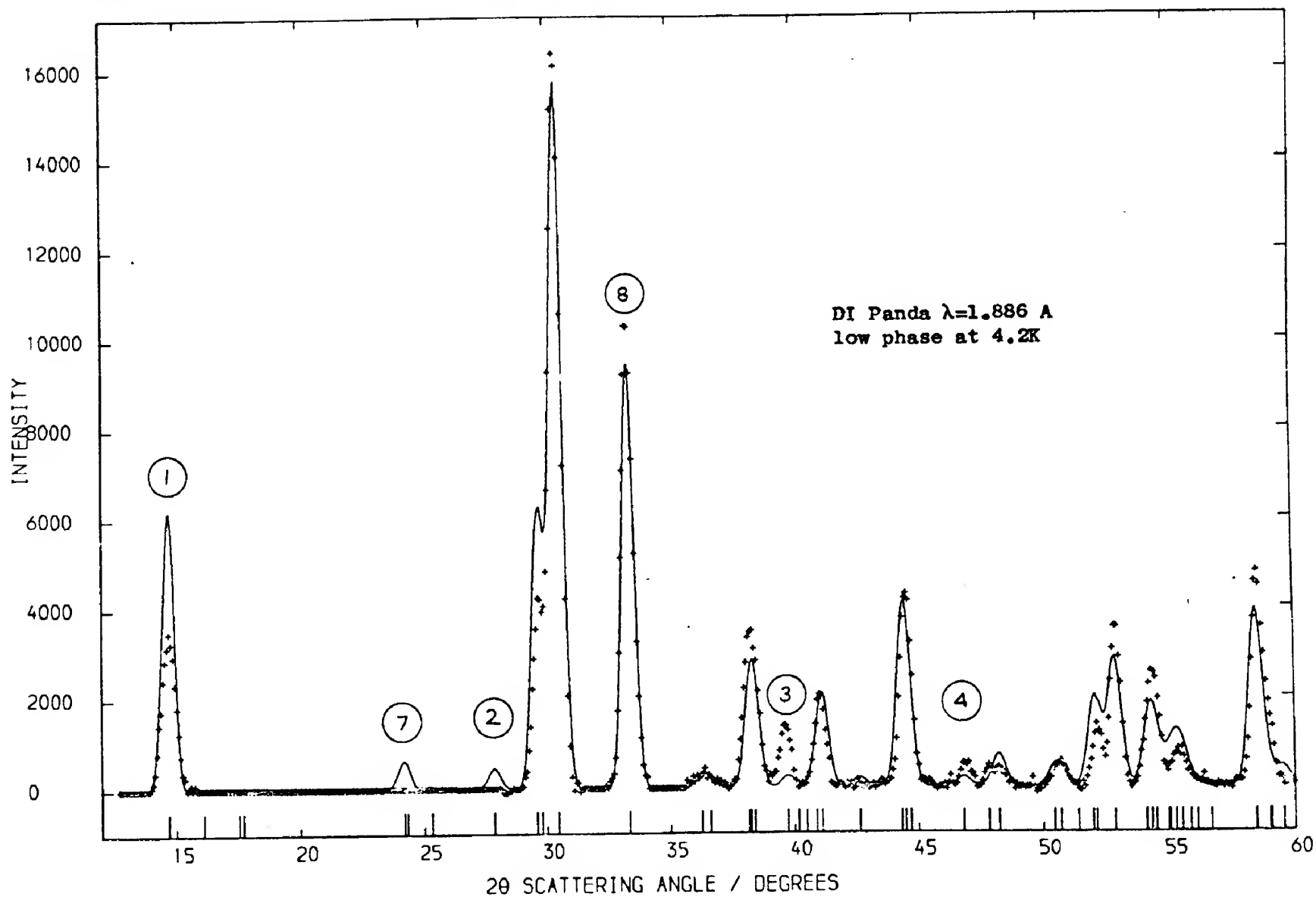


Figure 4.30 Observed (crosses) and calculated (solid line) intensities based on model No.5 for DI with Pluto Panda at 4.2K with the molecule tilted at 5° to the $(001)_m$ plane.

Peak No.	Miller indices Cell No.4	Change in calculated intensity of powder peak
(1)	$(1\bar{1}0) + (1\bar{1}\bar{1})$; little change,
(2)	$(1\bar{1}1) + (1\bar{1}\bar{2})$; significantly reduced,
(3)	$(3\bar{3}\bar{1}) + (3\bar{3}\bar{2})$; little change,
(4)	$(3\bar{3}0) + (3\bar{3}\bar{3})$; little change,
(7)	$(20\bar{2}) + (200)$; an unobserved peak which now has a finite intensity.
(8)	$(002) + (00\bar{2})$; reduced slightly, the presence of this peak and its neighbour (9) is strong evidence of a planar structure. In the orthorhombic unit cell these are the (002) and (020+200) reflections.
(9)	$(40\bar{2}) + (040)$; unchanged.

4.6 Analysis of the intensity transform of the neutron powder pattern of the low phase

Although only powder diffraction patterns were available for the low phase of DI, it was decided to explore whether the application of Fourier transform techniques would provide any useful information on the distribution of the DI molecules. For an isotropic powder, amorphous solid or liquid a pair-distribution function $g(r)$ may be defined as the probability per unit volume of finding a specific atom type at a distance r from another specific atom type. For DI there are three such pair-distribution functions; $g_{I-I}(r)$; probability of an iodine atom at distance r from another iodine atom, $g_{D-D}(r)$; probability of a deuterium atom at distance r from another deuterium atom, $g_{D-I}(r)$; probability of a deuterium atom at distance r from an iodine atom, where $g_{I-D}(r) = g_{D-I}(r)$.

Applying to DI the relationships derived by Powles (1973) for compounds

containing two types of atoms in equal concentration we can write;

$$4\pi\rho\left\{\frac{b_I^2[g_{I-I}(r)-1] + b_D^2[g_{D-D}(r)-1] + 2b_I b_D[g_{I-D}(r)-1]}{b_I^2 + 2b_I b_D + b_D^2}\right\} =$$

$$\frac{16\pi}{\lambda^2} \int_0^{\pi/2} I_{DI}(\theta) \sin\left[\frac{4\pi r \sin\theta}{\lambda}\right] \sin 2\theta d\theta \quad (101)$$

where b_I and b_D are the neutron scattering lengths of iodine and deuterium respectively, ρ is the number of atoms per unit volume and $I_{DI}(\theta)$ is the intensity of the neutron powder pattern observed at the diffraction angle θ .

If $b_D=0$ the LHS of equation (101) becomes

$$4\pi\rho[g_{I-I}(r)-1] \equiv d_{I-I}(r) \quad (102)$$

giving the pair-distribution function of the iodine sub-lattice.

Experimentally the powder diffraction pattern can only be observed up to a certain diffraction angle θ_{\max} . This restriction creates small oscillations in the Fourier transform of the diffracted intensity which can be reduced by the use of so-called window or modification functions $M(\theta)$ (see Wright 1974). The use of these functions worsens slightly the resolution of the pair-distribution function $g(r)$ in real space.

For the neutron powder diffraction pattern of the low phase of DI recorded on the 'Panda' at $\lambda = 1.886\text{\AA}$, the maximum value of θ was 47° . To determine the resolution of the intensity transform of these data a very simple model of the pair-distribution function was considered, namely a δ -function at 1\AA . The theoretical intensity distribution as a function

of scattering angle θ for this simple model is that of a diatomic molecule namely;

$$I(\theta) = \sin\left[\frac{4\pi r_1 \sin\theta}{\lambda}\right] / \left[\frac{4\pi r_1 \sin\theta}{\lambda}\right] \quad (103)$$

where $r_1 = 1\text{\AA}$.

The function $I(\theta)$ is a sine curve whose amplitude slowly decays as θ increases. Equation (101) can now be rewritten to include the window function on the RHS.

$$d(r) = \frac{16\pi}{\lambda^2} \int_0^{\theta_{\max}} I(\theta) M(\theta) \sin\left[\frac{4\pi r \sin\theta}{\lambda}\right] \sin 2\theta d\theta \quad (104)$$

and the window function chosen for this work, which decreases slowly in value from one at $\theta = 0$ to zero at $\theta = \theta_{\max}$, is that due to Lorch (1969).

$$M(\theta) = \sin\left[\frac{\pi \sin\theta}{\sin\theta_{\max}}\right] / \left(\frac{\pi \sin\theta}{\sin\theta_{\max}}\right) \quad (105)$$

Figure 4.31 and 4.32 show the intensity transforms of the function $I(\theta)M(\theta)$ [equations (104) and (101)] and the function $I(\theta)$, with the maximum value of θ equal to that of the 'Panda' neutron powder diffraction pattern i.e. the Fourier transforms of the intensity distribution below an angle of 47° of the model δ -function $g(r)$ described above with and without the window function $M(\theta)$ (105) respectively. The functions appear as broad δ -functions centred about $r = 1\text{\AA}$ with spurious small oscillations due to the finite value of θ_{\max} . For the window function of equation (105) the full width of this δ -function at half its maximum height (FWHM) is given by the expression (Wright 1974);

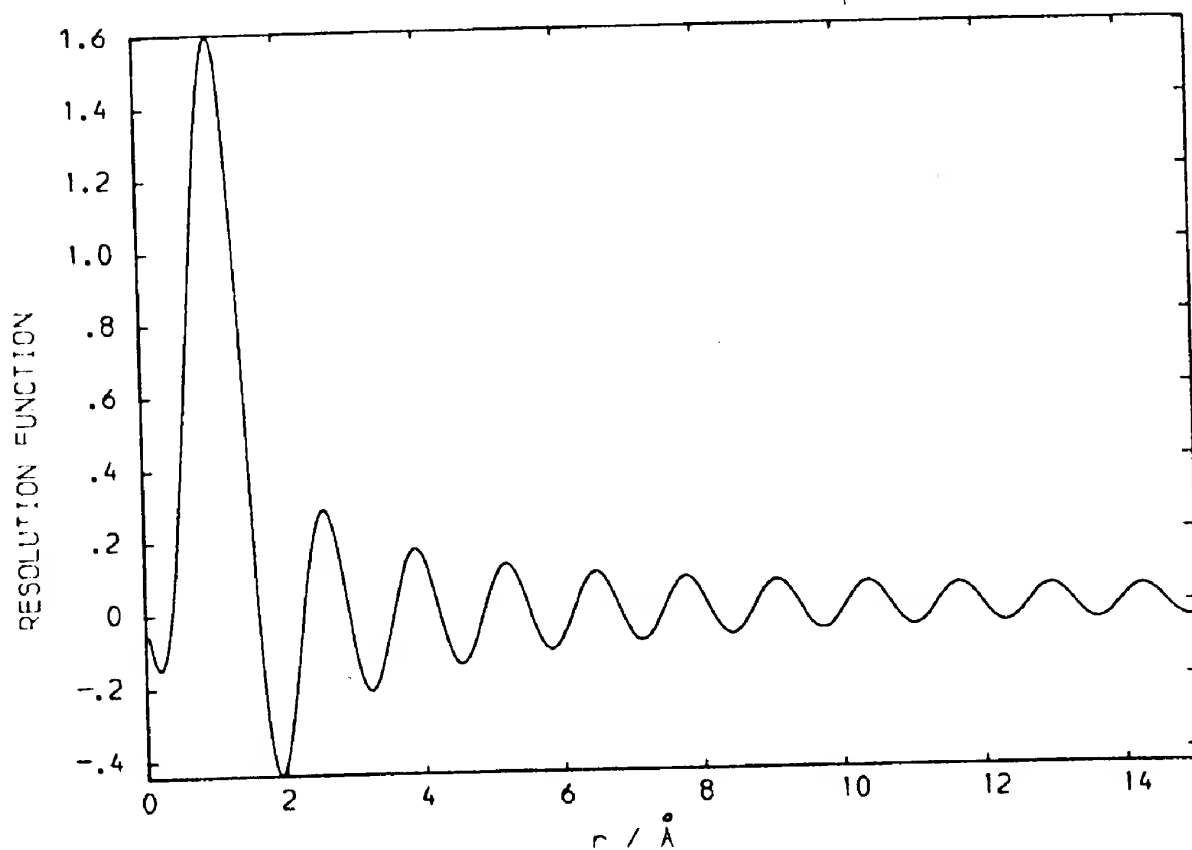
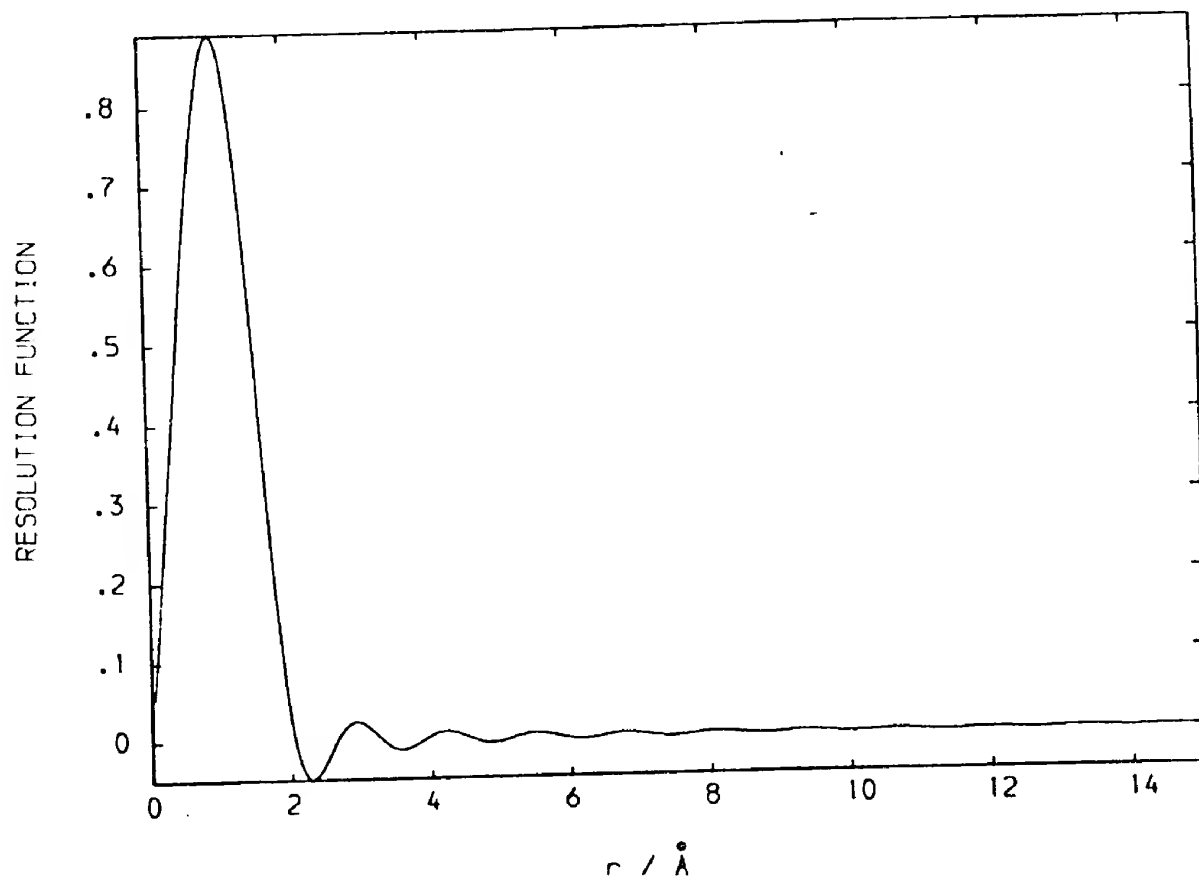


Figure 4.31 Resolution function of the intensity transform (using a 'window' function) of the neutron powder diffraction pattern of DI recorded on the Panda at 4.2K.

Figure 4.32 Resolution function of the intensity transform (using no 'window' function) of the neutron powder diffraction pattern of DI recorded on the Panda at 4.2K.

$$\Delta r(\text{FWHM}) = \frac{5.5\lambda}{4\pi \sin \theta_{\text{max}}} = 1.13\text{\AA} \quad (106)$$

where θ_{max} for the 'Panda' data is 47° and $\lambda = 1.886\text{\AA}$.

Figure 4.33 shows the Fourier transform of the observed neutron powder pattern of the low phase of DI at 4.2K. Figure 4.34 shows the transform of the powder pattern calculated for the model No.5 (figure 4.27). It is seen that the two transforms are very similar. The first peak at 1.4\AA corresponds to the separation of the deuterium and iodine atoms within a molecule. The peaks at 4, 8 and 12\AA correspond to first, second and third nearest DI molecules in the crystal.

Figure 4.35 shows the calculated neutron powder diffraction pattern of the iodine sublattice and figure 4.36 shows its Fourier transform. The vertical lines in figure 4.36 show the positions of the first six iodine nearest-neighbour distances calculated from the lattice parameters of table 4.2. There are no distances less than 4.18\AA [this is the separation between an atom at $(0,0,0)$ and one at $(\frac{1}{2}, \frac{1}{2}, 0)$] and the small oscillations below 3\AA in figure 4.36 are due to the low value of the maximum diffraction angle.

Figure 4.37 shows the neutron powder diffraction pattern of the low phase of DI recorded on 'Panda' at 4.2K [$DI_{(\text{obs})}$] minus the calculated powder diffraction pattern of the iodine sublattice [$I_{(\text{calc})}$]. The Fourier transform of this function is shown in figure 4.38. Figures 4.39 and 4.40 show the calculated powder diffraction pattern for the low phase of DI [$DI_{(\text{calc})}$] based on model No.5 minus the calculated iodine powder pattern [$I_{(\text{calc})}$] and the Fourier transform of this function.

The two transforms (figures 4.38 and 4.40) are the experimentally

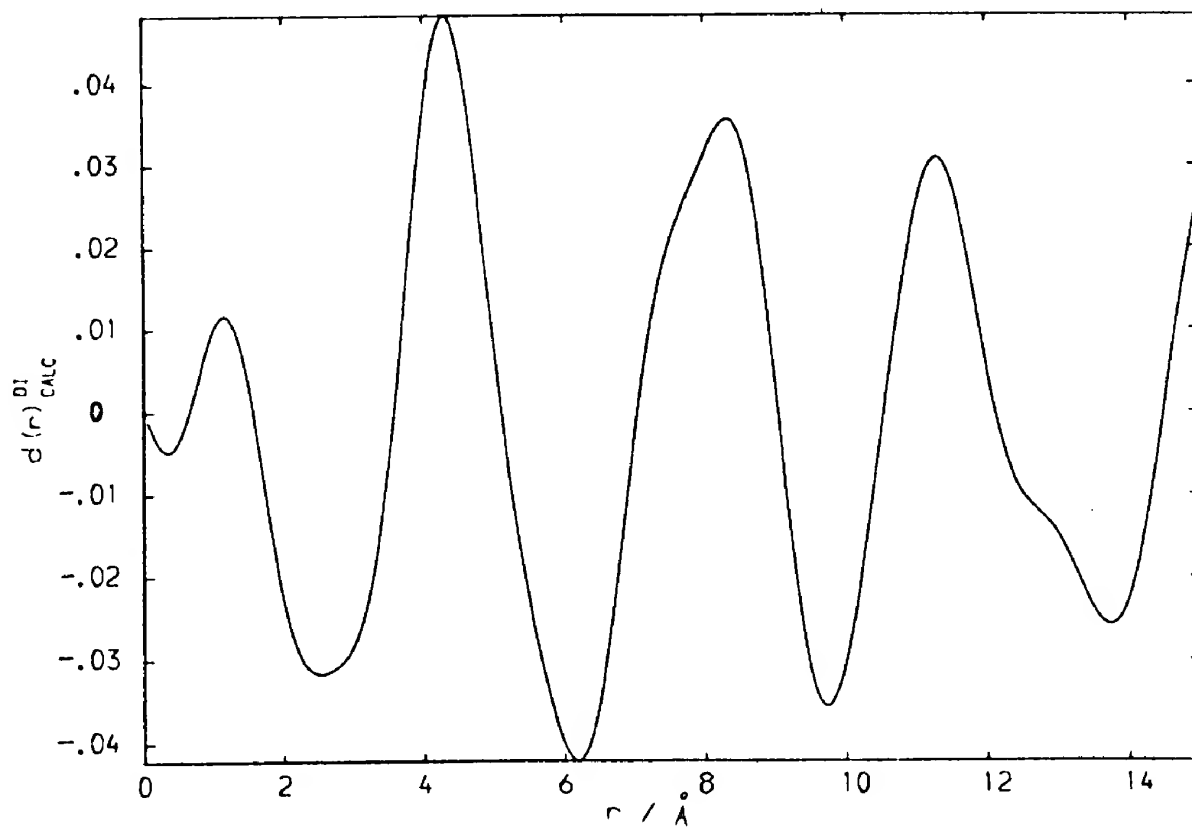
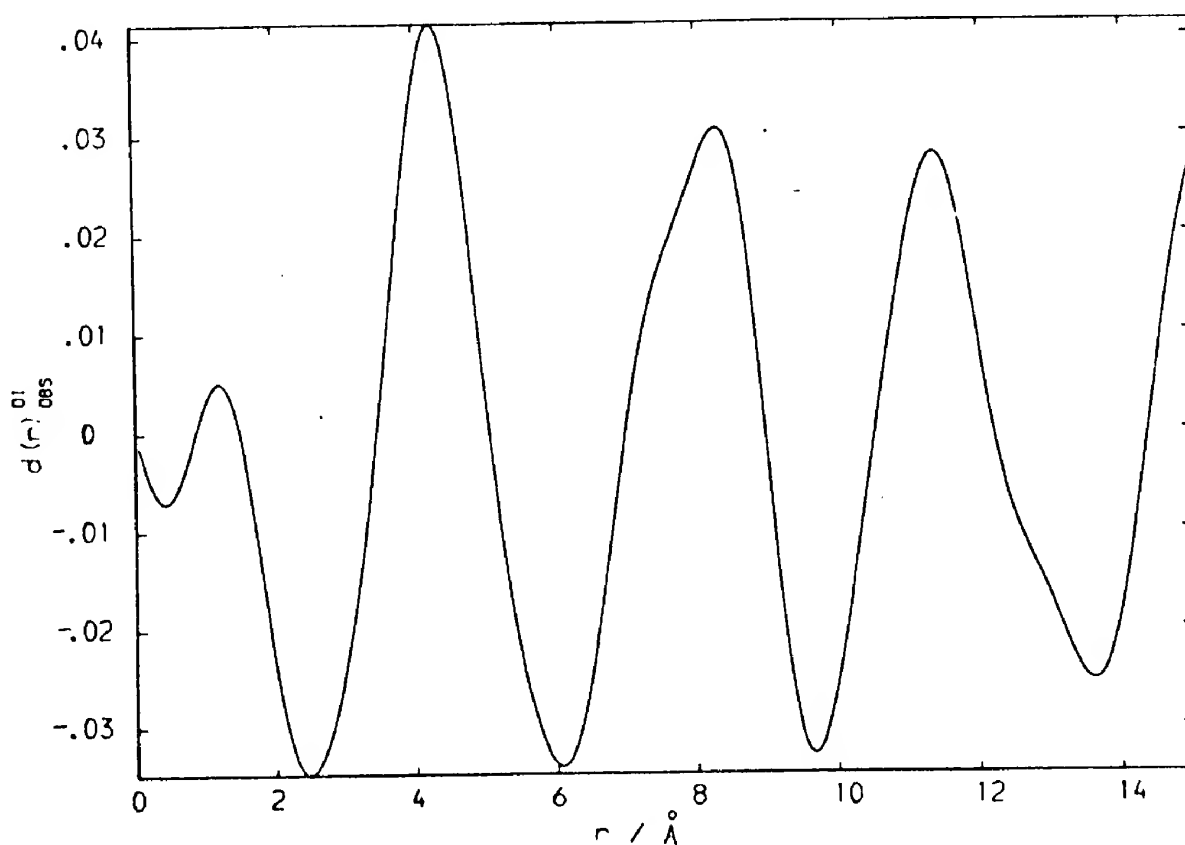


Figure 4.33 Intensity transform of the neutron powder diffraction pattern of DI recorded on the Panda at 4.2K.

Figure 4.34 Intensity transform of a neutron powder diffraction pattern of DI calculated on the basis of the model shown in figure 4.19.

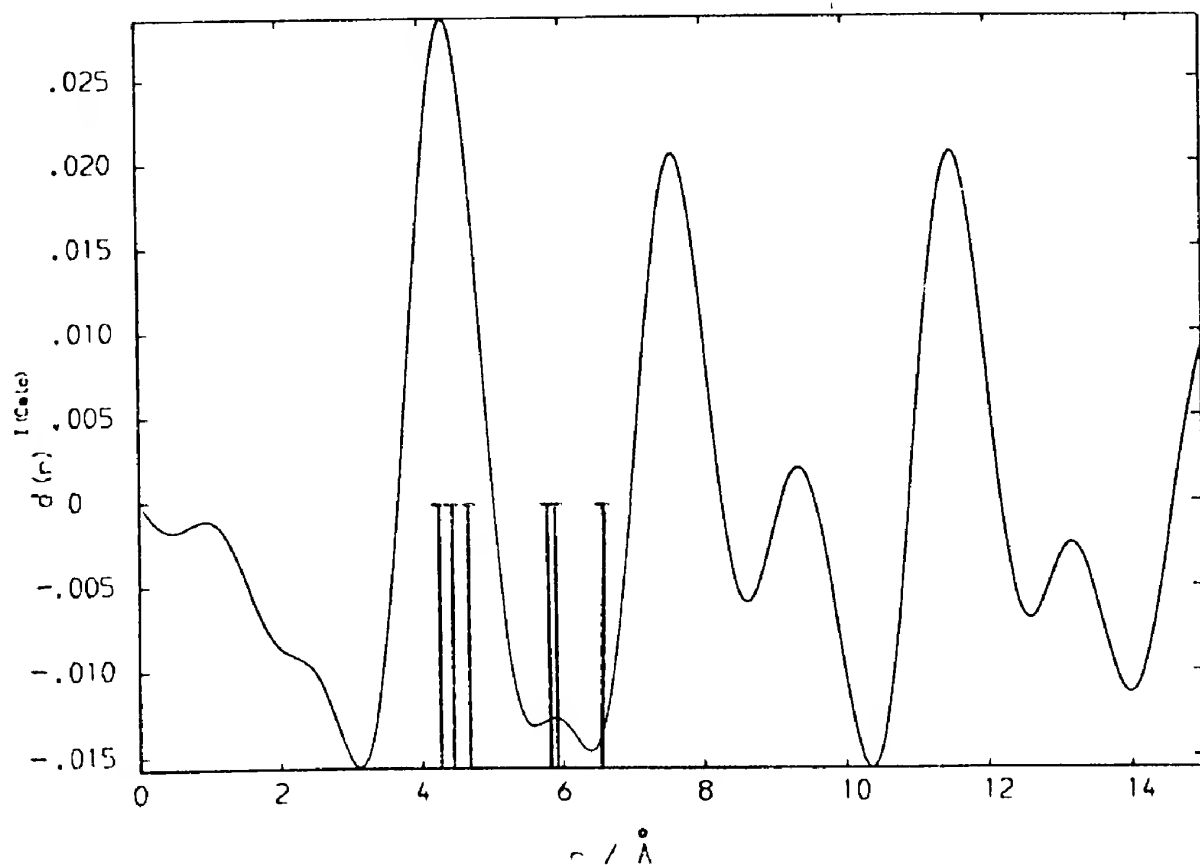
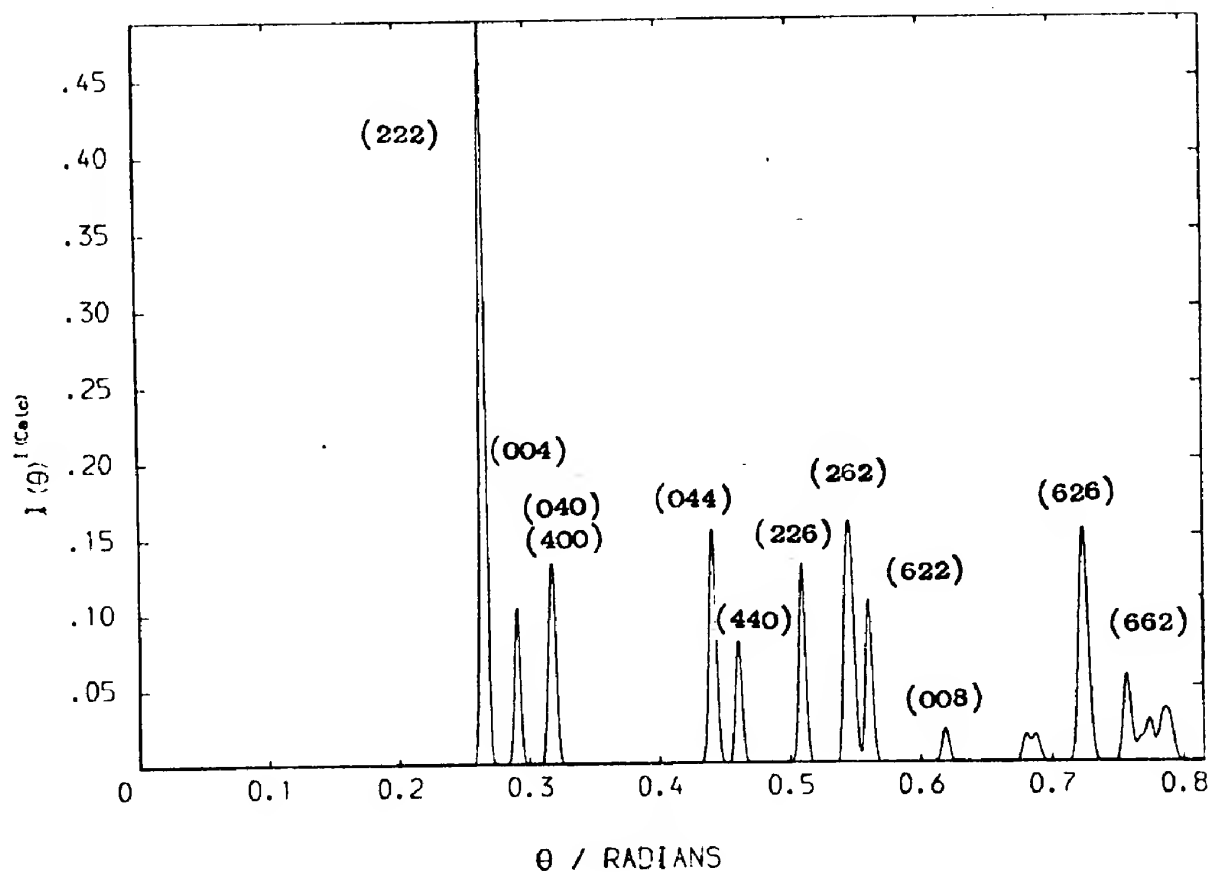


Figure 4.35 Calculated neutron powder diffraction pattern of the iodine sublattice.

Figure 4.36 Intensity transform of the calculated neutron powder diffraction pattern of the iodine sublattice showing the first six iodine nearest-neighbour distances calculated from the lattice parameters of Table 4.2.

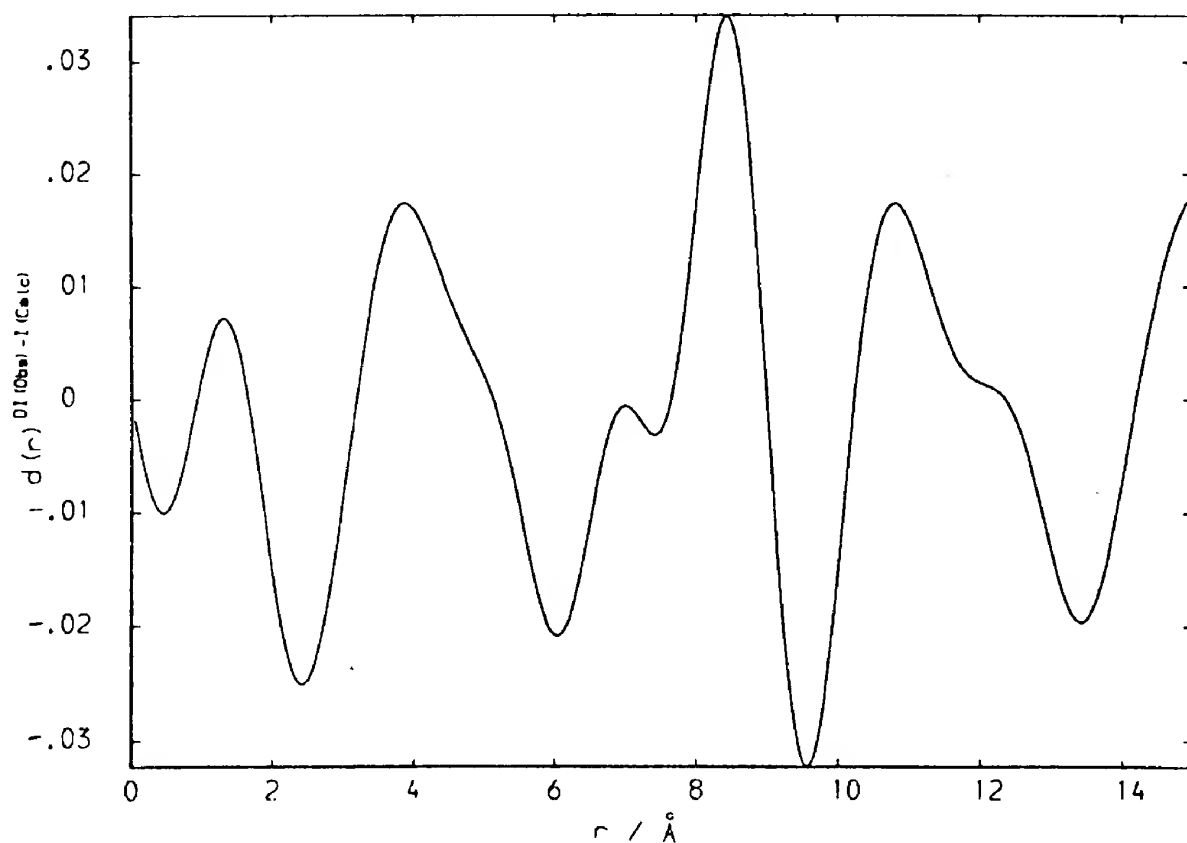
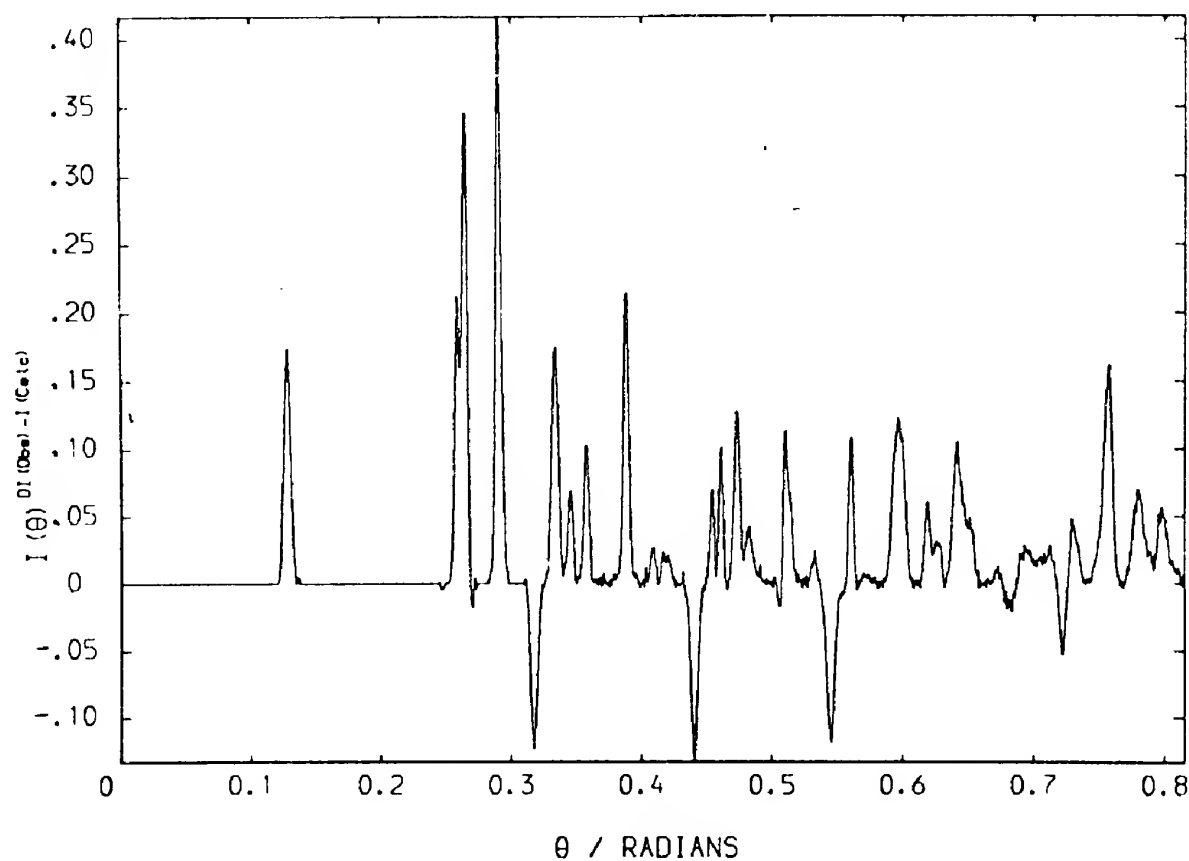


Figure 4.37 Neutron powder diffraction pattern of DI recorded on Panda at 4.2K minus the calculated neutron powder diffraction pattern of the iodine sublattice.

Figure 4.38 Intensity transform of the neutron powder diffraction pattern of DI recorded on Panda at 4.2K minus the calculated neutron powder diffraction pattern of the iodine sublattice.

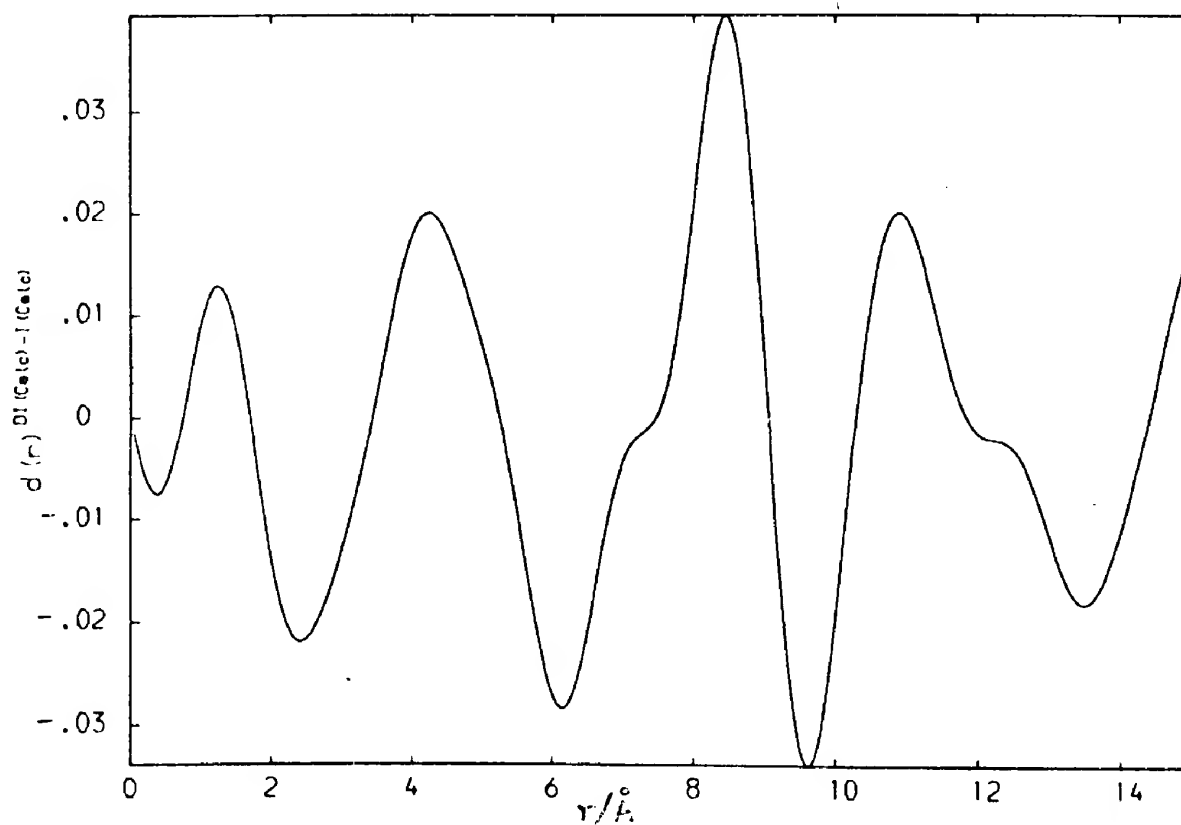
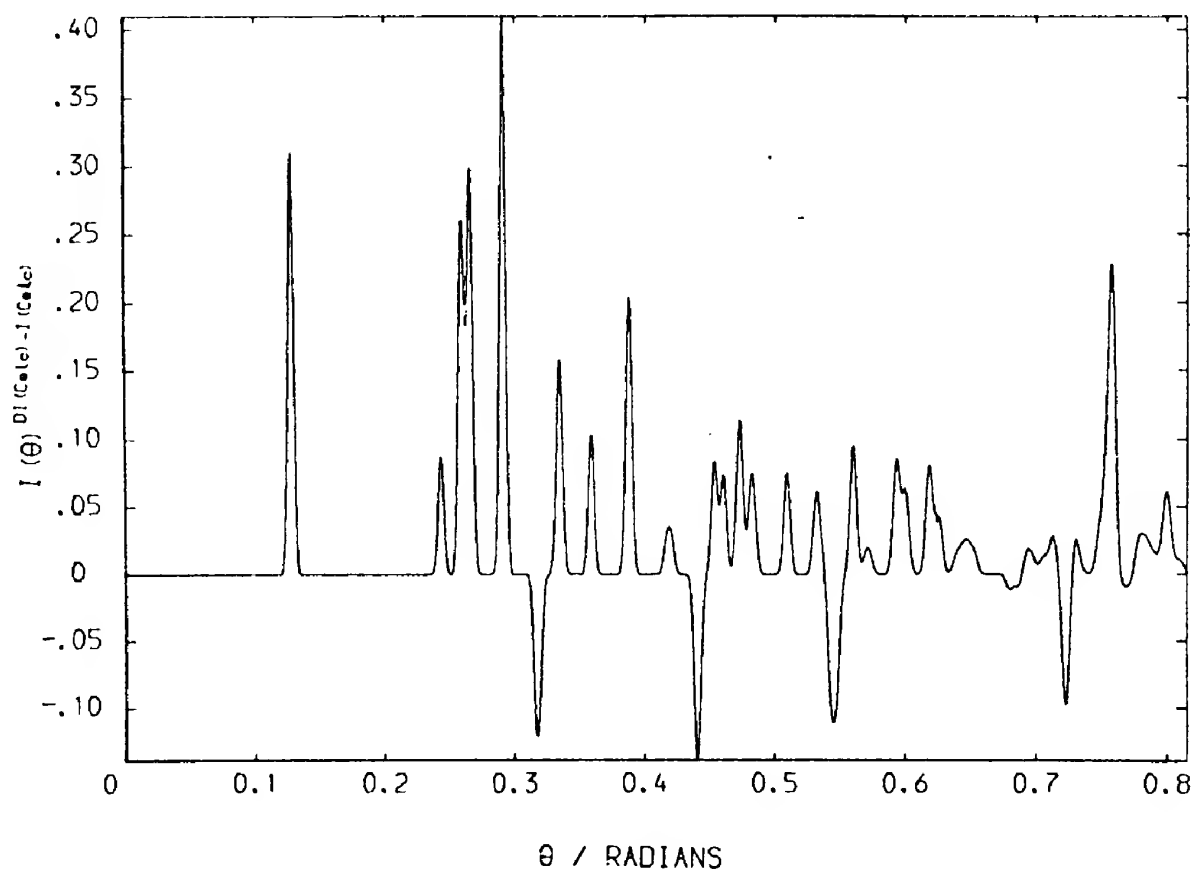


Figure 4.39 Neutron powder diffraction pattern of DI calculated on the basis of the model shown in figure 4.19 minus the calculated neutron powder diffraction pattern of the iodine sublattice.

Figure 4.40 Intensity transform of the neutron powder diffraction pattern of DI calculated on the basis of the model shown in figure 4.19 minus the calculated neutron powder diffraction pattern of the iodine sublattice.

derived and the calculated (model No.5) pair-distribution functions for D-I and D-D distances respectively. Equation (101) is the transform of DI and equation (102) is the transform of the iodine sublattice so that figures 4.38 and 4.40 are the function;

$$4\pi r\rho \left\{ \frac{b_D^2 [g_{D-D}(r)-1] + 2b_I b_D [g_{D-I}(r)-1]}{b_I^2 + 2b_I b_D + b_D^2} \right\} \quad (107)$$

The two transforms of figure 4.38 and 4.40 differ in the region of 7\AA but otherwise are very similar. The result is not surprising as this distance represents the diffraction peak (1) in figures 4.28 and 4.29. The difference between the iodine sub-lattice and the calculated DI lattice transforms (figures 4.36 and 4.34) can be seen as a broadening of the first peak centred at 4\AA , and represents the arrangement of deuterium atoms about the iodine atoms. Due to the poor resolution in real space ($> 1\text{\AA}$) and because the transform is only a one-dimensional representation of a three-dimensional structure, any direct interpretation of the transform in terms of a model is unfortunately not possible

4.7 Conclusion

Neutron powder diffraction patterns of the low phase of DI at 4.2K were recorded with three wavelengths (1.06, 1.886 and 2.66\AA) and were assigned Miller indices on the basis of a large face-centred orthorhombic unit cell of 32 molecules. These observed data are reasonably consistent with each other and there is no evidence of preferred orientation in the samples. The criterion was established that the low phase structure is related to the middle phase of DI by 180° (or possibly 90°) re-orientation of the deuterium atoms about the iodine atoms. On this basis the space group Fdd2(No.43) was considered and 32 models were generated. Of these only 3 were separate non-equivalent structures giving calculated diffraction

patterns quite unlike the observed neutron powder diffraction pattern of DI at 4.2K (particularly at low angles).

The large face-centred orthorhombic unit cell was transformed into 6 different C-centred monoclinic unit cells of 16 molecules each. The middle phase of DI was considered in these cells and it was found that; 2 cells supported no monoclinic symmetry operations, 2 supported space groups Cc(No.9) and C2/c(No.12) and 2 supported space group Cm(No.8). By allowing 180° re-orientation of the deuterium atoms, the cells supporting space groups Cc and C2/c each produced the same 8 models. Of these only 5 were separate non-equivalent structures and the calculated diffraction pattern of model No.5 (figure 4.19) gave reasonable agreement with the observed neutron powder diffraction pattern. Also in this unit cell the deuterium atoms were allowed to re-orientate through 90° intervals and a further 128 models were considered in space group Cc producing one new model whose calculated diffraction pattern was similar to the observed neutron pattern.

At this stage the large face-centred orthorhombic unit cell was re-considered with 8 molecules in the asymmetric unit and by allowing 180° re-orientation of the deuterium atoms produced 128 models. Of these there were only 17 non-equivalent structures of which 12 had unit cells of 32 molecules (these 12 included the 3 structures of space group Cc generated earlier). Diffraction patterns calculated on the basis of these 9 structures did not agree with the observed neutron powder diffraction pattern.

The 2 monoclinic cells supporting space group Cm were considered and produced 32 models when allowing the 6 molecules of the asymmetric unit to re-orientate through 180°. All of these 32 models were equivalent to models generated in the large orthorhombic unit cell and are included in the summary of structures considered shown in Table 4.3.

The model No.5 (figure 4.19) was refined by the computer program of Rietveld (Appendix one). The analysis of the data is complicated by the large number of unresolved Bragg peaks. Several different modes of distortion of the structure were introduced but these produced no significant improvement in the agreement between the calculated and observed powder diffraction patterns which differed from each other in a few low angle peaks.

Fourier transformation of the observed intensity distribution is not very productive because of the poor resolution in real space and because the transformed intensity is only a one-dimensional average of the nuclear density function.

To conclude this chapter it can only be said that the structure of the low phase of DI is probably very close to that described by the model shown in figures 4.19 and 4.27. The difference between the proposed model and the true structure is due to some small change in the symmetry, possibly involving a larger unit cell than the ones considered. Any further investigation of the structure will involve either recording powder patterns with much better resolution than is possible at present or else using diffraction data collected from a single crystal; if one can be grown.

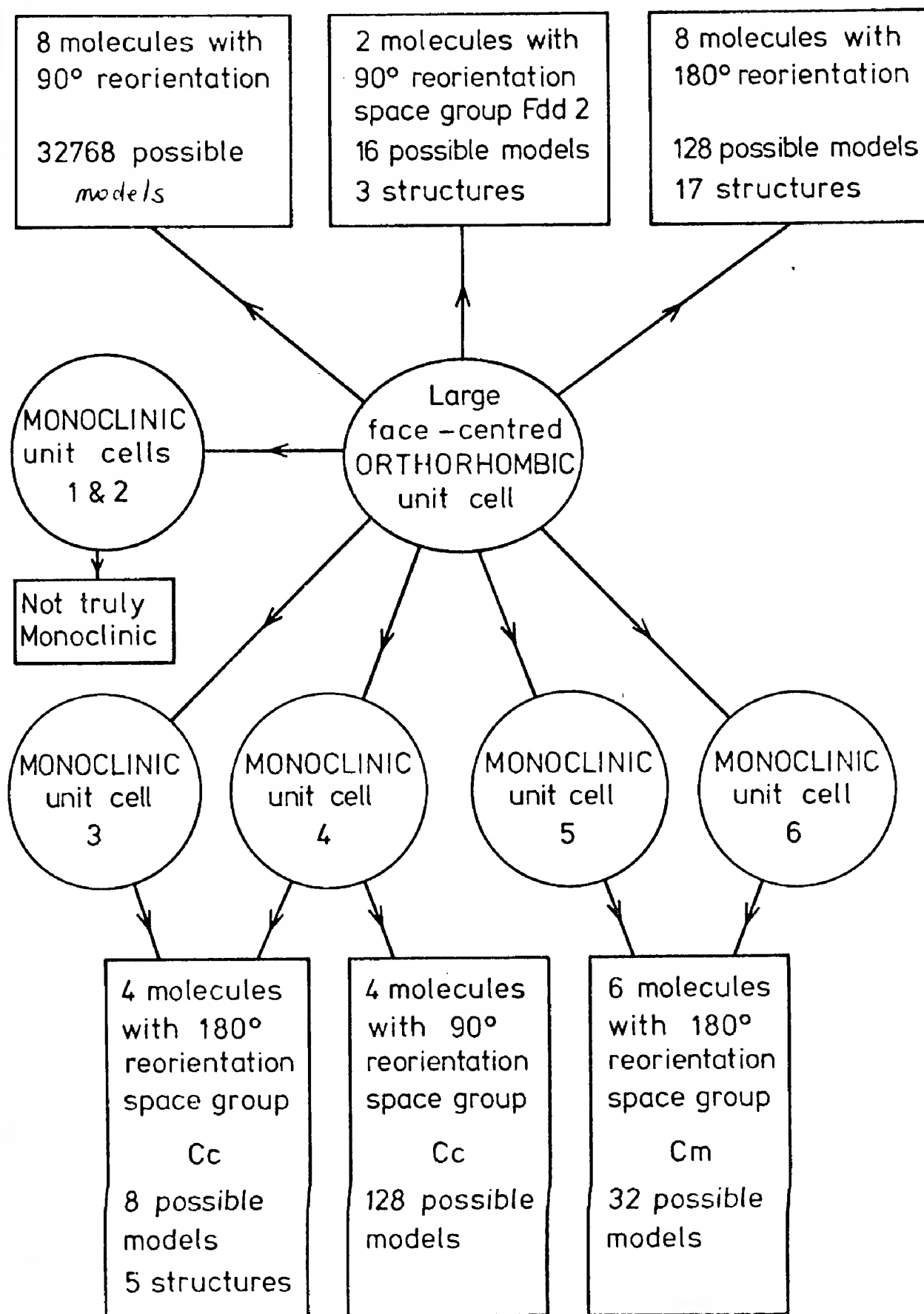


Table 4.3 Summary of the unit cells and space-groups considered for the structure of the low phase of D1.

CHAPTER FIVE

Neutron powder diffraction study of the crystal structure of the
middle phase of DI

The neutron powder diffraction pattern of the middle phase of DI was recorded with the Dido 'Curran' powder diffractometer described in Chapter 2.3(a) and shown in figures 2.6 and 2.7. The sample was contained in a thin-walled vitreous silica tube at a constant low temperature in a cryostat fitted with vanadium tails to provide isotropic background scattering. The outer container of the cryostat was filled with liquid nitrogen and the inner container (normally filled with liquid helium) held dry air. The equilibrium temperature of this cryostat arrangement was about 84K. At this temperature the heat conducted down the walls of the sample tube and the inner helium container from the exterior of the cryostat was balanced by the radiation loss to the liquid nitrogen container. The neutron powder diffraction pattern recorded at 84K is shown in figure 5.1. The broad 'hump' in the background scattering over the $2\theta = 10^\circ - 15^\circ$ range is due to the vitreous silica sample container.

Using lattice parameters derived from the X-ray powder diffraction pattern recorded at 84K (see table 3.1) the neutron powder peaks were assigned Miller indices on the basis of an orthorhombic unit cell containing four molecules. The following systematic absences were observed:

$$\begin{array}{ll}
 hkl; & h+l = 2n \\
 0kl; & k=2n \quad (l=2n) \\
 h0l; & l=2n \quad (h=2n) \\
 hk0; & (h=2n) \\
 h00; & (h=2n) \\
 0k0; & (k=2n) \\
 00l; & (l=2n)
 \end{array}
 \tag{108}$$

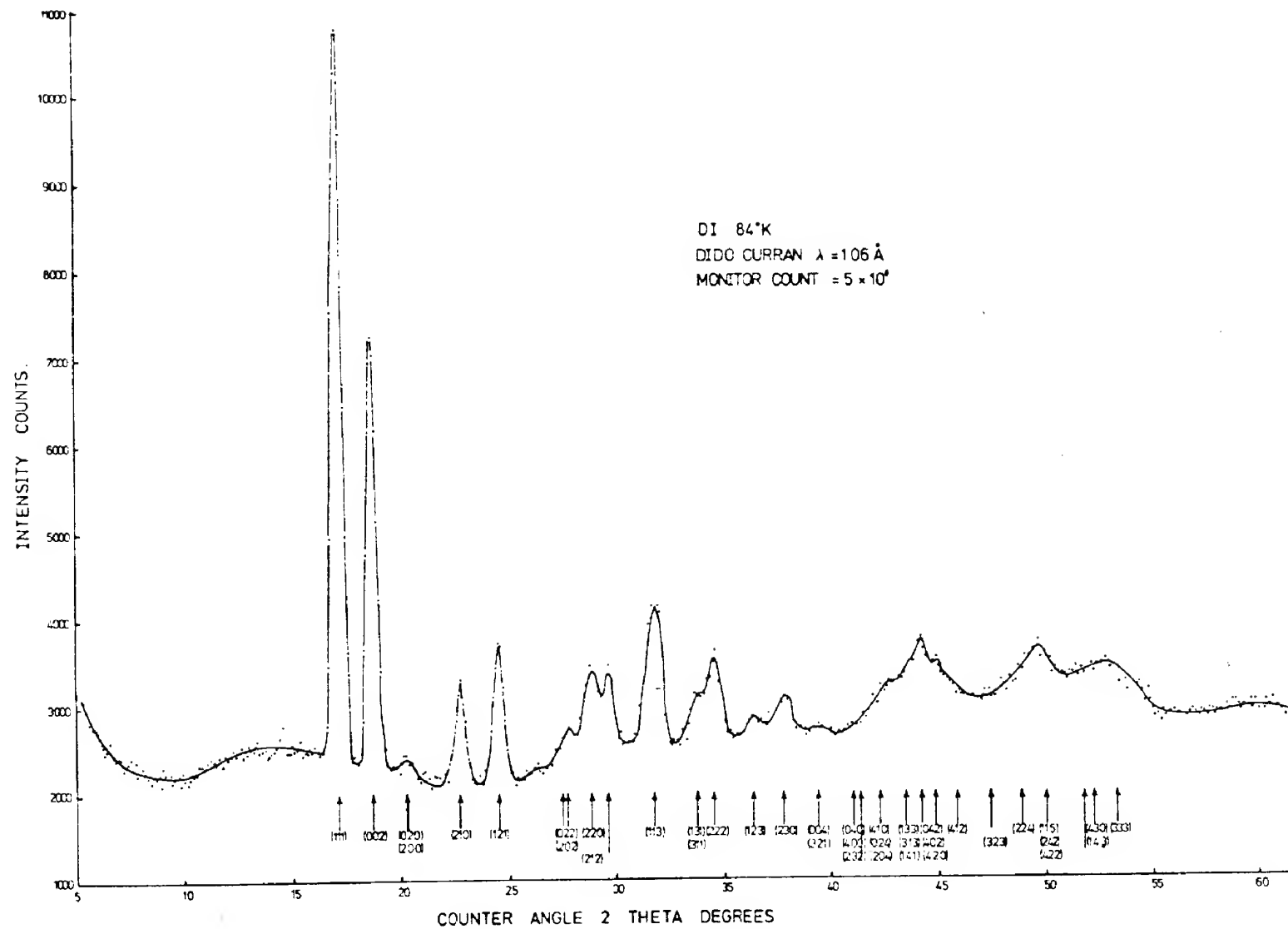


Figure 5.1 Neutron powder diffraction pattern of DI at 84K (middle phase) recorded with the Dido Curran diffractometer.

These conditions indicated a B-centred lattice with an a- or c-glide in the (010) plane. Of the twelve possible space groups satisfying the above condition of B-centring, only two were compatible with the full set of absences; these were Bba2 (No.41) and Bbcm (No.64).

Since the iodine atoms were known from X-ray data to form a face-centred orthorhombic lattice, it was necessary to choose special positions for these atoms in the space groups Bba2 (No.41) and Bbcm (No.64) which would provide such a lattice ('super-special' positions). The analysis and tabulation of these positions had already been performed, Sándor (1968).

If the special positions of these space groups are considered the following sites are obtained for the deuterium atoms.

Bba2 (No.41) general position 8b (Wyckoff notation)

Bbcm (No.64) special position 8f and general position 16g.

These positions provide either eight or sixteen sites, implying that the four deuterium atoms in the unit cell occupy either two- or four-fold disordered positions. Since the recorded neutron powder diffraction pattern is a space average over all possible states of the structure it is necessary to apply weighting factors ($\frac{1}{2}$ and $\frac{1}{4}$) to the scattering lengths of the deuterium atoms occupying two- or four-fold disordered positions respectively. Three models based upon the above atomic arrangements are shown in figures 5.2 to 5.4.

Least-squares refinements using the program ORFLS (described in Appendix one) were carried out on these models with the out-of-plane iodine-deuterium bond angle held constant. It was not possible to vary the z-co-ordinate of the deuterium atoms during the least-squares refinement of

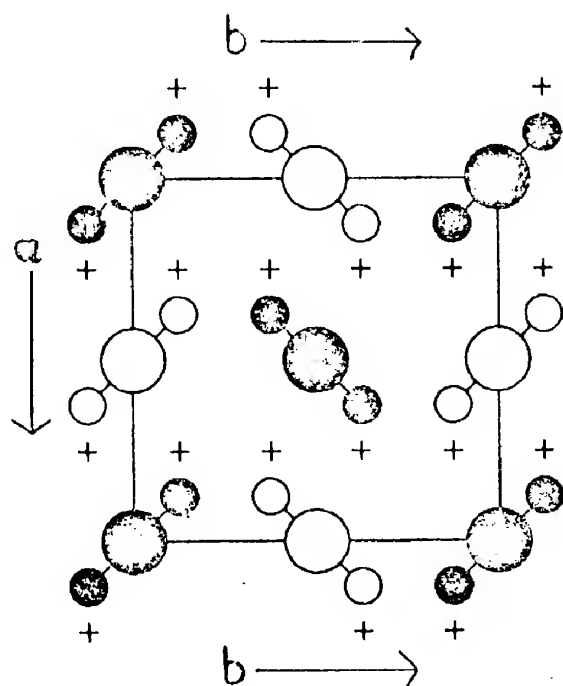


Figure 5.2 Two-fold disordered model for DI middle phase, space group Bba2 (no.41).

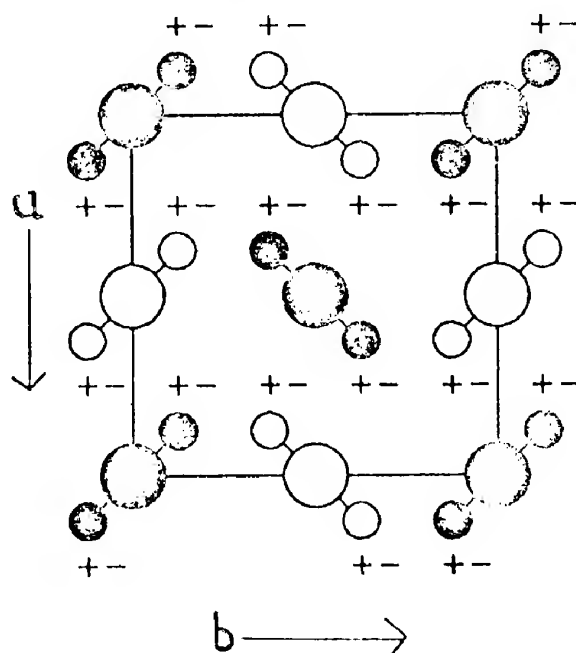


Figure 5.3 Four-fold disordered model for DI middle phase, space group Bbcm (no.64).

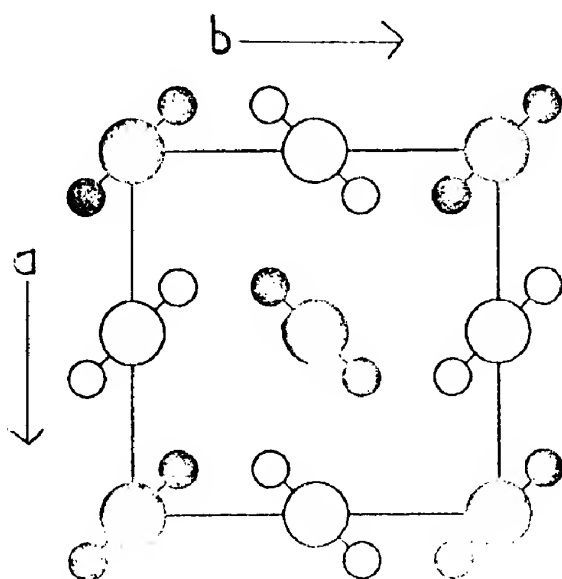


Figure 5.4 Proposed two-fold disordered model for DI middle phase, space group Bbcm (no.64).

the models shown in figures 5.2 and 5.3 as the program returned very large values for the z-co-ordinate (due probably to a singular solution of the set of normal equations). A series of refinements was therefore carried out and the out-of-plane angle increased by 5° between each refinement.

It was found that the model described by the space group Bbcm gave the lowest R-factor. The minimum R-factor occurred when the DI molecules lay in the (001) plane in which case the models become equivalent. These refinements were carried out with unit weights. Subsequently a full least-squares refinement was performed using anisotropic temperature factors and the weighting scheme proposed by Cruickshank (1953). The following parameters were varied by the program;

(a) Scale factor,

(b) For the deuterium atom;

$x, y, b_{11}, b_{22}, b_{33}$ and b_{12} ($z = 0, b_{13} = b_{23} = 0$)

(c) For the iodine atom;

b_{11}, b_{22} and b_{33} ($x=y=z=0, b_{12} = b_{23} = b_{13} = 0$)

The constraints applied to the parameters during the least-squares refinement were deduced from the theory of Levy (1956). They were due to the iodine being in a special position at the origin and to the deuterium atom lying in a mirror plane. This latter condition constrains the thermal ellipsoid tensor to be symmetrical about the (001) plane.

In addition to the atom multiplier of $(\frac{1}{4})$ applied to the deuterium atom scattering length to compensate for it being in a disordered position, a factor of $(\frac{1}{4})$ was applied to the iodine scattering length to correct for the effect of the iodine atom being in a special position (4a of space group Bbcm (No.64)).

The results of the least-squares refinement are given in table 5.1. Figures 5.5 and 5.6 show histograms of the observed intensities and those calculated. It was found that if the b_{11} and b_{22} parameters of iodine were allowed to vary simultaneously the fitted values of these two parameters were correlated. Two independent refinements were therefore performed to obtain values of these parameters.

DI middle phase at 84KLattice parameters

$$a = 5.979 \pm .007 \text{ \AA}$$

$$b = 6.024 \pm .007 \text{ \AA}$$

$$c = 6.517 \pm .009 \text{ \AA}$$

$$\alpha = \beta = \gamma = 90^\circ$$

Space group Bbcm (No.64); number of molecules in the unit cell is 4.

Co-ordinates of 8f special position in space group Bbcm (No.64) (centro-symmetric)

$$\begin{array}{lll} x & y & 0 \\ x+\frac{1}{2} & y & \frac{1}{2} \\ \frac{1}{2}-x & y+\frac{1}{2} & 0 \\ -x & y+\frac{1}{2} & \frac{1}{2} \end{array} + [(0,0,0); (\frac{1}{2},0,\frac{1}{2})]$$

Parameters

Iodine atoms, positional parameters: $x=y=0$

$$\begin{array}{ll} \text{thermal parameters:} & \left. \begin{array}{l} b_{11} = .025 \pm .002 \\ b_{22} = .033 \pm .002 \\ b_{33} = .030 \pm .0007 \\ b_{12} = b_{23} = b_{13} = 0 \end{array} \right\} \begin{array}{l} \text{determined independently} \\ \text{due to correlation} \end{array} \end{array}$$

scattering length: 5.2 fm.

Deuterium atoms, positional parameters: $x = -.171 \pm .001$

$$y = .169 \pm .001$$

$$z = 0$$

$$\begin{array}{ll} \text{thermal parameters:} & \begin{array}{l} b_{11} = .056 \pm .001 \\ b_{22} = .039 \pm .0015 \\ b_{33} = .044 \pm .001 \\ b_{12} = .007 \pm .002 \\ b_{23} = b_{13} = 0 \end{array} \end{array}$$

scattering length: 6.7 fm.

Unit weight R-factor = 6.7%

Weighted R-factor = 1.3%

Refinement carried out over 5 cycles on intensities

Bond length (uncorrected) = $1.44 \pm .01 \text{ \AA}$

Bond length (corrected for librational effect) = $1.49 \pm .01 \text{ \AA}$ (Cruickshank 1956)

TABLE 5.1 Structural parameters of DI at 84K (middle phase)

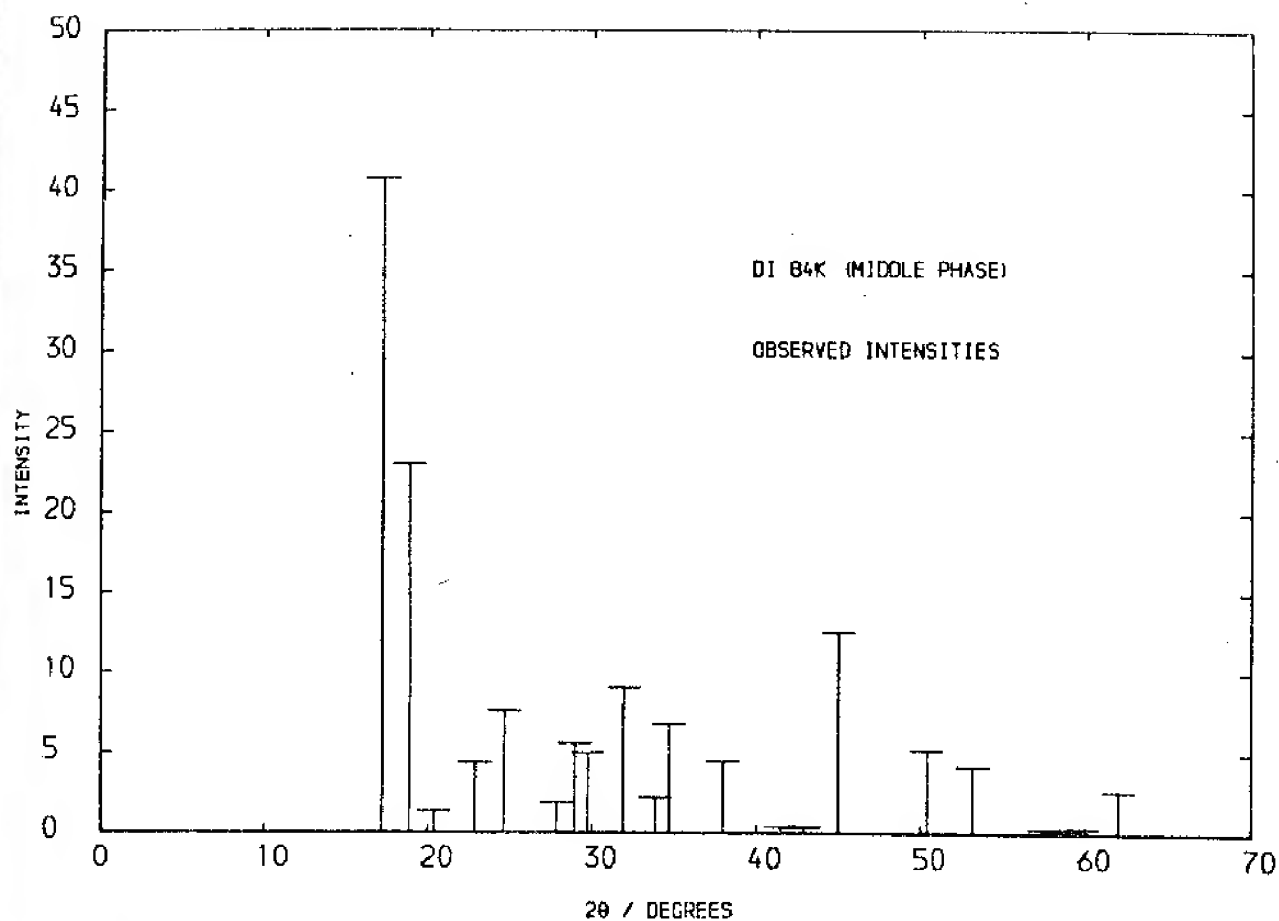


Figure 5.5 Observed intensities of neutron powder peaks for DI middle phase recorded at 84K with Dido Curran.

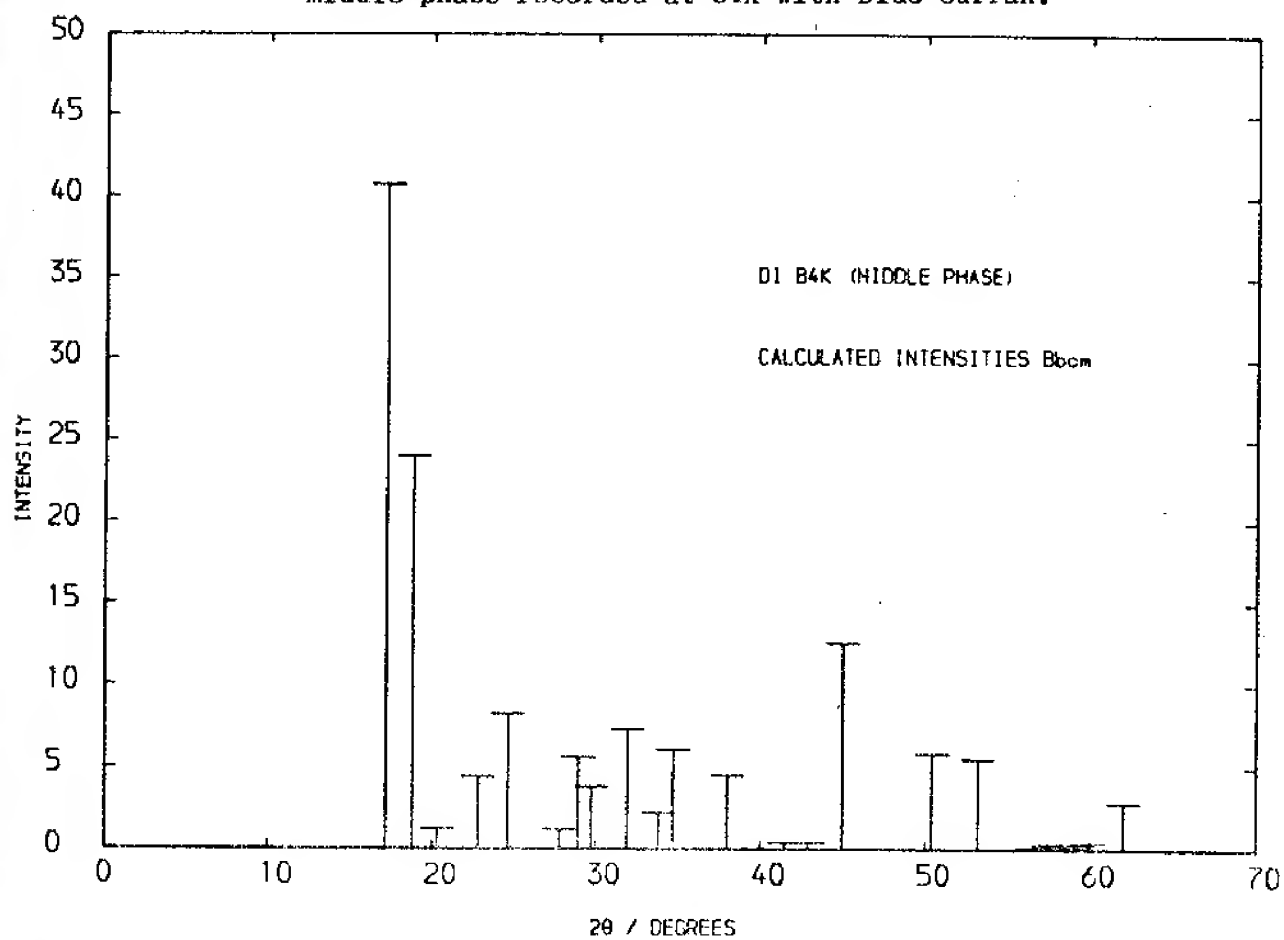


Figure 5.6 Calculated intensities of neutron powder peaks for two-fold disordered model of DI middle phase, space group Bbcm (no.64).

CHAPTER SIX

Neutron powder diffraction study of the crystal structure of the high phase of DI

The neutron powder diffraction pattern of the high phase of DI was recorded with the Dido 'Curran' diffractometer as described in section 2.3a. The sample was contained in a vanadium cryostat as in the middle phase experiments (chapter five) and maintained at a temperature of 137K by a low power electrical heater. The emf from a thermocouple mounted on the sample was monitored by a chart-recorder which controlled the power to the electrical heater by means of a microswitch.

The neutron powder diffraction pattern of the high phase of DI recorded at 137K is shown in figure 6.1. Using the lattice parameters derived from the X-ray powder photographs (see table 3.1), the neutron powder peaks were assigned Miller indices on the basis of a cubic unit cell containing four molecules. The systematic absences in the Miller indices were:

$$hkl: h+k, k+l, (l+h) = 2n \quad (109)$$

indicating an fcc lattice.

There are eleven face-centred cubic space groups of which five are compatible with these absences.

$F23$ (No.196), $Fm3$ (No.202), $F432$ (No.209), $F\bar{4}3m$ (No.216) and $Fm3m$ (No.225).

An ordered cubic high phase based on the space group $Fm3m$ can be easily disregarded. Since there are four molecules per unit cell, in an ordered

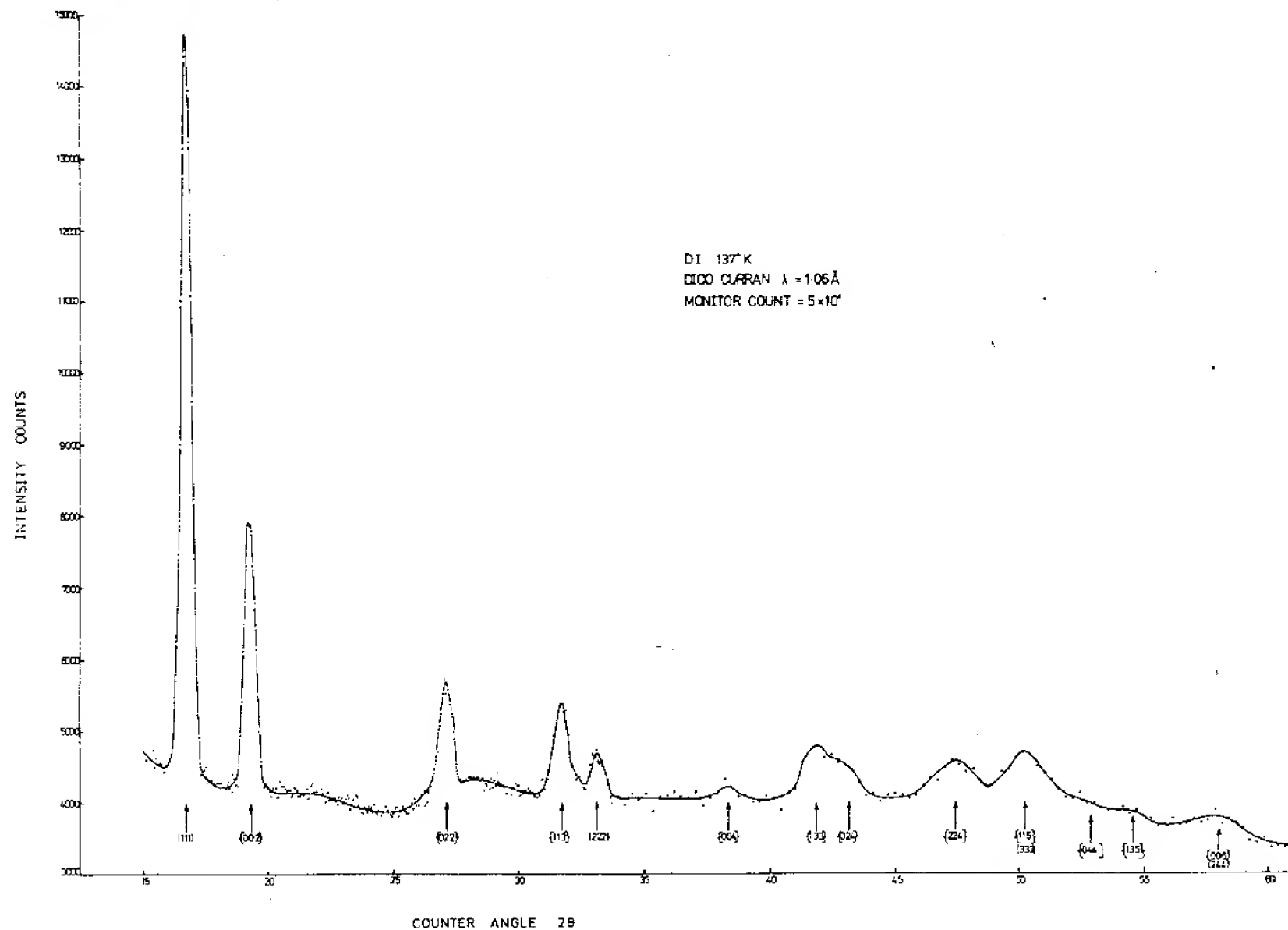


Figure 6.1 Neutron powder diffraction pattern of DI at 137K (high phase)
recorded with the Dido Curran diffractometer.

structure the deuterium atoms must occupy four-fold special positions. This condition leads to two possible models.

6.1 Zinc sulphide-type model space group $Fm\bar{3}m$ (No.225)

Iodine atoms in special position 4a (Wyckoff notation).

$(0,0,0)$, $(0,\frac{1}{2},\frac{1}{2})$, $(\frac{1}{2},0,\frac{1}{2})$, $(\frac{1}{2},\frac{1}{2},0)$

Deuterium atoms in special position 4c (Wyckoff notation).

$(\frac{1}{4},\frac{1}{4},\frac{1}{4})$, $(\frac{1}{4},\frac{3}{4},\frac{3}{4})$, $(\frac{3}{4},\frac{1}{4},\frac{3}{4})$, $(\frac{3}{4},\frac{3}{4},\frac{1}{4})$

This gives a D-I bond length of 2.82\AA .

6.2 Sodium chloride-type model space group $Fm\bar{3}m$ (No.225)

Iodine atoms in special position 4a (Wyckoff notation).

$(0,0,0)$, $(0,\frac{1}{2},\frac{1}{2})$, $(\frac{1}{2},0,\frac{1}{2})$, $(\frac{1}{2},\frac{1}{2},0)$

Deuterium atoms in special position 4b (Wyckoff notation).

$(\frac{1}{2},\frac{1}{2},\frac{1}{2})$, $(\frac{1}{2},0,0)$, $(0,\frac{1}{2},0)$, $(0,0,\frac{1}{2})$

This gives a D-I bond length of 5.65\AA .

In the gas phase the D-I bond length was found to be 1.609\AA from microwave measurements by Cowan and Gordy (1958) and in the middle phase it was found to be 1.49\AA from neutron diffraction measurements (Chapter five). Since these two models give unacceptable values for the D-I bond length they can be disregarded. Examination of the symmetry operations of the five space groups listed earlier shows that there are special positions of these space groups which describe disordered structures. Four of these will be discussed and the special case of a freely-rotating or randomly disordered model. As some of these space groups contain the lower symmetry groups as sub-groups, the special positions of the disordered structures will be described in terms of the highest symmetry space groups; $Fm\bar{3}$ (No.202), $F\bar{4}3m$ (No.216) and $Fm\bar{3}m$ (No.225).

6.3 Four-fold disordered model space group $F\bar{4}3m$ (No.216)

Iodine atoms in special position $4a$ (Wyckoff notation).

$$(0,0,0), (0,\frac{1}{2},\frac{1}{2}), (\frac{1}{2},0,\frac{1}{2}), (\frac{1}{2},\frac{1}{2},0)$$

Deuterium atoms in special position $16e$ (Wyckoff notation).

$$(x,x,x), (x,\bar{x},\bar{x}), (\bar{x},x,\bar{x}), (\bar{x},\bar{x},x)$$

$$+ [(0,0,0); (0,\frac{1}{2},\frac{1}{2}); (\frac{1}{2},0,\frac{1}{2}); (\frac{1}{2},\frac{1}{2},0)]$$

6.4 Six-fold disordered model space group $Fm\bar{3}m$ (No.225)

Iodine atoms in special position $4a$ (Wyckoff notation).

$$(0,0,0), (0,\frac{1}{2},\frac{1}{2}), (\frac{1}{2},0,\frac{1}{2}), (\frac{1}{2},\frac{1}{2},0)$$

Deuterium atoms in special position $24e$ (Wyckoff notation).

$$(x,0,0), (0,x,0), (0,0,x)$$

$$(\bar{x},0,0), (0,\bar{x},0), (0,0,\bar{x})$$

$$+ [(0,0,0); (0,\frac{1}{2},\frac{1}{2}); (\frac{1}{2},0,\frac{1}{2}); (\frac{1}{2},\frac{1}{2},0)]$$

This model represents a kind of close-packed structure which would occur if the hydrogen bonds were very weak.

6.5 Eight-fold disordered model space group $Fm\bar{3}$ (No.202)

Iodine atoms in special position $4a$ (Wyckoff notation).

$$(0,0,0), (0,\frac{1}{2},\frac{1}{2}), (\frac{1}{2},0,\frac{1}{2}), (\frac{1}{2},\frac{1}{2},0)$$

Deuterium atoms in special position $32f$ (Wyckoff notation).

$$(x,x,x), (x,\bar{x},\bar{x}), (\bar{x},x,\bar{x}), (\bar{x},\bar{x},x)$$

$$(\bar{x}\bar{x}\bar{x}), (\bar{x}xx), (x\bar{x}x), (xxx)$$

$$+ [(0,0,0); (0,\frac{1}{2},\frac{1}{2}); (\frac{1}{2},0,\frac{1}{2}); (\frac{1}{2},\frac{1}{2},0)]$$

6.6 Twelve-fold disordered model space group $Fm\bar{3}m$ (No.225)

Iodine atoms in special position $4a$ (Wyckoff notation).

$$(0,0,0), (0,\frac{1}{2},\frac{1}{2}), (\frac{1}{2},0,\frac{1}{2}), (\frac{1}{2},\frac{1}{2},0)$$

Deuterium atoms in special position 48h (Wyckoff notation)

$(x, x, 0), (x, 0, x), (0, x, x)$

$(\bar{x}, x, 0), (\bar{x}, 0, x), (0, \bar{x}, x)$

$(x, \bar{x}, 0), (x, 0, \bar{x}), (0, x, \bar{x})$

$(\bar{x}, \bar{x}, 0), (\bar{x}, 0, \bar{x}), (0, \bar{x}, \bar{x})$

+ $[(0, 0, 0); (0, \frac{1}{2}, \frac{1}{2}); (\frac{1}{2}, 0, \frac{1}{2}); (\frac{1}{2}, \frac{1}{2}, 0)]$

This model represents the case when hydrogen-bonding between neighbouring iodine atoms is strong. Since each iodine atom has twelve nearest-neighbours the deuterium atom can lie along each of the twelve nearest-neighbour bonds as it 'flips' between different disordered sites.

6.7 Freely-rotating or randomly-disordered model

This model has been suggested by several workers although, as discussed in section 1.6, it is shown to be unlikely. Since the neutron diffraction pattern records an average structure over space and time the two forms of the model, freely-rotating or randomly-disordered, cannot be distinguished (by neutron diffraction) and are described by the same mathematical expressions. A set of structure factors was calculated by the following method.

The position of the deuterium atom relative to the iodine atom was described by a Gaussian radial distribution function, $p(r)$;

$$p(r)dr = \frac{\exp}{Z} \left[-\frac{(r-l)^2}{2\sigma^2} \right] dr \quad (110)$$

where r is the distance of the deuterium atom from the iodine atom, l is the mean intramolecular bond length, σ is the width of the Gaussian and represents the mean amplitude of vibration along the bond and Z is a normalising constant.

The mean bond length of the molecule I was taken to be 1.49\AA and the half-width of the Gaussian σ was taken as 0.08\AA , the mean vibrational amplitude of the deuterium atom calculated from spectroscopic data. The normalizing constant Z was calculated from the equation:

$$Z = \int_0^{\infty} 4\pi r^2 \exp\left[-\frac{(r-1)^2}{2\sigma^2}\right] dr \quad (111)$$

The structure factor was given by the expression:

$$F'(hkl) = 4b_I \exp\left(-\frac{8\sin^2\theta}{\lambda^2}\right) + 4b_D \int_0^{\infty} \frac{4\pi r^2 \rho(r) \sin\left(\frac{4\pi r \sin\theta}{\lambda}\right)}{\left(\frac{4\pi r \sin\theta}{\lambda}\right)} dr \quad (112)$$

This expression was evaluated and integrated numerically using Simpson's rule.

6.8 Comparison of observed structure factors with structure factors calculated from disordered models

Projections of the seven models described above onto the (001) plane are shown in figures 6.2 to 6.8. Solid circles indicate atoms at $z = 0$ and open circles atoms at $z = \frac{1}{2}$. Histograms of calculated structure factors are shown in figures 6.9 to 6.13. The structure factors $F'(hkl)$ contain the expression for thermal motion and are defined in chapter three equation (30). In the histogram of the observed structure factors shown in figure 6.14 there are three places where the observed structure factor as a function of 2θ deviates appreciably from a monotonically decreasing function. In particular these are:

$$F'(222) > F'(113)$$

$$F'(133) > F'(004)$$

$$F'(224) > F'(024)$$

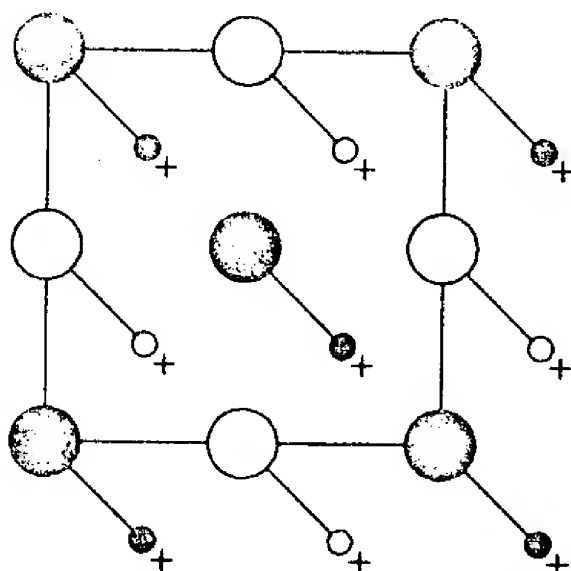


Figure 6.2 Zinc sulphide
model for DI high phase,
space group $Fm\bar{3}m$ (no. 225)

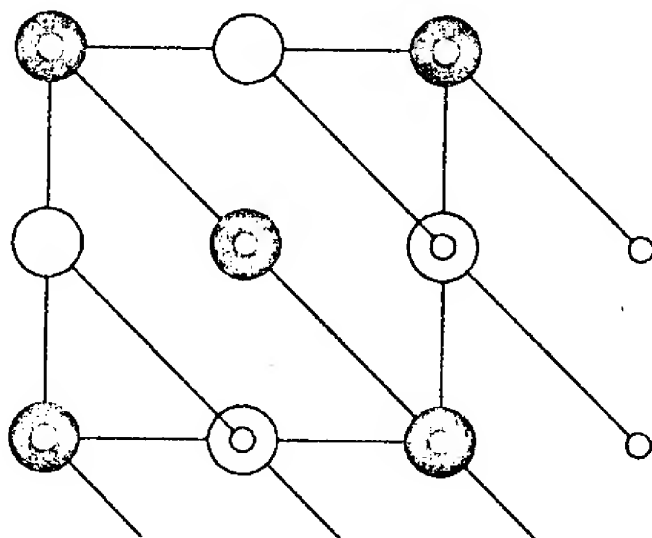


Figure 6.3 Sodium
chloride model for
DI high phase, space
group $Fm\bar{3}m$ (no. 225)

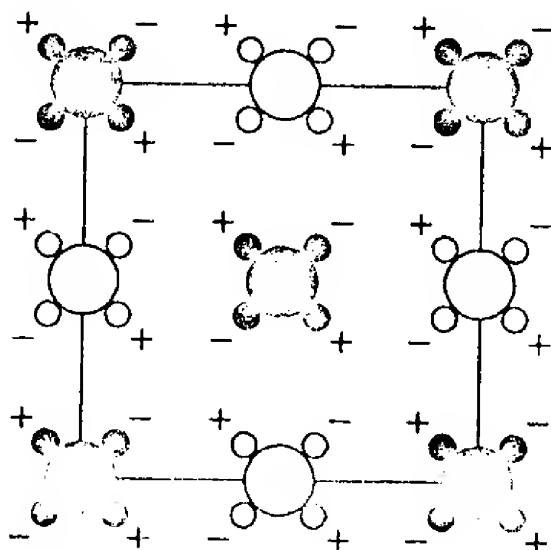


Figure 6.4 Four-fold
disordered model for DI
high phase, space group
 $F\bar{4}3m$ (no. 216).

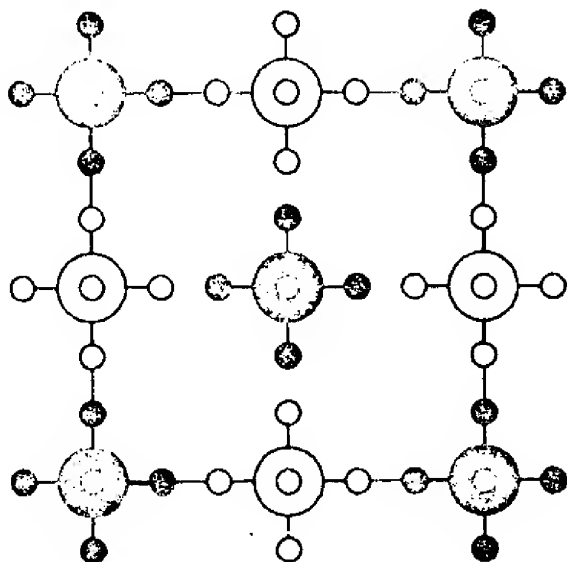


Figure 6.5 Six-fold disordered model for DI high phase, space group $Fm\bar{3}m$ (no. 225).

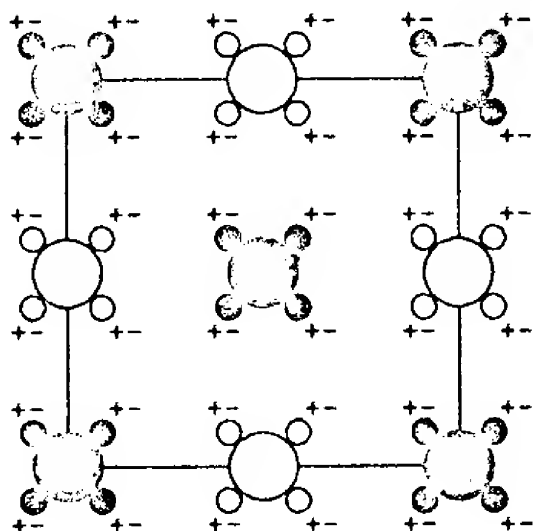


Figure 6.6 Eight-fold disordered model for DI high phase, space group $Fm\bar{3}$ (no. 202).

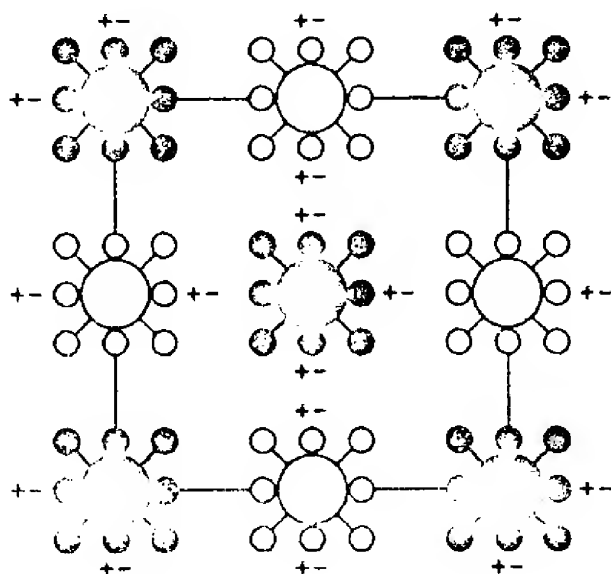


Figure 6.7 Twelve-fold disordered model for DI high phase, space group $Fm\bar{3}m$ (no. 225).

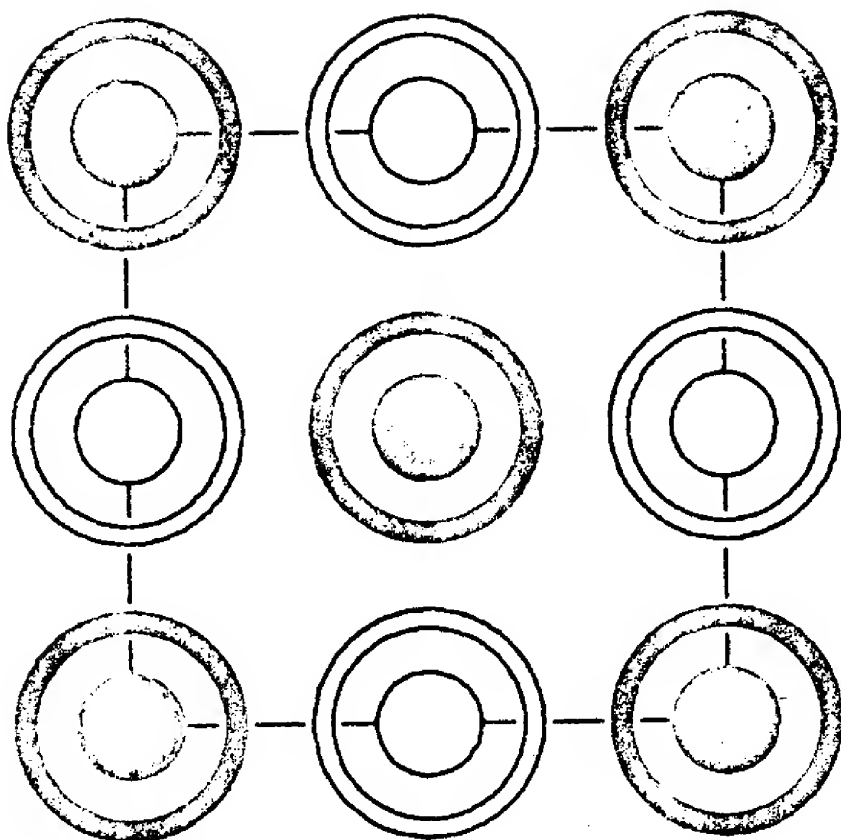


Figure 6.8 Freely-rotating
model for DI high phase.

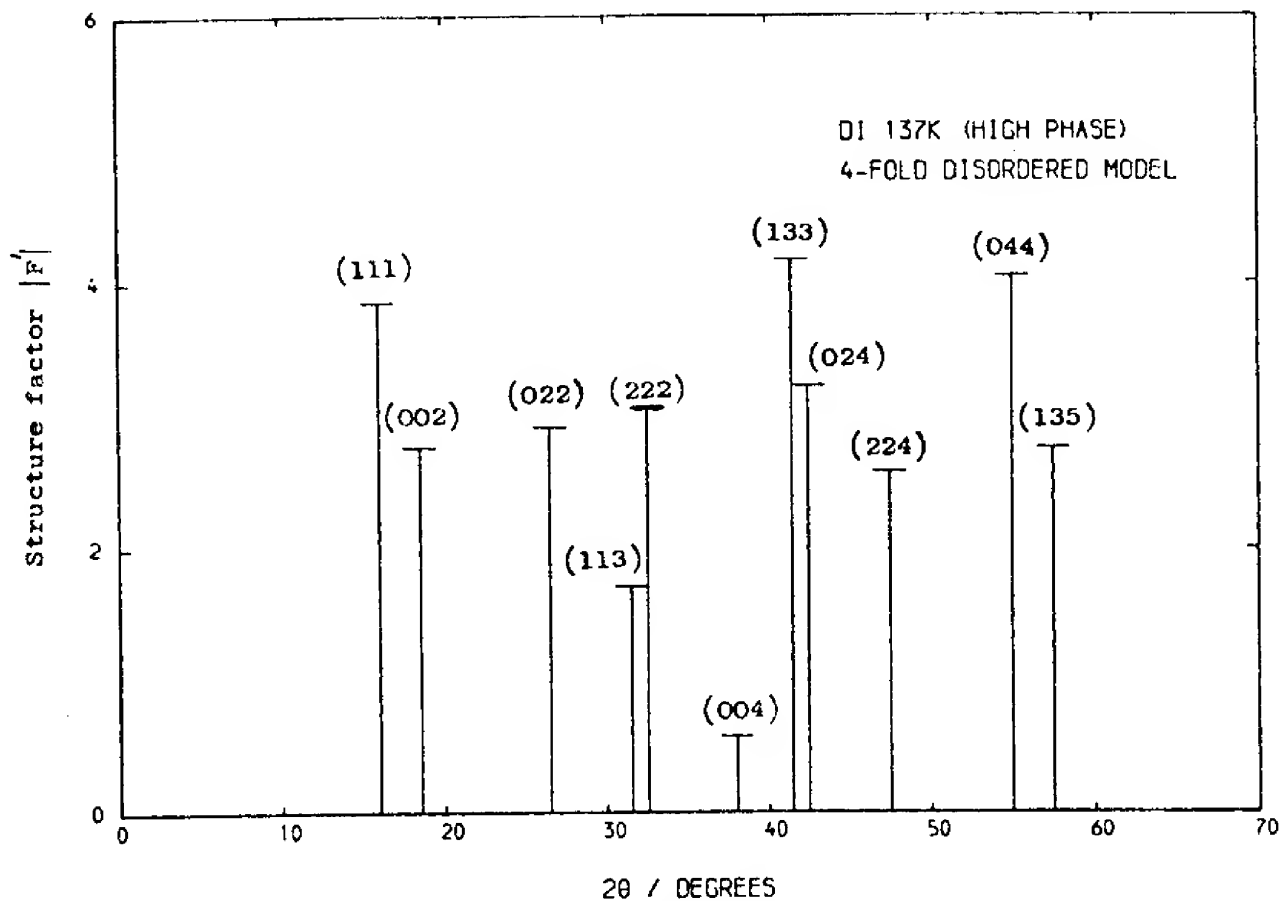


Figure 6.9 Calculated structure factors for four-fold disordered model of DI high phase, space group $F\bar{4}3m$ (no. 216).

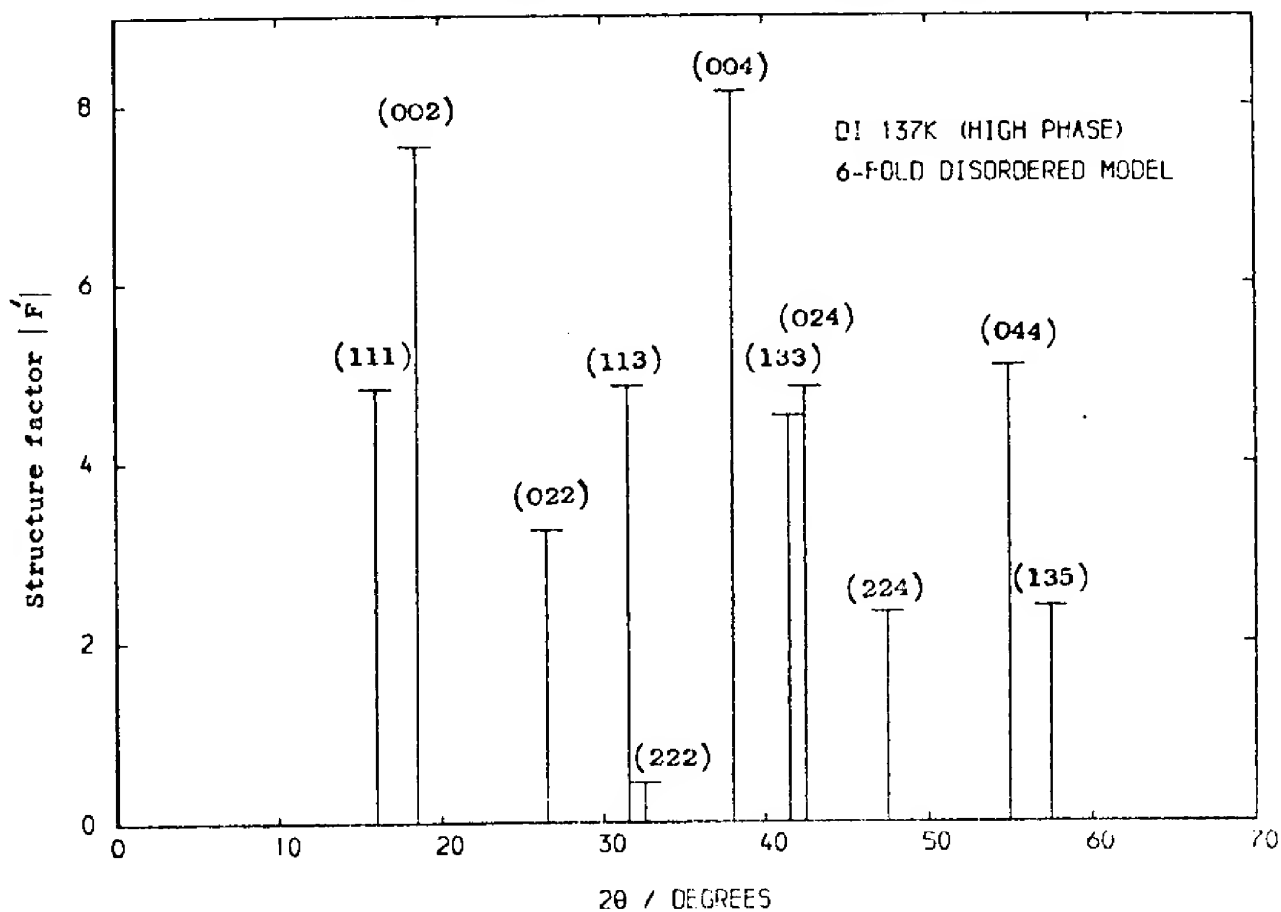


Figure 6.10 Calculated structure factors for six-fold disordered model of DI high phase, space group $Fm\bar{3}m$ (no. 225).

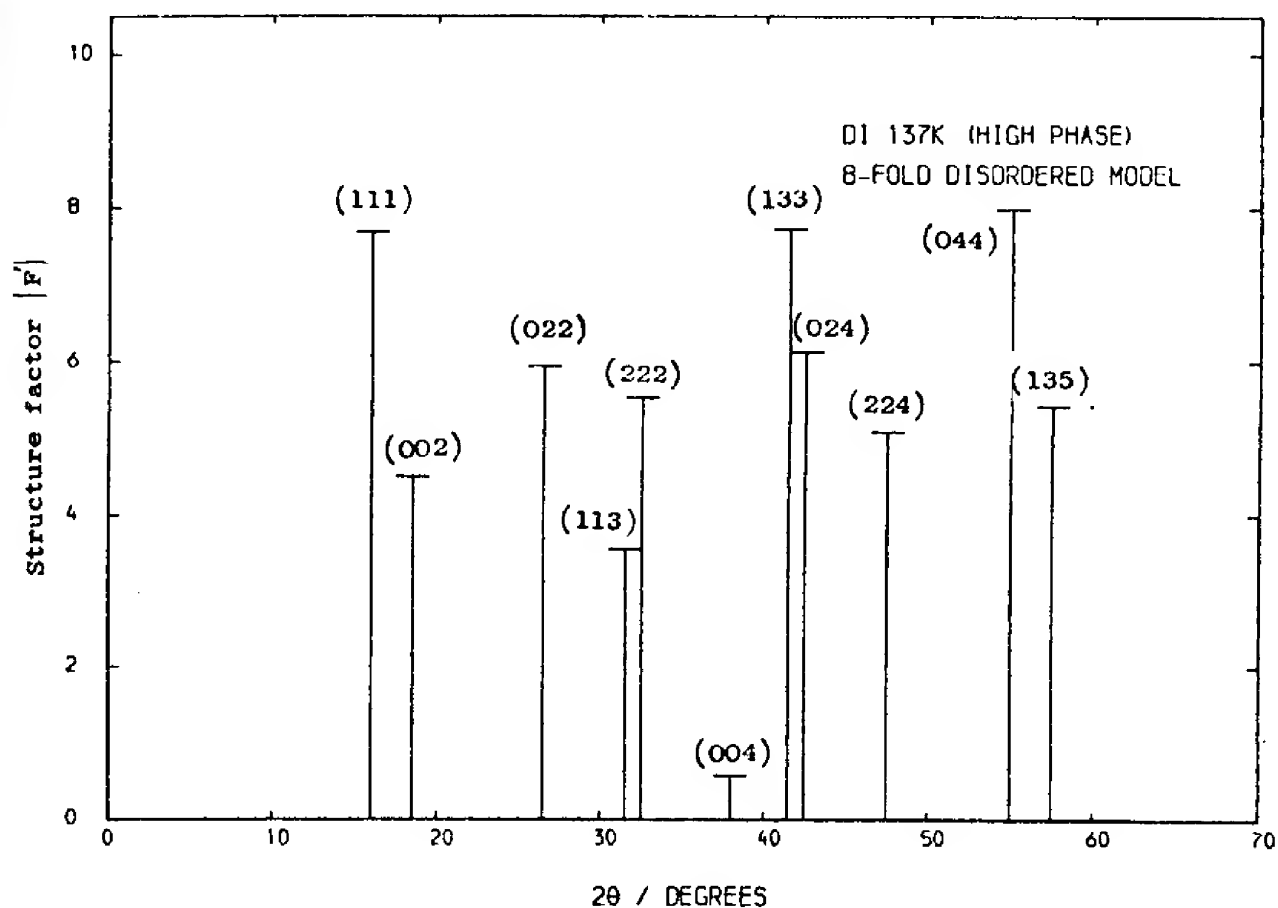


Figure 6.11 Calculated structure factors for eight-fold disordered model of DI high phase, space group $Fm\bar{3}$ (no. 202).

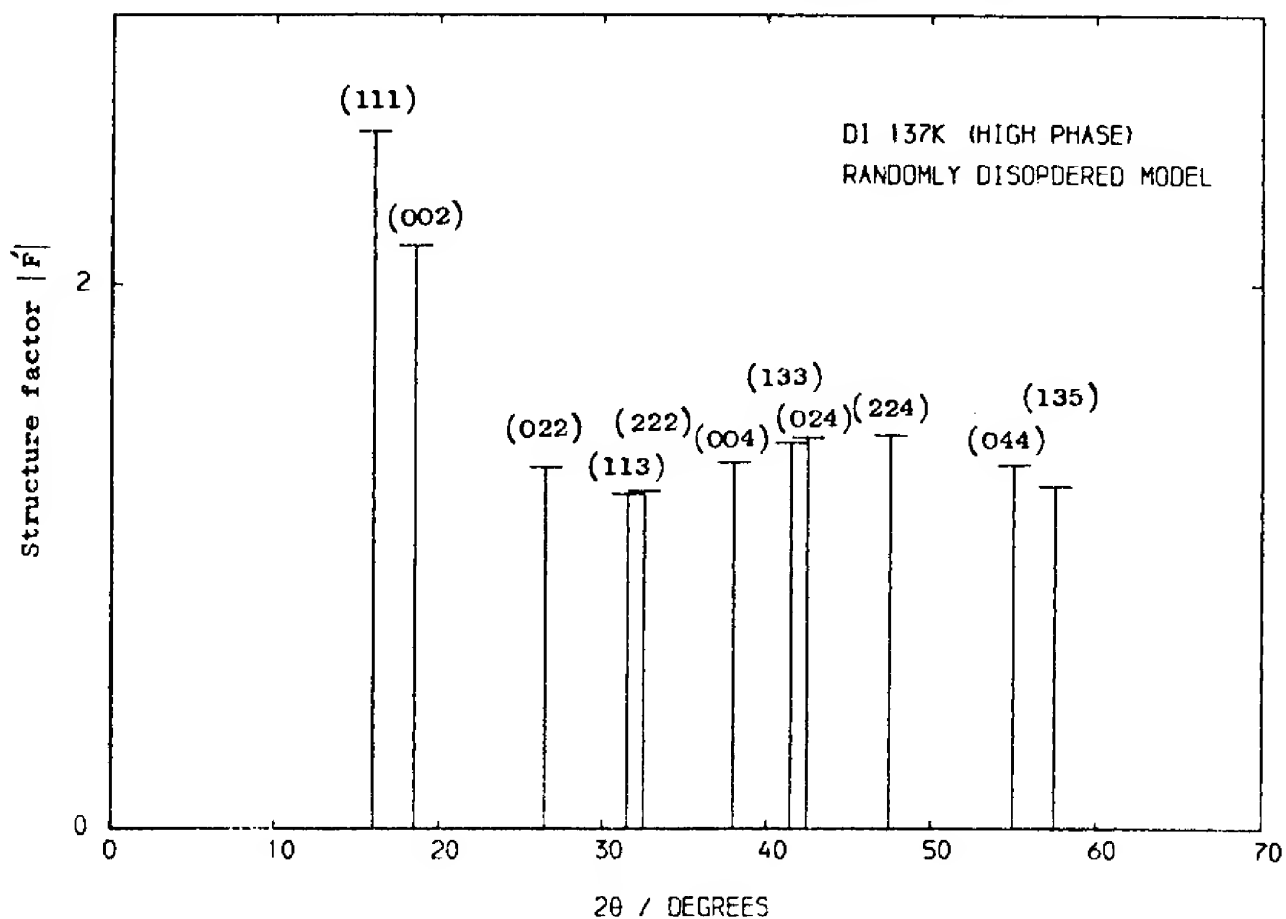


Figure 6.12 Calculated structure factors for freely-rotating model of DI high phase.

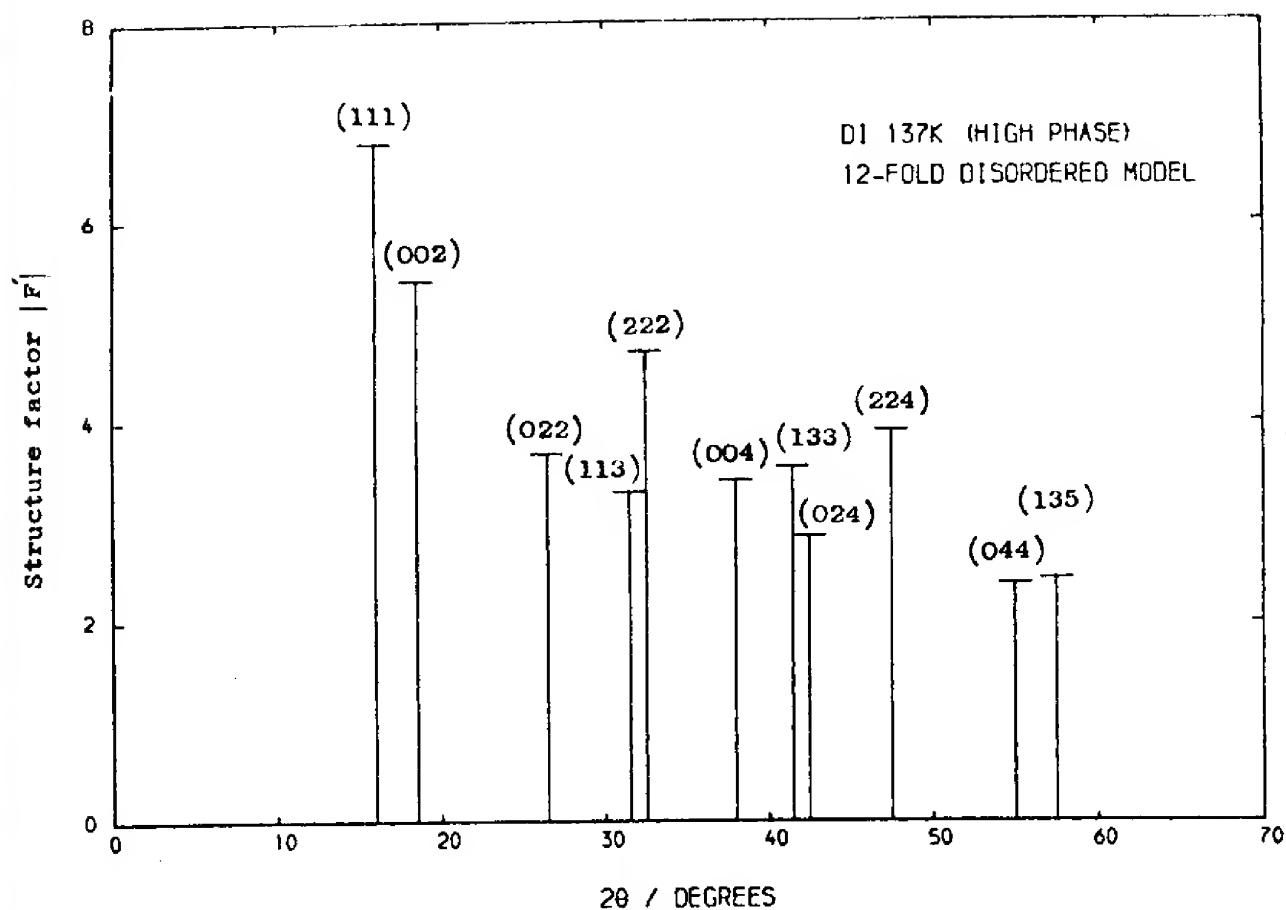


Figure 6.13 Calculated structure factors for twelve-fold disordered model of DI high phase, space group $Fm\bar{3}m$ (no. 225).

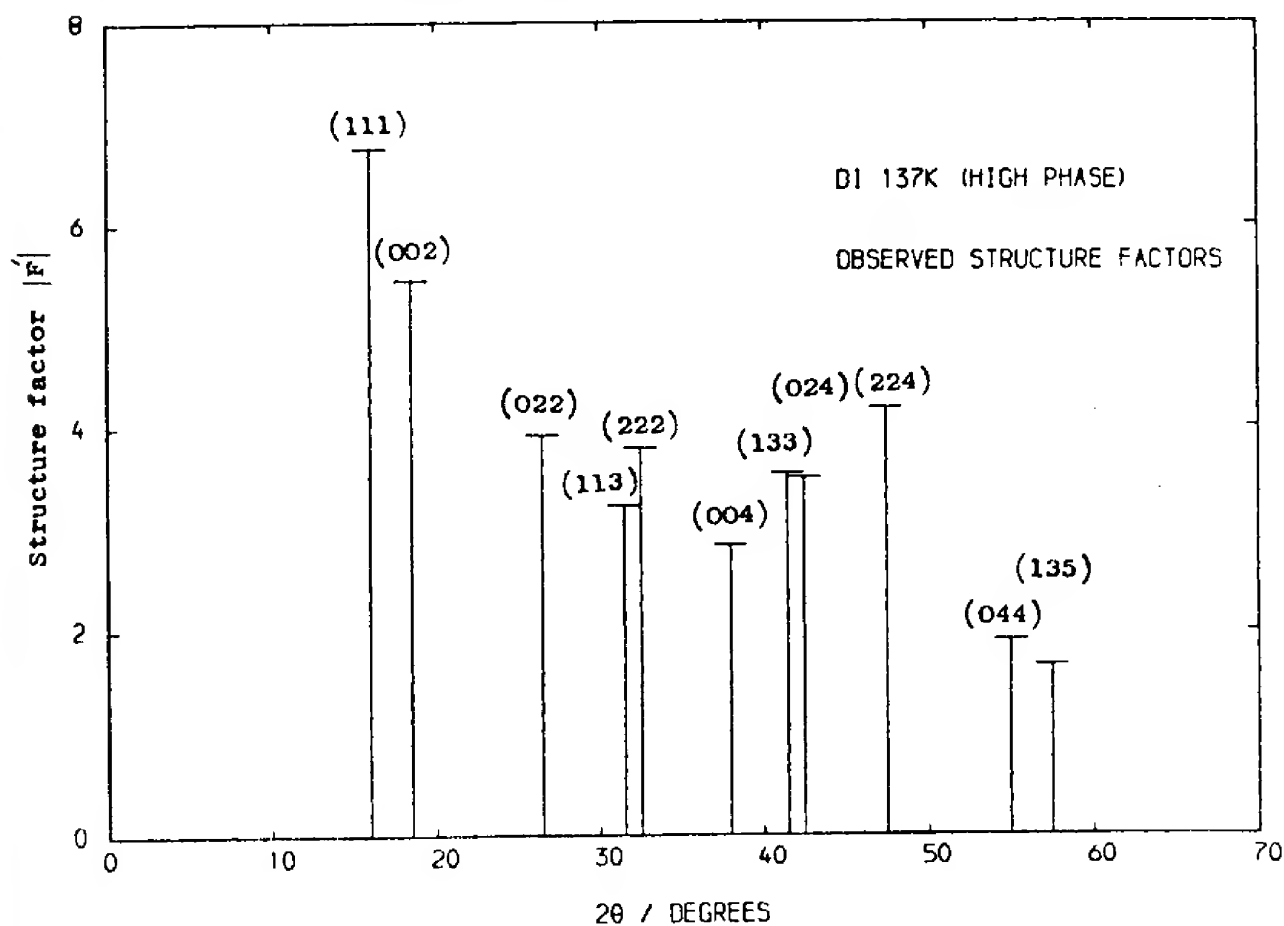


Figure 6.14 Observed and normalized structure factors for DI high phase recorded on Dido Curran at 137K.

These relationships also appear in the histogram calculated on the basis of the twelve-fold disordered model (see figures 6.7 and 6.14) but are absent in the histogram calculated on the basis of the randomly-disordered model (see figures 6.8 and 6.12) which shows an angular variation of intensity of a type normally associated with an amorphous material. Least-squares refinements were carried out on all but the last of the disordered models using peak intensities with unit weights as data. The results are shown in Table 6.1.

Model	Unit-weight R-factor (intensity)
4-fold	15.9%
6-fold	36.8%
8-fold	15.8%
12-fold	11%

TABLE 6.1. R-factors obtained in the least-squares refinement of four disordered models proposed for the high phase of D1.

The twelve-fold disordered model gave the best fit and the results of a least-squares refinement of this model using anisotropic temperature factors are shown in table 6.2. Because the iodine and deuterium atoms were in special positions it was necessary to apply Levy's rule to derive relationships between the temperature factors (Levy 1956). The following parameters were varied during a least-squares refinement based on the diffracted intensity.

(a) Scale factor,

(b) For the deuterium atom;

$x(x=y)$, $b_{11}(b_{11}=b_{22})$, b_{33} and b_{12} ($z=0$, $b_{13}=b_{23}=0$)

(c) For the iodine atom;

$$b_{11}(b_{11}=b_{22}=b_{33}) \quad (x=y=z=0, b_{12}=b_{23}=b_{13}=0)$$

The least-squares refinement of the 12-fold disordered model appeared insensitive to the value of the parameter $b_{33}(D)$. The computer program was altered to increase the value of $b_{33}(D)$ from zero to .06 in steps of .005. This produced no change in any of the fitting or structural parameters. A refinement was also carried out using only the single peaks of the cubic pattern with the unmodified version of the ORFLS program which refined upon the structure factor $|F'|$ and not the intensity. This produced a worse fit because of the smaller number of data and also gave a singular solution when varying $b_{33}(D)$. The weighting scheme used in these calculations was the one proposed by Cruickshank (1963).

DI high phase at 137KLattice parameters

$$a = b = c = 6.285 \pm .01 \text{ \AA}$$

$$\alpha = \beta = \gamma = 90^\circ$$

Space group Fm3m (No.225); number of molecules in the unit cell is 4.

Co-ordinates of 48h special position in space group Fm3m (No.225).

$$\begin{aligned} & (x, x, 0), (x, \bar{x}, 0), (\bar{x}, x, 0), (\bar{x}, \bar{x}, 0) \\ & (x, 0, x), (x, 0, \bar{x}), (\bar{x}, 0, x), (\bar{x}, 0, \bar{x}) \\ & (0, x, x), (0, x, \bar{x}), (0, \bar{x}, x), (0, \bar{x}, \bar{x}) \\ & + [(0, 0, 0); (0, \frac{1}{2}, \frac{1}{2}); (\frac{1}{2}, 0, \frac{1}{2}); (\frac{1}{2}, \frac{1}{2}, 0)] \end{aligned}$$

Parameters

Iodine atoms, positional parameters: $x = y = z = 0$

$$\text{thermal parameters: } b_{11} = b_{22} = b_{33} = .0177 \pm .0002$$

$$b_{12} = b_{23} = b_{13} = 0$$

$$\text{scattering length: } 5.2 \text{ fm.}$$

Deuterium atoms, positional parameters: $x = y = .1578 \pm .0002$

$$z = 0$$

$$\text{thermal parameters: } b_{11} = b_{22} = .0469 \pm .0001$$

$$b_{33} > .01$$

$$b_{12} = -.0289 \pm .0006$$

$$b_{13} = b_{23} = 0$$

$$\text{scattering length: } 6.7 \text{ fm.}$$

$$\text{Unit weight R-factor} = 6.3\%$$

$$\text{Weighted R-factor} = 0.1\%$$

$$\text{Bond length (uncorrected)} = 1.42 \text{ \AA}$$

TABLE 6.2. Structural parameters of DI at 137K (high phase)

CHAPTER SEVEN

Neutron powder diffraction study of the two phase transitions in solid D1

7.1 The lower phase transition

The analysis of the neutron powder diffraction experiments described in the preceding chapters revealed that the crystal structure of D1 is ordered monoclinic at 4.2K (low phase) and two-fold disordered orthorhombic at 84K (middle phase). The specific heat measurements of Clusius and Wolf (1947) (see Chapter One) suggest that the transition from the low phase to the middle phase is a gradual one extending over a temperature range of 45-80K. The progress of this transition can be followed by recording the gradual disappearance of the $(110, 11\bar{1})$ powder peak of unit cell No.4 which appears only in the low phase. Hereafter all monoclinic Miller indices refer to unit cell No.4.

To compensate for any variation in the measuring system with time (such as sample movement while filling the cryostat with liquid helium or change in the neutron detection efficiency) the recording was extended to a nearby 'reference' powder peak, whose intensity did not change appreciably over the transition region. The most convenient choice for the reference peak appeared to be the $(220, 22\bar{2})$ powder peak, which at the time of the phase transition experiment was thought to be a single peak. Subsequent experiments with higher angular resolution showed that this peak also contained contributions from the $(31\bar{2}, 31\bar{1})$ and $(130, 13\bar{1})$ powder peaks which appear only in the low phase. This contribution was rather small to have any appreciable effect on the results. The geometrical structure factor for the proposed model of the low phase (see figure 4.19) is;

$$F(hkl) = -8\sin 2\pi(hx+lz)\sin 2\pi ky \quad (h+k=2n, l=2n+1) \quad (113)$$

$$F(hkl) = 8\cos 2\pi(hx+lz)\cos 2\pi ky \quad (h+k=2n, l=2n) \quad (114)$$

Since the observed neutron powder diffraction pattern is a time average taken over the whole sample, the molecules are "seen" by the neutrons in all permissible equilibrium orientations. If the fractional number of deuterium atoms in the 180° "flipped" position at temperature T is denoted by $p(T)$, statistically averaged intensities of the low phase and reference peaks scanned over the lower transition region can be written in the form:

$$F_T^2(11\bar{1}) + F_T^2(110) = 64 b_D^2 [1-2p(T)]^2 [\sin^2 2\pi(x+y) + \sin^2 2\pi(x-y)] \quad (115)$$

$$F_T^2(31\bar{2}) + F_T^2(31\bar{1}) + F_T^2(13\bar{1}) + F_T^2(130) =$$

$$64 b_D^2 [1-2p(T)]^2 [\sin^2 2\pi(3x-y) + \sin^2 2\pi(3x+y) + 2\sin^2 2\pi(x-3y)] \quad (116)$$

$$F_T^2(220) + F_T^2(22\bar{2}) = 512 [b_I + b_D \cos 4\pi x \cos 4\pi y]^2 \quad (117)$$

where b_I and b_D are the iodine and deuterium thermal neutron coherent scattering lengths.

To simplify the above expressions the origin of the lattice has been moved to an iodine atom so that the two equilibrium positions of the deuterium atoms in the middle phase are at $(x, y, 0)$ and $(\bar{x}, \bar{y}, 0)$. The deuterium temperature factors were assumed to be equal in both orientations of the molecule.

The fraction $p(T)$ increases from zero in the ordered low phase to 0.5 in the two-fold disordered middle phase. In analysing the results it will be convenient to use a new function $q(T)$ defined as:

$$q(T) = 1-2p(T) = \sqrt{\frac{[F_T^2(110) + F_T^2(11\bar{1})]_{\text{observed}}}{[F_T^2(110) + F_T^2(11\bar{1})]_{\text{ordered}}}} \quad (118)$$

Because of the gradual nature of the phase transition, it is not possible to measure $F_T^2(hkl)_{\text{ordered}}$ directly over the transition region. Nevertheless, an approximation to equation (118) can be made by assuming that the following ratio is constant over the temperature range studied;

$$R(T)_{\text{ordered}} = \sqrt{\frac{[F_T^2(110) + F_T^2(11\bar{1})]_{\text{ordered}}}{[F_T^2(220) + F_T^2(22\bar{2})]_{\text{ordered}}}} \quad (119)$$

This approximation is acceptable for the following reasons;

a) The Lorentz-factor ratio $R_L(T)$ changes as the lattice parameters increase with temperature:

$$R_L(T) = \frac{\sin\theta_T(11\bar{1})\sin 2\theta_T(11\bar{1})}{\sin\theta_T(22\bar{2})\sin 2\theta_T(22\bar{2})} = \frac{\sin\theta_T(110)\sin 2\theta_T(110)}{\sin\theta_T(220)\sin 2\theta_T(220)} \quad (120)$$

This change is very slight since at all temperatures in the low phase:

$$2\sin\theta_T(11\bar{1}) = 2\sin\theta_T(110) = \sin\theta_T(22\bar{2}) = \sin\theta_T(220) \quad (121)$$

so that from figure 3.5, $R_L(4) = .389$ and $R_L(75) = .388$.

b) The ratio of the isotropic temperature factors for the two peaks $R_T(T)$ where:

$$R_T(T) = \frac{\exp[-B\sin^2\theta_T(11\bar{1})]}{\exp[-B\sin^2\theta_T(22\bar{2})]} = \frac{\exp[-B\sin^2\theta_T(110)]}{\exp[-B\sin^2\theta_T(220)]} \quad (122)$$

using equation (121)

$$R_T(T) = \exp[B\sin^2\theta_T(11\bar{1})] = \exp[B\sin^2\theta_T(110)] \quad (123)$$

changes very slightly over the temperature region investigated. At 4.2K

this ratio is 1.009 and at 84K is 1.025 representing a $2\frac{1}{2}\%$ change which is small compared with the standard deviations of the measured ratios.

According to equations (115) and (116), the structure factors of the Bragg reflections; $(110, 11\bar{1})$, $(31\bar{2}, 31\bar{1})$ and $(130, 13\bar{1})$ are proportional to $[1-2p(T)]$. The $(220, 22\bar{2})$ structure factor is an even function of x and y and is unchanged by the 'flipping' of the DI molecules. The ratio of peak intensities,

$$R_1(T) = \frac{I(110+11\bar{1})}{I(220+22\bar{2}+31\bar{2}+31\bar{1}+130+13\bar{1})} \quad (124)$$

was recorded at different temperatures over the lower transition region using the Dido 'Curran' diffractometer.

At 4.2K the structure was assumed to be ordered, i.e. $p(T)$ was zero. At this temperature the relative peak intensities of the $I(110+11\bar{1})$ and $I(31\bar{2}+31\bar{1}+130+13\bar{1})$ powder peaks were measured using the better angular resolution available with the Pluto 'Panda' diffractometer using a neutron wavelength of 2.66\AA . It was assumed that the ratio of the peak intensities did not vary with temperature in the low phase, so that if;

$$r(\lambda_1) = \frac{I(31\bar{2}+31\bar{1}+130+13\bar{1})}{I(110+11\bar{1})} \quad (125)$$

Is measured at 4.2K with neutrons of $2.66\text{\AA}(\lambda_1)$, then for the Dido 'Curran' diffractometer at $1.06\text{\AA}(\lambda_2)$ this ratio when corrected for the Lorentz-factor is;

$$r(\lambda_2) = r(\lambda_1) \sqrt{\frac{[4d^2(110) - \lambda_1^2][4d^2(312) - \lambda_2^2]}{[4d^2(110) - \lambda_2^2][4d^2(312) - \lambda_1^2]}} \quad (126)$$

where $d(110)$ etc. are the lattice spacings for these reflections.

The ratio;

$$R(T) = \sqrt{\frac{[I(110) + I(11\bar{1})]_{\text{observed}}}{[I(220) + I(22\bar{2})]_{\text{observed}}}} \quad (127)$$

can be calculated from the observed intensity ratio $R_1(T)$ equation (124) and $r(1.06)$ equation (126) as follows;

$$R(T) = \sqrt{\frac{R_1(T)}{1 - R_1(T) r(1.06)}} \quad (128)$$

Comparing equation (127) with (119) and (118) and using the approximations discussed above we can write;

$$q(T) = 1 - 2p(T) \propto R(T) \quad (129)$$

The anomalous λ -peak observed in the specific heat measurements of Clusius and Wolf (1947) over the lower phase transition (see chapter one, figure 1.1) can be attributed to the change in configurational entropy as a result of molecular re-orientation.

From the definition of specific heat used in statistical mechanics;

$$\int_{T_0}^T \frac{C_p^*(T) dT}{T} = \left[S_c \right]_{T_0}^T \quad (130)$$

T_0 is the temperature where the phase transition begins and $C_p^*(T)$ is the 'anomalous' specific heat at temperature T . The 'anomalous' specific heat is defined as the amount in excess of that due to vibrational motion (shown as a dotted line in figure 1.1).

Also;

$$S_c = k \ln \Omega \quad (131)$$

where k is the Boltzmann constant, S_c the molar configurational entropy, Ω the number of ways of distributing $p(T)N$ reversed molecules on N lattice sites and N is the Avogadro constant. It can be shown that for a two-fold disordered system in which the two equilibrium orientations are equally probable;

$$\Omega[p(T)] = \frac{N!}{\{Np(T)\}! \{N[1-p(T)]\}!} \quad (132)$$

Using Stirling's approximation for large values of N ;

$$\ln N! \approx N \ln N - N \quad (133)$$

so that

$$\int_{T_0}^T \frac{Cp^*(T)dT}{T} = -kN\{p(T)\ln p(T) + [1-p(T)]\ln[1-p(T)] - p(T_0)\ln p(T_0) - [1-p(T_0)]\ln[1-p(T_0)]\} \quad (134)$$

The ratio $R_1(T)$ and hence $R(T)$ was determined experimentally at several temperatures over the lower phase transition of DI from 45K to 80K using the 'Curran' neutron powder diffractometer shown in figures 2.6 and 2.7.

The majority of the measurements were taken at temperatures where $R_1(T)$ (the ratio of peak intensities) was expected to change appreciably. The sample was contained in a vitreous silica tube contained in a liquid helium cryostat as shown in figure 2.10. The temperature was controlled by the circuit described in Appendix two. Each measurement took approximately eight hours and after each temperature change the sample was allowed two hours to reach thermal equilibrium. Measurements were first made with

increasing temperature until the sample reached the middle phase, then with decreasing temperature going back into the low phase and finally again with increasing temperature to close the cycle with some overlap and interpolating between the earlier measurements to check the temperature measuring system for drift.

The phase transition appeared to be complete at 78K when recorded with increasing temperature, whereas the specific heat measurements indicated a transition temperature of 77.3K. This discrepancy is probably due to the radial temperature gradient in the sample used in the neutron diffraction work. Differences in the isotopic purities of the samples used in the calorimetric and diffraction studies may also have contributed to it. The radial and axial gradients were measured later as described in Appendix two and both were found to be approximately 0.5°K . A small thermal hysteresis of approximately 0.5°K was recorded. It is not possible to give a more accurate value for the width of the hysteresis due to the magnitude of the thermal gradients in the sample ($\sim 0.5^{\circ}\text{K}$).

Figure 7.1 shows the temperature dependence of the ratio $R(T)$, measured with both increasing and decreasing temperatures, and table 7.1 lists the observed peak intensities as well as the $R(T)$ ratios and the order parameters $q(T)$ derived from them. The expression for the configurational entropy equation (130) was evaluated graphically using the specific heat data of Clusius and Wolf (1947). The anomalous specific heat and the order parameters derived from these data are listed in table 7.2.

Clusius and Wolf measured the integrated heat input used in their measurement of the specific heat. This enabled values of the entropy change over the lower transition region to be calculated. Values of $p(T)$ and hence $q(T)$ were obtained from eqn.(134) by an interpolation technique.

$$\sqrt{\frac{I(110) + I(11\bar{1})}{I(220) + I(22\bar{2})}}$$

DI

LOWER PHASE TRANSITION

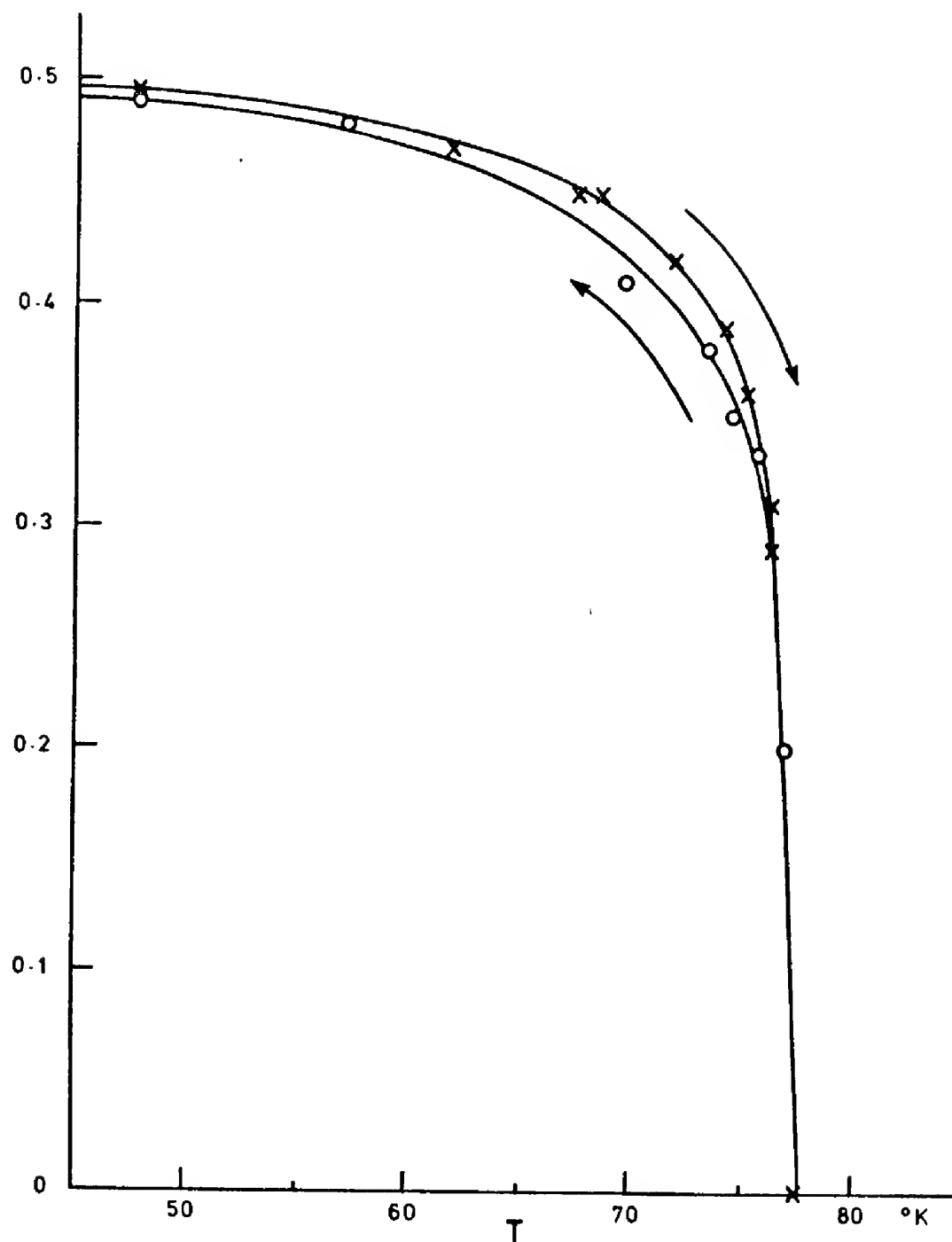


Figure 7.1 Temperature dependence of the intensity ratio

$$R(T) = \sqrt{\frac{I(110) + I(11\bar{1})}{I(220) + I(22\bar{2})}}$$

measured over the lower phase transition of DI with increasing (X) and decreasing (O) temperatures.

T°K	Direction	I(110+11 $\bar{1}$)	I(220+22 $\bar{2}$)	R(T)	q(T)
4.2 ± 1.0	Increasing	2383	9935	0.49 ± 0.03	1.0 ± 0.06
47.8 ± 1.0	"	5297	22230	0.49 ± 0.03	1.0 ± 0.06
61.8 ± 1.0	"	5368	24066	0.47 ± 0.03	0.96 ± 0.06
67.5 ± 1.0	"	6510	32873	0.45 ± 0.03	0.92 ± 0.06
68.5 ± 1.0	"	4675	23535	0.45 ± 0.03	0.92 ± 0.06
71.8 ± 0.5	"	3815	22188	0.42 ± 0.03	0.86 ± 0.06
74.1 ± 0.5	"	4725	30175	0.39 ± 0.03	0.80 ± 0.06
75.1 ± 0.5	"	4290	32336	0.36 ± 0.03	0.735 ± 0.06
76.2 ± 0.5	"	3138	31784	0.31 ± 0.04	0.63 ± 0.08
76.2 ± 0.5	"	1047	12077	0.29 ± 0.04	0.59 ± 0.08
77.5 ± 0.5	"	0	32829	0.0 ± 0.05	0.0 ± 0.10
76.9 ± 0.5	Decreasing	1240	29615	0.2 ± 0.04	
75.6 ± 0.5	"	3090	28011	0.33 ± 0.03	
74.5 ± 0.5	"	3080	24568	0.35 ± 0.03	
73.4 ± 0.5	"	4585	31650	0.38 ± 0.03	
69.6 ± 1.0	"	5170	30920	0.41 ± 0.03	
57.1 ± 1.0	"	6648	28900	0.48 ± 0.03	
47.8 ± 1.0	"	6235	26324	0.49 ± 0.03	

TABLE 7.1. Intensities of neutron powder peaks measured over the lower phase transition of DI with increasing and decreasing temperature and the R(T) and q(T) values derived from these measurements.

$T^{\circ}\text{K}$	$c_p^*(T)$	$p(T)$	$q(T)$	$T^{\circ}\text{K}$	$c_p^*(T)$	$p(T)$	$q(T)$
44.0	0.0	.015	.970	66.5	1.10	.030	.940
55.0	0.0	.015	.970	67.0	1.25	.031	.938
56.0	0.20	.015	.970	67.5	1.35	.033	.934
56.5	0.20	.016	.968	68.0	1.45	.034	.932
57.0	0.25	.016	.968	68.5	1.65	.036	.928
57.5	0.30	.016	.968	69.0	1.90	.038	.924
58.0	0.30	.017	.966	69.5	2.20	.041	.918
58.5	0.40	.017	.966	70.0	2.45	.044	.912
59.0	0.40	.017	.966	70.5	2.75	.047	.906
59.5	0.40	.018	.964	71.0	3.20	.051	.898
60.0	0.50	.018	.964	71.5	3.50	.055	.890
60.5	0.55	.019	.962	72.0	3.90	.060	.880
61.0	0.55	.019	.962	72.5	4.25	.065	.870
61.5	0.60	.020	.960	73.0	4.70	.072	.856
62.0	0.65	.021	.958	73.5	5.25	.079	.842
62.5	0.70	.022	.956	74.0	6.85	.088	.824
63.0	0.75	.022	.956	74.5	10.80	.105	.790
63.5	0.80	.023	.954	75.0	12.80	.126	.748
64.0	0.85	.024	.952	75.5	14.00	.149	.702
64.5	0.90	.025	.950	76.0	17.30	.185	.630
65.0	0.95	.026	.948	76.5	19.04	.232	.536
65.5	1.00	.027	.946	77.0	29.00	.336	.428
66.0	1.05	.028	.944				

TABLE 7.2. Temperature dependence of the anomalous specific heat over the lower transition of DI. The values listed were calculated from the data of Clusius and Wolf (1947).

Figure 7.2 shows the order parameters derived from the neutron diffraction experiments as crosses and those from the calorimetric data as a continuous line. Only data recorded with increasing temperature are shown in this figure as the specific heat measurements were made with increasing temperature.

A value of 0.015 was chosen for $p(T_0)$, effectively the residual disorder parameter at 45K, as this provided the best overall fit between order parameters derived from the calorimetric and the neutron diffraction data.

The reason for a non-zero residual disorder $p(T_0)$ at 45K is probably a combination of several effects; statistical errors in $R(T)$, temperature gradients, uncertainty in the magnitude of the components of the reference peak ($13\bar{1}$ etc.) and possibly also some short-range order over the transition region.

Short-range order implies the formation of groups of molecules whose re-orientation is coupled over short distances. The expression derived for Ω , equation (132), is then not applicable as in this case the two equilibrium orientations are not equally probable. As the combination of the effects of temperature gradients, statistical errors, etc. appears to be less than 1.5%, short-range order is unlikely to be important in the lower phase transition of DI.

7.2 The upper phase transition

In the upper transition the crystal structure of DI changes from two-fold disordered orthorhombic (middle phase) to twelve-fold disordered cubic (high phase). Specific heat measurements suggest that the transition takes place over the temperature range of 100-130K.

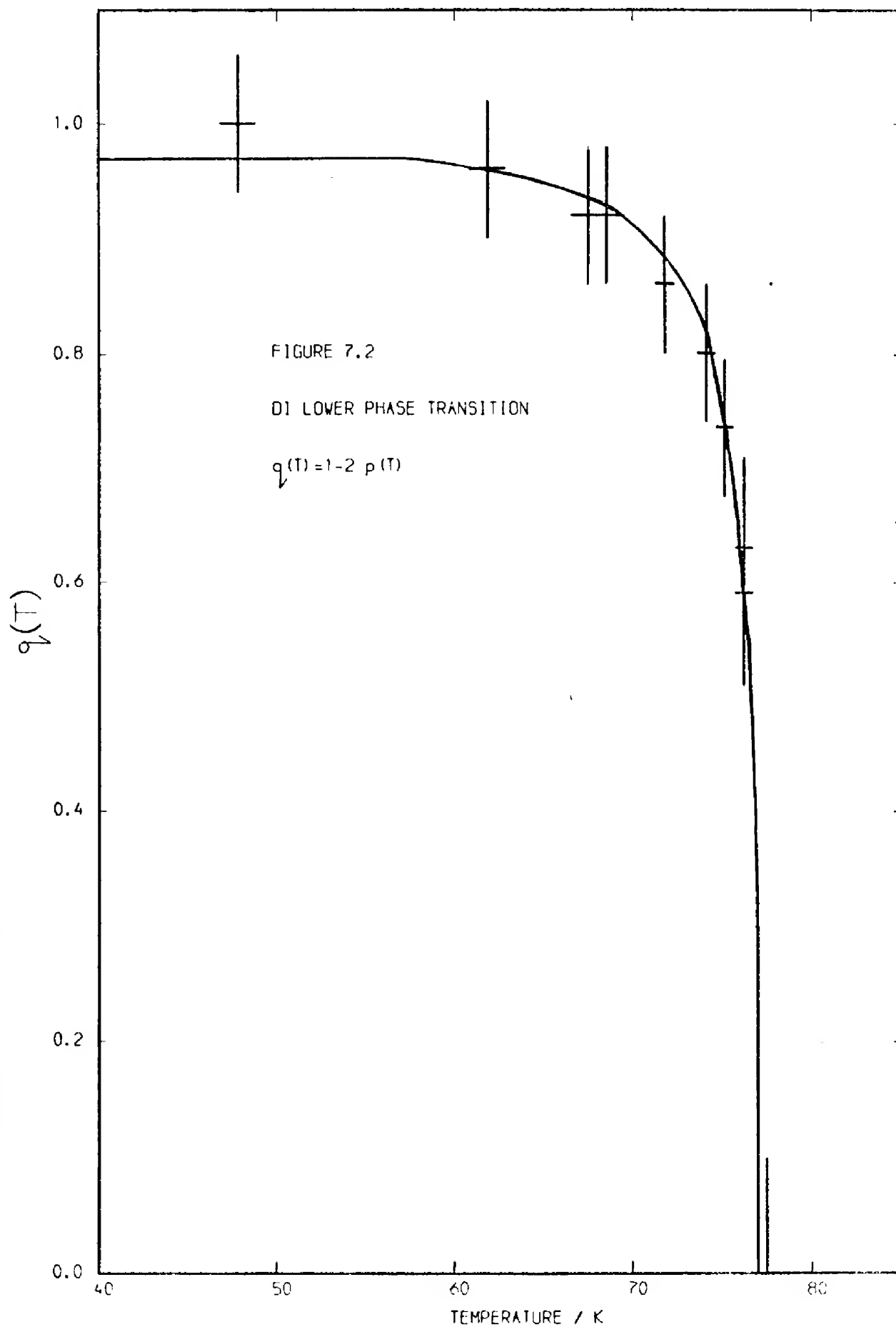


Figure 7.2 Order parameter $q(T)$ derived from neutron diffraction experiments (+) and specific heat measurements (solid line) over the lower phase transition region of D1.

When passing from the middle to the high phase (see figure 3.5), the gradual disappearance of the $(002)_{\text{orthorhombic}}$ peak of the middle phase can be easily monitored since it occurs at a lower angle than the $\{002\}_{\text{cubic}}$ peak of the high phase. The (111) peak however hardly changes either in position or in intensity over the upper transition region. Accordingly the neutron diffraction study of the upper phase transition of DI was carried out by measuring the intensity of the disappearing $(002)_{\text{orthorhombic}}$ peak as a function of temperature. The intensity of the nearly constant (111) peak was measured as a reference to correct for changes in counter efficiency, etc.

An occupation number, $p'(T)$ at a temperature T , can be defined for the high phase as the probability of a deuterium atom being in one of the ten equilibrium sites not occupied in the middle phase. It follows from its definition that $p'(T)$ will lie in the range $0 \leq p'(T) \leq 1/12$.

It is possible to consider two methods in which the upper phase transition occurs;

a) At low values of $p'(T)$, when the structure is orthorhombic, the ratio of the intensity of the $(002)_{\text{orthorhombic}}$ peak at temperature T (when $p'(T)$ deuterium molecules are in the twelve-fold disordered position) to the intensity of the $(002)_{\text{orthorhombic}}$ (when the deuterium molecules are all in the two-fold disordered position) is,

$$\frac{I_T(002)_{\text{orthorhombic}}}{I_0(002)_{\text{orthorhombic}}} = \left\{ \frac{4b_I + 4b_D[1-p'(T)(10-8\cos 4\pi x)]}{4b_I + 4b_D} \right\}^2 \quad (135)$$

x is the fractional deuterium co-ordinate and b_I , b_D are the coherent neutron scattering lengths of the iodine and deuterium atoms.

Inserting numerical values gives;

$$\frac{I_T(002)_{\text{orthorhombic}}}{I_0(002)_{\text{orthorhombic}}} = [1 - 7.8p'(T)]^2 \quad (136)$$

b) The DI powder samples used in the studies of the phase transitions were not entirely free of temperature gradients (see Appendix two). As the temperature and hence the value of $p'(T)$ increases, the temperature gradients in the DI powder sample cause the neutron powder diffraction to appear as a mixture of the orthorhombic middle phase and the cubic high phase. The intensity of the $(002)_{\text{orthorhombic}}$ peak decreases in direct proportion to the number of unit cells or crystallites which have the cubic (high phase) crystal structure. Thus the intensity of the $(002)_{\text{orthorhombic}}$ peak decreases according to the equation;

$$\frac{I_T(002)_{\text{orthorhombic}}}{I_0(002)_{\text{orthorhombic}}} = 1 - 12p'(T) \quad (137)$$

Following the treatment of the lower phase transition, it can be shown that the number of ways of arranging N molecules so that a fraction $p'(T)$ occupy the ten lattice sites (additional to the two already occupied in the two-fold disordered orthorhombic middle phase) with equal probability is given by;

$$\Omega'[p'(T)] = \frac{N!}{\left\{ \frac{[1 - 10p'(T)]N!}{2} \right\}^2 \{p'(T)N!\}^{10}} \quad (138)$$

where N is the Avogadro constant and $0 \leq p'(T) \leq 1/12$.

The two limits to equation (138) are the fully twelve-fold disordered high phase;

$$\Omega'(1/12) = \frac{N!}{\left(\frac{N!}{12}\right)^{12}} \quad (139)$$

and the two-fold disordered low phase;

$$\Omega'(0) = \frac{N!}{\left(\frac{N!}{2}\right)^2} \quad (140)$$

which is in agreement with the expression for the fully two-fold disordered middle phase used to describe the lower phase transition equation (132);

$$\Omega\left(\frac{1}{2}\right) = \frac{N!}{\left(\frac{N!}{2}\right)^2} \quad (141)$$

Using the expressions (130), (133) and (138) it can be shown that for the upper phase transition;

$$\int_{T_0}^T \frac{C_p^*(T)}{T} dT = -kN \left\{ [1-10p'(T)] \ln \left[\frac{1-10p'(T)}{2} \right] + 10p'(T) \ln p'(T) \right. \\ \left. - [1-10p'(T_0)] \ln \left[\frac{1-10p'(T_0)}{2} \right] - 10p'(T_0) \ln p'(T_0) \right\} \quad (142)$$

$p'(T_0)$ is the fractional number of deuterium atoms occupying the ten non-orthorhombic lattice sites at the temperature T_0 and k is the Boltzmann constant.

The ratio of the intensities of the $(002)_{\text{orthorhombic}}$ and the (111) powder peaks was measured as a function of temperature on the Dido 'Badger II' neutron powder diffractometer. The liquid nitrogen cryostat and the vitreous silica sample tube used in these experiments were already described in Chapter two. The $(002)_{\text{orthorhombic}}$ and $\{002\}_{\text{cubic}}$ peaks overlapped slightly in the powder diffraction pattern and were resolved by the use of the computer program MPR, Johnson (1970).

The temperature range of 114-130K was covered four times by measuring

with decreasing temperature then increasing, decreasing and increasing again. The temperature at which measurements were made were interleaved with each other to provide a 'closed-loop' of measurements and to check for any change in the temperature measuring system; none was found.

The transition appeared to be complete at 128K when measured with increasing temperature. Specific heat measurements, Clusius and Wolf (1947), gave a value of 128.3K, the difference probably being due to temperature gradients and differences of isotopic purity in the sample. In contrast to the lower transition, the upper transition of DI showed a marked thermal hysteresis, the width of the hysteresis loop being $1.75 \pm 0.5^\circ\text{K}$.

The measured variation of $\frac{I(002)}{I(111)}$ orthorhombic with temperature is shown in figure 7.3 and table 7.3. As can be seen, the phase transition occurs sharply over 5°K although in reality (because of the temperature gradients) it may be still more sharp. This contrasts with the width of approximately 30°K shown in the specific heat data of Clusius and Wolf (1947).

This discrepancy is due to the relative insensitivity of neutron diffraction compared to specific heat measurements in revealing the increase of molecular disorder occurring in the upper phase transition region. Table 7.4 lists the variation of the anomalous specific heat $C_p^*(T)$ with temperature over the upper transition region. To illustrate this difference in sensitivity it can be seen in table 7.4 that between the temperatures of 112K and 124K the value of $C_p^*(T)$, the anomalous specific heat, doubles but the neutron powder peak intensity ratio (which is proportional to $1-12p'(T)$) only changes by 3%. It is only when the specific heat increases by a large factor that the intensity ratio decreases by more than 10%.

The parameter $p'(T)$ was obtained by graphical integration of the specific

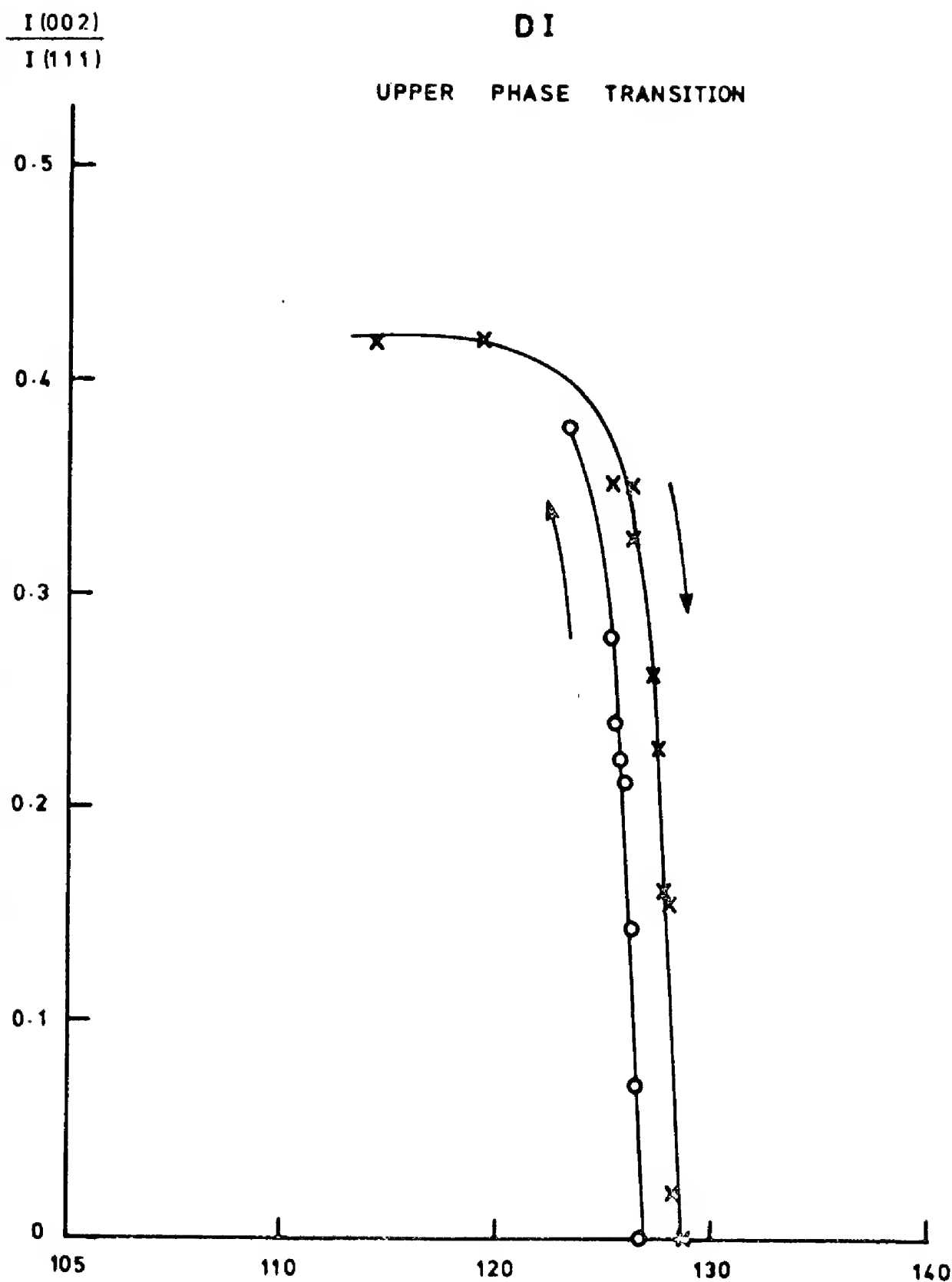


Figure 7.3 Temperature dependence of the intensity ratio

$$R(T) = \frac{I(002)^0}{I(111)}$$

measured over the upper phase transition of DI with increasing (x) and decreasing (o) temperatures.

T°K	Direction	I[002] ²	I[111]	I[002] ⁰ /I[111]	q'(T)
114.25±0.5	Increasing	39850	95400	0.418±0.02	1.000±0.05
119.25±0.5	"	39120	93400	0.419±0.02	1.000±0.05
125.25±0.5	"	23750	67500	0.352±0.02	0.842±0.05
126.25±0.5	"	33150	94310	0.351±0.02	0.839±0.05
126.25±0.5	"	24250	74450	0.326±0.02	0.779±0.05
127.25±0.5	"	19255	73280	0.263±0.03	0.629±0.07
127.50±0.5	"	15488	68040	0.228±0.03	0.545±0.07
127.75±0.5	"	11445	70860	0.162±0.03	0.387±0.07
128.00±0.5	"	10785	68980	0.156±0.03	0.373±0.07
128.25±0.5	"	14890	71900	0.021±0.05	0.050±0.12
128.75±0.5	"	0	94310	0.000±0.05	0.000±0.12
126.75±0.5	Decreasing	448	70320	0.006±0.05	
126.50±0.5	"	5016	70484	0.071±0.05	
126.25±0.5	"	10145	70720	0.144±0.03	
126.00±0.5	"	14698	69240	0.212±0.02	
125.75±0.5	"	15813	71080	0.223±0.02	
125.50±0.5	"	16950	70900	0.240±0.02	
125.25±0.5	"	20090	71800	0.280±0.02	
123.25±0.5	"	34905	92400	0.378±0.02	

TABLE 7.3. Intensities of neutron powder peaks measured over the upper phase transition of DI with increasing and decreasing temperature and the ratio and q'(T) values derived from them.

T°K	$C_p^*(T)$	$p'(T)$	$q'(T)$	T°K	$C_p^*(T)$	$p'(T)$	$q'(T)$
90.0	0.00	.0001	.9988	110.0	1.75	.0013	.9844
90.5	0.00	.0001	.9988	110.5	1.85	.0014	.9832
91.0	0.00	.0001	.9988	111.0	1.90	.0015	.9820
91.5	0.10	.0001	.9988	111.5	1.95	.0016	.9808
92.0	0.15	.0001	.9988	112.0	2.05	.0017	.9796
92.5	0.20	.0001	.9988	112.5	2.10	.0018	.9784
93.0	0.30	.0001	.9988	113.0	2.20	.0019	.9722
93.5	0.35	.0001	.9988	113.5	2.25	.0020	.9760
94.0	0.40	.0001	.9988	114.0	2.35	.0021	.9748
94.5	0.45	.0001	.9988	114.5	2.40	.0022	.9736
95.0	0.50	.0002	.9976	115.0	2.50	.0023	.9724
95.5	0.55	.0002	.9976	115.5	2.60	.0024	.9712
96.0	0.60	.0002	.9976	116.0	2.70	.0025	.9700
96.5	0.65	.0002	.9976	116.5	2.80	.0026	.9688
97.0	0.70	.0002	.9976	117.0	2.85	.0027	.9676
97.5	0.80	.0002	.9976	117.5	2.90	.0028	.9644
98.0	0.85	.0002	.9976	118.0	3.00	.0029	.9652
98.5	0.85	.0003	.9964	118.5	3.05	.0031	.9628
99.0	0.90	.0003	.9964	119.0	3.15	.0032	.9616
99.5	0.90	.0004	.9952	119.5	3.20	.0034	.9592
100.0	1.00	.0004	.9952	120.0	3.25	.0035	.9580
100.5	1.00	.0004	.9952	120.5	3.35	.0037	.9566
101.0	1.00	.0005	.9940	121.0	3.45	.0038	.9544
101.5	1.05	.0005	.9940	121.5	3.55	.0039	.9532
102.0	1.05	.0005	.9940	122.0	3.60	.0041	.9508
102.5	1.10	.0006	.9928	122.5	3.70	.0042	.9496
103.0	1.10	.0006	.9928	123.0	3.75	.0044	.9472
103.5	1.15	.0006	.9928	123.5	3.80	.0046	.9448
104.0	1.20	.0007	.9916	124.0	4.00	.0048	.9424
104.5	1.20	.0007	.9916	124.5	4.20	.0049	.9412
105.0	1.25	.0008	.9904	125.0	4.40	.0051	.9388
105.5	1.30	.0008	.9904	125.5	4.80	.0053	.9364
106.0	1.30	.0009	.9892	126.0	5.10	.0056	.9328
106.5	1.35	.0009	.9892	126.5	48.70	.0079	.9052
107.0	1.40	.0010	.9880	127.0	92.40	.0127	.8476
107.5	1.45	.0011	.9868	127.5	136.00	.0211	.7468
108.0	1.50	.0011	.9868	128.0	179.70	.0349	.5812
108.5	1.55	.0012	.9856	128.2	668.00	.0484	.4192
109.0	1.65	.0012	.9856	128.3	51.40	.0519	.3772
109.5	1.70	.0013	.9844				

TABLE 7.4. Temperature dependence of the anomalous specific heat over the upper phase transition of D1. The values in this table were calculated from the data of Clusius and Wolf (1947).

heat data and by numerical interpolation of equation (142). Figure 7.4 shows two curves;

$$\text{a) } [1 - 7.8p'(T)]^2 \quad (143)$$

$$\text{b) } 1 - 12p'(T) \quad (144)$$

together with the ratio $q'(T)$ derived from the neutron diffraction data. A residual order parameter $p'(T_0)$ of value 0.0001 was found to give the best overall fit between curve (b) and the order parameters derived from the neutron diffraction measurements. Curve (a) is only valid when $p'(T)$ is small, i.e. at lower temperatures when co-operative effects between neighbouring molecules are small and short-range order is negligible.

The poor agreement between these curves and the neutron diffraction data can be attributed predominantly to short-range order and partly to temperature gradients in the sample. The thermal gradients cause a rounding or softening of the order parameter curve as a function of temperature when observed by neutron diffraction.

In the twelve-fold disordered high phase a deuterium atom is assumed to lie along one of the directions pointing towards the twelve nearest-neighbour iodine atoms of its parent iodine atom. On the average each of these sites is occupied with equal probability. This model was used in the derivation of the configurational entropy change in equation (142) and it took no account of electrostatic repulsion between deuterium atoms of neighbouring molecules. Deuterium atoms in adjacent DI molecules are unlikely to lie along the same bond and this restriction modifies the disposition of sites available to each atom.

The change in configurational entropy was calculated by equation (142)

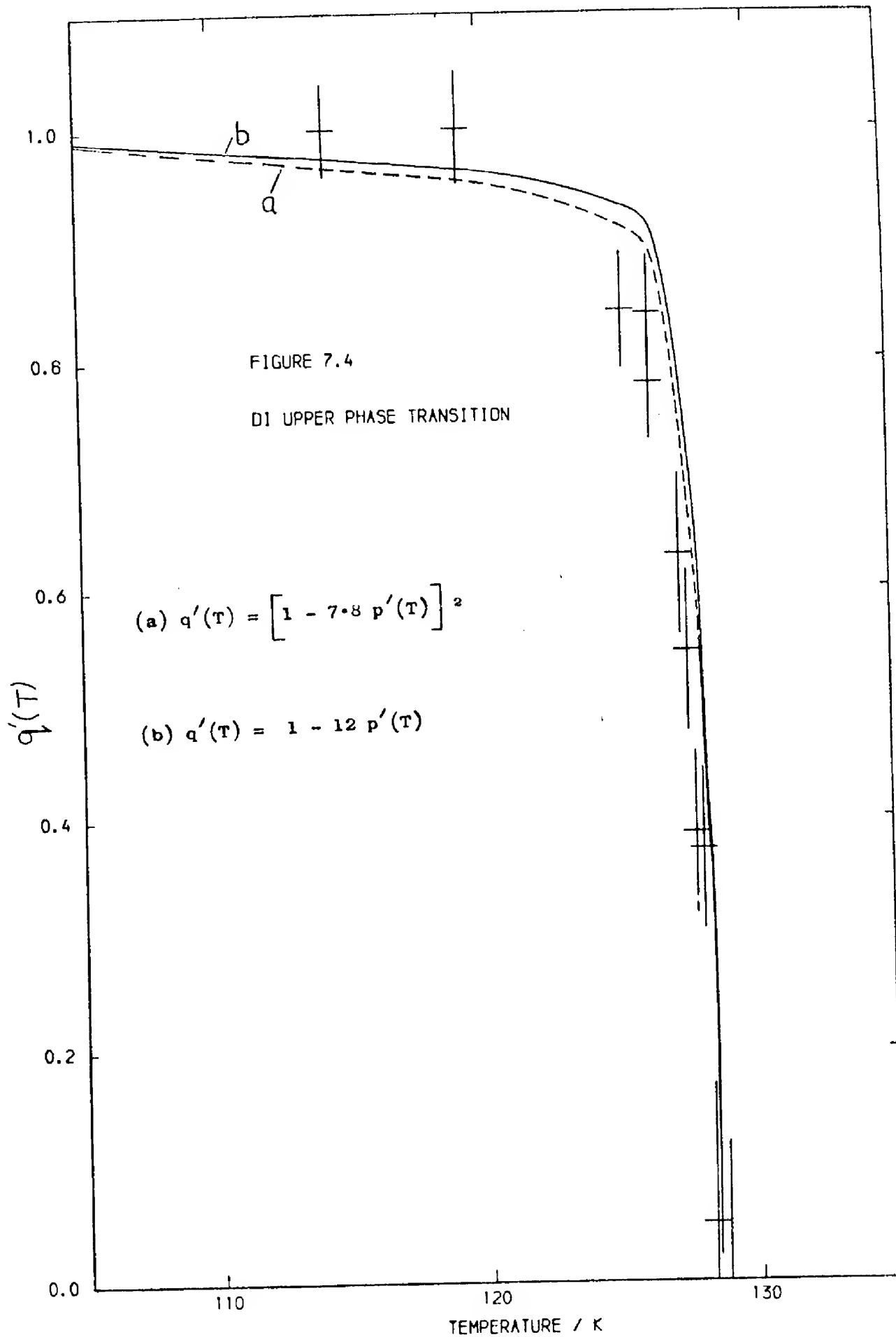


Figure 7.4 Order parameters $q'(T)$ derived from neutron diffraction experiments (+) and specific heat measurements (solid and dashed lines) over the upper phase transition of DI.

making the approximation that at a given instant all twelve sites are equally probable. Over a longer period all twelve sites of a given molecule are equally probable but not as an instantaneous neighbour of another deuterium atom (in the next molecule) due to electrostatic repulsion.

The change in configurational entropy over the phase transition was calculated from the specific heat measurements of Clusius and Wolf (1947) and was found to be $2.146 \text{ j mole}^{-1} \equiv k \ln 2.94$. The expected change in configurational entropy from a two-fold to a twelve-fold disordered structure is $3.566 \text{ j mole}^{-1} \equiv k \ln 6$. An entropy of $1.419 \text{ j mole}^{-1} \equiv k \ln 2.041$ therefore remains due to short range ordering.

It was shown by Schneider (1955) that, when hydrogen halides form chains, the molecular bonds are not collinear with one another but are at an angle. This angle is determined by the lone-pair electron orbitals in the outer shell of the halogen and for HI/DI is approximately 90° . In the low phase of DI this can be seen as the square rings in the proposed ordered model and in the middle phase as the two-fold disordered zig-zag chains. Using this information a very simple model can be proposed to describe the short range order.

It is assumed that in the high phase short chains of L molecules joined at 90° to each other are formed. Each chain has one molecule at its head so that the second molecule can be chosen twelve ways. The next molecule must be at 90° and it can be chosen in two ways. Hence the number of ways of choosing a chain of L molecules is;

$$12 \times 2^{L-2} \quad (145)$$

In the sample there are N molecules and N/L chains and the total number of ways of choosing these chains is;

$$[12 \times 2^{L-2}]^{N/L} \quad (146)$$

The total number of ways of arranging all N molecules in a chain is;

$$12 \times 2^{N-2} \approx 2^N \text{ (if } N \text{ is very large)} \quad (147)$$

$$\therefore \Omega = \frac{[12 \times 2^{L-2}]^{N/L}}{2^N} \quad (148)$$

The configurational entropy per mole due to the chain formation is;

$$k \ln \Omega = k \ln 3^{1/L} \quad (149)$$

and the additional entropy is;

$$1.419 \text{ jmole}^{-1} = k \ln 2.041 = k \ln 3^{1/L} \quad (150)$$

so that $L \approx 1.5$.

Therefore the average length of a 90° zig-zag chain is 1.5 molecules.

7.3 Conclusion

The lower and upper phase transitions of DI were studied by neutron powder diffraction. Order parameters describing the average configuration of disordered molecules were obtained as a function of temperature from these neutron powder peak intensities. A similar order parameter was derived by integration of the anomalous specific heat over each phase transition region. These two parameters agreed well with each other over the lower phase transition region, confirming that the lower transition was of second order from ordered to 2-fold disordered with an indication of a small thermal hysteresis. There was little evidence of short-range order in the low temperature region of the middle phase.

The upper phase transition appeared to be of first-order with a thermal hysteresis of approximately 1.75°K . The order parameter as a function of temperature for this transition obtained by integration of the specific heat

did not agree well with that obtained by neutron diffraction. This was attributed to some residual short-range order in the cubic high phase. A simple model showed that this extended on average over one to two neighbouring molecules.

CHAPTER EIGHT

SUMMARY

8.1 Conclusions of earlier experimental studies concerning the crystal structure of DI

Experimental investigations carried out prior to this thesis produced many interesting results directly relevant to the crystal structure of the HI/DI system of which the main results can be summarized as follows.

It was the specific heat measurements which first indicated that DI had three solid phases and two well-defined transition temperatures. For approximately 20°K below each transition point the specific heats increased rapidly then fell back abruptly thus forming the so-called 'lambda-points'. These anomalous changes in the specific heat were interpreted as due to the onset of orientational disorder as either free or hindered rotation of the DI molecules.

X-ray diffraction experiments indicated that the unit cells were face-centred tetragonal (in the low and middle phases) and face-centred cubic (in the high phase). In each case the edgelengths of the unit cell were approximately 6Å and it contained four DI molecules. Experiments using polarized light indicated that the low and middle phases were anisotropic and the high phase was isotropic. These results were in agreement with the ideas of two tetragonal phases and one cubic phase from X-ray data.

Conclusions derived from measurements of the static dielectric constant as a function of temperature were similar to those obtained from the calorimetric data. An increase in the static dielectric constant on approaching

the lower phase transition point was followed by a continuous decrease and a sharp drop at the upper transition point. This behaviour suggested an increase in the structural disorder at each transition.

The measurement of the frequency dependence of the dielectric constant provided relatively little direct information on the crystal structure. Its main contribution was the observation that the complex dielectric constant of solid DI was similar to that of several simple polar liquids such as glycols. It also showed that the phase transitions were co-operative phenomena with re-orientation frequencies higher than those of a typical "stiff" molecular vibration.

Early NMR work indicated that the phase transitions were from ordered to disordered structures with several equilibrium orientations rather than with freely rotating molecules. Later NMR work provided more detailed measurements of the different relaxation frequencies which were in general agreement with those obtained from the frequency-dependent dielectric constant measurements.

Investigations of the infra-red spectra indicated that the low phase of DI was different from those of HCl and HBr and they also suggested that the unit cell was larger at low temperatures.

Neutron diffraction experiments on solid DBr revealed that the deuterium atoms occupied several equilibrium positions in the orientationally disordered middle and high phases. As the calorimetric, dielectric constant and NMR data for the compounds DBr and HI/DI were similar this provided indirect evidence for the occurrence of orientationally disordered structures in DI.

By combining all the available experimental evidence one could conclude

that the structure of DI changes from an ordered to successively more disordered forms with increasing temperature. The disorder would probably be orientational rather than rotational; although the directional hydrogen bond would be weaker in HI/DI than in the other hydrogen halides. The edglength of the unit cells would be approximately 6\AA with its symmetry changing from tetragonal to cubic at the upper transition point. Co-operative phenomena would give rise to a phase transition extending over $10\text{--}20^\circ\text{K}$ at the lower transition point and a narrower region at the upper transition point.

8.2 The crystal structure of DI as determined by X-ray and neutron diffraction

The diffraction experiments described in this thesis using X-rays and neutrons mostly confirmed the expectations concerning the structures of each phase of DI. X-ray experiments on the low phase showed that the iodine atoms formed a face-centred orthorhombic unit cell of approximate size 6\AA . However, neutron experiments (which reveal the presence of deuterium as well) showed that the true unit cell of the low phase was C-centred monoclinic and four times larger in volume than the X-ray unit cell. The structure of this phase has not been determined unambiguously. A model has been proposed whose calculated diffraction pattern agrees reasonably well with the observed neutron powder diffraction pattern. The iodine atoms lie in face-centred positions of the iodine sublattice while the DI molecules lie in the $(001)_0$ plane. Sets of four molecules exist as rectangles which form a continuous stack when viewed along the monoclinic C-axis of unit cell No.4.

The middle and high phases were found to be B-centred orthorhombic (space group Bbcm) and face-centred cubic (space group Fm3m), both structures being isomorphic with the corresponding phases of DBr. The edglengths of the unit cells were approximately 6\AA with the middle phase only slightly

distorted from a tetragonal cell. The middle phase was two-fold disordered with the deuterium atoms having two equilibrium sites at 180° to each other. The high phase was twelve-fold disordered with the equilibrium sites lying along the twelve nearest-neighbour iodine-iodine bonds.

The three phases were studied by X-ray and neutron diffraction at 4.2K, 84K and 137K and the structural parameters refined by least-squares methods. Anisotropic temperature factors were obtained wherever possible, although in the high phase correlation between parameters did not completely allow this.

The lattice parameters were measured at several temperatures by X-ray methods and are shown in figure 3.5. The mean linear thermal expansion coefficient of DI was found to be $3.5 \pm .5 \times 10^{-4} \text{ K}^{-1}$. As the temperature increases the unit cell expands uniformly in the low phase. At the lower phase transition point there is no noticeable change in the lattice parameters as the DI molecules begin to 'flip' in the $(001)_O$ plane. As the temperature rises further in the middle phase the c -axis increases while the a and b axes decrease. Near the upper phase transition point the lattice parameters converge rapidly to the cubic high phase while the volume of the unit cell increases continuously with temperature. In general the lattice parameters of DI are shorter than those of HI, this is true also for HBr/DBr and HCl/DCI, because the amplitudes of vibration of the deuterium atoms are smaller than those of the hydrogen atoms and consequently the lattice is packed more tightly.

8.3 The nature of the two phase transitions in solid DI

At each phase transition neutron powder peaks which were disappearing over the transition region were studied as a function of temperature in relation to a stable reference peak. In this way the lower phase transition

was found to extend from 45-80K with a thermal hysteresis whose width was approximately 0.5°K . The upper transition (as observed by neutron powder diffraction) appeared to extend from 122-128K with a well-defined thermal hysteresis of width $1.5 \pm 0.5^{\circ}\text{K}$, although the specific heat data indicate that the upper phase transition may be a great deal sharper than observed in this neutron study.

Order parameters were obtained from these data as a function of temperature. The anomalous specific heat obtained from the calorimetric data was integrated to obtain an equivalent order parameter. The order parameters derived by these two methods were in good agreement over the lower transition. However, the upper transition neutron order parameter showed a more gradual change at the transition point than that calculated from the calorimetric data. The difference was possibly due to short-range order between the deuterium atoms which are able to form short chains consisting of a few molecules in the disordered high phase. The overall changes in configurational entropy between the three phases were evaluated as $1.01 \equiv k \ln 1.74$ (lower) and $2.146 \equiv k \ln 2.94$ (upper). The configurational entropy change associated with the lower phase transition is consistent with the proposed structural change from ordered to two-fold disordered. Moreover, it suggests that the two equilibrium orientations in the middle phase are occupied almost at random, without appreciable short range order. On the other hand, the configurational entropy change associated with the upper transition is considerably smaller than would be expected if the transition from two- to twelve-fold disordered were entirely random, with no short-range order. Hence the calorimetric data combined with the neutron diffraction results suggest the presence of appreciable short range order in the high phase of DI.

8.4 Suggested further experiments on HI/DI

a) Neutron powder diffraction

Instruments and facilities in experimental sciences often improve in large finite steps. This is particularly true of "big" science where facilities such as reactors and neutron diffractometers cost respectively tens of millions and tens of thousands of pounds. Over the period of three years in which the experimental work for this thesis was carried out, the most noticeable change was the considerable improvement in the angular resolution of the powder diffractometers at A.E.R.E., Harwell. In addition, this improvement was enhanced by the ability to vary the monochromator take-off angle on instruments such as Pluto 'Panda' and so to optimize the angular resolution in the region of $\frac{\sin\theta}{\lambda}$ where it was most useful.

Increases in angular resolution are always paid for by a reduction in the scattered intensity. High flux beam reactors such as the H.F.R. at the Institute Laue-Langevin, Grenoble, France, where the incident neutron flux is at least one order of magnitude higher than at Harwell, will with the development of suitable instruments provide increased intensities and higher angular resolution. In addition pulsed reactor or accelerator facilities provide opportunities for improved resolution and 'instantaneous' data recording.

Such 'instantaneous' recording can be achieved by the use of position sensitive detectors and electronic time-of-flight instruments. In such experiments the instrument behaves as an electronic powder camera and records the whole accessible range of $\frac{\sin\theta}{\lambda}$ simultaneously. This type of instrument, in addition to reducing the times of experiments, greatly simplifies the study of phase transitions as a function of temperature and reduces many uncertainties concerning counter efficiencies, etc.

The phase transition experiments described in this thesis each took approximately three weeks of reactor time and the temperature dependence of only a few peaks was studied. Multidetector instruments as available at I.L.L. and under construction at A.E.R.E. would provide complete diffraction scans at improved statistical accuracy, angular resolution or narrower temperature intervals. These data could be analysed using computer programs of the type developed by Rietveld (1967). With an order of magnitude increase in reactor flux an experiment previously taking over 2 months (which would rarely have been considered in the U.K.) would take one week.

b) Single-crystal neutron diffraction

Single crystal diffraction measurements on HI/DI would provide more detailed information on the crystal structure and particularly temperature factors and the related thermal motion parameters. It appears difficult to grow such crystals although some success has been reported for DCI, Hoshino (1970), Shimaoka (1971) and Maruyama (1970). High phases of molecular crystals can be grown from the liquid by the Bridgmann (1925) method. However, on cooling to lower temperatures through the phase transitions they invariably fragment into twins and multiple crystallites. The low phase of DI would most benefit from a single-crystal study out of all the hydrogen halides. This is due to its monoclinic symmetry on a pseudo-orthorhombic lattice as described in Chapter four. A powder diffraction experiment has a built-in degeneracy which combines several different peaks with the same d-spacing. Only a single-crystal experiment would be able to separate these reflections.

c) Inelastic neutron scattering

When suitable crystal-growing techniques have been developed the hydrogen halides will provide a very interesting field of study for

inelastic neutron scattering. Improved neutron sources as discussed earlier are even more welcome in inelastic scattering where many experiments involving energy analysis of the scattered neutrons become possible only with these high fluxes.

In particular, inelastic neutron scattering can provide information on the lattice modes of the crystals and enable the study of the re-orientation processes occurring in the middle and high phases. Such comprehensive data on the frequency of these re-orientations and the associated mechanisms and forces will, it is hoped, help the development of a satisfactory theory of the phase transitions.

APPENDIX ONE

Computer Programs

Four different computers were used during the course of this work:

- (a) The Science Research Council ICT, Atlas Computer at the Atlas Computer Laboratory, Chilton, Oxon.
- (b) The London University ICT, Atlas Computer at the Institute of Computer Science, Gordon Square, London.
- (c) The London University CDC 6600 computer at the University of London Computer Centre, Guilford Street, London
- (d) The IBM 370 computer at A.E.R.E., Harwell.

All programs used were written in subsets of FORTRAN, at one stage sections of ORFLS were rewritten from FORTRAN V to FORTRAN IV for compatibility with all computers.

A1.1 Least-squares refinements of crystal structures

The least-squares refinements of crystal structures were performed using a modified version of ORFLS, Busing (1962). The modifications are described elsewhere by Ogunade (1969) and Johnson (1971), and a brief outline only will be given here.

Because of the relatively poor angular resolution of the neutron powder diffractometers and the near-equality of the lattice parameters of DI, this ratio being typically 1:1.01:1.09, it was not possible in the low and middle phases to obtain a set of intensities for single powder peaks.

The modified version of ORFLS performs least-squares refinements with sets of intensities grouped as multiplets. ORFLS minimizes:

$$E = \sum_{\ell=1}^{NO} W_{\ell} \Delta_{\ell}^2 \quad \text{where } NO = \text{Number of observations}$$

$$W_{\ell} = \text{Weight of } \ell^{\text{th}} \text{ observation}$$

$$\text{and } \Delta_{\ell} = F'_{\text{obs}} - s F'_{\text{calc}} \quad \text{where } F'_{\text{obs}} = \text{Observed structure factor}$$

$$F'_{\text{calc}} = \text{Calculated structure factor}$$

$$\text{or } \Delta_{\ell} = |F'_{\text{obs}}|^2 - |s F'_{\text{calc}}|^2 \quad s = \text{Scale factor}$$

In the modified program, MP-ORFLS minimizes:

$$E = \sum_{\ell=1}^{NO} W_{\ell} \Delta_{\ell}^2 \quad \text{where } \Delta_{\ell} = I_{\text{obs}} - \sum_{m=1}^{NPK} \frac{j_m (s F'_{\text{calc}})_m^2}{\sin \theta_m \sin 2\theta_m} \quad (151)$$

where NPK = Number of peaks in multiplet

j_m = Multiplicity of m^{th} peak

θ_m = Bragg angle of m^{th} component peak

$$\text{and } I_{\text{obs}} = \sum_{m=1}^{NPK} \frac{j_m F_{\text{obs}}^2}{\sin \theta_m \sin 2\theta_m} \quad (152)$$

Further modifications were made to this program at a later date and included; extended error messages, optimization of the available core store and a printing of the calculated Bragg angle beside each peak to enable easy checking of the Miller indices. This was useful when dealing with a monoclinic unit cell.

Al.2 Least-squares refinements of cell dimensions

Least-squares refinements of lattice parameters were performed using the program PARAM. This is a part of the overlaid suite of programs called X-RAY 70 (Stewart 1970) which are stored on magnetic disks at all three computer establishments.

PARAM minimizes E where:

$$E = \sin^{-1} \left[\sqrt{\sin^2 \theta_{\text{calc}}} \right] - \theta_{\text{obs}}$$

The program performs 5 cycles of least-squares refinement and, depending on the type of lattice specified initially, varies only the necessary parameters.

A1.3 Calculation of powder peak positions

The program THETA was used to calculate the full set of allowed Bragg reflections for a particular lattice. Symmetry conditions of two types could be imposed to provide constraints on the allowed reflections.

e.g. Type 1: A single letter, F, I, A, B, C ...

Type 2: More general conditions 00ℓ ($\ell=2n$) etc.

A1.4 Calculation of random orientation structure factors

A Simpson's rule method of integration was used to evaluate the integrals derived in Chapter 3.

A1.5 LPSG, Low phase symmetry generator

This program used an analytical expression for the structure factor of space group Cc in which four independent molecules were chosen as the basis. An inner loop produced the first 13 Bragg reflections and four outer loops varied the molecular orientations to generate the separate 128 structures.

Each structure was numbered and contained a listing of the deuterium atomic co-ordinates.

A1.6 The Rietveld program

This program was written for the refinement of neutron diffraction powder patterns by Rietveld (1967, 1969). The implementation used here is that of Hewat (1973). The program computes the neutron diffraction powder pattern to be expected from a model crystal structure and a particular diffractometer. The following parameters are supplied by the user;

(a) Describing the crystal structure

- (i) Symmetry operations.
- (ii) Atomic co-ordinates, scattering lengths, atom multipliers and temperature factors.
- (iii) Scale factor.
- (iv) Unit cell dimensions.

(b) Describing the diffractometer

- (i) Wavelength.
- (ii) Zero-angle of the 2θ scan.
- (iii) The angular resolution as a function of angle.

The width of the powder peak (FWHM) is described by a function;

$$H^2(\theta) = U \tan^2\theta + V \tan\theta + W \quad (153)$$

The program minimizes by successive iterations the following quantity;

$$\chi^2 = \sum_i w_i \left[y_i(\text{obs}) - \frac{y_i}{c}(\text{calc}) \right]^2 \quad (154)$$

The summation is taken over all the points of the diffraction pattern where $y_i(\text{calc})$ and $y_i(\text{obs})$ are the calculated and observed intensities of weight w_i and c is the scale factor.

Any or all of the parameters listed above may be varied during the structure refinement. This program has the advantage that all the information contained in the unresolved multiple peaks of a complicated powder diffraction pattern can be utilised in refining the structure. The complexity of these peaks is due to the poor angular resolution of neutron powder diffractometers necessitated by their low incident flux compared with X-ray diffractometers.

The disadvantage of the program is that convergent refinements only occur when all the parameters are close to their correct values, i.e. the user must know all the instrumental parameters accurately and the structural parameters tolerably well before refinement.

APPENDIX TWO

Temperature measurement and control circuit of the variable temperature cryostat

The control circuit is shown in figure A2.1 and the cryostat system in figure 2.10. The sample is held in a vacuum insulated exchange space at S. The sample temperature measuring thermocouples, of 0.005in. diameter copper and constantan wire, are fixed at T_1 and T_2 and pass through neoprene vacuum seals, Batchelder (1969) at S1 and S2 to a liquid helium reference junction, H. The thermocouple leads then pass to

- (a) A chart recorder C2.
- (b) A temperature controller, W, manufactured by the West Division of Gulton Industries Ltd., Brighton. This was a West Viscount, three term controller, consisting of a preset potentiometer and a sensitive balance circuit. The heater output current was automatically varied to maintain a constant thermocouple emf. The manufacturers specified a control stability of $10\mu\text{V}$ under optimized conditions corresponding approximately to 0.5°K at 80K. However, the recorded stability on the other measuring devices, including the centre reading galvanometer in the controller, was nearer $2\mu\text{V}$.

Three additional parameters could be varied.

- (1) the percentage of feedback control in the circuit;
- (2) the integration time of the circuit, i.e. the response time of the measuring system;
- (3) the differentiation time of the measuring circuit.

The feedback control was set at the recommended value of 10%. The thermal response time of the sample system was recorded and found to be approximately 5 minutes. The integration time was set to this value and the differentiation time to $1/3$ of this value as recommended by the manufacturers.

Continuous thermocouple leads were used throughout, with no soldered joints other than at the measuring junctions. This avoided any errors due to thermal gradients at vacuum seals, etc. The leads to the controller were screened by an earthed cable, and the junctions to the controller were insulated with cotton wool.

The level of liquid helium in H was monitored by another copper-constantan thermocouple T3 with a liquid nitrogen reference junction N. The emf was recorded on another chart recorder C1 which was connected via relays to an alarm bell and to a micro-switch in series with the heating circuit. The thermocouple T3 was positioned approximately 10cm above the T_1 , T_2 reference junctions. The cryostat was filled with liquid helium and nitrogen every 8 hours for the duration of the experiment.

The liquid helium transfer lines were always precooled before filling with liquid helium. Due to the configuration of apparatus in the Dido shell it was necessary to operate from a gantry some 10ft above the cryostat, using multi-sectioned transfer lines. At no time during the experiment was the liquid helium level allowed to fall below the level of the monitoring thermocouple T3.

The temperature controller W provided a controlled heater current at 25V D.C. This was passed through the heaters in series and a neoprene vacuum seal S3. Resistances R1 and R2 (both 160Ω) were wound on fine Eureka wire above and below the sample space S. Resistance R3 (500Ω) acted

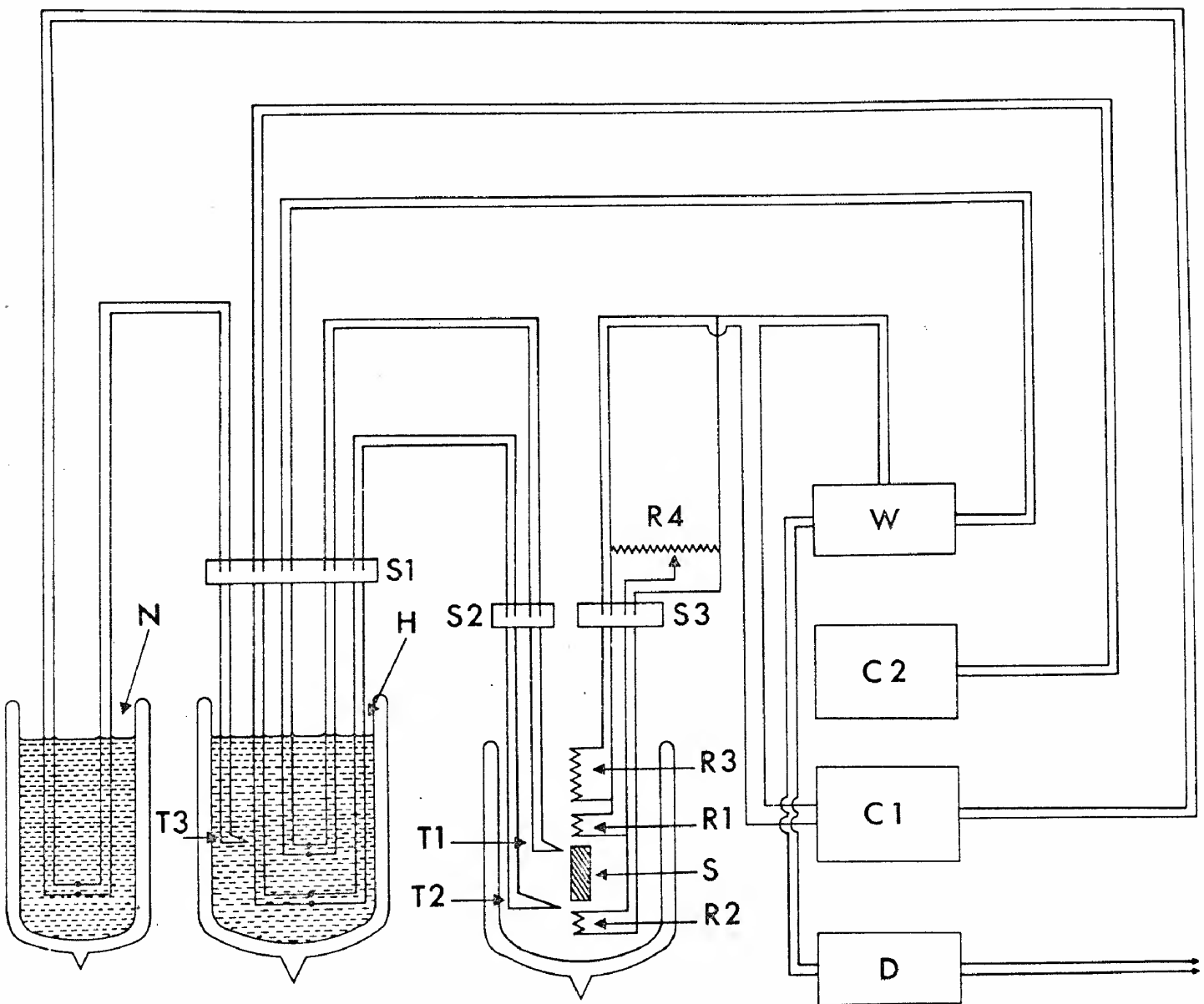


Figure A2.1 Temperature measurement and control circuit for the variable-temperature cryostat used in neutron diffraction experiments.

as an antisublimation heater. This prevented any sample sublimation to cooler parts of the tube while performing experiments at 78K. Because the sample space was supported only from above, a thermal gradient existed down the tube between T_1 and T_2 to which the heat from R3 also contributed. For this reason a trimming potentiometer R4 (50K Ω) was used to balance the currents in R1 and R2. Unfortunately the system was only sensitive to this adjustment over a period of 2 hours. In order to complete the experiment within the allocated period a compromise technique of maintaining a minimum gradient at 78K was adopted.

A graph showing the variation of this gradient with the mean temperature is shown in figure A2.2. The gradient measured from the lower thermocouple T_2 increases with lower mean temperature due to the decreased effect of R1 and R2. The lower thermocouple T_2 was positioned 15mm above the centre of R2 and T_1 was positioned 9mm below the centre of R1. This accounts for the weighted value of ΔT in figure A2.2.

The thermocouple emf was also recorded on a digital voltmeter D and printed on the teleprinter output of the diffractometer.

The radial temperature gradient in the DI sample system was measured in the following way. A small diameter glass probe was inserted from the top of the cryostat system into the sample space with a thermocouple inside. DI was then sublimed into the sample space and a gradient of approximately 0.5°K was measured between the probe and T_1 . However, the true gradient may be greater than this value because the probe and thermocouple provided a substantial input of heat from outside the system which would not be present in an actual experiment.

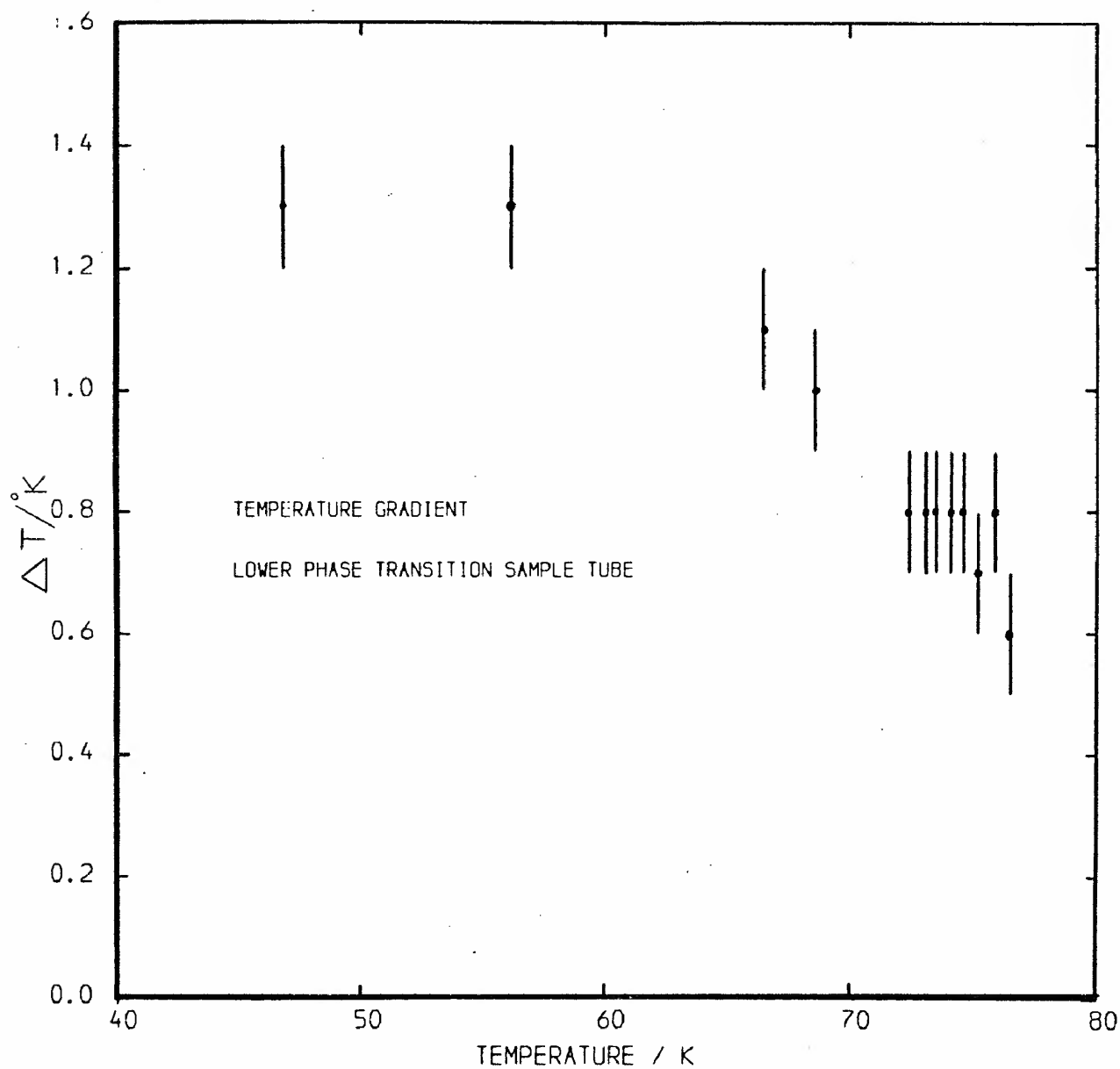


Figure A2.2 Temperature gradient across sample, as a function of temperature, for the sample tube used for the lower phase transition neutron diffraction experiment on DI.

References

- Abragam A., Oxford University Press (1961).
 'Principles of nuclear magnetism'.
- Adam G., J.Chem.Phys. 43, 662-669 (1965).
 'On the molecular kinetic theory of co-operative relaxation processes in dipolar liquid and crystalline phases'.
- Alpert N L., Phys.Rev. 75, 398-410 (1949).
 'Study of phase transitions by NMR phenomena'.
- Azaroff L V., Acta.Cryst. 8, 701-704 (1955).
 'Polarization correction for crystal-monochromatized X-radiation'.
- Bacon G E., Oxford University Press a) 61 b) 86 c) 217 d) 90 (1955).
 'Neutron diffraction'.
- Baker T W., George J D., Bellamy B A. and Causer R., Nature 210, 720-721 (1966)
 'Very high precision X-ray diffraction'.
- Batchelder D N. and Sidey G R., J.Sci.Instr. 2, (Series 2), 533 (1969).
 'A simple seal for leading wires into a vacuum system'.
- Bhagavantam S. and Venkataryuda T., Proc. Ind.Acad.Sci. 9, 224-258 (1939).
 'Raman effect in relation to crystal structure'.
- Bloch F., Hansen W W. and Packard M., Phys.Rev. 69, 127 (1946).
 'Nuclear induction'.
- Bloch, F., Hansen W W. and Packard M., Phys.Rev. 70, 474-485 (1946).
 'The nuclear induction experiment'.
- Bragg W L. and Williams E J., Proc.Royal Soc. A145, 699-730 (1934).
 'The effect of thermal agitation on atomic arrangements in alloys'.

Brauer G., Academic Press, N.Y., U.S.A. (1963).

'Handbook of preparative inorganic chemistry'.

Bridgman P.W., Proc.Amer.Acad.Arts & Sciences, 60, 303-383 (1925).

'Certain physical properties of single crystals of tungsten, antimony, bismuth, tellurium, cadmium, zinc and tin'.

Brown N. and Cole R H., J.Chem.Phys. 21, 1920-1926 (1953).

'Dielectric properties of hydrogen halides I. hydrogen bromide'.

Busing W R. and Levy H A., Acta.Cryst. 17, 142-146 (1964).

'The effect of thermal motion on the estimation of bond lengths from diffraction measurements'.

Busing W R., Martin K O. and Levy H A., ORNL-TM-305 (1962).

'ORFLS - a least-squares structure refinement program'.

Chang T S., Proc.Camb.Phil.Soc. 33, 524-533 (1937).

'Specific heats of solids due to molecular rotations'.

Clusius K. and Wolf G., Zeit.Naturforschung 2a, 495-504 (1947).

'Ergebnisse der Tieftemperaturforschung. IV. Molwärmen, Umwandlungs- und Schmelzwärmen sowie Entropien von DCl, DBr und DI.'

Cole R H., J.Chem.Phys. 42, 637-643 (1965).

'Correlation function theory of dielectric relaxation'.

Cole K S. and Cole R H., J.Chem.Phys. 9, 341-351 (1941).

'Dispersion and absorption in dielectrics. I. alternating current characteristics'.

Cole R H. and Havriliak S., Disc.Fara.Soc. 23, 31-38 (1957).

'Dielectric relaxation in solid hydrogen halides'.

Cowan M. and Gordy W., Phys.Rev. 111, 209-211 (1958).

'Precision measurements of millimeter and submillimeter wave spectra: DCl, DBr and DI'.

Cruickshank D W J. and Robertson A P., Acta.Cryst. 6, 698-705 (1953).

'The comparison of theoretical and experimental determinations of molecular structures, with applications to naphthalene and anthracene'.

Cruickshank D W J., Acta.Cryst. 9, 747-758 (1956).

(a) 'The determination of the anisotropic thermal motion of atoms in crystals'.

(b) 'The analysis of the thermal motion of molecules in crystals'.

(c) 'Errors in bond lengths due to rotational oscillations of molecules'.

Davidson D W., Can.J.Chem., 39, 571-594 (1961).

'Dielectric relaxation in liquids I. The representation of relaxation behaviour'.

Davidson D W. and Cole R H., J.Chem.Phys. 19, 1484-1490 (1951).

'Dielectric relaxation in glycerol, propylene glycol and n-propanol'.

Debye P., Chemical Catalogue Co., N.Y. (1929).

'Polar molecules'.

Denbigh K G., Trans.Fara.Soc. 36, 936-948 (1940).

'The polarisabilities of bonds'.

Eucken A. and Karwat E., Zeit.Phys.Chem. 112, 467-490 (1924).

'Die Bestimmung des Wärmehaltes einiger kondensierter Gase.'

Farrow R F C., Ph.D. Thesis, London University (1969).

'The phase transformations in solid hydrogen chloride and deuterium chloride'.

Fowler R H., Proc.Royal.Soc. London, A149, 1-28 (1935).

'A theory of the rotations of molecules in solids and the dielectric constant of solids and liquids'.

Fowler R H., Macmillan Co., N.Y., U.S.A. Chapter 21 (1936).

'Statistical mechanics'

Frenkel J., Oxford University Press, Chapter 2 (1946).

'Kinetic theory of liquids'.

Genin D J. O'Reilly D E., Peterson E M. and Tsang T., J.Chem.Phys. 48,
4525-4532 (1968).

'NMR of the solid phases of HCl, HBr and HI'.

Giauque W F. and Wiebe R., J.Amer.Chem.Soc., 51, 1441-1449 (1929).

'The heat capacity of hydrogen iodide from 15K to its boiling point
and its heat of vaporization. The entropy from spectroscopic data'.

Glarum S H., J.Chem.Phys. 33, 1371-75 (1960).

'Dielectric relaxation of polar liquids'.

Groenewegen P P M. and Cole R H., J.Chem.Phys. 46, 1069-1074 (1966).

'Dielectric properties of hydrogen halides III high frequency
dispersion in solid phases of HI and HBr'.

Halford R S., J.Chem.Phys. 14, 8-15 (1946).

'Motions of molecules in condensed systems. I. Selection rules,
relative intensities and correlation effects for Raman and infra-red
spectra'.

Hanamura E., J.Chem.Phys.Soc. Japan, 28, 192-194 (1970).

'On the phase transitions of hydrogen halide crystals'.

Hanamura E., J.Chem.Phys. 52, 797-802 (1970).

'Effect of charge transfer on Raman scattering of hydrogen halides'.

Havriliak S. and Cole R H., J.Chem.Phys. 23, 2455-2456 (1955).

'On dielectric properties of solid hydrogen and deuterium halides'.

Hewat A W., Harwell Report RRL 73/239 (1973).

'The Rietveld computer program for the profile refinement of neutron diffraction powder patterns modified for anisotropic thermal vibrations'.

Hiebert G L. and Hornig D F., J.Chem.Phys. 26, 1762-63 (1957).

'New phase transition in HI'.

Hornig D F. and Osberg W E., J.Chem.Phys. 23, 662-670 (1955).

'Infra-red spectrum and the structure of the low-temperature phases of crystalline HCl, HBr and HI'.

Hoshino S., Shimacka K., Niimura N., Motegi H. and Maruyama N.,

J.Phys.Soc. Japan, 28, 189-191 (1970).

'Ferroelectricity and phase transitions in solid hydrogen halides'.

International tables for crystallography, I.U.Cr., Kynoch Press II, 299 (1959).

Johnson M W., Ph.D. Thesis, London University (1970).

'Structure and phase transformations in solid hydrogen and deuterium bromides'.

Johnson M W., Private communication.

Johnson M W. and Sándor E., Acta.Cryst. (1975) in press.

'The crystal structure of deuterium fluoride'.

Kittel C., Wiley, N.Y., a) 390 b) 389 c) 518 (1967).

'Introduction to solid state physics'.

King H W. and Preece C M., Advances in X-ray analysis 10, 354-365 (1967).

'Precision lattice parameter determination at liquid helium temperatures by double-scanning diffractometry'.

Kirkwood J G., J.Chem.Phys. 8, 205-212 (1940).

'On phase changes in crystals arising from hindered molecular rotation'.

Kobayashi K K. Hanamura E. and Shishido F., Phys.Lett. 28A, 718-719 (1969).

'On the phase transitions in hydrogen halides'.

Krieger T J. and James H M., J.Chem.Phys. 22, 796-814 (1954).

'Successive orientational transitions in crystals'.

Kruis A. and Kaischew R., Z.Phys.Chem. B41, 427-432 (1938).

'Untersuchung der Umwandlungen der kondensierten Halogenwasserstoffe mit dem Polarisationsmikroskop.'

Kubo R., J.Phys.Soc. Japan, 12, 570-586 (1957).

'Statistical-mechanical theory of irreversible processes'.

Landau L., Physik Zeit Sowjetunion 11, (26) 545-555 (1937).

'Zur Theorie der Phasenumwandlungen.II.'

Levy H A., Acta.Cryst. 9, 679 (1956).

'Symmetry relations among coefficients of the anisotropic temperature factor'.

London F., Z.Physik 63, 245-279 (1930).

'Zur Theorie und Systematik der Molekularkräfte.'

London F., Trans.Fara.Soc. 33, 8-26 (1937).

'The general theory of molecular forces'.

Loopstra B O., Nucl.Instr.Methods, 44, 181-187 (1966).

'Neutron powder diffractometry using a wavelength of 2.6Å'.

Lorch E., J.Phys. C2, 229-237 (1969).

'Neutron diffraction by germania, silica and radiation-damaged glasses'.

Maruyama N., J.Jap.Phys.Soc., 40, XV 20 (1970).

'Stress-free single crystals of ferroelectric hydrogen halides'.

Mauer F A. and Keffer C J., J.Chem.Phys. 42, 1465 (1964).

'Polymorphism in hydrogen iodide'.

Natta G., Nature, 126, 97 (1930).

'The crystal structure of hydrogen iodide and its relation to that of xenon'.

Natta G., Nature, 127, 235 (1931).

'The crystal structure and polymorphism of hydrogen halides'.

Ogunade S O., M.Phil. Thesis, London University (1969).

'Phase transitions in solid hydrogen and deuterium sulphides'.

O'Reilly D E., J.Chem.Phys. 28, 1262-1264 (1958).

'Quadrupolar broadened nuclear magnetic resonance of polycrystalline solids'.

O'Reilly D E. and Tsang T., J.Chem.Phys., 46, 1291-1304 (1967).

'Deuteron magnetic resonance and proton relaxation times in ferro-electric ammonium sulphate'.

Pauling L., Phys.Rev. 36, 430-443 (1930).

'The rotational motion of molecules in crystals'.

Powles J G., Trans.Fara.Soc. 32, 430-439 (1952).

'The phase transitions in the solid hydrogen halides'.

Powles J G., Adv.in Physics, 22, 1-56 (1973).

'The structure of molecular liquids by neutron scattering'.

Purcell E.M., Torrey H C. and Pound R V., Phys.Rev. 69, 37-38 (1946).

'Resonance absorption by nuclear magnetic moments in a solid'.

Reeves R B., Ph.D. Thesis, John Hopkins University (1964).

'The infra-red spectra of silylacetylene and methylsilylacetylene and solid HI'.

Savoie R. and Anderson A., J.Chem.Phys. 44, 548-556 (1966).

'Infra-red and Raman studies of crystalline HCl, DCl, HBr and DBr'.

Schneider W G., J.Chem.Phys. 23, 26-30 (1955).

'Properties of the hydrogen bond. The role of the lone-pair electrons'.

Science Research Council, N.B.R.C. Report on Neutron Beam Facilities (1973).

Shimaoka K. Niimura N. and Hoshino S., Japan J.of Applied Physics 10, 933 (1971).

'Special cryostat for neutron diffraction'.

Shirane G. and Minckiewicz V J., Nucl.Instr. and Meth. 89 109-110 (1970).

'Pyrolytic graphite as a high-efficiency filter for 13-15 MeV neutrons'.

Simon A., Zeit.Naturforsch B25, 1489 (1970).

'Phasentransformationen in festem HBr und HJ'.

Smyth CP. and Hitchcock C S., J.Amer.Chem.Soc. 55, 1830-1840 (1933).

'Dipole rotation and the transitions in the crystalline hydrogen halides'.

Stewart J M., Computer Science Center, Univ. Maryland, U.S.A.

'X-ray 70 computer program manual'.

Swenson R W. and Cole R H., J.Chem.Phys. 22, 284-288 (1954).

'Dielectric properties of hydrogen halides II hydrogen chloride'.

Tisza L., Phys.Rev. 72, 161-162 (1947).

'Phase transition in the hydrogen halides'.

Torrey H C., Phys.Rev. 92, 962-969 (1953).

'Nuclear spin relaxation by translational diffusion'.

Winston H W. and Halford R S., J.Chem.Phys. 17, 607-616 (1949).

'Motions of molecules in condensed systems. V. Classification of motions and selection rules for spectra according to space symmetry'.

Wright A C., Adv.in Structure Research by Diffraction Methods 5, 1-84 (1974).

'The structure of amorphous solids by X-ray and neutron diffraction'.

Zunino J., Z.Physik 100, 335-344 (1936).

'Die kernschwingungsbaden des festen brom-und jodwasserstoffs im gebiet ihrer umwandlungspunkte'.

Zwanzig R W., J.Chem.Phys. 38, 2766-2772 (1963).

'Dielectric relaxation in a high temperature dipole lattice'.